

CO₂ and O₂ Dynamics
and Ocean-Atmosphere Fluxes
in the Eastern Tropical North Atlantic

Dissertation zur Erlangung des Doktorgrades der
Mathematisch-Naturwissenschaftlichen Fakultät
der Christian-Albrechts-Universität zu Kiel

vorgelegt von **Björn Fiedler**

Kiel, Dezember 2012

Referent/in: Prof. Dr. Arne Körtzinger

Korreferent/in: Dr. Hermann W. Bange

Tag der mündlichen Prüfung: 22.01.2013

Zum Druck genehmigt: 22.01.2013

gez. Prof. Dr. rer. nat. Wolfgang J. Duschl

- Dekan -

Τα πάντα ρει, μηδέποτε κατά τ'αυτό μένειν
Everything flows, nothing stands still.

Heraclitus, ~500 B.P.

Manuscript List

This thesis contains the following manuscripts which have been prepared in collaboration with other authors:

Manuscript A:

Citation: Fietzek, P., **B. Fiedler**, T. Steinhoff, and A. Körtzinger, 2013: In situ accuracy assessment of a novel underwater CO₂ sensor based on membrane equilibration and NDIR spectrometry, *to be submitted to J. Atmos. Oceanic Technol.*, in preparation.

My contribution:

- Operating pCO₂ sensors, reference instruments and measurements during two research cruises
- Pre-processing sensor data and processing of reference data
- Discussing results, illustrating meta data and commenting on the manuscript

Manuscript B:

Citation: **Fiedler, B.**, P. Fietzek, N. Vieira, P. Silva, H. C. Bittig, and A. Körtzinger, 2013: In situ CO₂ and O₂ measurements on a profiling float, *J. Atmos. Oceanic Technol.*, **30**, 112-126.

My contribution:

- Developing, field-testing and deploying/recovering the float prototype
- Performing CTD tests and measuring reference samples
- Processing float data and calculating results
- Writing the publication

Manuscript C:

Citation: Karstensen, J., **B. Fiedler**, P. Brandt, R. Zantopp, J. Hahn, A. Körtzinger, M. Visbeck, G. Fischer, O. Melicio, and D. R. Wallace, 2012: Dead-Zone Eddies in the Tropical Eastern North Atlantic Ocean, *Nature*, under review.

My contribution:

- Processing float data
- Performing the biogeochemical calculations
- Discussing results and commenting on the manuscript

Contents

1 Introduction	15
1.1 Scientific Background	15
1.2 Study Area	22
1.3 Observational Oceanography.....	25
1.4 Thesis Structure.....	29
2 Material & Methods	31
2.1 Laboratory Measurements.....	31
2.2 In Situ Instrumentation	34
2.2.1 In Situ Sensors for $p\text{CO}_2$	34
2.2.2 In Situ Sensors for $p\text{O}_2$	36
2.2.3 Profiling Floats.....	38
2.3 Development of Profiling Float Prototypes.....	39
2.3.1 First and Second Float Generation	40
2.3.2 In Situ Oxygen Offset Correction.....	42
2.4 CVOO & CVAO Facilities	43
3 Technical Results	47
3.1 Sensor Evaluations	47
3.1.1 Evaluation of the PSI CO_2 -Pro sensor	47
3.1.2 Evaluation of the HydroC sensor [Manuscript A].....	53
3.2 Float Evaluations	77
3.2.1 1G Float	77
3.2.2 2G Float [Manuscript B]	81
3.3 Discussion.....	99
4 Scientific Results	105
4.1 Surface Processes.....	105
4.1.1 Long-term Temporal Variability	105
4.1.2 Seasonal Variability	110
4.1.3 Diel variability.....	120
4.2 Subsurface Processes	122
4.2.1 Carbon and Oxygen Distributions.....	122
4.2.2 Episodic Anoxic and Hypoxic Events [Manuscript C].....	127
5 Conclusions & Outlook	137
6 References	143
7 Acknowledgements	153
I. Appendix	155

Abstract

Detailed knowledge about the CO₂ exchange between ocean and atmosphere plays a key role in understanding the past and present state of the global carbon cycle and predicting its future. Despite a growing data base, the present global uptake rate of the world ocean for anthropogenic CO₂ still has an uncertainty of 50 % (+2.0 ±1.0 Pg C yr⁻¹) which to a major extent is due to limited temporal and spatial coverage of CO₂ measurements within large parts of the oceans. This calls for an improvement.

So far vertical profiles of CO₂ and O₂ can only be assessed through laborious discrete sampling. Therefore, a major aim of this thesis was to develop simultaneous sensor based measurements of CO₂ and O₂ from an autonomous profiling device. For this purpose, a small-sized and submersible pCO₂ sensor was assessed for accuracy of measurements in underway mode during two independent cruises. Sensor accuracy for underway measurements was found to be <4 µatm. Subsequently, a typical profiling Argo float was equipped with this pCO₂ sensor and an optode O₂ sensor for high resolution measurements in the surface ocean layer. Consecutive deployments of the prototype profiling float were carried out at the Cape Verde Ocean Observatory (CVOO) in the eastern tropical North Atlantic. The profiling float performed upcasts every 31 h while measuring pCO₂, O₂, salinity, temperature and hydrostatic pressure in the upper 200 m of the water column. Accuracies for float-borne measurements of pCO₂ were found to be 10 – 15 µatm for water column and 5 µatm for surface measurements. Elaborate in-air measurements for in situ offset correction of O₂ measurements yielded an accuracy of 2 µmol kg⁻¹.

Time series observations for CO₂ and O₂ were established at CVOO over the course of this thesis. By combination of float-borne and ship-based ocean time series data with atmospheric measurements at the Cape Verde Atmospheric Observatory (CVAO) a first assessment of seasonal cycles for O₂ and CO₂ air-sea gas exchange (ASE) was conducted. Continuous O₂ supersaturation of the surface layer drives a permanent outgassing over the year (5.0 ±2.5 mol m⁻² yr⁻¹) with only minor seasonal variation, while CO₂ air-sea fluxes show a pronounced uptake of atmospheric CO₂ during winter/spring which turns into a moderate outgassing during early summer. On an annual scale in- and outgassing was found to be nearly balanced with a residual net CO₂ influx of -0.08 ±0.32 mol m⁻² yr⁻¹. The summer decrease in dissolved inorganic carbon (DIC) of ~35 µmol kg⁻¹ was found to be mainly driven by net community production (NCP; ~79 %) and to a lesser extent by ASE (~21 %). Overall NCP derived from mass budget calculations was found to be 3.4 mmol C m⁻² d⁻¹.

Furthermore, this thesis reports on the occurrence of hypoxic to anoxic waters in the normally well-oxygenated open North Atlantic Ocean observed by an autonomous profiling float as well as by

mooring based observations at CVOO. In general, oxygen depletion within the water column due to bacterial oxidation of organic matter is a common feature in ocean water masses. Severe hypoxic ($<20 \mu\text{mol O}_2 \text{ kg}^{-1}$) as well as anoxic ($<1 \mu\text{mol O}_2 \text{ kg}^{-1}$) waters as a consequence of limited lateral exchange and/or ventilation combined with enhanced production of organic matter can be observed in many coastal areas of the world ocean. However, within the framework of this thesis exceptionally low O_2 concentrations just below the mixed layer were found in the open North Atlantic Ocean ($0 - 20 \mu\text{mol kg}^{-1}$). Such low concentrations have never been reported before for this region. The O_2 depleted water masses were isolated and transported by mesoscale eddies which originated in the coastal Mauritanian upwelling and propagated westwards. Obtained data suggest that the eddies' subsurface layers were subject to intensified respiration (up to $0.15 \mu\text{mol O}_2 \text{ kg}^{-1} \text{ d}^{-1}$) due to elevated payloads of organic matter resulting in strong hypoxic and anoxic conditions. A carbon export flux of $0.24 \pm 0.07 \text{ g C m}^{-2} \text{ d}^{-1}$ out of the euphotic zone was determined for one of these eddies.

Zusammenfassung

Um den globalen Kohlenstoffkreislauf von seiner Vergangenheit bis hin zu zukünftigen Veränderungen besser verstehen und beschreiben zu können, bedarf es eines präzisen Verständnisses des Gasaustausches von CO₂ zwischen dem Ozean und der Atmosphäre. Obgleich die Datengrundlage hierfür stetig zunimmt, beinhaltet die Abschätzung der ozeanischen Senke von anthropogenem CO₂ immer noch eine Unsicherheit von 50 % (+2.0 ±1.0 Pg C a⁻¹). Diese ist zu großem Teil auf eine unzureichende raumzeitliche Abdeckung von CO₂ Messungen in den Ozeanen zurückzuführen und es bedarf daher einer deutlichen Verbesserung dieser Situation.

Bisher konnten Vertikalprofile für CO₂ und O₂ nur durch verhältnismäßig aufwendige diskrete Probennahmen aufgelöst werden. Daher war eines der Ziele der vorliegenden Arbeit die Entwicklung und Erprobung von sensorbasierten CO₂ und O₂ Messungen auf einem autonom profilierenden Tiefendrifter. Zu diesem Zweck wurde ein neuartiger Unterwasser CO₂ Sensor während zwei Forschungsexpeditionen hinsichtlich seiner Genauigkeit untersucht. Messungen dieses Sensors im Durchflussbetrieb ergaben eine Genauigkeit von <4 µatm. Ein konventioneller Argo Tiefendrifter wurde mit einem solchen CO₂ Sensor und zusätzlich einem O₂ Sensor ausgestattet, um hochaufgelöste Messungen im Oberflächenozean autonom durchführen zu können. Der Prototyp Tiefendrifter wurde insgesamt viermal im tropischen Nordostatlantik in unmittelbarer Nähe zum kapverdischen Ozeanobservatorium (CVOO) eingesetzt und lieferte alle 31 h hochaufgelöste Vertikalprofile für CO₂ Partialdruck ($p\text{CO}_2$), O₂, Salzgehalt, Temperatur und hydrostatischen Druck in den oberen 200 m der Wassersäule. Gemessener $p\text{CO}_2$ während dieser Vertikalprofile erreichte eine Genauigkeit von 10 – 15 µatm, wohingegen die $p\text{CO}_2$ Messungen unmittelbar an der Oberfläche eine Genauigkeit von 5 µatm aufwiesen. Eine neu entwickelte Methode zur in situ Drift-Korrektur des O₂ Sensors ergab eine Genauigkeit von 2 µmol kg⁻¹.

Im Rahmen dieser Doktorarbeit wurden Zeitserienbeobachtungen für CO₂ und O₂ bei CVOO erfolgreich etabliert. Diese schiffsbasierten Messungen wurden zusammen mit den Tiefendrif-tergestützten Beobachtungen, sowie mit atmosphärischen CO₂ und O₂ Messungen am kapverdischen Atmosphärenobservatorium (CVAO) verwendet, um die jahreszeitliche Variabilität des Ozean-Atmosphäre Flusses für CO₂ und O₂ zu bestimmen. Für O₂ wurde ein kontinuierliches Ausgasen aus dem Ozean in die Atmosphäre mit nur geringer saisonaler Variabilität beobachtet (5.0 ±2.5 mol m⁻² a⁻¹), wohingegen für atmosphärisches CO₂ der Ozean eine ausgeprägte Senke im Winter/Frühling darstellt, welche sich dann in eine Quelle während der Sommermonate entwickelt. Über den Zeitraum eines gesamten Jahres befinden sich diese beiden Prozesse annähernd im Gleichgewicht (-0.08 ±0.32 mol m⁻² a⁻¹). Die beobachtete Erniedrigung im gelösten anorganischen

Kohlenstoff (DIC) von $35 \mu\text{mol kg}^{-1}$ wurde hauptsächlich aufgrund von Netto-Kohlenstoffaufnahme durch die Planktongemeinschaft (NCP; $\sim 79\%$) und zu einem geringeren Anteil vom Gasaustausch ($\sim 21\%$) verursacht. Für diesen Zeitraum wurde mit Hilfe eines Massenbudgets eine NCP Rate von $3.4 \text{ mmol C m}^{-2} \text{ d}^{-1}$ bestimmt.

Weiterhin wird in dieser Dissertation über die ungewöhnliche Beobachtung von hypoxischen als auch anoxischen Wassermassen im offenen tropischen Nordatlantik berichtet. Die Detektion solcher Wassermassen erfolgte durch autonome Sauerstoffmessungen sowohl auf der CVOO Verankerung als auch durch einen profilierenden Tiefendrifter. Allgemein können hypoxische ($< 20 \mu\text{mol O}_2 \text{ kg}^{-1}$) als auch anoxische ($< 1 \mu\text{mol O}_2 \text{ kg}^{-1}$) Wassermassen als Konsequenz aus limitierender Wassermassenventilation und erhöhter Respiration von organischen Material entstehen, welches im Atlantik eigentlich nur für küstennahe Ozeanregionen bekannt ist. Jedoch gelang es im Rahmen dieser Arbeit solche Wassermassen mit außerordentlich niedrigen Sauerstoffgehalten direkt unterhalb der Deckschicht ($0 - 20 \mu\text{mol kg}^{-1}$) und dazu im offenen tropischen Nordatlantik zu identifizieren. Solche drastischen O_2 Anomalien sind gänzlich unbekannt in dieser Region. Die Analyse der Daten zeigt, dass diese Wassermassen aus mesoskaligen Wirbelstrukturen mit Ursprung im Mauretanischen Küstenauftrieb resultieren. In diesen Wirbeln findet eine erhöhte Sauerstoffzehrung von bis zu $0.15 \mu\text{mol O}_2 \text{ kg}^{-1} \text{ d}^{-1}$ statt, welche begünstigt durch eine hohe Fracht an organischem Material bis zur völligen Aufzehrung von O_2 führen kann. Für einen dieser Wirbel konnte eine Exportrate von Kohlenstoff von insgesamt $0.24 \pm 0.07 \text{ g C m}^{-2} \text{ d}^{-1}$ in die darunterliegenden Wasserschichten ermittelt werden.

1 Introduction

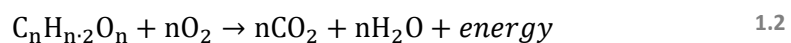
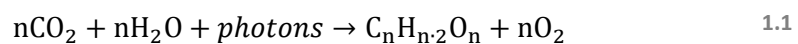
Observing and understanding the global carbon cycle with all its mechanisms and processes in different reservoirs and on various timescales is one of the key challenges when assessing anthropogenic perturbations of the global ecosystem. This work focuses on the interplay of carbon species between oceanic and atmospheric reservoirs within the region of the eastern tropical North Atlantic and on how to better resolve processes occurring at this interface. Therefore this chapter provides background information about

- the global carbon cycle with an emphasis on the marine reservoir and the air-sea gas exchange (1.1),
- the characteristics of the study area in the eastern tropical North Atlantic (1.2) and
- the challenges of better assessing carbon cycle dynamics in the world's oceans and how to master these (1.3).

1.1 Scientific Background

The Global Carbon Cycle and its Anthropogenic Perturbation

Carbon is one of the most important elements on earth as it forms the basis for all organic life forms whose metabolism is primarily based on the following (simplified) stoichiometry:



where eqn. 1.1 describes construction of biomass by photosynthesis (e.g., carbohydrates) and eqn. 1.2 aerobic respiration of organic matter to gain energy. These processes are the key drivers for the global carbon cycle in the terrestrial and marine biospheres (Figure 1.1) and can be clearly observed (Hall et al. 1975; Steinberg et al. 2001).

Furthermore, carbon dioxide (CO₂) in the atmosphere is known to be an important greenhouse gas which is responsible for maintaining moderate temperatures and thereby sustaining life on earth. However, human activities over the past 200 years have significantly altered this cycle (Falkowski et al. 2000). For instance, atmospheric levels of CO₂ have increased from pre-industrial values of ~280 ppmv to recently observed 400 ppmv which is mainly due to emissions of CO₂ by fossil fuel combustion (Boden et al. 2012).

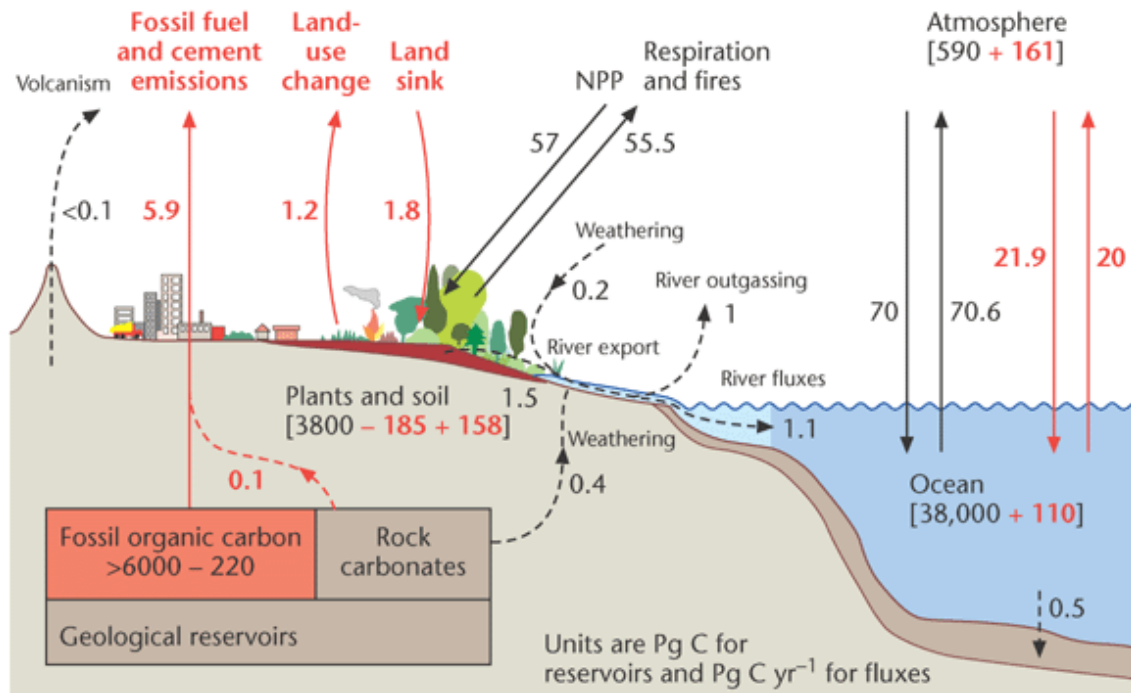


Figure 1.1 Scheme of the global carbon cycle including preindustrial carbon reservoir sizes (in brackets) and carbon fluxes between those (arrows incl. numbers). Red arrows and numbers denote anthropogenic carbon. Credit: PMEL Carbon Group, NOAA.

However, only half of the anthropogenic CO_2 has accumulated in the atmospheric reservoir (Solomon et al. 2007) which points at pronounced sinks in remaining reservoirs. Sabine et al. (2004) determined the ocean as a significant sink for atmospheric anthropogenic CO_2 of up to $\sim 48\%$. Thus, the ocean as the largest carbon reservoir on earth plays a dominant role in buffering anthropogenic CO_2 emissions (Sabine and Tanhua 2010). The main process that drives the exchange of carbon between both reservoirs is air-sea gas exchange (hereafter ASE) – a process that is tightly connected to the carbonate system in seawater (refer to next paragraph).

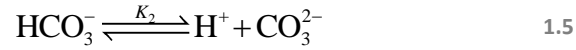
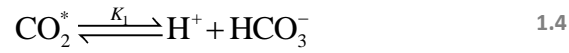
The Marine Carbon Cycle

Figure 1.1 illustrates the partitioning of carbon between the oceanic and the atmospheric reservoirs and denotes the ocean to host the largest one. This relation cannot be found for other gases even with similar solubilities (e.g., O_2 or N_2). This illustrates the relevance of the complex carbon chemistry in seawater for exchange of carbon between the ocean and the atmosphere. Hence, this paragraph provides a brief and simplified introduction into the marine carbon chemistry and ends with a short description of processes affecting this cycle.

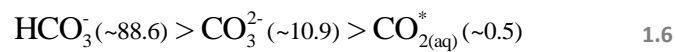
When atmospheric $\text{CO}_{2(\text{gas})}$ enters the surface ocean it becomes hydrated ($\text{CO}_{2(\text{aq})}$) and formally reacts with water to carbonic acid (eqn. 1.3):



However, true carbonic acid is only a minor form in seawater as its concentration is less than 0.3% of $\text{CO}_{2(\text{aq})}$. The sum of both species is often summarized as CO_2^* which is a weak acid and can dissociate into the following ions:

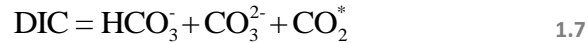


where K_1 and K_2 are the stoichiometric dissociation constants which are a function of temperature and ionic strength (salinity). At common seawater **pH** ranges of 7.8 – 8.4 ($\text{pH} = -\log_{10}(\text{H}^+)$) thermodynamic equilibrium creates the following typical proportions of carbon species:



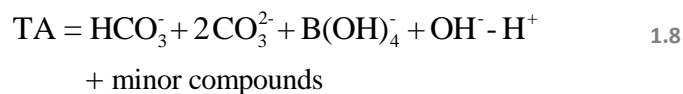
where values in parenthesis represent the relative abundance of each form in percentage for global mean surface seawater properties (Sarmiento and Gruber 2006). This speciation of carbon forms in seawater is the reason for the buffer capacity of the oceans when taking up atmospheric CO_2 .

Since direct quantification of each species in a seawater matrix is not feasible, these inorganic species are summarized as one parameter abbreviated as **DIC** (dissolved inorganic carbon):



The total amount of DIC in seawater can be determined accurately (Millero 2007).

Another important measure of the marine carbonate system is the total alkalinity (**TA**) of seawater (Wolf-Gladrow et al. 2007) which is defined as follows:



This parameter summarizes the seawater's overall charge balance or in other words the total buffer capacity of seawater to bind free protons.

The smallest fraction of the marine carbonate system, CO_2^* , is the parameter of most interest when assessing the net flux of CO_2 between the ocean and the atmosphere since it is the only volatile species of the marine carbonate system (see next subsection). It usually is being determined as the partial pressure of CO_2 (**$p\text{CO}_2$**) in seawater and is related to CO_2^* by Henry's law:



where K_{H} is the Henry's law constant as a function of temperature and salinity.

The four important parameters of the carbonate system described above (pH, TA, DIC and $p\text{CO}_2$) can be accurately quantified by analytical methods. However, due to precisely determined dissociation constants for the speciation of the carbonate system (Millero 2007) one has to only determine two out of these four parameters in order to compute the remaining ones. Figure 1.2 illustrates the relationships among the four main parameters.

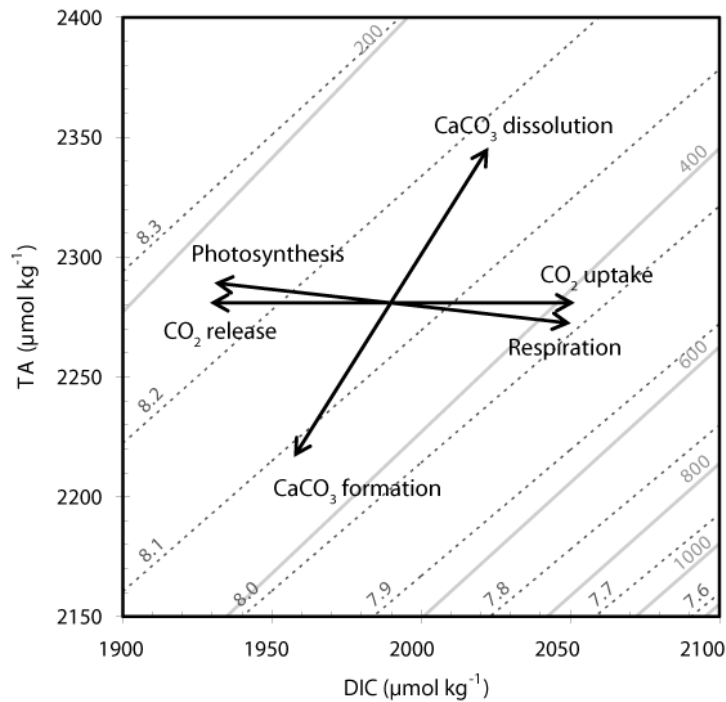


Figure 1.2 Degrees of freedom for the marine carbonate system. By determining two out of the four measurable parameters the remaining ones can be computed. Black dotted isolines denote pH and gray solid isolines $p\text{CO}_2$. Black arrows illustrate processes affecting the carbonate system (as vectors). Figure adapted from Körtzinger (2010).

Changes in carbonate parameters (illustrated as vectors in Figure 1.2) can have different reasons. Basically, there are three major processes that actively alter the marine carbon cycle and thereby atmospheric CO_2 levels as well:

- Solubility pump: Deep convection of cold surface water masses is the key mechanism for a net transport of CO_2 into the deep ocean until thermohaline circulation brings water masses up to the surface again. As CO_2 solubility increases with decreasing sea surface temperature (SST), cold water masses being transported to depth (e.g., in high latitudes) are enriched in CO_2 . The process for taking up atmospheric CO_2 is ASE which has a clear impact on DIC, $p\text{CO}_2$ and pH but no impact on TA (Figure 1.2).
- Soft tissue pump: Biological production of organic matter is a net fixation of DIC as most of organic matter is being transported as (dead) particles or fecal pellets to the interior ocean (Figure 1.3). The strength of this pump highly depends on availability of nutrients such as nitrate and iron and is thus unevenly distributed over the world's oceans. Photosynthesis and

respiration (eqn. 1.1 & 1.2) are the dominant processes that alter the marine carbonate system. As a consequence, distinct changes in DIC and only minor changes in TA can be observed (Figure 1.2).

- **Hard tissue pump:** Formation of inorganic calcium carbonate (CaCO_3) in surface layers is driven by calcifying organism that take up DIC in order to form their shells. At the same time $p\text{CO}_2$ levels increase since CO_2 is being released during CaCO_3 formation (Figure 1.2). As organisms die, utilized inorganic carbon sinks to subsurface layers (Figure 1.3) and to most extent dissolves due to decreasing pH at greater depth. A net flux of DIC out of the euphotic zone is caused by this pump. The hard tissue pump has the strongest impact on TA as Figure 1.2 illustrates.

Processes described above show that a comprehensive and accurate assessment of the carbonate system helps to better detect and understand the marine carbon cycle with its recent changes.

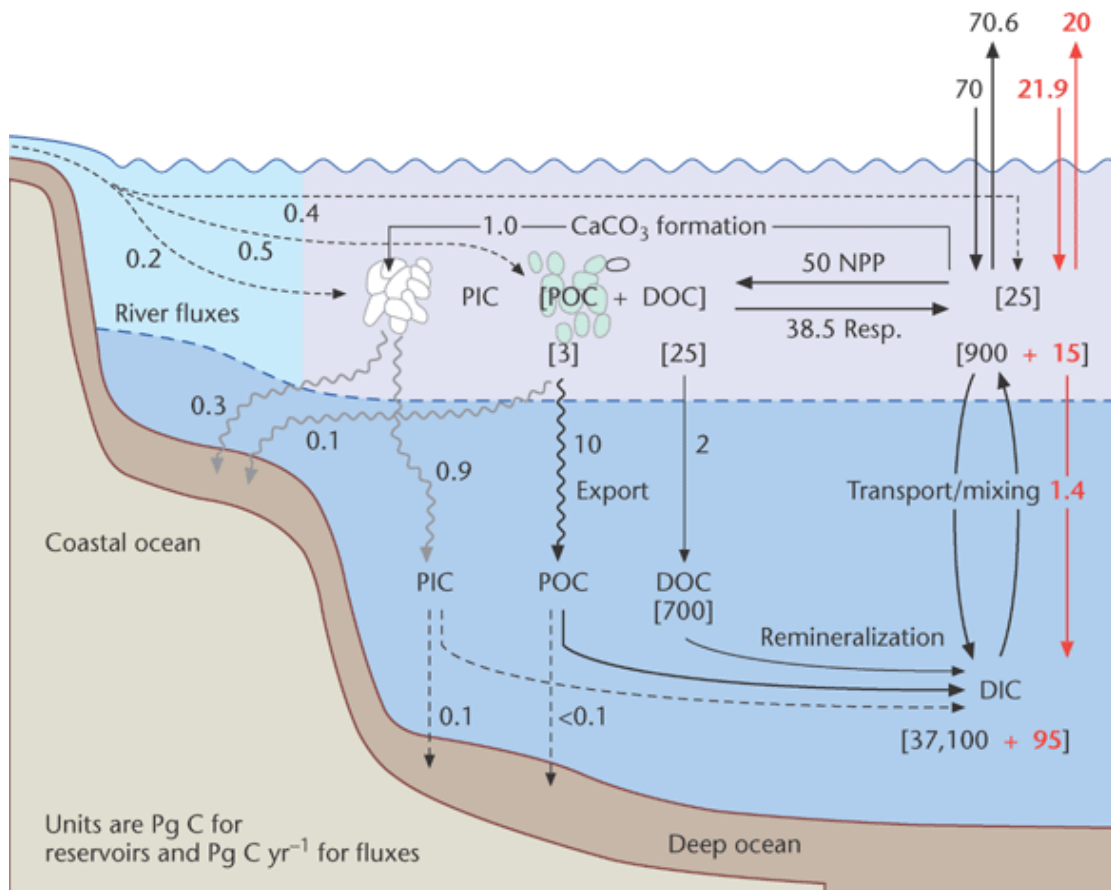


Figure 1.3 Detailed scheme of the marine carbon cycle and related mechanisms (refer to text) incl. preindustrial carbon reservoir sizes (in brackets) and carbon fluxes between those (arrows incl. numbers). Red arrows and numbers denote anthropogenic carbon. Credit: PMEL Carbon Group, NOAA.

Air-Sea Gas Exchange

The exchange rate (flux density) of a dissolved gas (here CO_2) in seawater with an overlying air mass is in general determined by the following bulk equation:

$$F_{\text{CO}_2} = k \cdot K_{\text{H}} \cdot \Delta p\text{CO}_2 \quad 1.10$$

where k is the transfer velocity (typically parameterized as a function of wind speed; see below), K_{H} the temperature and salinity dependent CO_2 solubility and $\Delta p\text{CO}_2$ the difference of $p\text{CO}_2$ between the surface ocean and the atmosphere as the thermodynamic driving force of F_{CO_2} .

The transfer velocity k can be parameterized as a power function of wind speed at 10 m height. Several studies have investigated this wind speed dependence over more than two decades with varying results (Liss and Merlivat 1986; Wanninkhof 1992; Nightingale et al. 2000; Sweeney et al. 2007). Figure 1.4 illustrates dependencies of F_{CO_2} to wind speed derived from such parameterizations (refer to figure caption for details).

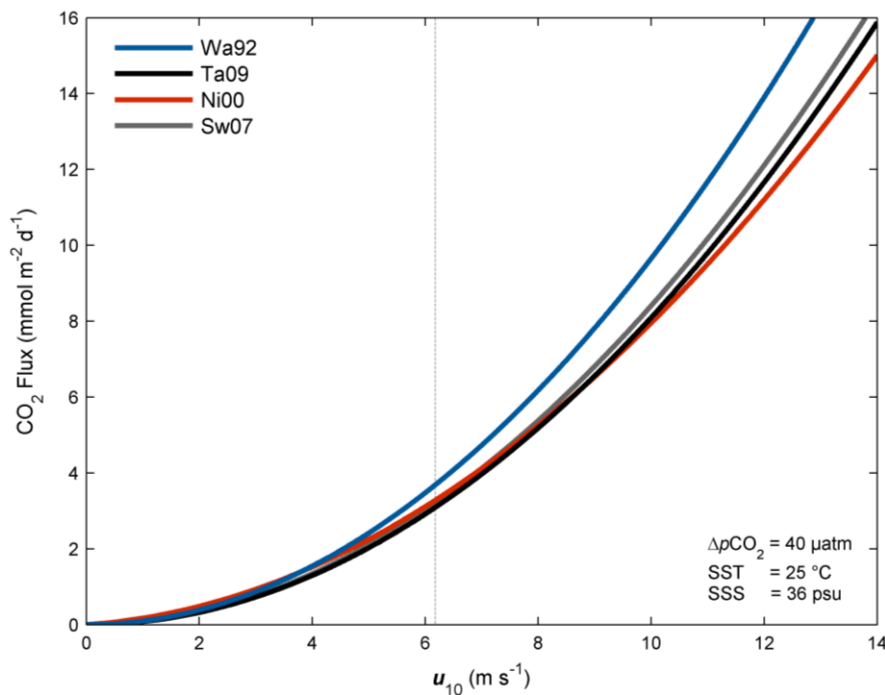


Figure 1.4 Relation between ASE flux densities and wind speed at 10 m height (u_{10}) at constant $\Delta p\text{CO}_2$, SST and sea surface salinity (SSS). Different parameterizations from the literature were used for flux calculations (Wa92: Wanninkhof 1992; Ta09: Takahashi et al. 2009; Ni00: Nightingale et al. 2000; Sw07: Sweeney et al. 2007). The grey dashed line denotes the average wind at Cape Verde over the past 7 years.

Flux estimates show a distinct deviation at higher wind speeds which result from both limited capacities for field or laboratory observations at these wind speeds and processes such as bubble entrainment which are not precisely parameterized yet. Flux calculations presented in this thesis (section 4) were done on the basis of the Wanninkhof (1992) parameterization.

Variations in $\Delta p\text{CO}_2$ are due to both biological as well as physical processes as described in the subsection above. Hence, pronounced seasonal cycles for $p\text{CO}_2$ in both atmospheric and oceanic hemispheres (section 1.3 & 4) affect the magnitude of F_{CO_2} on a seasonal scale. Regional processes such as coastal or equatorial upwelling further alter spatial distribution of F_{CO_2} on regional scales (Takahashi et al. 2009).

For calculation of O_2 ASE fluxes the gradient for O_2 between the ocean and the atmosphere (ΔO_2) is computed as follows:

$$\Delta\text{O}_2 = \text{O}_{2,\text{sat}} - \text{O}_{2,\text{amb}} \quad 1.11$$

where $\text{O}_{2,\text{amb}}$ is the ambient O_2 concentration in the ocean and $\text{O}_{2,\text{sat}}$ the related O_2 saturation concentration derived from O_2 solubility as a function of atmospheric pressure, temperature and salinity (García and Gordon 1992). Thus, ΔO_2 can be also used to investigate temperature independent changes in oceanic O_2 (section 4). Subsequently, O_2 ASE flux is calculated after eqn. 1.12:

$$F_{\text{O}_2} = k \cdot \Delta\text{O}_2 \quad 1.12$$

Due to biological processes (e.g., photosynthesis, bacterial oxidation of organic matter) CO_2 is strongly linked to O_2 in both the ocean and land biospheres (eqn. 1.1 & 1.2). However, the exchange of both gases at the ocean-atmosphere interface is rather decoupled from each other due to the chemistry of the carbonate system and their markedly different equilibration time scales (Keeling et al. 2010). Stephens et al. (1998) have used this fact to construct the atmospheric tracer APO (atmospheric potential oxygen) that applies concurrent measurements of atmospheric O_2 and CO_2 in order to reveal ASE of O_2 :

$$\text{APO} = \text{O}_2 + 1.1 \cdot \text{CO}_2 \quad 1.13$$

Atmospheric measurements of APO therefore mainly reflect O_2 variations due to ASE since land biota with a fixed O_2/C stoichiometric ratio of 1.1 are neutral for APO according to eqn. 1.13. Furthermore, APO is only slightly sensitive to the fossil fuel burning signal which has an O_2/CO_2 ratio of about 1.4 (Keeling 1988). APO therefore responds to oceanic fluxes of mostly O_2 and to some extent also CO_2 (Lueker 2003; Van-Der-Laan-Luijkx et al. 2010).

1.2 Study Area

Oceanographic Setting

The Eastern Tropical North Atlantic (hereafter ETNA) is located next to West Africa (e.g., Mauritania, Senegal, etc.) with the Cape Verde archipelago in its center (Figure 1.5). This ocean region is characterized by comparatively sluggish flow fields and low water mass ventilation due to the Cape Verde Frontal Zone (CVFZ) at the northwestern rim. This boundary separates most of the ETNA from the anticyclonic subtropical gyre system in the North Atlantic (Stramma et al. 2005). Thus, the region is also being referred to as an ocean shadow zone. However, water masses enhanced in salinity and oxygen right below the mixed layer (hereafter ML) were often found in the vicinity of Cape Verde. Such water masses (Subtropical Underwater, SUW) originate from the subtropical gyre system where they are being subducted and transported towards the equator (Tomczak 1981; Pastor et al. 2008).

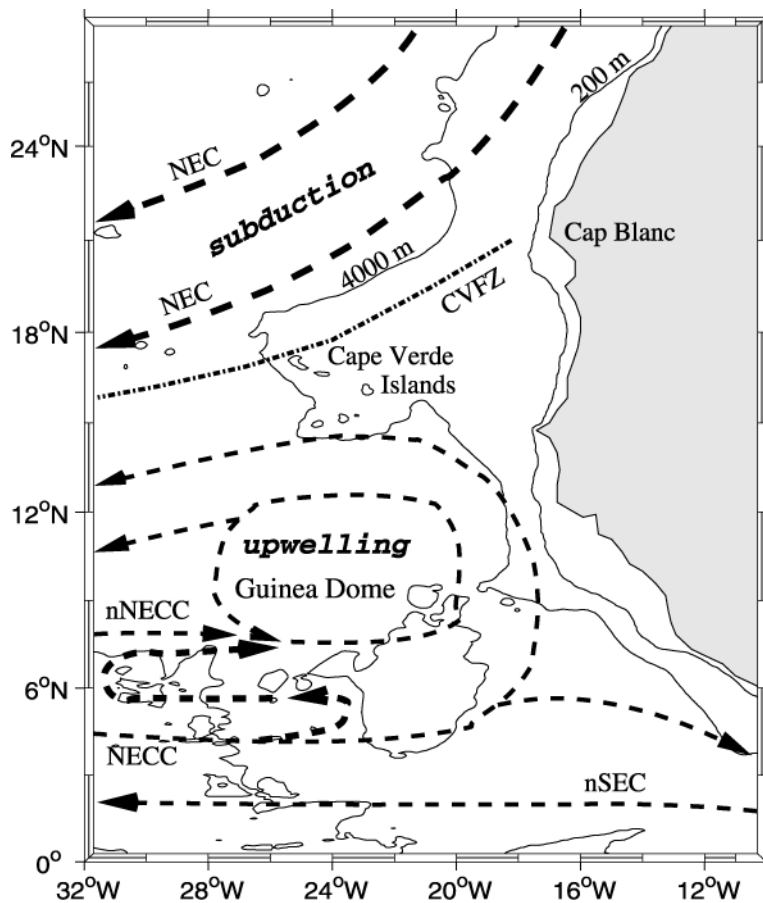


Figure 1.5 Overview map of the ETNA, superimposed by ocean currents found in this region (Stramma et al. 2005). The dashed-dotted line north of Cape Verde denotes the Cape Verde Frontal Zone (CVFZ) as described in the text.

As the Intertropical Convergence Zone (ITCZ) does seasonally migrate north- and southwards a resulting change in northeast (NE) trade winds strength also affects ocean circulation. Stramma and Siedler (1988) showed that the southeastern rim of the subtropical gyre describes a northward shift

of about 3° in fall due to the seasonal evolution of the ITCZ. Another result of this atmosphere-ocean interaction is the eastern boundary upwelling system (EBUS) located along the Mauritanian coast. NE trade winds create net Ekman transport of coastal surface waters offshore and sub-surface water masses are being uplifted to the surface (Mittelstaedt 1991). The upwelled water masses mainly originate in the South Atlantic (South Atlantic Central Water, SACW) and are lower in salinity and higher in nutrient levels when compared to North Atlantic Central Water (NACW; Hagen 2001, Pastor et al. 2008). Hence, both NACW and SACW are found north of Cape Verde (section 4.2.1) with the CVFZ acting as a barrier between these.

The EBUS in the ETNA region has impacts on biogeochemical cycles even for the open North Atlantic Ocean, as will be shown at the end of this thesis (section 4.2.2). The following paragraph provides further information about the ETNA from a biogeochemical perspective.

Biogeochemical Setting

The key process in the ETNA region around Cape Verde is the coastal upwelling system off Mauritania. This EBUS is one of the most productive upwelling regions in the world's oceans and as such hosts a rich and highly diverse ecosystem (Chavez and Messié 2009). The Mauritanian upwelling system shows a strong seasonal evolution due to variable strength of the NE trade winds (see above). During winter months strong upwelling is being observed off the Mauritanian coast while during summer months upwelling diminishes due to less intense wind curl stress (Mittelstaedt 1991). This seasonal pattern is illustrated as surface Chlorophyll a (hereafter chl a) distributions in the ETNA (Figure 1.6).

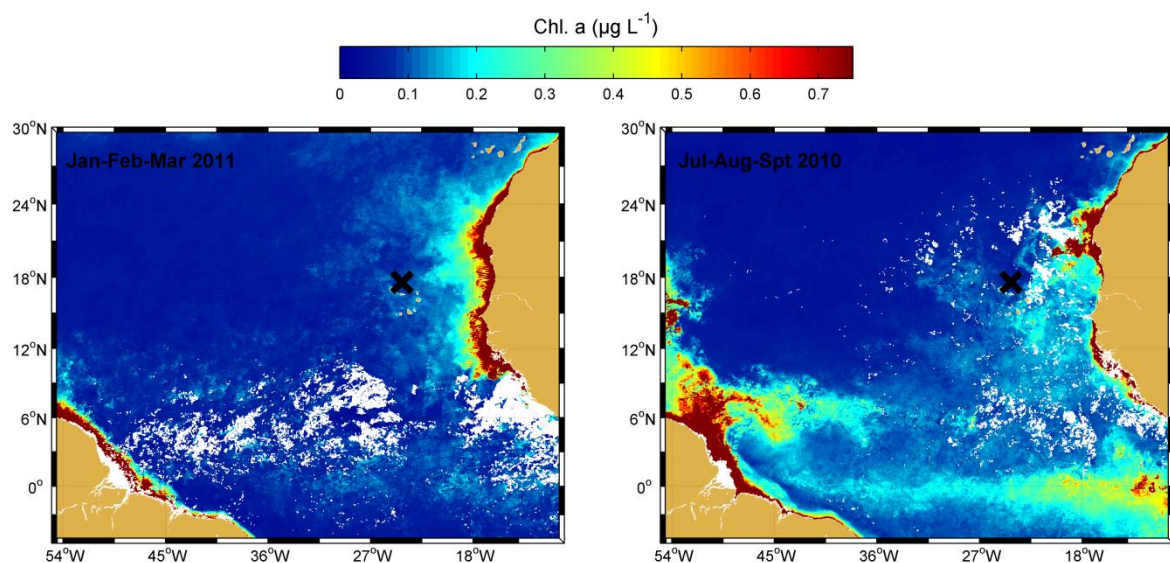


Figure 1.6 Seasonal distribution of surface ocean chl a in the ETNA obtained from satellite data (MODIS-Terra, <http://oceancolor.gsfc.nasa.gov/>). The left panel shows the 3 months averaged chl a concentrations for spring 2011, the right panel averaged chl a for fall 2010. A pronounced difference of chl a concentrations along the west African coast is observed between the two seasons (see text). Black crosses denote the location of the Cape Verde Ocean Observatory (CVOO).

Nutrient rich subsurface waters were upwelled to the sunlit surface layer and thereby fuel production of organic matter through photosynthetic processes (Pennington et al. 2006). Freshly upwelled water is supersaturated for $p\text{CO}_2$ and undersaturated for O_2 as a consequence of respiration processes that occur in subsurface layers. Horizontal advection transports these surface patches westwards into the open ocean while biological (photosynthesis and respiration) as well as physical (ASE) processes occur (Steinhoff et al. 2012).

Figure 1.6 clearly shows elevated levels of chl a (organic matter) in the upwelling. Propagation of such waters with high organic payload further offshore facilitate high respiration rates which are found in the water column (Karstensen et al. 2008). A distinct oxygen minimum zone (OMZ) with lowest values of $\sim 40 \mu\text{mol kg}^{-1}$ at depth of 400 – 500 m is observed in the ETNA (Figure 1.7). Accumulation of respiratory water masses in the ETNA as a consequence of limited ventilation and high input of organic matter from the EBUS favor the establishment of a large scale OMZ. Historical as well as recent observations provide evidence for an expansion of the ETNA OMZ both in terms of vertical extent and intensity (Stramma et al. 2008).

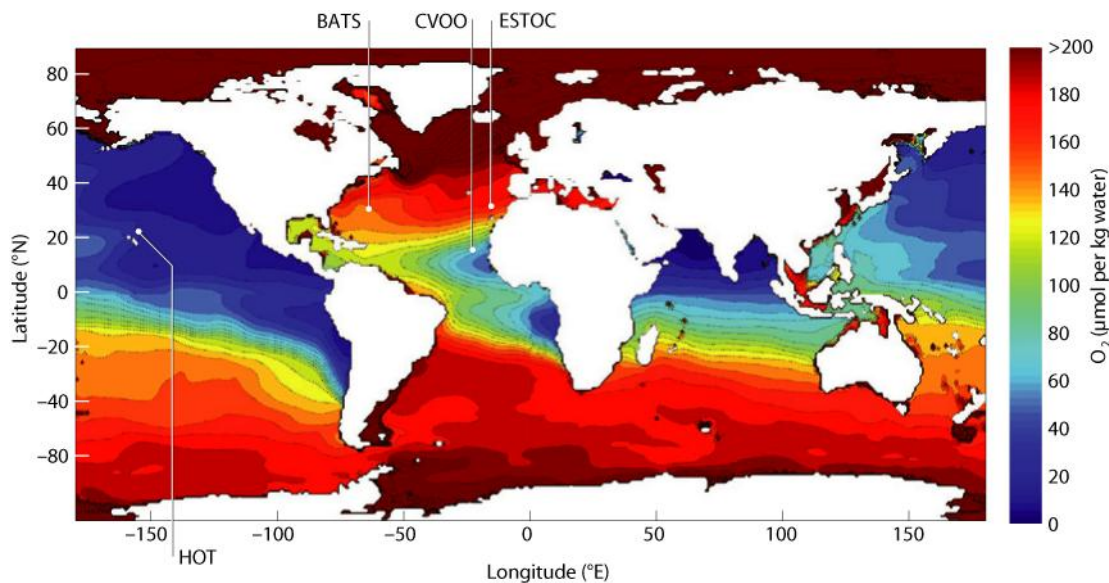


Figure 1.7 Global map of minimum O_2 concentrations in the water column. Data are based on the World Ocean Atlas 2009 (Garcia et al. 2010). Superimposed are international ocean time series programs which are highlighted in this thesis. Figure adapted from Wright et al. (2012).

Another major feature in the ETNA region is atmospheric deposition of dust, which follows a seasonal pattern with enhanced dust deposition at Cape Verde during winter months (Figure 1.8). Globally, nearly half of total ocean dust deposition takes place in the North Atlantic which is fueled by the proximity of the Saharan desert (Jickells et al. 2005). Atmospheric dust transports micronutrients such as iron and perhaps phosphorus into the surface ocean as observations of elevated iron concentrations in the ETNA showed (Sarhou et al. 2003, 2007). However, the resulting

impact on the ecosystem has not been fully understood yet. In an oligotrophic ocean environment iron supply can only stimulate primary production via N_2 fixation as found in the ETNA (Moore et al. 2009). In contrast, observations at ESTOC (European Station for Time Series in the Ocean) near Canary Islands have revealed no significant impacts of dust deposition on overall primary production (Neuer et al. 2004). However, as dust deposition is assumed to be highly affected by climate change (Jickells et al. 2005) the questions remains of how the ecosystem and thus biogeochemical cycling for carbon and other elements will respond in the future in the ETNA.

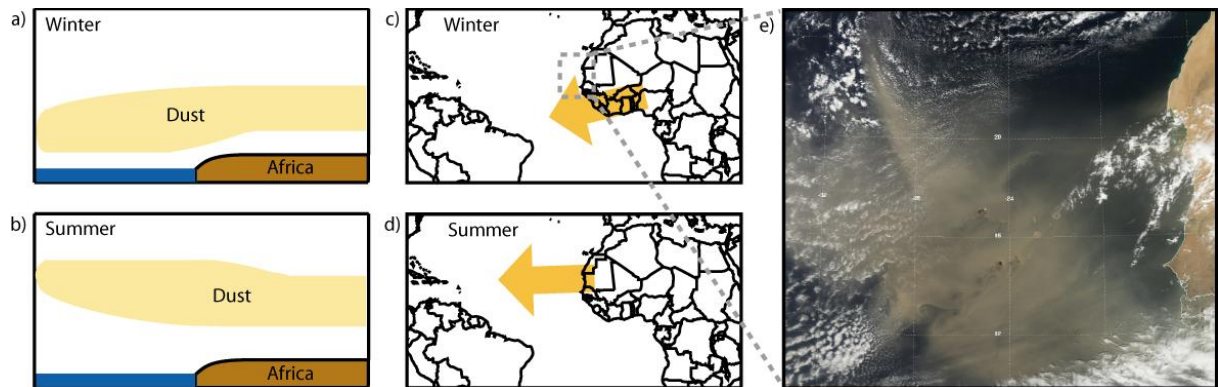


Figure 1.8 Atmospheric dust transportation and deposition for West Africa and the ETNA. Panel a) – d) show the seasonal difference of dust transportation paths, taken from Schepanski et al. (2009). Panel e) shows a snapshot of a massive dust event hitting the Cape Verde archipelago on Feb 7th 2012 (MODIS-Aqua, Truecolor, <http://oceancolor.gsfc.nasa.gov/>).

1.3 Observational Oceanography

Anthropogenic climate change through greenhouse gas emissions into the atmosphere and their reduction is one of the largest challenges for mankind. The interaction between the atmosphere and the ocean via air-sea CO_2 exchange plays a key role in understanding the past and present state of the global carbon cycle and predicting its future (Takahashi et al. 2009). However, as large parts of the oceans are widely remote an accurate determination of biogeochemical processes is a rather challenging task (Ducklow et al. 2009). The present global uptake rate of the world ocean for anthropogenic CO_2 is estimated at $+2.0 \pm 1.0 \text{ Pg C yr}^{-1}$ (Takahashi et al. 2009). Large uncertainties still remain although this estimate is based on over 3 million single measurements. Such uncertainties can be explained to some extent by limited temporal and spatial coverage of the oceans particularly in regions at higher latitudes (e.g. Southern Ocean).

In recent years mainly two approaches, ocean time series observations as well as autonomous sensor arrays, have greatly facilitated our knowledge about physical, chemical and biological processes in the oceans (Ducklow et al. 2009; Roemmich et al. 2009; Karl 2010). Merging and extending these approaches in the next decade will become more important to better understand the coupling of biogeochemical processes in space and time (Johnson et al. 2007, 2009; Byrne et al.

2010; Gruber et al. 2010a). As the scope of this thesis covers both approaches a brief description for these will be given in the following paragraphs.

Time Series

Fixed point (Eulerian) and sustainable long-term time series observations in the oceans have been established about 3 decades ago. The most prominent ones are the Bermuda Time Series Station (BATS) in the North Atlantic and the Hawaii Ocean Time Series (HOT) in the Pacific (Figure 1.7). Time series sites may have different design and pursue different approaches to observe the regional ecosystem, ranging from monthly ship-borne site occupations over repeat hydrography sections to autonomous (moored) buoy operations (Steinberg et al. 2001; Gutiérrez et al. 2008; Parard et al. 2010).

Highly resolved long-term observations of inorganic carbon at these stations provided first remarkable insights into the marine carbon cycle and how it responded to global climate forcing (Figure 1.9). Bates (2007) showed that observed temporal evolution of the inorganic carbon pool in the surface ocean reflects the atmospheric increase in CO_2 with similar rates (Figure 1.9). Simultaneously, acidification of surface ocean layers occurred thereby possibly altering crucial biogeochemical processes such as calcium carbonate formation of marine organisms (Doney et al. 2009). Similar observations were made in the Pacific Ocean at HOT (Dore et al. 2009).

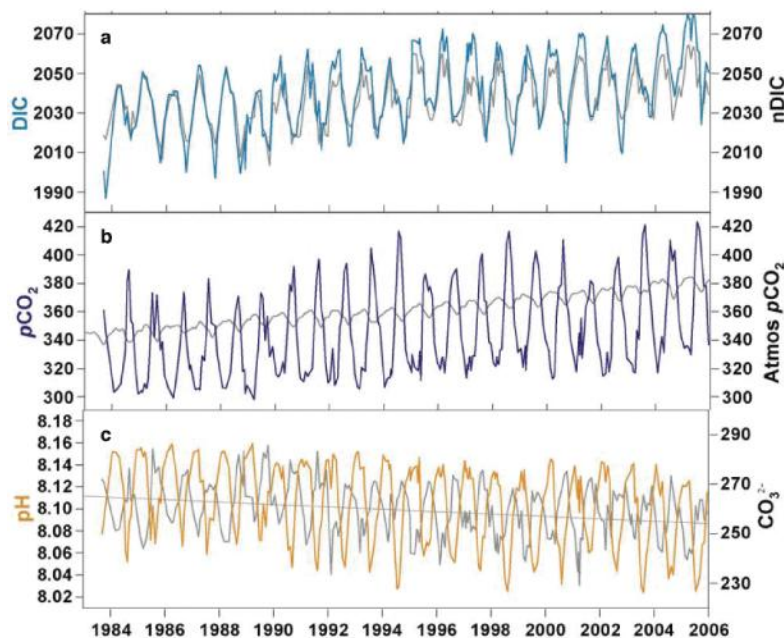


Figure 1.9 Time series measurements of carbon cycle parameters at BATS. Clear long-term trends were revealed from this record, superimposed by distinct seasonal signals. Figure taken from Gruber et al. (2010a).

Despite these observed long-term trends in DIC, Gruber et al. (2002) revealed significant inter-annual variability of DIC at BATS. They found a strong correlation with SST and mixed layer depth

(MLD) anomalies which, in turn, are correlated to inter-annual to decadal climate variability patterns as known as the North Atlantic Oscillation (NAO, Hurrell 1995). Their findings, obtained from elaborate time series measurements, provided first insights into the temporal (inter-annual) variability of the North Atlantic Ocean carbon sink.

Within the framework of this thesis time series observations for biogeochemical parameters have been established in the ETNA at the Cape Verde archipelago (Figure 1.7 and Figure 1.10). Compared to other ocean regions this area is not well studied and understood (Chavez and Messié 2009) although it features a highly interesting ecosystem which is being affected by various environmental conditions (section 1.2). Time series observations at the Cape Verde Ocean Observatory (CVOO) will provide a valuable contribution to an improved assessment of this ecosystem as early results at the end of this thesis will show (section 4).

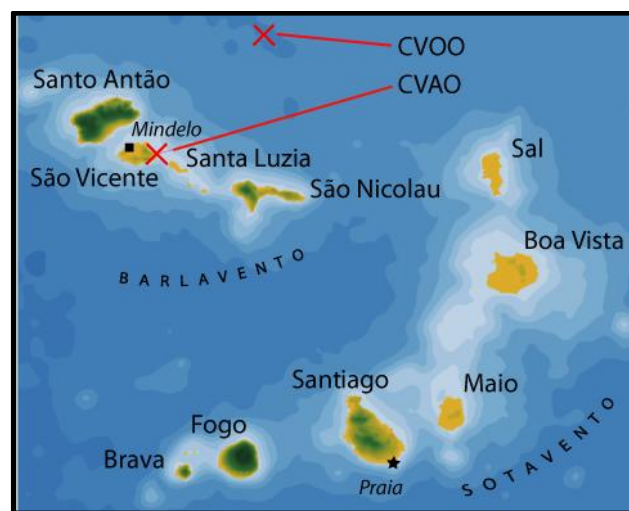


Figure 1.10 Overview map of the Cape Verde archipelago off western Africa. Red crosses denote locations of the Cape Verde Atmospheric Observatory (CVAO) and the Cape Verde Ocean Observatory (CVOO) which is located 60 nautical miles NE of CVAO.

The Argo Project

In the last decade, observational oceanography has made much progress regarding the establishment of a global ocean monitoring network featuring an excellent temporal and spatial coverage. Due to the limited availability of ship-borne (e.g., research vessels, volunteering observing ships) or fixed-location observations (e.g., time series stations, mooring arrays) a new approach for in situ observations of the ocean's physical state was pursued. Since novel and cost-effective instrumentation became available, scientists teamed up for the worldwide Argo project which aimed at deploying and maintaining a number of 3000 autonomously operating devices distributed over the world's oceans (Roemmich et al. 2004, 2009).

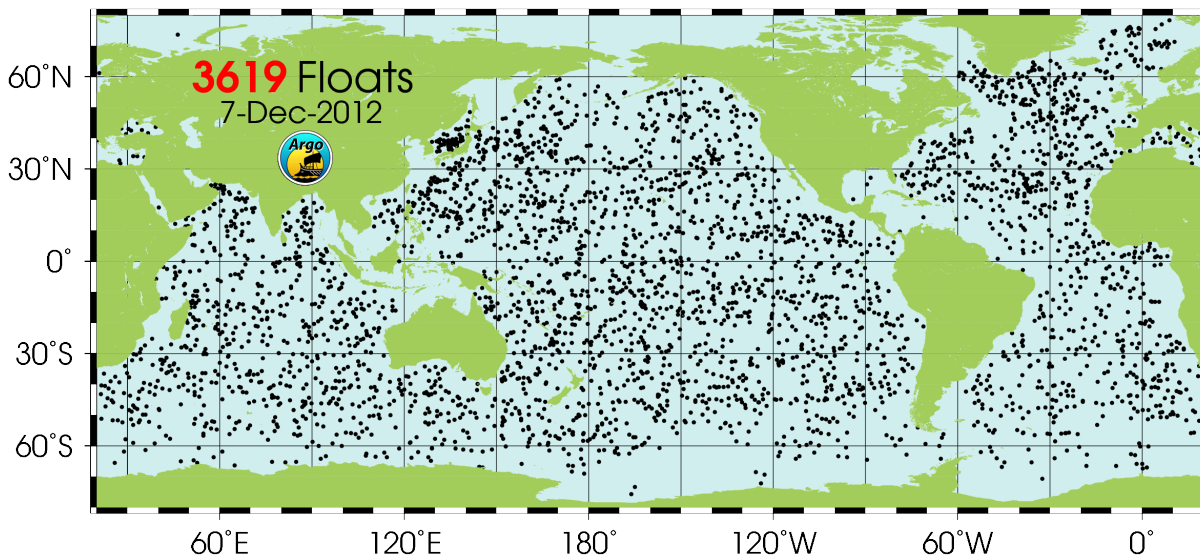


Figure 1.11 Global distribution of deployed Argo floats which are still in operation. Map taken from <http://www.argo.ucsd.edu/>.

This profiling float array (Figure 1.11) significantly improved the data basis for a global assessment of ocean salinity and temperature patterns on timescales of days to years and therefore led to a better understanding of large-scale ocean circulation, heat content and other scientific questions.

Because of the great success of the Argo project, profiling floats became interesting also for biogeochemists. At the same time as the Argo network developed, a new generation of sensors for biogeochemical parameters (e.g., O_2 , chlorophyll, pH, nitrate, etc.) came into reach (Johnson et al. 2007). These sensors were specifically developed to be suitable for deployments on autonomous platforms. However, accuracy and sensor reliability of those instruments are still being assessed (Bittig et al. 2012). Early success with O_2 measurements on profiling floats were achieved by Körtzinger et al. (2004, 2005) and Riser and Johnson (2008). Further pilot studies for other biogeochemical parameters (Bishop et al. 2004; D’Asaro and McNeil 2007; Boss et al. 2008; Johnson et al. 2010) show that float platforms are suitable sensor carriers for biogeochemical investigations. Nowadays, profiling floats equipped with biogeochemical sensors become more frequently used during dedicated field studies in order to deliver highly resolved observations in space and time (Bishop et al. 2004; D’Asaro and McNeil 2007; Alkire et al. 2012). Therefore, recently efforts are being made to extend the Argo network for a biogeochemical perspective (Gruber et al. 2010b).

So far, profiling floats haven’t yet been used for direct measurements of the carbonate system in the ocean due to a lack of suitable sensors. This thesis provides first-ever float-borne and direct measurements of the carbon cycle in the ocean. Technical results of this pilot study will be presented in section 3, followed by a scientific evaluation of obtained data in section 4.

1.4 Thesis Structure

New pathways for high resolution observations of the marine carbon cycle were pursued within the framework of this thesis. Thus, the first part of this thesis covers a comprehensive evaluation of developed and applied technology followed by a characterization of the marine carbon cycle and related ASE fluxes in the ETNA in the second part.

Chapter **3.1** begins with a thorough evaluation of novel sensor technology for $p\text{CO}_2$ measurements which became available recently. Two submersible in situ $p\text{CO}_2$ sensors were evaluated in an underway operation mode for reliability, accuracy and precision by referencing sensor data to established methods.

A major step forward towards unattended $p\text{CO}_2$ measurements on autonomous profiling platforms was made during this PhD project and is presented in chapter **3.2**. Two generations of prototype profiling floats have been developed and tested successfully at CVOO. Major achievements of this development are highlighted and first-ever water column $p\text{CO}_2$ measurements on profiling float are assessed for robustness and accuracy.

Chapter **4.1** describes the marine carbon cycle of the ocean's surface layer at the recently established CVOO. Within the framework of this thesis a ship-based (monthly) sampling program for carbon and oxygen was established. Early results of this program in combination with high resolution float data were used to describe variability of the carbon cycle from annual to diel timescales.

In chapter **4.2** subsurface processes at CVOO were revealed by means of different observational approaches. First, measurements of DIC and TA at CVOO were combined with float-borne carbon measurements for a description of the subsurface carbonate system. Second, O_2 measurements performed on the long-term mooring at CVOO as well as on a profiling float have discovered anoxic water masses ($< 1 \mu\text{mol kg}^{-1}$) in the upper 100 m water column of the open North Atlantic. The processes behind this finding are described at the end of this chapter.

2 Material & Methods

The main focus of this work is placed on autonomous in situ observations of dissolved O₂ and CO₂ in the pelagic ocean. In comparison to established oceanographic methods for measurement of O₂ and CO₂ this approach of unattended in situ measurements is novel and a rather challenging one. Three conditions have to be met in such an approach:

- Precise and accurate instruments which meet the special requirements of in situ observations are needed
- A suitable platform serving as an instrument carrier has to be available
- Finally, these two components need to be adapted to each other and intensive lab and field trials have to prove the system's overall reliability.

The following subsections describe the development of an autonomously operating profiling device for high resolution measurements of pO_2 and pCO_2 .

First, widely established methods for O₂ and CO₂ quantification, such as discrete water sampling or underway measurements during ship surveys, used for evaluation are briefly introduced.

Second, a brief overview of the autonomous measurement instruments used during this study is given, followed by a general introduction of the profiling float platform. Different approaches and development steps of the prototype floats are presented as well.

Finally, next to the autonomous operation of profiling devices described above other approaches to investigate O₂ and CO₂ dynamics in the ETNA region have been pursued. Facilities at CVOO for seasonal and inter-seasonal observations considered in this thesis are presented at the end of this chapter.

2.1 Laboratory Measurements

To ensure adequate accuracy and reliability of the sensors used on the newly developed profiling devices, results were compared to those of established and accurate methods. One example for such a method is the determination of dissolved oxygen in seawater after Winkler (1888) which, with some later improvements (e.g., Carpenter 1965), has remained the standard method until today. All discrete seawater samples collected for this work were determined for dissolved oxygen after Winkler (1888).

Regarding determination of carbonate parameters in seawater (e.g., DIC and TA) collected samples were measured either directly onboard the research vessel or were preserved and stored for later onshore analysis, following procedures recommended by (Dickson et al. 2007). Briefly, 500 mL

borosilicate glass bottles were filled air bubble-free with seawater and then poisoned with 100 μL of saturated mercuric chloride solution. Samples were stored at room temperature in the dark and in case of later onshore analysis shipped to GEOMAR for analysis within 6 month after sampling. Preserved samples as well as samples directly analyzed onboard were measured using automated high precision analyzing systems performing a coulometric titration for DIC (SOMMA, Johnson et al. 1993) and a potentiometric titration for TA (VINDTA, Mintrop et al. 2000). In order to maintain accuracy and assess the system's performance, regular measurements of certified reference material (CRM, A. Dickson, Scripps Institution of Oceanography, La Jolla, USA; Dickson, 2010) and duplicate samples were conducted. Due to somewhat varying performance during the different field campaigns details about precision are given separately for each dataset within this thesis. Obtained results can be converted to $p\text{CO}_2$ using a set of the carbonic acid dissociation constants (see chapter 1.1). This method, however, produces a relatively large error for $p\text{CO}_2$ of $\sim 10 \mu\text{atm}$ (Millero 2007).

A more robust and accurate method to determine the mole fraction of CO_2 ($x\text{CO}_2$) and thus the $p\text{CO}_2$ of a given gas sample is the detection via a non-dispersive infrared (NDIR) analyzer. In order to determine the $p\text{CO}_2$ of a distinct water parcel one has to equilibrate it with a gas phase. The CO_2 concentration of the gas phase is then measured within the NDIR unit. Following Henry's law (see chapter 1.1) this equilibration has to be made in a way in which the partial pressure of CO_2 in the water phase does not change during equilibration. This can be achieved by an infinitely large water sample (not applicable for determination of $p\text{CO}_2$ in a discrete water sample). When providing a continuous and sufficiently high flow of seawater ($\sim 3 \text{ L min}^{-1}$) for the equilibration with a small gas volume it is assumed that the $p\text{CO}_2$ of the seawater does not change measurably by the equilibration process due to the short passage time through the equilibrator. Therefore this method, when used in an underway measurement setup, can serve as a high accuracy reference for $p\text{CO}_2$ measurements.

Since several environmental conditions affect the measurement of $x\text{CO}_2$, such as pressure, temperature and the presence of water vapor analysis, using an NDIR is not trivial. To account for these varying effects and to guarantee a complete equilibration under controlled conditions, *ex situ* $p\text{CO}_2$ underway measurement related to this work were therefore performed with an automated $p\text{CO}_2$ measuring system (Model 8050, General Oceanics (GO), Miami, Florida, USA) equipped with an NDIR analyzer model 6262 or 7000 (LI-COR, Lincoln, Nebraska, USA), respectively, and with a spray-head equilibration chamber. A schematic picture of this system is shown in Figure 2.1. Further details about the experimental setup as well as applied data reduction and calibration routines can be found in Pierrot et al. (2009).

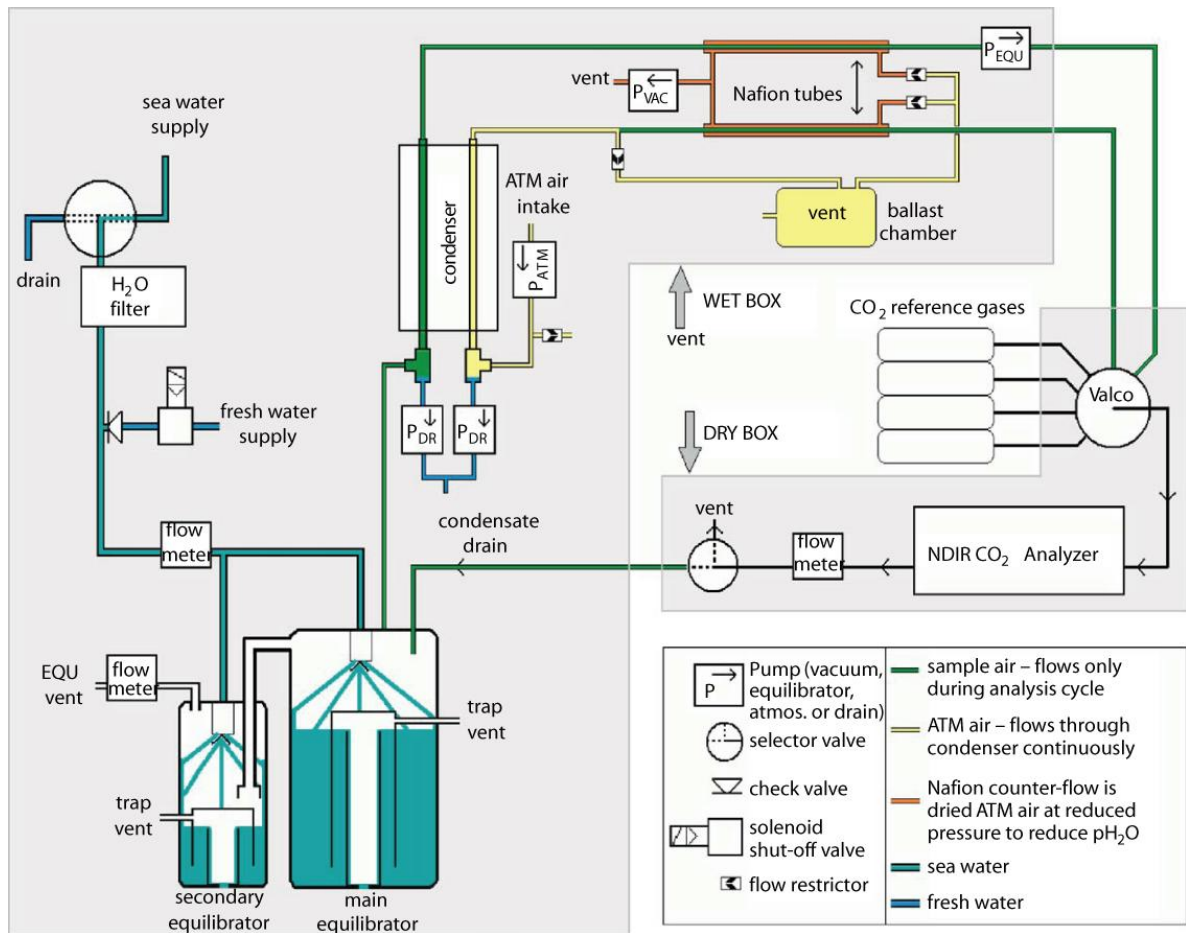


Figure 2.1 Scheme of the experimental setup for the GO $p\text{CO}_2$ system used within the framework of this thesis (picture from Pierrot et al. (2009)). Continuous seawater supply is usually provided by the ship's clean seawater system.

Underway measurements onboard of research vessels can provide a suitable basis for precise validation of new sensor techniques (as will be shown later in this thesis, see chapter 3.1). For this purpose a thermally insulated flow-through box (total volume: 80 L, flow rate: $\sim 10 - 12 \text{ L min}^{-1}$) was operated in parallel to a GO $p\text{CO}_2$ system on the ship's clean seawater supply (centrifugal pump) and used to deploy submersible in situ sensors (e.g., $p\text{CO}_2$, O_2 , gas tension or further sensors). Near the seawater intake, located at the ship's keel, a thermosalinograph measured salinity and temperature. Temperature probes at the intake, in the flow-through box and in the GO equilibrator were used to match all data sets and to correct $p\text{CO}_2$ measurements to in situ sea surface $p\text{CO}_2$ following eqn. 2.1 (Takahashi et al. 1993)

$$p\text{CO}_{2,\text{is}} = p\text{CO}_{2,\text{equ}} \cdot e^{[-0.0423(T_{\text{equ}} - \text{SST})]}, \quad 2.1$$

where $p\text{CO}_{2,\text{is}}$ is the $p\text{CO}_2$ corrected to SST, T_{equ} is the water temperature at the place of equilibration and $p\text{CO}_{2,\text{equ}}$ the measured $p\text{CO}_2$ at T_{equ} .

2.2 In Situ Instrumentation

Due to their complex and often large setup, intensive energy consumption and other constraints the reference measurement systems presented in section 2.1 are not suitable for in situ deployment. They are hence restricted to platforms that provide the necessary conditions (e.g., vessels, land-based stations or large buoys). This section provides information about state-of-the-art instrumentation that overcomes these restrictions and thereby permits biogeochemical in situ investigations. The following section makes no claim to provide a complete overview of available instruments but rather highlights sensors which have been considered in this thesis.

2.2.1 In Situ Sensors for $p\text{CO}_2$

The first operational sensor for autonomous *in situ* $p\text{CO}_2$ measurements (DeGrandpre et al. 1995) has been used primarily in long-term observations from buoys and moorings (Körtzinger et al. 2008; Moore et al. 2011). The success has fostered many other developments towards small-sized $p\text{CO}_2$ sensors with low energy consumption (Byrne et al. 2010). The crux of the matter is a fair balance between the downsizing of the instrumentation and the incurred compromises in terms of accuracy and precision. Another major constraint is the pressure resistance of the entire system, in particular for the gas equilibration interface between the inner detector and ambient seawater. Two recently developed sensors were found to fulfill the above criteria (Figure 2.2): The PSI CO_2 -Pro (Pro Oceanus, Bridgewater, Canada) and the HydroC (CONTROS, Kiel, Germany). During this work, both sensors have been successfully integrated into profiling float prototypes and are briefly introduced below. More detailed information about the PSI CO_2 -Pro and the HydroC sensors are provided in chapter 3.1.



Figure 2.2 Left: The PSI CO_2 -Pro sensor with a diameter of 19 cm and a length of 49 cm. The sensor features a tubular membrane interface with an in- and outlet on the front cap. Right: Two HydroC sensors with a planar membrane interface. The housing has a diameter of 9 cm and a length of 38 cm.

PSI CO₂-Pro

Membrane Interface: The sensor contains a tubular polydimethylsiloxane (PDMS) membrane placed in spiral arrangement within the sensor head (Figure 2.3). On the outer side, this membrane is continuously flushed with seawater using an external water pump which can be powered by the sensor itself and maintains a constant flow rate between 3 and 5 L min⁻¹. This setup causes a decrease in the thickness of the diffusive mass transfer boundary layer on the outer membrane side and thus reduces the e-folding response time to approximately 3 min (depending on water flow, temperature and hydrostatic pressure). The dissolved gases diffuse through the membrane thereby equilibrating with the inner gas volume which is circulated in counter-flow direction. The membrane is surrounded by a copper wire which minimizes the effect of biofouling at the interface. Due to a rigid and permeable support layer beneath the tubular membrane no hydrostatic pressure is exerted on the inner gas phase.

Detector assembly: The PSI CO₂-Pro is equipped with a single beam, single-wavelength NDIR detector unit (SBA-4, PP-systems, Haverhill, USA) which is connected to the membrane interface. A continuous (pumped) gas flow supplies the NDIR detector with the equilibrated gas from the membrane interface in a closed circuit. The temperature-stabilized infrared cell (40°C) is factory calibrated (0-600 ppm). In order to maintain accuracy an automated zero-point calibration (ZP) is performed periodically by switching to a short-circuited gas loop containing a CO₂ scrubber to provide CO₂-free air (Figure 2.3). This correction accounts for a potential zero drift which is typical for NDIR instruments (Eckles et al. 1993; McDermitt et al. 1993).

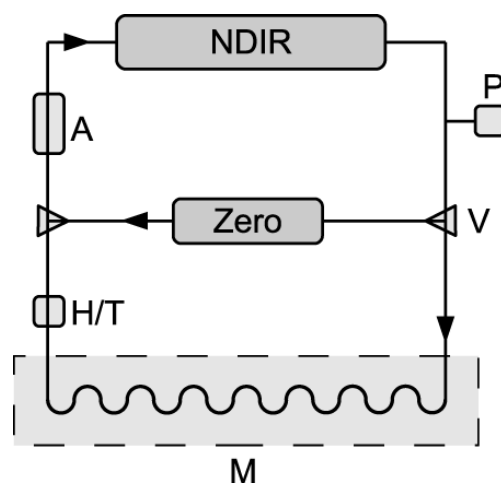


Figure 2.3 Schematic overview of the CO₂-Pro sensor design. Equilibration with ambient $p\text{CO}_2$ occurs via CO₂ transport across the membrane (M) into or out of the internal gas volume which is circulated by a gas pump (A). Gas sample properties are detected by a humidity/temperature (H/T) and a pressure (P) probe. Cell temperature and $x\text{CO}_2$ are determined within the NDIR cell. Regular zero-point calibration is carried out by short-circuiting the gas loop with the zero loop via two solenoid valves (V).

HydroC

Membrane Interface: The HydroC is equipped with a thin and planar PDMS membrane located on a rigid and permeable support layer. The membrane interface can be equipped with a flow-through head which can be continuously flushed with seawater by means of an external pump. Further details about the interface design as well as a complete description of the sensor features can be found in chapter 3.1.2.

Detector assembly: The HydroC is equipped with a temperature-stabilized, single beam, dual-wavelength NDIR detector. The HydroC also features a ZP calibration which is also used to monitor sensor performance. Again, a detailed description of the detector assembly can be found in chapter 3.1.2 as part of the HydroC evaluation.

2.2.2 In Situ Sensors for pO_2

In contrast to in situ pCO_2 sensors and their relatively recent appearance in oceanography, sensors for the determination of the O_2 content in seawater have existed for many decades now (Clark Jr. 1959; Kanwisher 1959). However, most of these were not suitable for long-term deployments on autonomous platforms. The most recent version of the electrochemical Clark electrode as well as the optode sensor (Tengberg et al. 2006) were both used within the framework of this thesis and are thus briefly introduced below.

Clark Electrode

This sensor was first proposed by Clark Jr. (1959) and has over the years been advanced to become suitable for high-quality oceanographic measurements. The measurement principle is based on the electrochemical reduction of O_2 molecules to hydroxyl ions by utilizing an amperometric electrode (Figure 2.4).

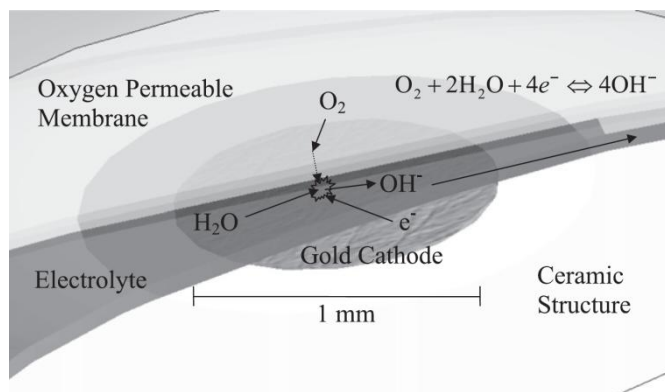


Figure 2.4 Scheme of the electrochemical reduction of O_2 molecules in a Clark-type Electrode (SBE 43). Scheme taken from Edwards et al. (2010).

This electrode is covered by a gas-permeable membrane where dissolved O_2 diffuses from ambient seawater to the cathode. Ambient pO_2 can be derived from the current that is being driven by the electrochemical reduction of O_2 molecules. The most established and perhaps advanced Clark-type sensor for measurements in the water column is the SBE 43 (Sea-Bird Electronics Inc., Bellevue/WA, USA). This sensor is mainly used for accompanying measurements on CTD rosette sampler but also on autonomous platforms such as profiling floats (Martz et al. 2008). One remaining major concern for this kind of sensor is the often insufficient measurement stability that troubles this method in long-term deployments on unattended platforms.

Optode

The optode sensor technique is a comparatively new one. It has been used in oceanographic research since almost one decade. Unlike the Clark electrode, the measurement principle is optical and based on fluorescence quenching (Tengberg et al. 2006). A platinum-porphyrine complex is immobilized in a thin sensing foil that is attached to a sapphire window and is illuminated through this window by light, which is being emitted from a blue LED. The light induces a fluorescence of the dye (Figure 2.5). The optode measures the lifetime of the red fluorescence signal by a photo diode behind the optical window. In presence of O_2 , the fluorescence intensity and lifetime is decreased due to an energy transfer from the excited luminophore complex to the O_2 molecule. This decrease in fluorescence is proportional to the pO_2 in the sensing foil and thus can be related to the ambient pO_2 in the seawater.

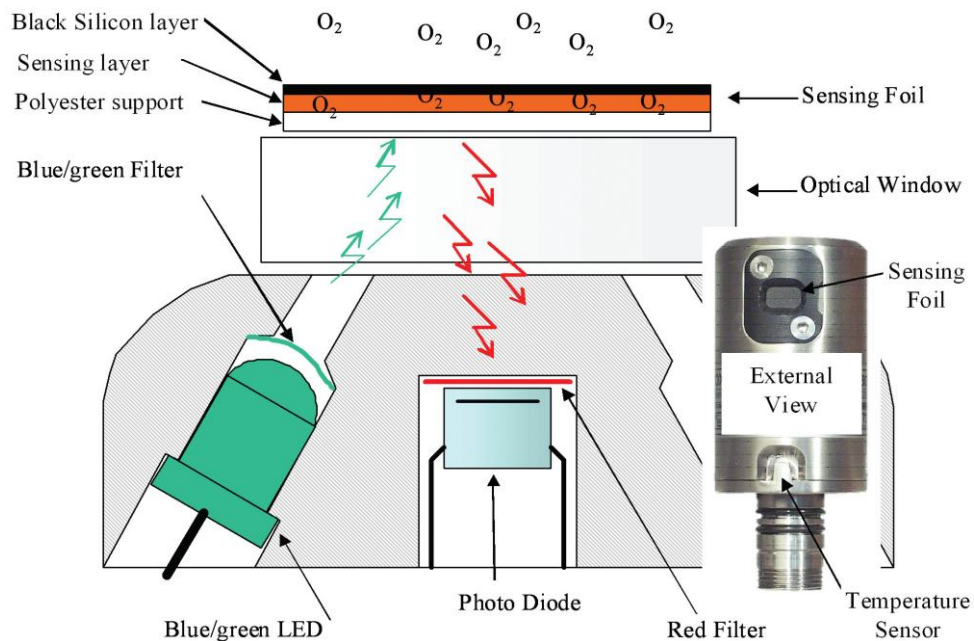


Figure 2.5 Setup of the optical components of an Aanderaa 3830 Optode including the sensing foil. A detailed description of the measurement procedure is given in the text. Scheme taken from Tengberg et al. (2006).

Since changes in fluorescence lifetime instead of intensity are detected degradation of the dye by photo bleaching or other effects that may occur over longer periods have no negative effect on the sensitivity of the sensor. Two version of this sensor, the Aanderaa Optode Model 3830 or 4330 (Aanderaa Data Instruments AS, Bergen, Norway; Figure 2.5), have been used successfully during this and several other studies, such as ship-borne underway measurements, CTD profiles, moorings and even on profiling floats (Bates et al. 2002; Körtzinger et al. 2005; Tengberg et al. 2006; Uchida et al. 2008; Bittig et al. 2012). These long-term deployments overall have shown good long-term stability that exceeds that achievable by Clark-type sensors. Additionally, having low energy requirements and small housing dimensions, this sensor is highly suitable for long-term deployments on autonomous platforms.

In order to compute oxygen concentration from calibrated sensor output (as pO_2) one has to account for ambient total pressure of all gases (preferably gas tension in water or if not applicable ambient atmospheric pressure) as well as O_2 solubility as below.

$$O_{2, \text{conc}} = \frac{P_{O_2} \cdot O_2^*}{(P_{\text{total}} - P_{H_2O}) \cdot 0.20946 \cdot 1013.15}, \quad 2.2$$

where O_2^* is the pressure-corrected O_2 solubility after Benson and Krause (1984) and García and Gordon (1992), P_{total} either the gas tension or atmospheric pressure, p_{H_2O} the actual water vapor pressure after Weiss (1980) and 0.20946 the O_2 mole fraction in dry air.

When applying sophisticated methods for sensor calibration, an accuracy in the field of up to $2 \mu\text{mol kg}^{-1}$ can be achieved, which is sufficient for autonomous platforms (Bittig et al. 2012; Fiedler et al. 2012).

2.2.3 Profiling Floats

A profiling float consists mainly of the following components (Figure 2.6): (i) a pressure resistant housing (usually rated to 2000 dbar), (ii) a buoyancy unit for active profiling through the water column, (iii) a telemetry unit for positioning and data transmission and (iv) a sensor compartment for hosting scientific sensors. Power supply, controlling boards and the buoyancy unit including an oil reservoir are located in the inner part of the housing. A connection to an outer oil reservoir (inflatable bladder) enables the float to control its overall volume by pumping oil from the inner reservoir to the outer one (and vice versa). When the outer oil bladder inflates, it increases the float's total volume and thereby its buoyancy. To lose buoyancy for a downcast, oil is pumped back into the rigid pressure housing and the oil bladder deflates. As a float surfaces, a second bladder around the pressure housing (SOLO- or NEMO-type floats, Davis et al. (2001)) is being filled with air

from inside the housing. This additional bladder can only be used at the surface (low hydrostatic pressure) and pushes the telemetry unit above the water level as far as possible to allow for improved data transmission via a satellite link.

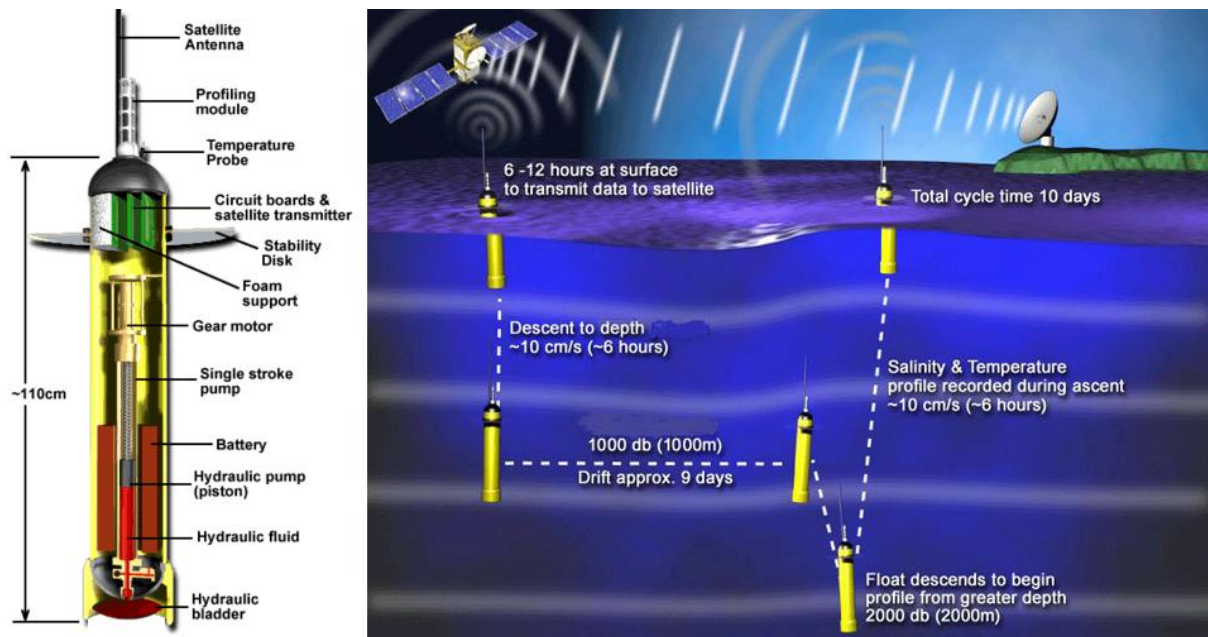


Figure 2.6 Left: Schematic of an APEX profiling float (Webb Research, Falmouth, Massachusetts, USA). Right: A typical profiling scenario of an Argo Float. Given numbers in the figure may vary depending on the user configuration. Figures taken from <http://www.argo.ucsd.edu/>.

The lifetime of a profiling float first and foremost depends on the battery payload and the chosen profiling interval. It usually lasts for 3-4 years with a 2000 dbar profile every 7 days. Such a profiling cycle usually begins with a controlled downcast to a parking depth below the euphotic zone where biofouling and corrosion issues are small (~ 500 dbar). The float then drifts at the parking depth for the cycle time (here 7 days) until it finally descends to its profile depth (here 2000 dbar) followed directly by a controlled ascent to the surface. During this ascent (usually at 0.05 to 0.1 m s^{-1}) scientific data are measured according to a predefined depth grid. As soon as the float surfaces and inflates the air bladder, the recorded vertical profile data is transmitted to shore and the next cycle begins.

2.3 Development of Profiling Float Prototypes

Since reasonably small submersible $p\text{CO}_2$ sensors are nowadays available (see 2.2.1), highly resolved in situ observations of carbon parameters within the water column come into reach. Next to cabled profiling oceanographic devices (e.g. CTD), profiling floats can be used for these observations, which are a rather sophisticated profiling platform. This chapter provides an overview of the different development stages for the implementation of an in situ $p\text{CO}_2$ sensor on a profiling float, made within the framework of this thesis.

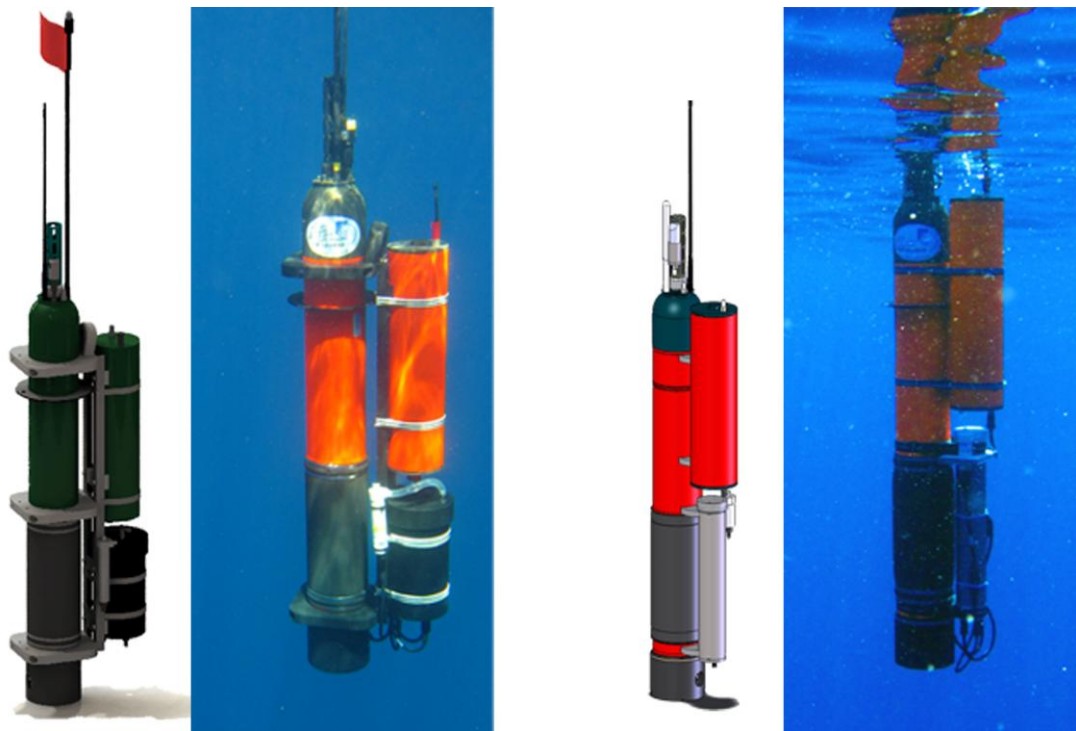


Figure 2.7 Overview of float prototypes developed and deployed within the framework of this thesis. The figure shows technical design as well as finally constructed floats during operation for generation-I (two left panels) and generation-II (two right panels).

2.3.1 First and Second Float Generation

In tight cooperation with a German float manufacturer (Optimare GmbH, Bremerhaven, Germany) a prototype float platform was designed, suitable of carrying additional sensor and battery payload. This involved a whole suite of modifications on mechanical components (sensor mounting, extra battery housing, antenna design, etc.) as well as intensive software modifications ($p\text{CO}_2/p\text{O}_2$ measurement cycles, in situ calibration procedures, data telemetry, etc.). Over the course of this thesis basically two generations of prototype floats (Float 1G and 2G) have been developed and deployed successfully (Figure 2.7). Specifications for each prototype are listed in Table 2.1 and summarized information about all deployments can be found in chapter 3.2.1 and 3.2.2.

	Float 1G		Float 2G	
	Sensor	Calibration	Sensor	Calibration
CTD	SBE 41	Factory	SBE 41	Factory
O_2	AADI 3830	Laboratory ¹⁾	AADI 4330	Laboratory ²⁾
$p\text{CO}_2$	PSI CO_2 -Pro	Factory	CONTROS HydroC	Laboratory ³⁾
Profiling method	Semi-continuous (STS)		Continuous	
Number of deployments	3		4	
Total number of profiles	92		123	
$p\text{CO}_2$ k_{63} (surface/depth)	6.4 / 23.8		2.7 / 3.6	

Table 2.1 Comparison of the two different prototype floats and related field deployments. Mean $p\text{CO}_2$ sensor response times (k_{63} , in minutes) are given for determinations at surface (s) and depth (d). ¹⁾ 2-point calibration prior to deployment. ²⁾ multiple-point (O_2 , T) calibration prior to deployment, as well as in situ air calibration. ³⁾ multiple-point ($p\text{CO}_2$, T) calibration prior to deployment.

The main difference between both setups is the different $p\text{CO}_2$ sensor used (PSI CO_2 -Pro and CONTROS HydroC). Since these two $p\text{CO}_2$ sensors perform quite differently, their properties for this particular profiling application have to be considered. The major constraint for a measurement system that moves relatively fast through steep environmental gradients is the response time of the sensor signal. Measurements with the two $p\text{CO}_2$ sensors in underway applications, vertical profiles conducted on a CTD and measurements on the prototype floats itself indicated a pronounced difference in sensor response time (e-folding time constant, hereafter k_{63}) of both systems. In general, the two $p\text{CO}_2$ sensors have comparable values of k_{63} at the surface but they highly differ at depth (see Table 2.1). This contrasting response time of the respective $p\text{CO}_2$ sensor was the main determining factor of how the float prototypes made their profiles.

The 1st generation float (hereafter 1G) was programmed to perform a semi-continuous “stop-then-sample” (STS) approach, in which the float stopped during the upcast at three predefined depths, each followed by a $p\text{CO}_2$ measurement cycle (Figure 2.8 , upper panel). Between these depths all other parameters were measured on a regular 5 dbar grid.

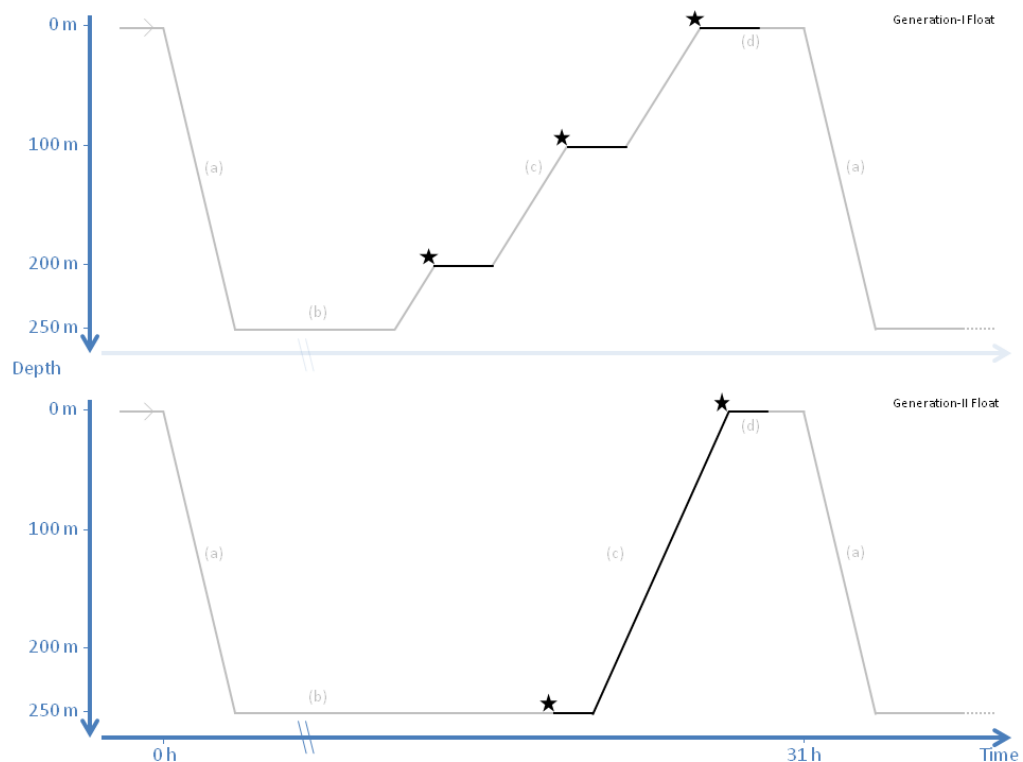


Figure 2.8 Chronological sequence for profiling cycles of the 1G (upper panel) and 2G (lower panel) float prototypes. A profile begins with a downcast (a) towards the parking depth (b). After parking time has elapsed the float begins an upcast (c) followed by the surfacing time for data telemetry (d) and the next downcast (a). Profile parts highlighted in black indicate runtimes of the particular $p\text{CO}_2$ sensor and black stars note a ZP calibration.

The 2nd generation float (hereafter 2G) could benefit from the much better performance of the HydroC sensor in terms of k_{63} . This enabled the instrument to carry out continuous measurements of all parameters during the entire upcast without interruptions (Figure 2.8 , lower panel).

2.3.2 In Situ Oxygen Offset Correction

Next to several improvement steps from the 1G float towards the 2G float (e.g. continuous instead of STS profiling) another major achievement was the establishment of an in situ calibration method for optode-based O_2 measurements. This method makes use of the float's airbladder which pushes the float's topmost part above the water level in order to allow for improved satellite data transmission. The procedure of the method is briefly described below (see also Figure 2.9):

- After the float approaches the surface (CTD, optode and telemetry are right beneath the surface at $\sim 0.1 - 0.3$ dbar) the HydroC is set into calibration mode; pCO_2 , O_2 and CTD data is recorded in 90 s intervals for 5 times (d1)
- After these measurements the airbladder inflates thereby increasing the float's buoyancy significantly; CTD, optode and telemetry are now above the water level.
- pCO_2 , O_2 and CTD data are recorded again in 90 s intervals at which optode and CTD sensors are measuring in air (d2)
- Satellite transmission is being performed (d3), airbladder deflates and downcast begins (a).

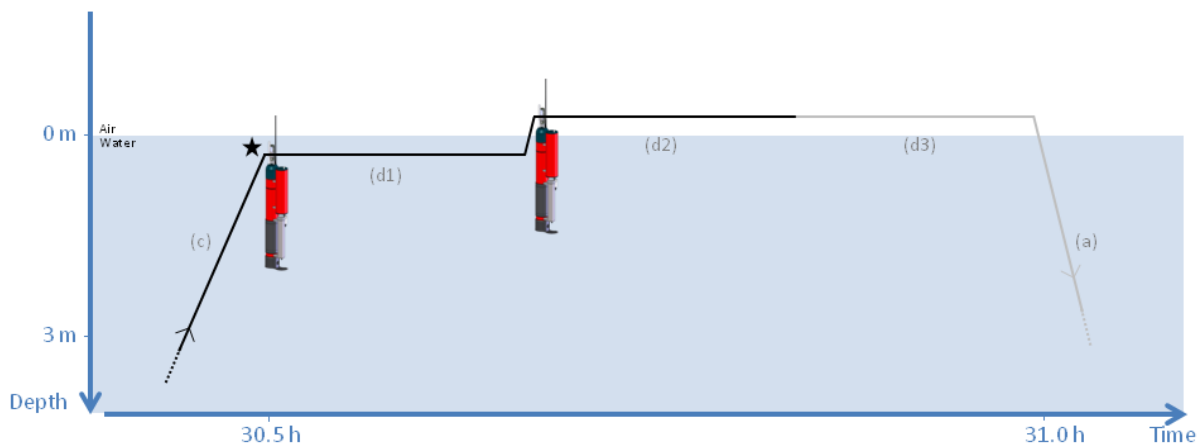


Figure 2.9 Enlargement of the chronological sequence (see Figure 2.8, lower panel) for the developed in situ calibration of optode measurements while the float approaches the surface (d1-d2). Profile parts highlighted in black indicate runtime of the HydroC and the black star notes a ZP. Refer to main text for detailed description.

When conducting optode measurements in water, pO_2 or $O_{2,conc}$ can be derived simply by applying eqn. 2.2, assuming p_{H_2O} levels to be at saturation state. However, this assumption is not valid for optode measurements in air as p_{H_2O} in the atmosphere might differ significantly from saturation levels (relative humidity $<100\%$). When knowing the amount of water vapor close above the sea

level (nearby CVAO measurements at 10 m height were used within the framework of this thesis) this method allows for an accurate assessment of the partial pressure of O₂ in air. Hence, an in situ calibration and drift control of the optode sensor can be applied (see chapter 3.2.2) which, for instance, does increase the accuracy of derived air-sea gas fluxes significantly (see chapter 4.1).

2.4 CVOO & CVAO Facilities

The major research platform which has been used over the course of this thesis was the Cape Verde Observatory with its oceanic and atmospheric components (section 1.3). Below, the equipment and resources used from the Cape Verde Observatory within the framework of this thesis are briefly described.

CVOO – Cape Verde Ocean Observatory

The core component of the ocean time-series observations at CVOO is the monthly occupation of the time-series site (17.589 °N, 24.252 °W) using the local R/V Islândia. The vessel is equipped with a rosette sampler (SBE 32, 12 Niskin bottles à 5 L), a CTD unit (SBE 19plus), an O₂ sensor (SBE 43, all Sea-Bird Inc, Bellevue, Washington, USA) as well as sensors for chlorophyll/turbidity (CHL/TURB; Eco FLNTURT, WETLabs, Philomath, OR, USA) and photosynthetically active radiation (PAR; QSP-2350, Biospherical Instruments, San Diego, CA, USA). Hydrocasts can be performed down to a depth of 600 m.

The regular monthly sampling program includes the following bottle parameters, followed by established standard analysis protocols (refer to section 2.1):

- Nutrients (nitrate, nitrite, phosphate, silicate)
- Dissolved O₂
- Dissolved inorganic carbon (DIC)*
- Total alkalinity (TA)*
- Total organic carbon (TOC)*
- Total organic nitrogen (TON)*
- Particulate organic carbon (POC)*
- Particulate organic nitrogen (PON)*
- Chlorophyll

*) Analysis at GEOMAR

The sampling program started in Oct. 2008 and a collection of obtained data is presented in section 4. However, the intended sampling interval of 1 month could not always be met in the past due to very limited capacities for maintenance and thereby frequent technical problems with the

vessel. However, additional samples at the CVOO site were taken during various international research cruises in the ETNA region, filling gaps in time and extending vertical coverage (deep hydrocasts, > 600 m). Data obtained by these cruises are also presented in section 4.

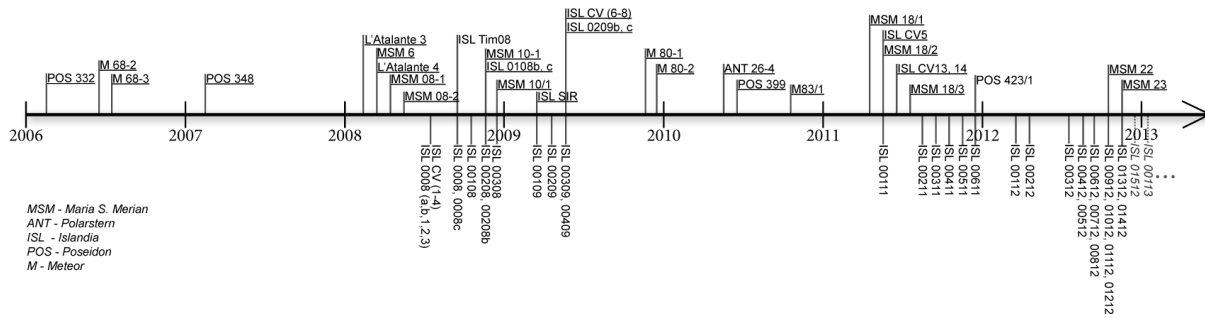


Figure 2.10 Timeline of conducted research cruises that have occupied the CVOO site. Scheme taken from cvo0.geomar.de.

Besides these laborious sampling approaches described above a second pillar of the ocean observatory is a long-term mooring directly co-located to the CVOO sampling site (Figure 2.11). It consists of many self-recording instruments at various depths that measure salinity, temperature, pressure, current speed and direction, vertical particle flux, O₂ (Aanderaa optode) and pCO₂ (SAMI). A detailed description for each deployment, including nominal depths for each sensor, can be found in the appendix I.b.

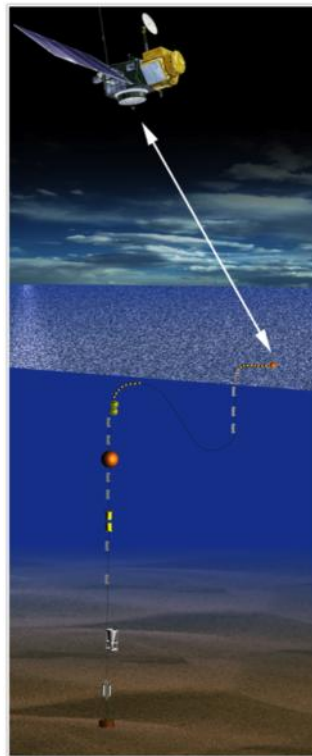


Figure 2.11 A schematic drawing of the deployed long-term mooring at CVOO. Picture taken from cvo0.geomar.de

The mooring is maintained since July 2006 with recovery and redeployment occurring approximately every 18 months. So far, 4 deployments have been carried out and data of the first 3 deployments are finalized. First results of this data set can be found in section 4.

CVAO – Cape Verde Atmosphere Observatory

The counterpart of the ocean observatory is the atmospheric measurement site located at the most northeastern tip of the island São Vicente (Figure 1.10). The observatory is equipped with a measurement tower of 30 m height, which is located close to the shoreline. Several lab containers in this area are hosting various autonomous analyzing systems for continuous measurements of the following parameters:

- Meteorological basic data (atmospheric pressure, wind speed, radiation, etc. at 10 m height)
- Greenhouse gases, such as CO₂, CO, N₂O, CH₄*
- Halocarbons
- O₂, O₃, APO, NO, NO₂, NO_y and VOCs
- Dust deposition, particle size distribution, chemical composition, etc.

*) flask sample & continuous data

A comprehensive overview of the applied sampling and analysis techniques applied at CVAO is given by Carpenter et al. (2010).

Within the framework of this thesis CVAO data have been used for the analysis of obtained CVOO and float data. These are mainly the meteorological data kindly provided by the University of York (UK), used in sections 3.2.2 and 4.1, as well as greenhouse gas measurements performed by the MPI-BGC Jena (Germany), used for the investigation presented in section 4.1.

3 Technical Results

The following chapter provides a detailed evaluation of the scientific instrumentation used within the framework of this thesis. It gives information about performance, robustness and reliability of different instrument setups, thereby allowing a better assessment of the scientific results presented later in section 4.

Section 3.1 focuses on the evaluation of the in situ CO₂ sensors used in this thesis (PSI CO₂-Pro; HydroC) in order to assess their strengths and weaknesses. Section 3.2 describes the application of the two sensors named above together with the prototype floats introduced in chapter 2.2. Presented results of section 3.1 and 3.2 will be shortly summarized and discussed in section 3.3, which focuses on the improvement achieved for the instruments during the different development stages.

3.1 Sensor Evaluations

3.1.1 Evaluation of the PSI CO₂-Pro sensor

Field tests with the PSI CO₂-Pro sensor were carried out in April/May 2010 during a 6-week cruise in the Atlantic with R/V *Polarstern* (ANT-XXVI/4, see Figure 3.1 for cruise track). During the cruise oligotrophic (i.e., subtropical gyres) as well as mesotrophic regions (e.g., on continental shelves) provided a fairly wide range in $p\text{CO}_2$ (295 – 440 μatm).

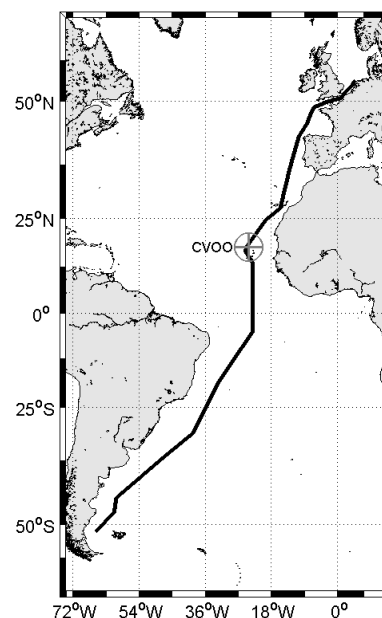


Figure 3.1 Cruise track of R/V *Polarstern* cruise (ANT-XXVI/4) from Punta Arenas (Chile) via Mindelo (Cape Verde) to Bremerhaven (Germany) in April/May 2010. The cruise covered a large latitudinal span with different biogeochemical and hydrographic characteristics (temperature and salinity varied from 7° C to 30° C and 33.2 psu to 37.6 psu, respectively).

Furthermore, strong $p\text{CO}_2$ gradients were found on smaller spatial scales. Thus, the conditions were ideal for a robust evaluation of the PSI CO_2 -Pro, which was tested in an underway setup (as described in 2.1). The following two sections present the internal sensor data and performance of the instrument itself (section a.) and the comparison with reference datasets (section b.).

Sensor Performance

For precise spectroscopic measurements of a gas it is crucial to know the physico-chemical properties of the sample in order to account for several effects (e.g. pressure broadening, humidity dilution etc.). These properties were determined by sensors for temperature, pressure and humidity within the gas circuit (Figure 2.3). The detector board internally corrects for the effect of variations in these properties on the CO_2 measurement and provides corrected CO_2 mole fraction ($x\text{CO}_2$). These peripheral data are stored and can be used as indicators of sensor performance during the field deployments (Figure 3.2).

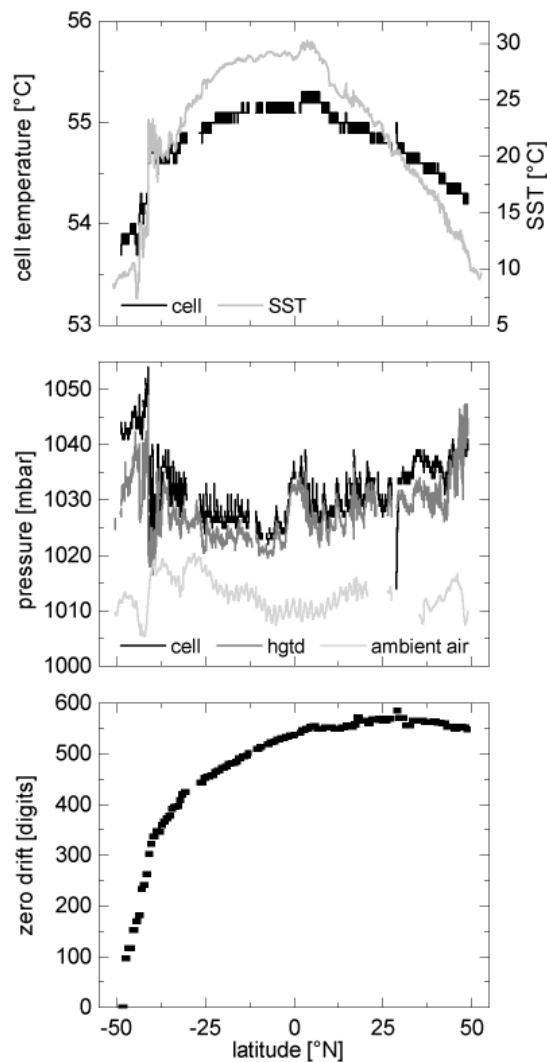


Figure 3.2 Peripheral sensor data of the PSI CO_2 -Pro during ANT-XXVI/4. NDIR cell temperature (upper panel, black) clearly follows SST patterns (gray). Internal PSI CO_2 -Pro pressure (middle panel, black) corresponds with gas tension measurements (hgt, light gray) and values for ZP (lower panel) show no dependence on environmental conditions.

Measurements of the PSI CO₂-Pro showed a strong correlation ($r^2=0.95$) between the controlled temperature of the NDIR cell and the SST during this cruise (data not shown). The cell temperature deviated by up to 1.5°C from the set temperature of 55°C within the observed SST range. This points at an insufficient temperature control of the NDIR unit which cannot fully compensate heat loss or accumulation through the sensor housing, respectively. This may bias the sensor calibration and thus the measurement (see below).

At equilibrium, the internal gas phase pressure (accuracy ± 2 mbar) should equal the total gas tension of the seawater. We found good agreement with HGTD measurements, despite a pronounced offset at the initial phase of each cruise. A slight inconsistency of gas tension data is mainly due to the impact of the PSI CO₂-Pro internal gas pump.

The ZP was carried out every 6 h for maintaining accuracy of measurements. The lower two panels show raw readings of the NDIR cell during ZP. The drift of these values indicates several effects that are responsible for detector drift (e.g. light source aging, particle deposition within light path). The non-linear drift pattern of the zero reading emphasizes the need for regular ZP in adequate intervals during operation.

Intercomparison of Datasets

Established methods as described in section 2.1 were operated in parallel and used as reference measurements, in order to assess accuracy of the PSI CO₂-Pro measurements. Discrete DIC ($\pm 1.1 \mu\text{mol kg}^{-1}$) and TA ($\pm 1.6 \mu\text{mol kg}^{-1}$) measurements were converted into $p\text{CO}_2$ for comparison purposes, using the carbonic acid dissociation constants of Mojica Prieto and Millero (2002). Due to propagation of errors in the used set of constants and errors of the measurements the uncertainty of derived $p\text{CO}_2$ reference values is estimated at $\pm 10 \mu\text{atm}$ (Millero 2007). Discrete reference samples as well as GO $p\text{CO}_2$ measurements show consistent pattern and can thus be used as reference (Figure 3.3, left panel). High data quality of continuous measurements allow for an adequate assessment of sensor accuracy and precision. Figure 3.3 (black + light gray, right panel) presents the correlation of all measurements between the PSI CO₂-Pro and the GO system which yields a precision for $p\text{CO}_2$ of $3.4 \mu\text{atm}$. When excluding biased data from this assessment (due to few major events on shorter timescales; Figure 3.3, light gray) enhanced precision of $1.5 \mu\text{atm}$ is obtained. The significant intercept and slope of the regressions points at a systematic offset of the PSI CO₂-Pro data from the reference dataset.

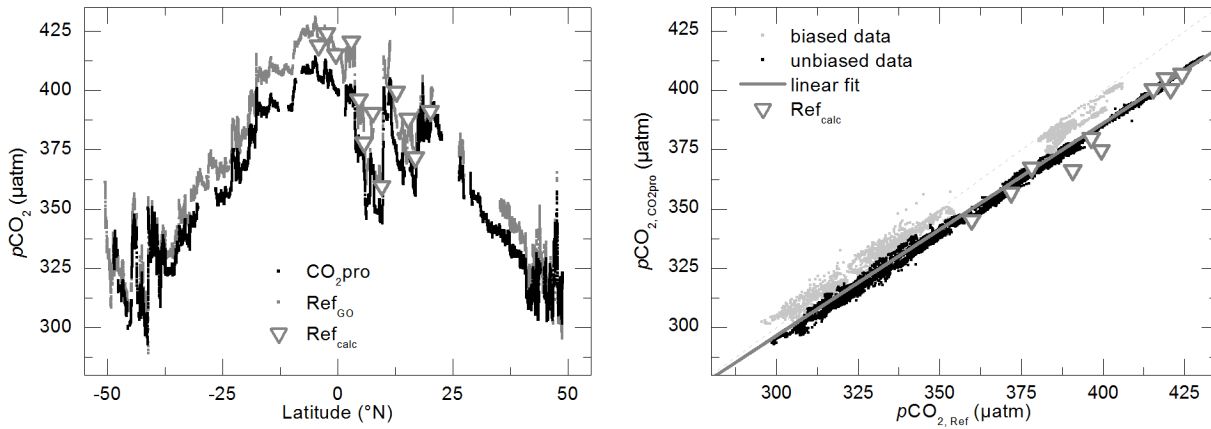


Figure 3.3 Results of $p\text{CO}_2$ intercomparison during R/V *Polarstern* evaluation cruise (both panels). A correlation with GO reference $p\text{CO}_2$ (right panel, gray solid line) was found to be $y=0.90*x+27.9$ ($\pm 3.4 \mu\text{atm}$, $r^2=0.99$). Accuracy improves significantly when single events of critical data (right panel, gray dots) were excluded from the dataset ($y=0.91*x+20.9$ ($\pm 1.5 \mu\text{atm}$, $r^2=0.99$)). Data are in agreement with independent reference samples (gray triangles).

These differences in $p\text{CO}_2$ between both systems ($p\text{CO}_{2,\text{CO}_2\text{Pro}} - p\text{CO}_{2,\text{GO}}$) are more clearly visible in the corresponding offset plot (Figure 3.4, left panel). The offset pattern clearly shows a pronounced drift over the entire cruise. Thus, accuracy of the PSI CO_2 -Pro ranges between 1 and 15 μatm for $p\text{CO}_2$ (neglecting biased data). A mean offset of $-11.8 \pm 3.4 \mu\text{atm}$ (RMSE: 12.3 μatm) was determined. After exclusion of the distinct events of stronger deviations a negative correlation with $p\text{CO}_{2,\text{GO}}$ ($r^2=0.80$; Figure 3.4, right panel, black dots) and SST ($r^2=0.66$; data not shown) was found, indicating cell-temperature driven effects on the sensor calibration.

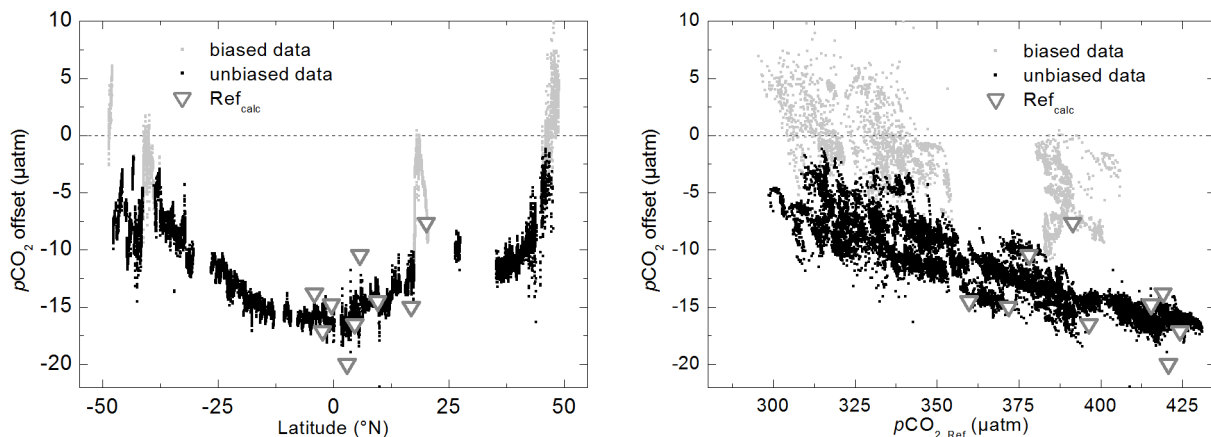


Figure 3.4 Difference between $p\text{CO}_2$ measured by the PSI CO_2 -Pro from GO reference system or independent reference samples during R/V *Polarstern* cruise (left panel). Excluded events (light gray) stick out from the background of a drift pattern that is strongly correlated with ambient $p\text{CO}_2$ (right panel).

The reason for the two pronounced peaks in the offset data (excluded above as biased data) is not fully clear. No correlation of these offsets with measured parameters has been found. Problems with the data of the reference systems can be ruled out due to the fact that both reference measurements, which are fully independent of each other, show a very similar offset pattern. Thus,

either an inconsistency of internal PSI CO₂-Pro processing or membrane-related effects (e.g., air bubble accumulation within the interface) could explain these mismatches.

However, results of this field evaluation pointing out a strong dependence of sensor accuracy on environmental conditions such as water temperature. In the presence of steep temperature gradients, as encountered during profiling applications, these effects are expected to get amplified and thereby limiting the sensor accuracy.

3.1.2 Evaluation of the HydroC sensor [Manuscript A]

This chapter is based on a manuscript that is in preparation for being submitted to the *Journal of Atmospheric and Ocean Technology*. Please refer to the manuscript list given at the outset of this thesis for more detail.

Citation: Fietzek, P., **B. Fiedler**, T. Steinhoff and A. Körtzinger, 2013: In situ accuracy assessment of a novel underwater CO₂ sensor based on membrane equilibration and NDIR spectrometry, *to be submitted to J. Atmos. Oceanic Technol.*, in preparation.

Abstract

We present a detailed accuracy assessment of a novel $p\text{CO}_2$ sensor based on field deployments carried out between 2010 and 2011. The commercial underwater sensor (HydroC™-CO₂, CONTROS Systems & Solutions GmbH, Kiel, Germany), which is based on membrane equilibration and NDIR spectrometry is small and can be integrated into mobile platforms. It is calibrated in water against a proven flow-through $p\text{CO}_2$ instrument within a custom-built calibration setup. The aspect of highest concern with respect to the data quality of the sensor is the compensation for signal drift inevitably connected to absorption measurements. We use three means to correct for drift effects: (i) a filter correlation or dual-beam setup, (ii) regular zero gas measurements realized automatically within the sensor and (iii) a zero based transformation of two sensor calibrations flanking the time of sensor deployment.

Three sensors were tested against an underway $p\text{CO}_2$ system during two major cruises providing an in situ temperature range from 7.4 to 30.1°C and $p\text{CO}_2$ values between 289 and 445 μatm . The average difference between sensor and reference $p\text{CO}_2$ was found to be $-0.7 \pm 3 \mu\text{atm}$ with an RMSE of 3.7 μatm .

A.1 Introduction

The measurement of dissolved carbon dioxide (CO_2) is important and valuable for a large number of scientific, industrial as well as socio-economic issues. Major scientific interest is related to the anthropogenic increase of atmospheric CO_2 concentrations and the resulting oceanic uptake of this most important anthropogenic greenhouse gas (Sabine et al. 2004; Rogner et al. 2007). The exchange of CO_2 across the air-sea interface and the dynamics and trends of the carbon cycle in coastal and open ocean regions (Takahashi et al. 2009; Gruber et al. 2010a) as well as in the interior ocean are key aspects of current marine carbon cycle research.

Dissolved CO_2 reacts with water to form carbonic acid (H_2CO_3), which rapidly dissociates into hydrogen (H^+), bicarbonate (HCO_3^-), and carbonate ions (CO_3^{2-}). The exact speciation within the marine CO_2 system, i.e. between the above species of the carbonic acid dissociation system, strongly affects the pH of the solution (Millero 2007) and is of major interest. An increasing amount of dissolved CO_2 therefore leads to a decreasing pH, a process also referred to as ocean acidification in the context of the anthropogenic CO_2 transient. Its impact on calcifying organisms (Orr et al. 2005; Riebesell et al. 2000) as well as on the physiology and reproduction of other marine species is presently not well understood. The potential long-run acidification influences on fisheries as well as carbon capture and underwater storage scenarios (IPCC 2005) show the socio-economic relevance of CO_2 measurements and highlight the demand for baseline monitoring of CO_2 parameters in the ocean.

Since the thermodynamic constants of the marine carbonate systems are known rather precisely (e.g., Millero 2007), the marine CO_2 system can be fully determined by measurement of any two of the following variables: dissolved inorganic carbon (DIC), total alkalinity (TA), pH and CO_2 fugacity ($f\text{CO}_2$) or CO_2 partial pressure ($p\text{CO}_2$; Millero 2007). Although the sole measurement of $p\text{CO}_2$ is not sufficient to fully characterize the marine CO_2 system, $p\text{CO}_2$ is still a versatile key parameter: It is the determining factor for air-sea gas exchange and responds sensitively to biogeochemical processes such as photosynthesis and respiration. Hence $p\text{CO}_2$ is both, a valuable stand-alone measurement parameter as well as a useful measured variable within multi-parameter measurements for the determination of the CO_2 system. So far only $p\text{CO}_2$ and pH can be measured autonomously by means of commercial underwater sensors (DeGrandpre et al. 1995; Seidel et al. 2008; Martz et al. 2010). Sensors for autonomous measurements of other carbonate system parameters (TA, DIC; Byrne et al. 2002; Wang et al. 2007) and even for direct measurements of carbonate ions are under development (Byrne and Yao 2008).

Due to a lack of a commercially available underwater $p\text{CO}_2$ sensor with a sufficient accuracy and platform integratability, we have advanced the development of an autonomous, continuously measuring and commercially produced underwater $p\text{CO}_2$ sensor (HydroC™-CO₂, CONTROS GmbH, Kiel, Germany). Its versatility and specifications allow for an easy integration into various platforms and provide a suitable tool for $p\text{CO}_2$ measurements at an improved spatial and temporal resolution in the water column. Here, we present a comprehensive overview of the sensor's measurement principle as well as calibration and assess the achievable data quality by means of a detailed analysis of data from field applications.

A.1.1 Suitable Sensor Platforms

Beside classical moving sensor platforms on the one hand (e.g., voluntary observing ships (VOS), research vessels equipped with water sampling rosettes) and stationary buoys and moorings on the other hand, trends towards innovative mobile platforms are identified (Fietzek et al. 2011). These platforms, e.g. autonomous underwater vehicles (AUV), floats and gliders, provide an increased autonomy, mobility and versatility as opposed to the classical carriers. They allow for a more cost-efficient data collection on so far largely unexplored temporal and spatial scales. These newly accessible scales are of high interest for the investigation of various biogeochemical processes, making these modern mobile platforms desirable carriers for $p\text{CO}_2$ sensors (Gruber et al. 2010a). By equipping autonomous platforms as a regional or global sensor array with high spatiotemporal resolution, such as the prominent Argo project, a high scientific potential can be achieved (Alkire et al. 2012; Riser and Johnson 2008; Roemmich et al. 2004). However, in order to be easily installed on modern mobile platforms, new sensors need to cope with the demands of the more complex carriers and fulfill the more stringent requirements with respect to payload capacity, power availability, response time, etc. A more detailed discussion of these facts and circumstances can be found in Fietzek et al. (2011).

A.1.2 $p\text{CO}_2$ Measurements

The first measurements of dissolved CO₂ were developed for medical applications already in the 1950's. These were based on wet-chemical pH-determination behind a Teflon™ membrane (Stow et al. 1957; Severinghaus and Bradley 1958). Today optical CO₂ measuring techniques are prevailing. One method is to detect and quantify CO₂ molecules within an equilibrated gas stream by means of direct absorption in the infra red (IR) region of the electromagnetic spectrum. Another technique is an indirect measurement making use of the pH affecting property of CO₂ by applying spectrophotometry within an equilibrated pH-sensitive dye solution of known characteristics (Lefèvre et al. 1993; DeGrandpre et al. 1995). An overview of current sensor techniques for carbonate system

species can be found in Byrne et al. 2010. A technical evaluation of $p\text{CO}_2$ sensors that also includes an early version of the sensor discussed here is presented in Tamburri et al. (2011).

The usage of underway flow-through instruments to measure $p\text{CO}_2$ both, in the oceanic surface layer and in the atmosphere dates back to the 1960s (Takahashi 1961). While in the beginning the application of these systems was restricted to research vessels, current strongly improved systems are suitable also for application on unattended platforms (e.g., VOS; Watson et al. 2009; Pfeil et al. 2011; Pierrot et al. 2009). Continuous optimization of the overall setup and the components used lead to some standardized design that is nowadays also commercially available. The key components of such a flow-through instrument are the air-seawater equilibrator and the IR gas analyzer. The equilibrator is used to achieve partial pressure equilibrium between the dissolved gases in a continuous stream of sea water and air that is re-circulated between the equilibrator and a benchtop IR analyzer. The achievable measuring accuracy is $2 \mu\text{atm}$ for surface seawater $p\text{CO}_2$ measurements (Pierrot et al. 2009). The flow-through system data are commonly reported as $p\text{CO}_2$ although the $f\text{CO}_2$ is the value suggested for most accurate carbonate system calculations. Based on approximated expressions the $f\text{CO}_2$, which considers the slightly non-ideal behavior of CO_2 in the gas phase, can be calculated from temperature and $p\text{CO}_2$, which presumes ideal gas behavior. Underway or flow-through systems are commonly and correctly referred to as “instruments” as they comprise a large number of different sensors for pressure, temperature, humidity as well as for CO_2 . Based on this definition of an instrument the sensor discussed below should actually be referred to as an instrument as well. Since the community commonly calls small and self-contained measuring devices sensors regardless of the amount of individual sensors installed therein, we consistently refer to the presented device as a sensor.

A.2 Sensor Description

A.2.1 Starting Situation and Development Aims

The development aims of the $p\text{CO}_2$ sensor among others were to obtain (i) a versatile and autonomous sensor that could be deployed on a float with (ii) a response time of less than 5 min, (iii) an accuracy better $5 \mu\text{atm}$, and (iv) a stability and reliability that would allow for long-term deployments of several months.

The starting point of the CO_2 sensor development was an early version of the HydroC™- CH_4 (CONTROS). The key components, a flat silicone membrane, a pumped gas circuit and the IR

detector, were retained. Setup changes were conducted with respect to the following aspects: tubing system, gas heater, thermal insulation, additional sensors and overall design.

Perfluoroalkoxy (PFA) tubing was introduced and the gas tightness of the internal gas stream as well as of the integrated 3/2-way-valves was checked thoroughly prior to calibration. Opposed to $p\text{CO}_2$ underway systems in which gas stream leakages are a major source for measuring errors (Pierrot et al. 2009), the biggest “leak” within the gas stream of this sensor remains the equilibration membrane; the high gas permeability of the membrane related to the volume of the gas stream compensates for possible influences caused by small leaks. If unwanted bigger leakage occurred within the gas stream, the entire, much larger internal gas volume of the sensor would be equilibrated, leading to noticeably slower response times. A gas heater was developed whose heating control system is also used to stabilize the temperature of the IR detector. The gas heater buffers seawater temperature gradients ($\Delta T_{\text{seawater}}$) in such a way that large $\Delta T_{\text{seawater}}$ are related to a much smaller ΔT_{gas} . We chose to set the control temperature just high enough for the heating control circuit to keep the controlled temperature stable also at the maximum temperature expected during deployment. If the control temperature is set higher than necessary, avoidably high power consumption is the consequence and the abundant absolute temperature differences between the surrounding water and the internal gas becomes larger. The temperature aspect is picked up again below. Aiding the gas heater and the temperature stabilization, the insulation of the pressure housing was optimized and temperature sensitive components were separately protected. Within the gas stream additional sensors for pressure, temperature and relative humidity (RH) were introduced. Their position was chosen upon extensive laboratory tests to be most beneficial for their consideration within the IR sensor data analysis. The internal overall design of the sensor was revised and the new arrangement of the components on a mounting plate was paralleled by various improvements to the sensor electronics such as the introduction of a microcontroller based setup.

A.2.2 Sensor Specifications

Table 3.1 lists the specifications of the developed sensor as applicable for the measurements discussed in this work. Different data communication options are available as well as an internal data logger that can either be used as a stand-alone memory or for backup storage (Fiedler et al. 2012). A sleep mode function rounds the abilities for autonomous installations. The sensor development also comprised a surface water flow-through version of the sensor which is not further addressed here.

Parameter/Component	Specification
Measurement principle	IR absorption measurement in a membrane equilibrated headspace
Detector	Single beam dual wavelength NDIR detector; zeroings at desired intervals
Housing, dimensions	Cylindrical titanium housing, 90 x 530 mm (without connector)
Depth capability	2000 m (standard)
Weight	5.5 kg in air, approx. 2.6 kg in water
Operating temperature	3 – 30°C
Supply voltage	11-24 VDC
Power requirements	<3 W for the detector and all the electronics, + <1 W – 3.5 W for temperature stabilization, + <6 W during warm-up for 2 – 30 min, + 4 W during zeroing, + water pump: 7 W or 1.5 W (pump SBE 5T and 5M respectively)
Sampling rate	≤ 1 Hz
Response time ($t_{63\%}$)	Approx. 70 s or 130 s (pump SBE 5T and 5M respectively)
Measurement range	200 μatm – 1000 μatm (standard)

Table 3.1 Specifications of the developed $p\text{CO}_2$ sensor as used during the deployments discussed in this paper. The specifications of the latest available sensor model differ from these values with respect to size and power consumption. The power required for the temperature stabilization as well as the warm-up duration depend on the actual water temperature, the chosen control temperature as well as on the thickness of the insulation material. The given warm-up times correspond to 24 V supply voltage in 20°C water and to 12 V supply voltage in 3°C water. Refer to the text for further details regarding the warm-up and the zeroing interval. The response times refer to the usage of two different pump models at 20°C water temperature. The pump SBE 5T (Sea-Bird Electronics) has a flow rate of approx. 105 mL s⁻¹, while the smaller model, SBE 5M, provides a flow rate of approx. 35 mL s⁻¹.

A.2.3 Sensor Design

Since the developed sensor is based on the same measuring principle as proven flow-through systems, it has the same key components: an equilibrator and an IR CO₂ detector. A planar, semi-permeable membrane with a silicone active layer is installed in the head of the sensor (Figure 3.5). It acts as an equilibrator as well as a phase boundary between the ambient water and an internal headspace. The sensor is commonly equipped with a water pump that provides a continuous seawater flow to the membrane and thus reduces the thickness of the static boundary layer in front of the silicone. By that the response time is effectively shortened and made independent of a relative movement between the membrane and the surrounding water. In order to withstand the high hydrostatic pressures the membrane is mechanically supported from behind by means of a sintered metal disc. A gas pump continuously circulates air between the membrane equilibrator and a non-

dispersive IR detector (NDIR). The gas circuit also features a gas heater upstream of the NDIR detector as well as additional sensors for pressure, temperature and RH.

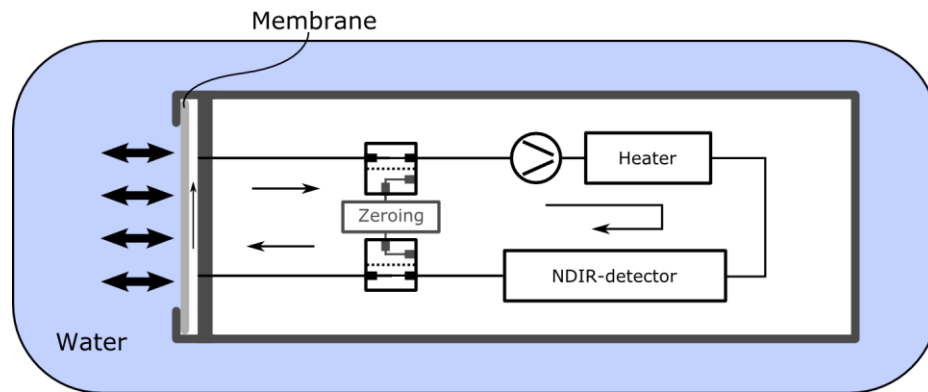


Figure 3.5 Schematic drawing of the HydroC™. Dissolved CO₂ in the water permeates the planar membrane and a gas pump continuously circulates air between the membrane interface and the NDIR-detector. A second circuit incl. a soda lime cartridge provides zero gas with respect to CO₂ for regular zeroings (refer to text).

The quality and a deep understanding of the NDIR detector are crucial for the data quality of both, underway instruments as well as the new underwater sensor. All additional components within underway instrument's and the underwater sensor's gas circuit beside the equilibrators and NDIR detector such as the additional sensors mentioned above are required for accurate and precise absorption measurements and allow for preferably long deployments.

In contrast to common practice of underway instruments the absorption measurement within the sensor is carried out in wet air and without interrupting the gas flow for measurement. In the underwater sensor regular zero gas measurements can be carried out. Therefore valves are included into the circuit that lead the pumped air through a soda lime cartridge instead of the membrane equilibrators at desired intervals (Figure 3.5). In the presence of water vapor soda lime scrubs the CO₂ and bonds it as calcium carbonate (CaCO₃) thus creating a zero gas with respect to CO₂.

The sensor operates by consecutively switching through different intervals, the durations of which can be individually set. As soon as the sensor is powered it starts with a warm up interval followed by continuous repetition of measuring cycles. One measuring cycle consist of three intervals: zero, flush and measure (Figure 3.6).

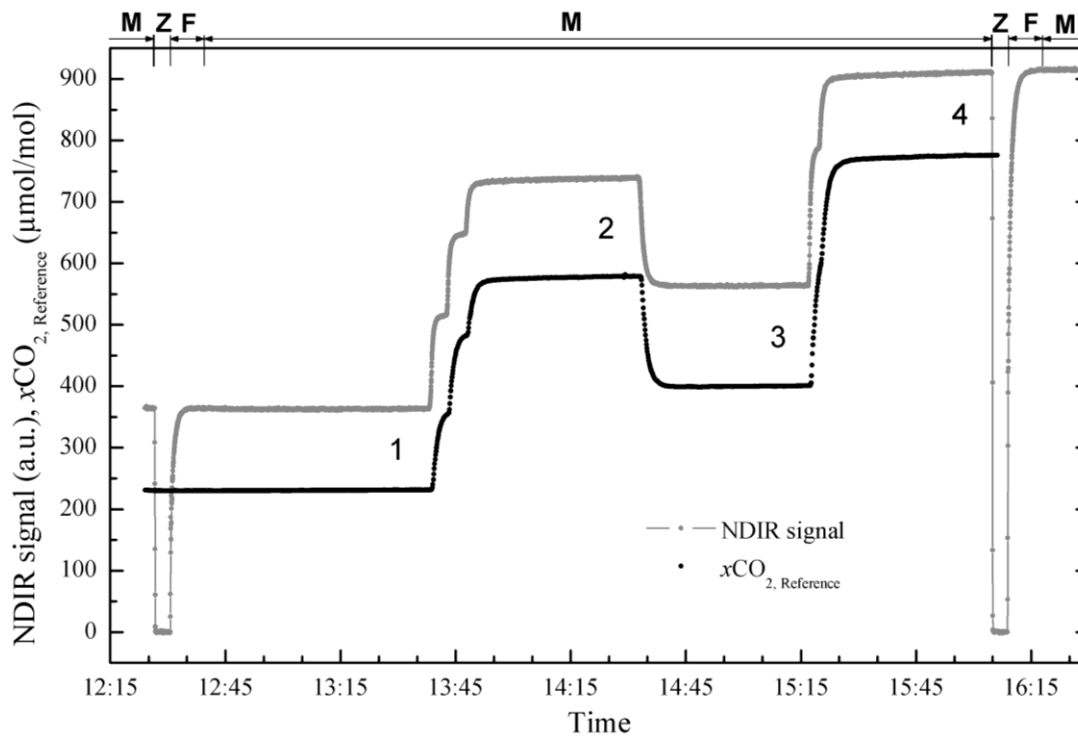


Figure 3.6 Course of a calibration carried out at a constant water temperature within the calibration setup described in the text. The absorbance NDIR signal shown in arbitrary units is dual-beam and zero corrected. The given CO_2 mole fraction is the dry $x\text{CO}_2$ measured by the reference flow-through system. The numbers 1 – 4 indicate the calibrations steps and “Z”, “F” and “M” mark the sensor intervals: zero, flush and measure.

The warm up interval is only passed through once after the sensor has been turned on. The required warm-up time depends on the water temperature and the supplied voltage (c.f. Table 3.1). During the warm up the water pump is disabled and data are neither transmitted nor stored in the internal logger. During zero intervals, a zero CO_2 gas is created as described above and the sensor provides the current zero reading used later for drift correction. The zeroing typically lasts a few minutes and is recommended to be repeated at least every 12 or 24 h. Data stored during that time are specially flagged for easy handling during analysis. Flush intervals are only used to flag data acquired during the signal recovery from the zero value to the ambient $p\text{CO}_2$ reading. Technically the measuring process of the sensor does not differ between the flush and the subsequent measuring interval. The time the sensor needs for full equilibration depends on the sensor configuration and the environmental conditions, mainly the water temperature. The warmer the water, that faster is the response time and thus the shorter the required flush time. The actual response time of the sensor can be derived based on the course of the signal recovery as applied within Fiedler et al. (2012). It is typically faster than the 2-min response time of the flow-through system (Pierrot et al. 2009) and allows for measurements on moving platforms; especially if a response time correction is applied (Fiedler et al. 2012). A more detailed analysis of the sensor’s response characteristics is in preparation. During flush and measurement intervals the water pump is active and data are recorded

as configured. The interval settings simplify the data processing and provide the means to generate measurement data from a fully equilibrated and internally well temperature stabilized sensor. Figure 3.6 shows the sensor signal during calibration. Therein the zero, flush and measure intervals are denoted.

The comparatively fast response time, small size and operability of the sensor allow for deployments on various platforms. Due to its design and compared to classical flow-through systems the maintenance intensity and the risk for leaks in the gas stream are low. If used in situ, the sensor lacks the demand for an accurate water temperature probe as it is crucial for typical flow-through systems (Körtzinger et al. 2000). In order to derive the actual amount of dissolved CO₂ ([CO₂]) from the measured partial pressure, the sensor is commonly deployed together with a CTD probe, as the solubility of CO₂ depends on temperature and salinity (Weiss 1974).

A.2.4 CO₂ Measurements by Means of NDIR Spectrometry

The properties of the NDIR detector are relevant for the overall performance of the sensor. Drift, cross-sensitivities and the signal-to-noise ratio (S/N) of the NDIR detector directly affect the data quality.

NDIR spectrometry in general is a proven direct measuring technique for mole fractions of gases absorbing in the IR. It is non-destructive and traceable to standards. NDIR detectors for CO₂ have small dimensions (several cm) and moderate power consumption (here: about 0.5 W) that allow for easy integration. In addition they provide good mechanical strength and are unaffected by vibrations if realized without moving parts. Due to their high selectivity and limited cross sensitivity NDIR detectors are well suited for qualitative analysis. NDIR detectors are composed of three main components: light source, absorption/beam path and detector. Each of them has different influences on the final sensor signal and depends differently on environmental variables, e.g. temperature. This may lead to particularly complex overall sensor properties. Hence these parts need to be carefully matched in order for a NDIR detector to meet the measuring requirements of a certain application. Their choice defines the S/N, the sensitivity and the measuring range (detection limit and upper range value) of a NDIR unit. The basic idea is to get enough light energy at the desired wavelength to the detector and to make the absorption path sufficiently long such that changes in absorbed light intensity can be clearly resolved by the detector and amplifying electronics. Various options exist to optimize and dovetail these components.

The linear relation between the transmitted light intensity, I , and molecule concentration, c , as described by the Beer–Lambert Law makes the technique suitable for quantitative analysis:

$$I = I_0 10^{-\varepsilon cl} \quad 3.1$$

with I_0 being the initial light intensity, l the distance the light travels through the absorbing medium and ε the molar absorption or extinction coefficient of the target molecule to be detected. According to eqn. 3.1 the absorbance, A , or extinction is defined to be directly proportional to the molecule concentration in the medium:

$$A = \log\left(\frac{I_0}{I}\right) = \varepsilon cl \quad 3.2$$

In reality there is a small non-linearity of the NDIR detector characteristic due to the fact that Beer–Lambert law is only defined for a single wavelength of infinitesimal small width, while in applications spectral dependencies occur.

The NDIR unit used features a black body radiator as a broad band IR light source and a pyro-electrical IR detector which requires pulsed operation of the IR emitter. Interference filters in front of the detectors select the desired measurement as well as reference wavelength and together with the required electronics for control and evaluation complete the single beam dual wavelength NDIR detector. CO₂ is typically sensed around 4.26 μm where it shows its highest absorption due to its fundamental asymmetric stretching vibration (2349.1 cm^{-1}) and the reference wavelength is chosen to be placed in the water vapor window at around 4.0 μm .

Within an NDIR detector, several temperature influences exist that either require a compensation, calibration or stabilization. The spectral properties of the filters are temperature dependent: The central filter wavelength can shift as well as the transmission width can vary. A temperature influence on the sensor can occur in the form of thermal noise, a thermal background signal and changes in sensitivity. In the case of a dual beam setup the influences might even be different for both channels. The emission properties and emitted intensities of the light source show a temperature influence as well. Thermal expansion of the cuvette or other mechanical deformations of the absorption path may have an additional effect on the measurements. Finally temperature dependencies of the analog electrical components directly behind the detector need to be considered. The overall effect caused by temperature changes is hence very variable in magnitude and sign for measuring channels of two products of the same kind as well as for a measuring and reference channel within the same instrument with its two filters, two detectors and two electronics. For this reason and to enhance the measurement quality the entire NDIR detector is temperature stabilized within the sensor. Active temperature stabilization furthermore helps to reduce the required warm-up time present in any NDIR detector due to self heating effects. A separation of the light source and the detector from the gas stream by windows further enhances the temperature

stabilization capability and protects the sensitive detector with the filter. A gas heater further reduces the temperature gradient within the cuvette and simultaneously reduces the risk of condensation within the optical components of the sensor.

Any sensor based on an absorption principle such as a NDIR detector “sees” the highest raw signal in the case of a zero concentration of the target molecules in the beam path as in that case no absorption occurs and the maximum radiation intensity reaches the detector (see eqn. 3.1). Therefore the regular determination of the sensor signal of a zero gas is essential to account for drift effects that alter the light intensity with time and that otherwise would be erroneously interpreted as changes in target gas concentration. Typical effects are:

- (i) Intensity variations or spectral shifts of the light source over time,
- (ii) Contamination of any component within the beam path that might cause shadowing or growing reflectivity losses in the cuvette,
- (iii) Aging effects that alter the detector sensitivity over time,
- (iv) Changes in the pre amplifier gain of the detector.

Within the sensor the zeroing does not only account for longer term zeroing influences but also for large changes of the measurement conditions such as large changes in water temperature that cause internal temperature gradients and different water vapor concentrations within the gas stream.

Drift compensation by means of a differential setup in our case realized in the form of filter correlation is referred to as a two-beam/two-wavelength method. It is supposed to compensate any unwanted influences that cause signal drift of both channels in the same manner (aspects (i) and (ii) above) as the measured signal is supposed to be continuously referenced. Any effects that cause changes in the detector signals and that are not caused by actual concentration changes within the cuvette shall be compensated in real time and parallel to measurements. In reality, this technique has its limitations in accounting for influences resulting from the usage of the two different channels with their own filters and detectors. Theoretically the zero-point of a two-beam instrument should not be affected by the above mentioned drift reasons ((i) through (iv)) but as we are measuring at two different wavelengths spectral effects as well as effects related to the two physically different detectors still affect the zero signal of the “two-beam corrected” signal. Therefore we combine the zeroing and the two-beam drift correction means within our sensor. The latter provides a continuous correction mean applied parallel to measurements, while the zeroing discontinuously further enhances the drift correction capabilities by correcting for effects that differently affect the measured intensities at both detectors.

The zero correction of a two-beam sensor signal does not cover concentration dependent effects that equate to changes in the characteristics of the NDIR sensor's calibration polynomial. Hence for achieving best accuracies with especially two-beam NDIR sensors, the sensor needs to be re-calibrated after deployment at different concentrations beside the regular zeroings.

A.2.5 Membrane Equilibration

The solution-diffusion model can be used to describe gas transport through a dense, semi permeable membrane material. Assuming a partial pressure gradient between the water phase and the internal gas stream, the first step within the transport process is adsorption of the molecule at the membrane surface. In the case of a sufficiently small gas concentration the absorption process into the membrane can be explained by the Henry-Dalton Law, which states the linearity between the partial pressure of a gas and the concentration of that gas in solution connected by a temperature, pressure and, in the case of sea water, salinity dependent constant. The dissolution process is followed by diffusion based transport of the molecules within the membrane along the concentration gradient. Desorption into the headspace again follows the Henry-Dalton Law. This process continues within the membrane of the sensor until partial pressure equilibrium with respect to every single gas component is achieved. Hence semi permeable membranes can be used as equilibrators for dissolved gas measurements (McNeil et al. 2006) and enable the application of gas phase based measuring techniques in the aquatic medium. The time limiting and overall response time dominating step within the entire transport process is the diffusion within the membrane material as well as within a boundary layer in front of the membrane. A parameter composing both, the solubility of a gas within the membrane substance as well as its diffusion constant within the membrane according to Fick's Law, is called permeability. Like the solubility and the diffusion coefficient, the permeability is also concentration independent. The permeabilities of different gases for a given membrane material differ (Robb 1968; Merkel et al. 2000) and hence determine the time constant for the corresponding partial pressure equilibration. The direction of the transport process is defined by the orientation of the individual partial pressure gradient. Silicone, polydimethylsiloxane (PDMS), was chosen as the membrane material due to its high permeability for CO₂ (Merkel et al. 2000).

In addition to the dissolved gases, water vapor also permeates through the membrane. The amount of gaseous H₂O in the gas stream is related to the temperature driven water vapor pressure. The risk of condensation within the headspace and especially within the NDIR absorption path induced by steep gradients of warm to cold water is minimized by the heating of the gas on the way to the NDIR detector. Furthermore the permeability of water vapor is more than a magnitude higher than for CO₂ (Robb 1968) with the sensor response time for CO₂ already being in the order of 70 s.

Typically silicone layer thicknesses of around 10 μm are used. The thickness is determined during membrane production by permeability measurements. Pure silicone monolayer membranes of stated thickness could not be easily handled. Hence we use thin film composite membranes consisting of the dense silicone layer on top of a porous support and a non-woven substructure. In the case of no or minor fouling the membranes can be deployed for several months to years. Cleaning of the membranes with e.g. diluted sulfuric or oxalic acid with pH 2 has successfully been tested. The response time of the sensor determined from the flush interval data can also be used to identify organic growth, since heavy fouling slows down the membrane permeation process or the volume rate of pumped water, which both leads to a reduced response time of the sensor.

A.3 In Water Calibration Setup

Along with the development of the sensor we established a laboratory calibration setup for direct underwater $p\text{CO}_2$ calibration that can hold up to three sensors simultaneously (Figure 3.7). An early version of the setup was successfully used in the past for characterization experiments of a new CO_2 instrument based on cavity ring-down spectroscopy (Friedrichs et al. 2010).

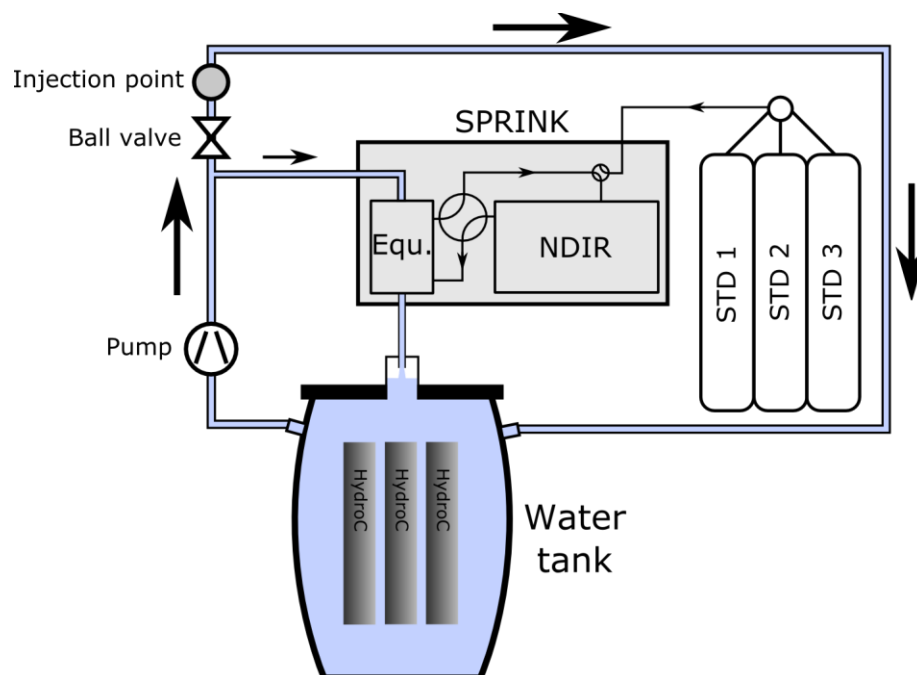


Figure 3.7 Schematic drawing of the calibration setup for highly accurate and precise $p\text{CO}_2$ sensor calibrations in water. Refer to text for further detail.

The setup includes a 120 L insulated and temperature stabilized water tank. The water temperature can be controlled over the temperature range 0°C and 30°C to within ± 0.02 °C. It is filled with de-ionized water. Sodium carbonate and bicarbonate are added in the required quantities in order to mimic the CO_2 buffer system of seawater (DIC-TA ratio) and thereby allow for a better $p\text{CO}_2$ level control. Silver nitrate is added as an anti-foulant. Water is continuously pumped through a reference

flow-through $p\text{CO}_2$ system (Körtzinger et al. 1996), which was slightly modified to suit the laboratory conditions and which was additionally equipped with drying components to facilitate continuous reference measurements in dry gas. Special care was taken that the return flow of the water from the combined bubble-type and subsequent laminar-flow equilibrator into the main tank occurs without restrictions and thus without altering the pressure conditions within the equilibrator. Temperature probes within the equilibrator and the main tank are regularly calibrated against a reference probe with an accuracy of ± 0.02 °C. The flow-through system is equipped with a bench top IR analyzer (LI-6262 or LI-7000, LI-COR Inc, Lincoln, Nebraska, USA), which is calibrated against 3 primary or secondary CO_2 -in-natural air standards relating to National Oceanic and Atmospheric Administration (NOAA) certified standards in the beginning and in the end of each calibration run. Processing of the flow-through system data is carried out according to the procedures described in Dickson et al. (2007) and Pierrot et al. (2009) thus leading to $p\text{CO}_2$ reference values referred to the water temperature in the tank with an accuracy of 2-3 μatm . During a full calibration run, the $p\text{CO}_2$ of the tank water is altered by pH variation through injection of NaOH or HCl solutions. A new concentration in the tank water is set and resolved by the reference system with a time constant of approx. 150 s. By application of the pH-varying technique a wide $p\text{CO}_2$ -range can be realized and calibration steps can be set as desired. Since the overall setup cannot be entirely encapsulated from the surrounding air a small drift of the partial pressures in the tank of typically around 3 $\mu\text{atm hr}^{-1}$ can be observed. Magnitude and timescale of this drift as well as the fact that both, the flow-through system and the underwater sensor, detect this $p\text{CO}_2$ change make this effect negligible with respect to the assumed accuracy of the calibration process. The maximum adjustable range is limited by the measurement range of the IR-analyzer of the flow-through system, which is 3000 $\mu\text{mol mol}^{-1}$ for the dry CO_2 mole fraction in the equilibrated gas stream of the flow-through system ($x\text{CO}_2$). Neither the fact that the injection of NaOH and HCl alter the TA of the tank water, nor the knowledge about the actual present pH is of relevance for the calibration of the $p\text{CO}_2$ sensor. It was found that four calibration steps are sufficient for a sensor calibration in the range of 200 to 1000 μatm . The course of a calibration is depicted in Figure 3.6.

There are several reasons to calibrate the sensor in water with a setup as described above against a proven underway system as opposed to a mere dry gas calibration of the IR detector. The fact that some of the following influences are already considered in data processing corrections or their minimization was addressed in sensor design, does not debilitate the following compensatory advantages of an in water calibration. Firstly, the temperature stabilization including the gas heater used in the sensor does not completely avert the presence of temperature gradients within the instrument's housing, components and gas stream. Hence the temperature stabilization can only

minimize the above mentioned possible temperature effects on NDIR sensors. An in water calibration at a temperature as close as possible to the expected temperature range in the field helps to further reduce these signal influences. Secondly, an in water calibration as described above compensates for all effects related to the fact that there is a large absolute humidity present in the sensor's gas stream. These effects are gas-gas-interactions leading to band broadening, potential cross sensitivities of the NDIR signal against H₂O, or H₂O molecule interaction with the cuvette's surface. It is knowingly accepted that the humidity related compensations are only entirely compensated for a deployment at a water temperature equal to the calibration temperature. Thirdly, an in water calibration compares the overall signal of the instrument with a reference value. Hence it characterizes the overall instrument including the entire membrane equilibration process of the gas stream as identified to be important by Byrne et al. (2010). Any not otherwise considered effects occurring in the sensor's gas stream and behind the membrane are taken care of by an in water calibration.

A.4 Data Processing

The dual-beam NDIR detector provides two signals. The raw signal, S_{raw} , corresponds to the transmitted light intensity around the wavelength at which CO₂ efficiently absorbs (4.26 μm) and the reference signal, S_{ref} , expresses the intensity at around 4 μm where practically no relevant absorption occurs. A continuously referenced sensor signal, the "two-beam signal", is:

$$S_{\text{2beam}} = \frac{S_{\text{raw}}}{S_{\text{ref}}} \quad 3.3$$

As a result of the regular zeroing (Z), we obtain "two-beam zero signals" at discrete points in time:

$$S_{\text{2beam,Z}} = \frac{S_{\text{raw,Z}}}{S_{\text{ref,Z}}} \quad 3.4$$

Linear interpolation in time between two adjacent $S_{\text{2beam,Z}}$ provides zero reference signals for every point in time: $S_{\text{2beam,Z}}(t)$.

A NDIR signal that is improved by both drift correction (DC) means, dual beam and zeroing, is derived as follows:

$$S_{\text{DC}}(t) = \frac{S_{\text{2beam}}(t)}{S_{\text{2beam,Z}}(t)} \quad 3.5$$

The final and drift corrected NDIR signal, which is assumed to be directly proportional to the amount of target molecules in the beam path is related to $S_{\text{DC}}(t)$.

During calibration the flow-through system provides a reference $p\text{CO}_2$ for every calibration step. $p\text{CO}_2$ equilibrium is assumed to be present in the membrane equilibrator of the sensor at that time. Using data of the peripheral sensors in the gas stream, the CO_2 mole fraction ($x\text{CO}_2$) present at the NDIR detector is derived. As the NDIR signal is proportional to the number of molecules in the beam path and not to $x\text{CO}_2$, the reference $x\text{CO}_2$ needs to be density corrected by using data of the additional temperature and pressure sensors built into the gas stream of the HydroC™. A polynomial of rank 3 with a forced zero crossing is then used to calibrate the individual sensor characteristics. It correlates the absorbance signal of the NDIR detector with the corresponding and density corrected $x\text{CO}_2$ in the gas stream (c.f. Figure 3.8).

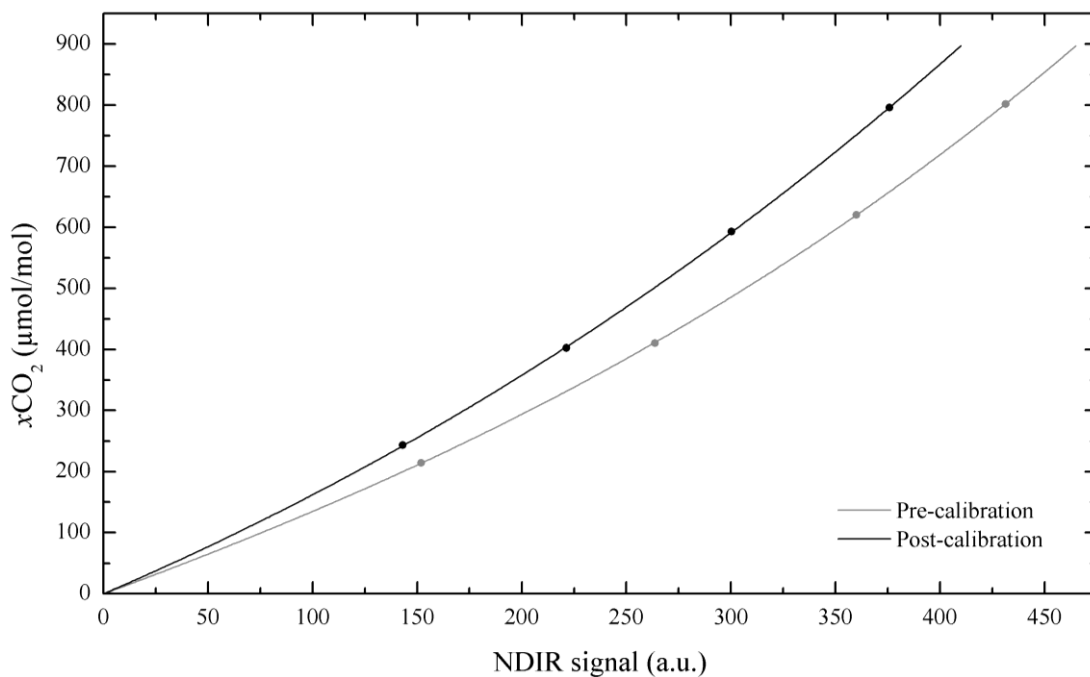


Figure 3.8 Calibration polynomials of sensor HC1 before and after the deployment on R/V *Polarstern*. The absorbance NDIR signal is calibrated against the $x\text{CO}_2$ within the sensor's gas stream obtained according to the text. The polynomials match well the sensor's response characteristics (R^2 in both cases >0.999). A concentration dependent change in the sensor characteristics between the different points in time (e.g., before and after deployment) of the calibrations is clearly visible.

Now, all required dependencies are known and the HydroC™ provides a $p\text{CO}_2$ based on the absorbance signal of its NDIR detector in combination with the data of the peripheral sensors in its gas stream. Beside the density correction no other NDIR signal correction covering for example dilution by water, a band broadening effect as a consequence of CO_2 - H_2O molecule interactions or any other H_2O cross sensitivity is explicitly included in the sensor sided data processing at this point. These aspects are considered through the in water calibration as mentioned in section A.3.

Since the consideration of the zeroings as discussed above requires a fit in time, this calculation step is best applied during post processing of field data. In order to achieve the best measurement

accuracy, changes in the sensor characteristics should also be included into the processing. Therefore the polynomial of a pre-deployment calibration is converted into the polynomial of a post-deployment calibration throughout the course of the deployment. This conversion is not applied as linearly in time, but proportional to the often non-linear course of the zero signals throughout a deployment. This approach assumes change in the zero signals to be correlated in magnitude with changes of the concentration dependent sensor characteristics.

The entire calibration calculations as well as the post processing are accomplished with custom-designed LabVIEW routines (National Instruments, Austin, Texas).

A.5 Field Evaluation

Field evaluations of HydroC™ sensors were carried out in April/May 2010 during a 6-week cruise in the North and South Atlantic (R/V *Polarstern*, ANT-XXVI/4) and in June/July 2011 during a 4-week cruise in the eastern tropical Atlantic (R/V *Maria S. Merian*, MSM-18/3; Figure 3.9).

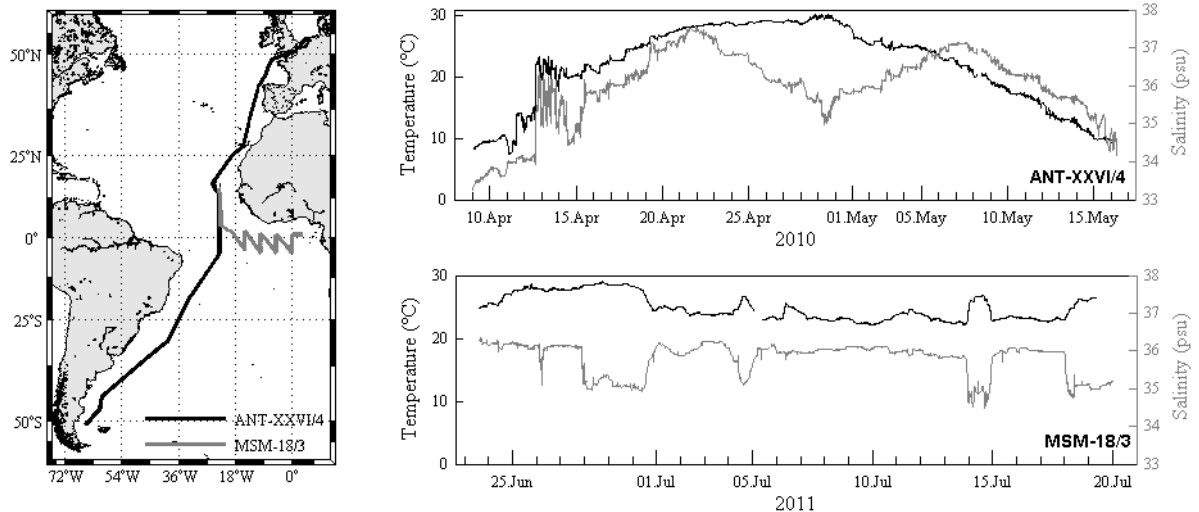


Figure 3.9 The cruise track of R/V *Polarstern* cruise ANT-XXVI/4 and of R/V *Maria S. Merian* cruise MSM-18/3 (left) as well as the encountered sea surface salinity and temperature (right panel). R/V *Polarstern* sailed from Germany to Chile and R/V *Maria S. Merian* from Cape Verde to Gabon.

During these cruises, oligotrophic (i.e., subtropical gyres) as well as mesotrophic regions (e.g., on continental shelves, equatorial upwelling) provided a reasonably wide range in $p\text{CO}_2$ (289 to 445 μatm ; c.f. Figure 3.10 and Figure 3.11, top panel) and temperature (7.4 to 30.1°C). Furthermore, strong $p\text{CO}_2$ and temperature gradients were found on shorter spatial scales. Thus, the conditions were ideal for a thorough evaluation of the HydroC™, which was tested during both cruises with almost identical underway setups: Seawater, either supplied by the ship's clean seawater supply systems (ANT-XXVI/4) or from the ship's keel through the moon pool (MSM-18/3), was pumped to the laboratory into a thermally insulated flow-through box (80 L volume) with a constant flow rate of approx. 12 L min^{-1} . Sea surface temperature (SST) and sea surface salinity (SSS) were determined for

both cruises at the seawater intake. A sensor package containing the HydroC™ (two units during ANT-XXVI/4, HC1 and HC2, and one unit on MSM-18/3, HC3) and an oxygen optode (Model 3830 or 4330, Aanderaa Data Instruments AS, Bergen, Norway), which also provided the water temperature in the flow-through box with an accuracy of $\pm 0.05^\circ\text{C}$, were placed in the underway box and data were binned into 1-min intervals. Since the HydroC™ data was initially stored at 5-s intervals the transformation to the 1-min intervals represents an averaging of typically 12 values. The membrane interface of the HydroC™ was supplied with a constant seawater flow by a SBE 5T pump (Sea-Bird Electronics Inc., Bellevue, Washington). A fully automated $p\text{CO}_2$ underway instrument (GO, General Oceanics, Miami, USA) based on a spray head equilibrator and a LI-7000 CO_2 analyzer (LI-COR Inc, Lincoln, USA) was connected to a bypass at the underway box and operated in parallel. Throughout the expeditions and beside the deployment in the flow-through box the sensors were additionally used for measurements on a profiling water sampler (HC1 five times, HC3 twice; Fiedler et al. 2012) as well as on a surface drifter (HC3 five times; unpublished data).

The two HydroC™ sensors, HC1 and HC2, were in water calibrated at 19.67°C before and after the deployment. HC3 was pre- and post-calibrated at 27°C and 26°C , respectively.

The averaged HydroC™ data were prepared for processing by filtering for obvious outlier zero values as, for example, caused by improper sensor warm-ups, as well other outliers and data biased through insufficient water supply to the flow-through box. All HydroC™ data recorded during flush and zero intervals were excluded from the comparison with the reference. The data of HC2 obtained between 28th of April and 4th of May were excluded from the comparison as well, as the excessively high water temperature did not allow for temperature stabilization at the calibration control temperature anymore. Although the control temperature within HC1 also temporarily exceeded the set point, no data were removed here, as the unit seemed to be more robust in this respect as compared to HC2.

Figure 3.10 and Figure 3.11 show the $p\text{CO}_2$ measured by the flow-through reference system as well as the $p\text{CO}_2$ data of the HC1-HC3 sensors with all datasets corrected to SST for direct comparison (Takahashi et al. 1993).

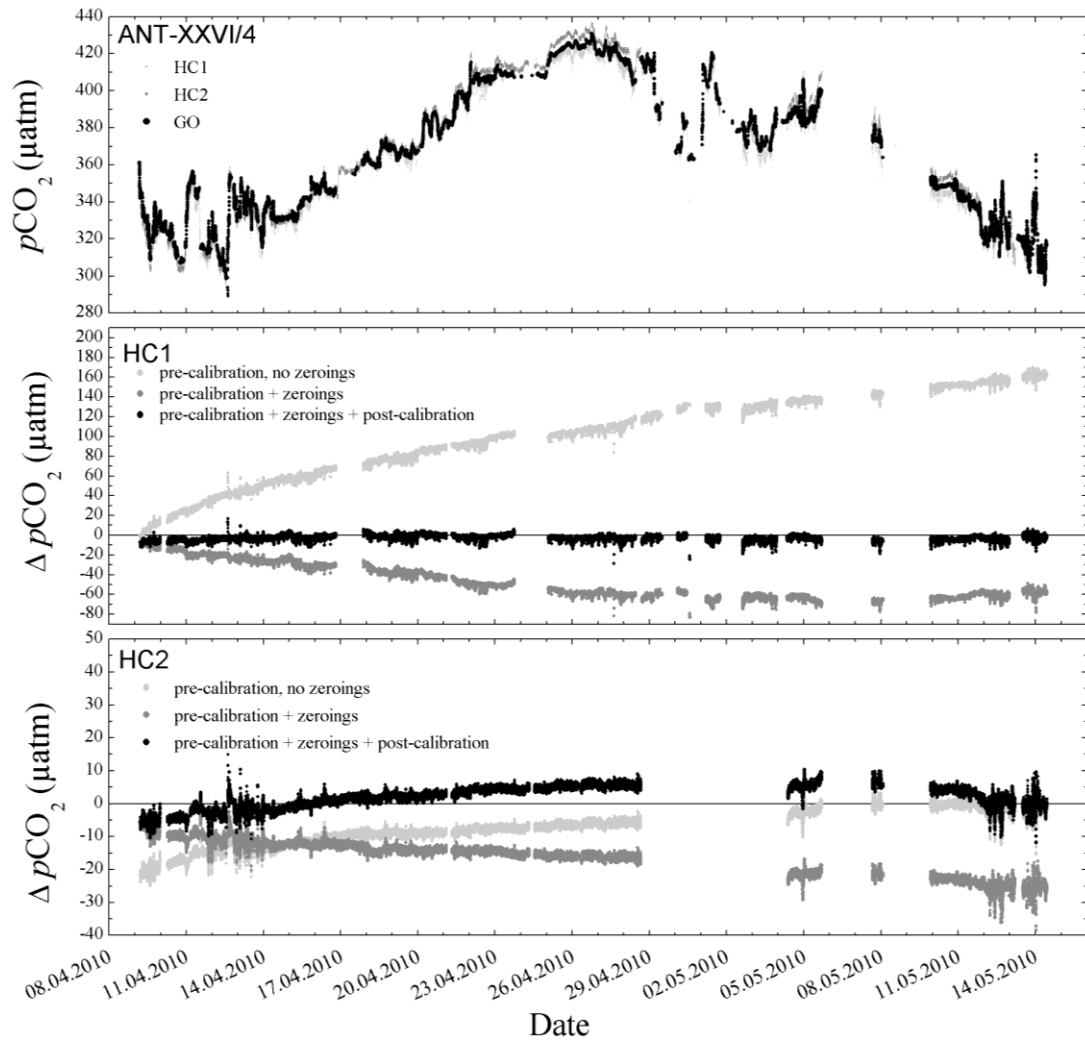


Figure 3.10 $p\text{CO}_2$ data obtained by the GO-system as well as two HydroC™ sensors, HC1 and HC2, during ANT-XXVI/4. The top panel shows the absolute values, while the middle and bottom panel show the differences between the HydroC™- $p\text{CO}_2$ and the reference ($\Delta p\text{CO}_2$) over time for three different processing methods in order to visualize the potential of different drift compensation mechanisms (refer to text). The black curve of HC1 and HC2 represent the final drift corrected and post-processed signal.

In addition, the $p\text{CO}_2$ differences ($\Delta p\text{CO}_2$) between the sensor and the reference data ($p\text{CO}_{2,\text{GO}}$) are plotted vs. time. The three $\Delta p\text{CO}_2$ curves for every sensor are related to different drift compensation mechanisms:

- (i) “pre-calibration, no zeroings”
- (ii) “pre-calibration + zeroings”
- (iii) “pre-calibration + zeroing + post-calibration”

In the case of (i) only the dual-beam correction is applied and the polynomial of the pre-deployment calibration is used. Since in this case data are processed by referencing all signals to the zeroing carried out during calibration, a big offset can already occur at the beginning of a deployment

due to a sensor drift that occurred during transport or due to measurement conditions that strongly deviate from calibration conditions.

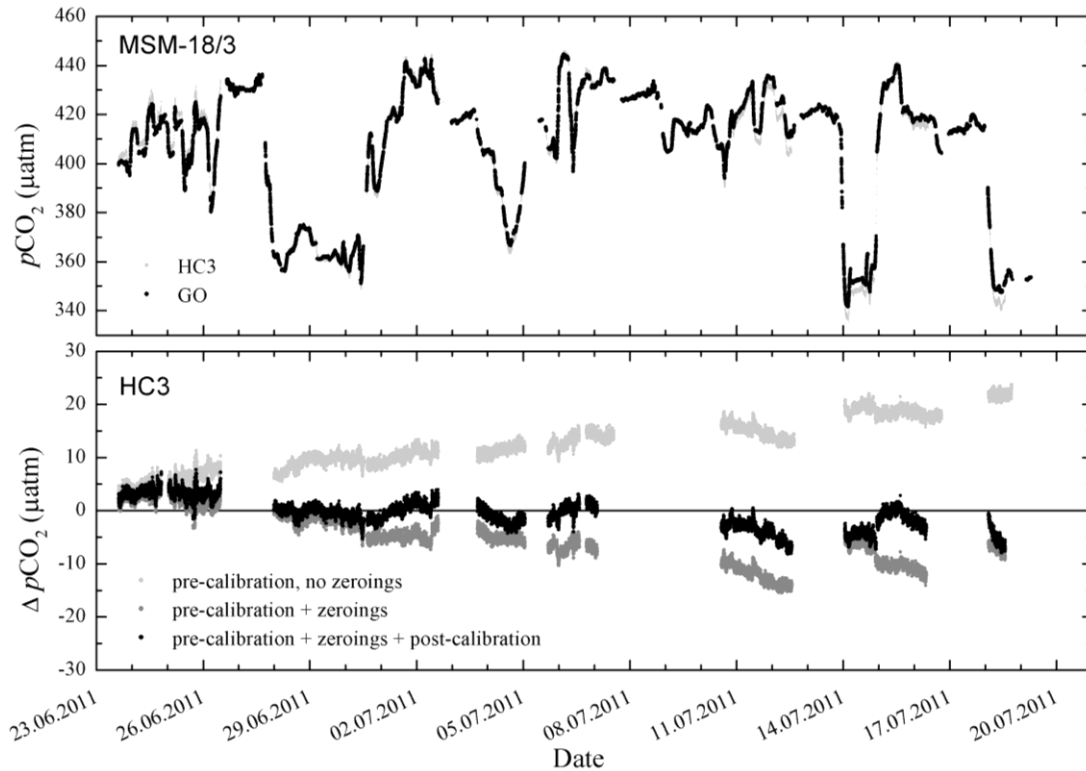


Figure 3.11 The $p\text{CO}_2$ trace during MSM-18/3 measured by the GO reference $p\text{CO}_2$ system, and a HydroC™ sensor, HC3 (top panel). The lower panel shows the $p\text{CO}_2$ residuals between the HydroC™ and the reference ($\Delta p\text{CO}_2$) for three different drift compensation scenarios. The black curve in the lower panel represents the final drift corrected and post-processed signal.

For HC1 and HC3 it can be clearly seen that not considering the zeroing can lead to a large drift. For (ii) the regular zeroings were implemented into the processing (section A.4) thus reducing the offsets over the course of the deployment (HC1 and HC3). It can also compensate for initial offsets (HC2). However, smallest residuals were obtained for methods (iii) by considering both, zeroings as well as pre- and the post-deployment calibration polynomials for post-processing (section A.4). Table 3.2 presents the statistics that correspond to the $p\text{CO}_2$ residuals obtained by the last mentioned, optimal processing routine.

Sensor ID	Mean	σ	RMSE	n
HC1	-3.1	2.9	4.2	24791
HC2	1.8	3.4	3.9	24163
HC3	-0.7	2.8	2.8	12770
Mean	-0.6	3.0	3.7	

Table 3.2 The mean value along with the corresponding standard deviation (σ) and the root mean square error (RMSE) of a total of n $\Delta p\text{CO}_2$ values for every sensor separately as well as averaged (last line).

The mean $\Delta p\text{CO}_2$ and the corresponding standard deviation for all 3 sensors, which is related to the sensor's mean accuracy over the entire dataset, is $-0.7 \pm 3.0 \mu\text{atm}$. The corresponding averaged RMSE, a measure for the uncertainty of the sensor, is $3.7 \mu\text{atm}$. The accuracy of the flow-through system is assumed to be $2 \mu\text{atm}$. The performance of the sensors is convincing against the fact that a large temperature range ($>20^\circ\text{C}$) was covered and that the sensors only received a single point calibration with respect to potential water temperature/water vapor influence by the in water calibration at one temperature. Since the sensors were used for other measurements beside the deployment in the flow-through box, they were restarted and moved back into the box more than twelve times in total. Hence the observed RMSE, which is also affected by large signal variation, is also related to the precision of the sensors during the deployments. As can be seen, the HC3, although restarted the most throughout the deployment, shows the smallest RMSE. The RMSEs of HC1 and HC2 are about 40% larger. The deployment duration as well as the bigger SST and $p\text{CO}_2$ ranges covered during ANT-XXVI/4 seem to affect the RMSE more than do the sensor restarts.

The compensation routines applied, which exclusively rely on data measured by the sensors themselves and the information obtained from calibrations, account well for the signal drift for all 3 sensors. After processing the data quality does not seem to be dominated anymore by unwanted drift effects. This is especially the case for the most strongly drifting sensor HC1, whose signal change over time is also nicely resembled by the change in its calibration polynomials (c.f. Figure 3.8). Although an NDIR detector drifting as strong as the one of HC1 would not pass current quality controls within the manufacturer's production anymore, it is still a good example to show the effectiveness of the processing algorithms. Furthermore the data of HC1 were also included here due to the fact that it is the same unit that participated within a different sensor evaluation project (Tamburri et al. 2011). At that time, the sensor showed a strong drift as well that could not be well compensated due to lack of a full understanding of the required post-processing steps. Although the drift of HC1 could be well corrected for, it in the end still shows a slightly larger mean value and RMSE as compared to HC2 and HC3. NDIR detectors that show a smaller zero drift, typically show a smaller concentration dependent signal change over time as well. This conclusion is further corroborated by the observation that a transformation of the pre-deployment into the post-deployment calibration polynomial based on the course of the zero values finally provides a better correction as opposed to a transformation assumed to occur linear in time (data not shown here).

In order to identify any remaining issues in the drift corrected HydroC™ sensor data, the final $\Delta p\text{CO}_2$ was plotted against $p\text{CO}_{2,\text{GO}}$, SST and $p\text{H}_2\text{O}$ (c.f. Figure 3.12). All sensors indicate a weak correlation with all three parameters. Sensor HC2 shows it clearest. A weak NDIR signal dependency on $p\text{H}_2\text{O}$ might be due to the fact that sensor calibrations were only conducted at one temperature

(section A.3). This circumstance is highlighted by the fact that HC2 and HC3 show the smallest $\Delta p\text{CO}_2$ around the water temperature of their calibration.

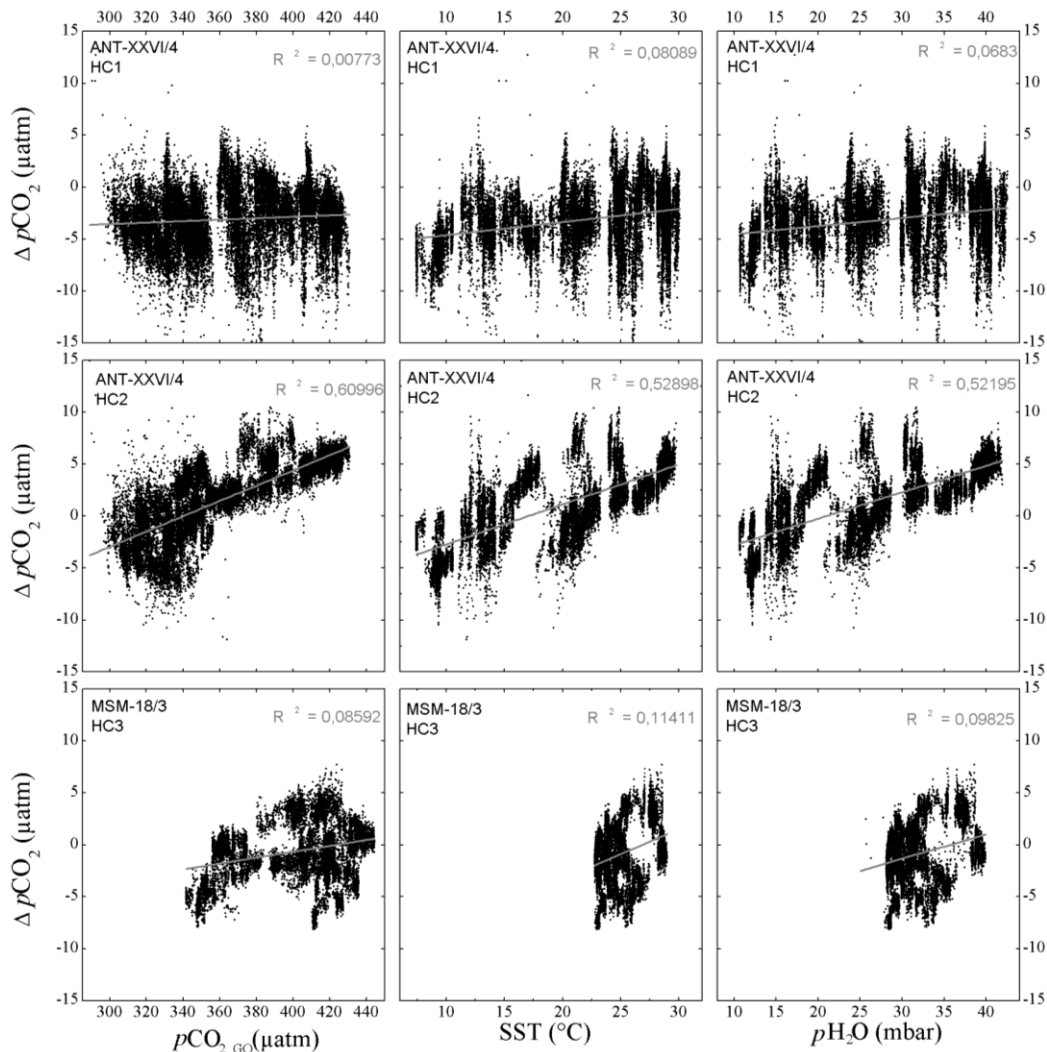


Figure 3.12 In the top row the residuals of HC1 are plotted over the reference $p\text{CO}_2$ (left), the SST (middle) and over the $p\text{H}_2\text{O}$ in the internal gas stream (right). The middle and the bottom row show the same parameter plots for HC2 and HC3 respectively. Although not statistically significant in all cases, a general positive correlation with all three parameters can be made out and is further discussed in the text.

A.6 Summary and Outlook

The development of a new underwater $p\text{CO}_2$ sensor based on membrane equilibration and NDIR spectrometry was described. Special emphasis was put on compensation measures for NDIR sensor drift as well as on the in water calibration of the sensor. The performance of the HydroC™ was assessed based on field data obtained during two cruises both lasting at least one month and covering a wide range in $p\text{CO}_2$ (289 to 445 μatm) and temperature (7.4 to 30.1°C). A wet gas stream within a small underwater sensor represents a demanding environment for NDIR detectors. Against this background the observed mean offset of $-0.7 \pm 3.0 \mu\text{atm}$ with a RMSE of 3.7 μatm is a very promising result, especially since the sensors were also used for various other measurements

including profiling applications in the water column during the deployments. For a measurement range of up to 800 μatm from the calibrations done in the present study the observed mean $p\text{CO}_2$ difference corresponds to less than 1 ‰ and the RMSE to less than 5 ‰. No fouling influence on the data was observed. The given results underline the efficiency of the applied processing algorithms described in this text. The acquisition of high-quality field data by the HydroC™ demands for regular checks of the sensor parameters gas temperature, pressure, RH and control temperature to guarantee proper measuring conditions of the sensor. In addition, regular zero gas measurements need to be carried out under deployment conditions as a second drift correction mean beside the inherent single-beam dual wavelength setup of the sensor. To properly apply the zero information during post processing measurement data should always be flanked by zeroings. Thirdly, in order to also account for the concentration dependant effects on zero and dual beam corrected signals, the sensor needs to be re-calibrated at different concentrations on a time scale of several months to achieve the highest accuracies through data post processing. A water calibration as presented in this paper at a temperature close to the expected water temperatures in the field is beneficial. Nevertheless, the RMSE found within this work is based on field data gathered by sensors that experienced water temperatures around $\pm 10^\circ\text{C}$ with respect to the calibration temperature.

The assessment given here represents an important milestone within the development of the sensor. The procedures discussed are planned to be further automated and made available to other HydroC™ users. Including further NDIR data processing steps or adapting the in water calibration procedure, both aiming at an improved correction of water vapor influence might result in a smaller RMSE during future deployments. Further development steps include investigations of the long-term stability during deployments on moorings and profiling buoys as well as a performance analysis on different moving platforms. Especially the latter has been simplified by a recently released smaller and faster version of the HydroC™.

Acknowledgments.

The authors would like to thank all members of the “(C)O₂” working group at the GEOMAR for fruitful discussions and helpful advice. Furthermore, we thank the entire CONTROS team for their support in this development project. We explicitly acknowledge Christian Rettich for his sustained assistance especially during the construction of the first prototypes as well as Claus Hinz and Matthias Lunge for valuable help with laboratory experiments. Janna Bohlen and Christoph Kirbach are thanked for commenting on the manuscript. We would also like to thank captain and crew of R/V *Polarstern* (cruise leg ANT-XXVI/4) and of *Maria S. Merian* (cruise leg MSM-18/3). This work was partly funded by the WGL SAW project OCEANET (2008-2010).

3.2 Float Evaluations

3.2.1 1G Float

The two sensors for in situ $p\text{CO}_2$ measurements evaluated above were both tested for their performance on Argo floats. With intensive adaptations of the NEMO platform as well as modifications on the sensor side, a 1st generation prototype float (1G) was designed and developed within the framework of this thesis. $p\text{CO}_2$ measurements of the 1G-float were conducted with the PSI CO_2 -Pro sensor technology and as such performed for the first time ever in Oct. 2008.

Field testing as well as regular field deployments were carried out at CVOO since float-borne $p\text{CO}_2$ measurements were supposed to complement regular time series observations at Cape Verde. Figure 3.13 illustrates the spatial coverage of all 3 deployments (D1 – D3) of the 1G float and vertical profiles for temperature (T) and salinity (S) show the range of environmental conditions (O_2 and $p\text{CO}_2$ data is presented further down).

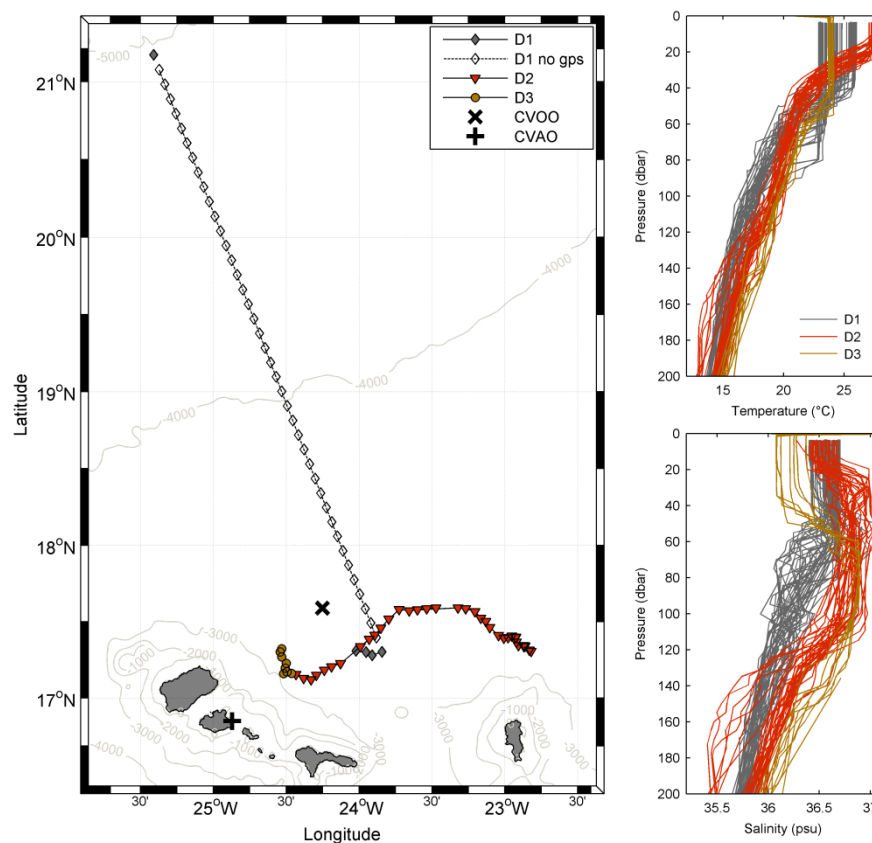


Figure 3.13 Left: Overview map of performed field deployments with the 1G float in the vicinity of CVOO. During deployment 1 (D1) no GPS positions were obtained due to a technical malfunction shortly after deployment (profile no. 4). Open diamonds therefore suggest positions for these profiles in a linearly interpolated manner (between last reported location and the place of recovery), assuming the float was propagating in a straight northwestern direction. Right: Recorded temperature and salinity profiles during D1- D3.

D1 – D3 provide a good basis for the evaluation of these first float-borne $p\text{CO}_2$ measurements ever taken. In sum, 92 vertical profiles (cycle time: 30 h) could be obtained with the 1G float, which yielded a fairly large amount of data for T, S and O_2 (Table 3.3).

ID	Deployment time	No. of profiles	Duration (days)	No. of individual measurements		
				T,S,P	O_2	$p\text{CO}_2$ (proc./raw)
D1	Oct. 2008 – Dec. 2008	45	56	2070	2070	135/3375
D2	Aug. 2009 – Oct. 2009	39	48	1794	1794	117/2925
D3	Jan. 2010 – Jan 2010	8	10	368	368	24/600
Total		92	114	4232	4232	276/6900

Table 3.3 Overview of conducted field deployments with the 1G float. Overall 3 deployments were performed, yielding the first-ever float-borne $p\text{CO}_2$ measurements. Note: Each processed $p\text{CO}_2$ measurement (representing one value of ambient $p\text{CO}_2$ in space and time) were derived from a larger set of measurements (raw). Details are described in the text.

Due to technical constraints of the PSI CO_2 -Pro sensor only a comparatively small number of $p\text{CO}_2$ measurements could be obtained. This is due to the fact that the PSI CO_2 -Pro sensor has a long response time and therefore cannot be operated continuously during an upcast. The profiling approach pursued during the 1G float mission (see section 2.3.1) therefore allows only to resolve the respective $p\text{CO}_2$ profile on 3 certain depths during each upcast. Most reliable $p\text{CO}_2$ measurements for each profile were obtained as follows: The initial warm-up phase of the PSI CO_2 -Pro (20-30 min) was followed by a ZP and then by the recovery of the sensor signal from the ZP towards ambient $p\text{CO}_2$ (named as raw in Table 3.3). Due to the rather slow sensor response at depth as well as limited energy resources of the float platform, a full equilibration of the sensor signal for each depth level could not be obtained (see example in Figure 3.14).

To determine the actual $p\text{CO}_2$ at the respective depth level, an exponential model needs to be applied to the data (section 3.2.2, eqn. 3). With this, proper extrapolation of the recovery signal towards the final and hypothetically fully equilibrated sensor signal (obtained from fitting parameters) was possible. This method is the only way to obtain profile-like $p\text{CO}_2$ values in the water column when using this setup. However, it contains a considerable degree of uncertainty and thereby produces large errors in determined $p\text{CO}_2$ levels (as shown in section 3.3).

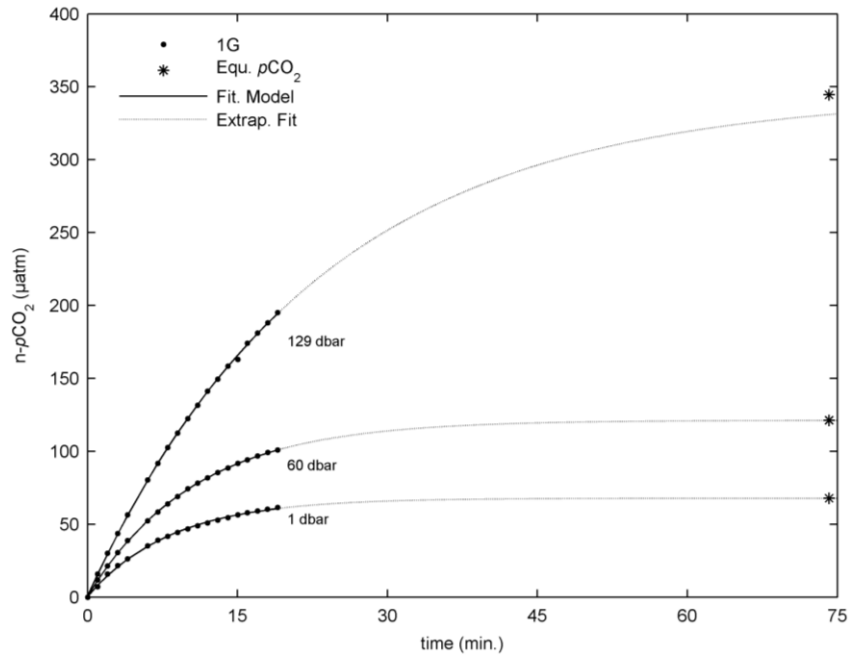


Figure 3.14 Measurements for normalized $p\text{CO}_2$ ($n\text{-}p\text{CO}_2$) recorded during profile no. 71 during D2 (1G float). On each depth level (here 129, 60 and 1 dbar) the PSI CO_2 -Pro sensor was recording the $p\text{CO}_2$ signal straight after a ZP was conducted. These data were fitted with a first-order kinetic model (see section 3.2.2, eqn. 3 for more detail) and thereby extrapolating (black dotted lines) the sensor signal to the fully equilibrated $p\text{CO}_2$ value (black stars). Note that $p\text{CO}_2$ as well as time were normalized to the values at the first data point after the ZP.

Figure 3.15 presents $p\text{CO}_2$ data from all three deployments derived using the model named above. Cumulative profiles show the expected shape as well as expected range of $p\text{CO}_2$ for the CVOO region (left panel). Despite a few outliers obtained $p\text{CO}_2$ measurements seem to follow a consistent pattern over time. However, when illustrating data in space and time one can clearly see the poor vertical data coverage and the rather high noise level of the data.

Measurements close to the base of the ML show a higher scattering of values, which might result from a steep gradient in $p\text{CO}_2$ at these depths. Performing measurements in such steep gradients with an STS approach from a mobile and thus freely moving platform such as the 1G float can lead to a large bias of data in these parts of the water column. Unfortunately, no reference samples for $p\text{CO}_2$ (DIC/TA derived) were available for comparison as collected samples at CVOO prior to 2010 turned out to be contaminated (due to insufficient cleaning of sample bottles). However, beneath the ML a clear negative correlation with simultaneously measured O_2 concentrations was found, as expected for water masses affected by microbial respiration. In sum, $p\text{CO}_2$ data show a reasonable distribution for the CVOO region, even though technical constraints and limitations of this observational approach are large. Due to a lack of reference measurements no information about accuracy of derived $p\text{CO}_2$ data can be given at this time.

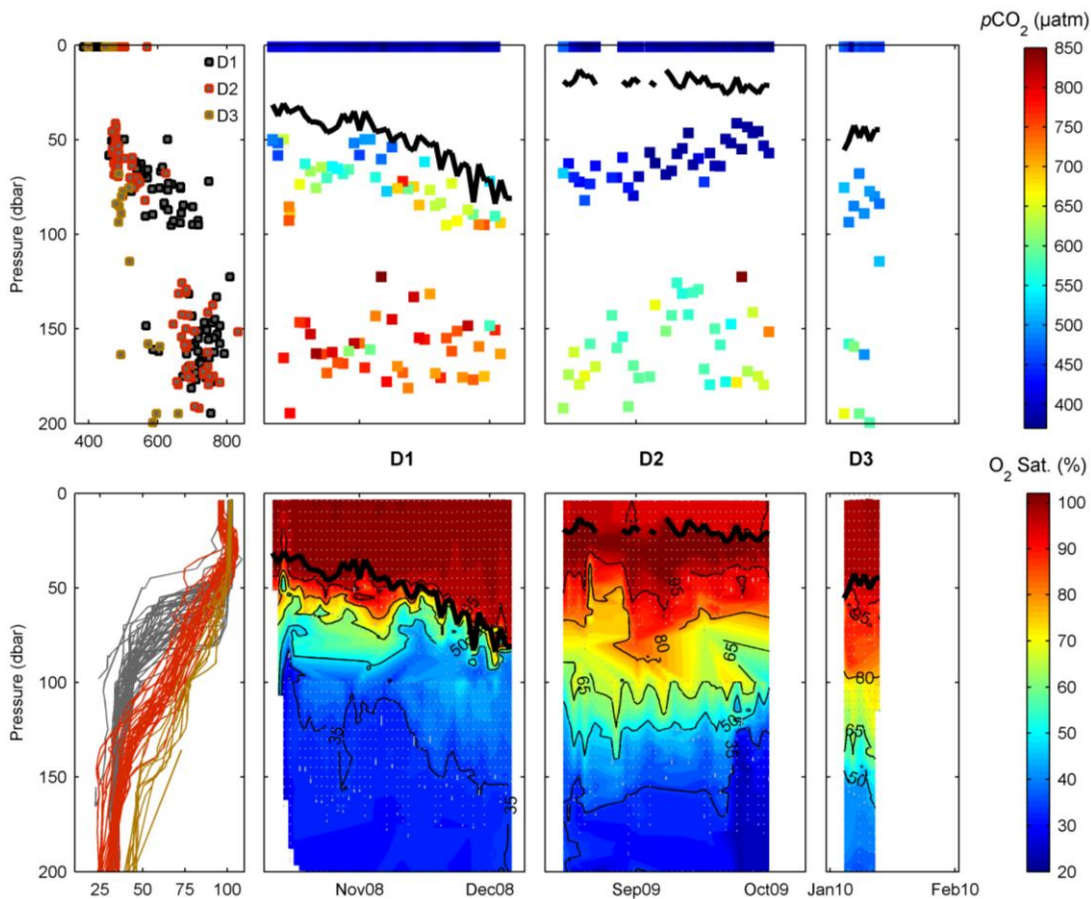


Figure 3.15 Summarized O_2 and pCO_2 data recorded by the 1G-float during D1 – D3 in the vicinity of CVOO. The upper panel illustrates the vertical and temporal distribution of pCO_2 and the lower panel distribution of O_2 saturations levels along the float trajectories (Figure 3.13). The black line indicates the MLD and gray dots are locations where T, S, P and O_2 measurements are available. Note that the x-axis in both panels is interrupted.

Two of the 1G-prototype floats were lost during missions D2 and D3 for unknown reason. During D2 the 1G-float was performing quite well and no indications of technical problems were recognized. Shortly before the scheduled recovery the float disappeared however. The other 1G-float prototype (used during D1 and D3) disappeared 8 profiles after the beginning of D3. Again, detailed analysis of all housekeeping parameters (broadcasted during mission) yielded no clear signs of malfunctions. Due to large modifications on the float's operating software and simultaneous implementation of new features, in particular for D3, programming errors cannot fully be ruled out. Another potential explanation for the loss of the instrument could be a constructional one: During an underway mission with another PSI CO_2 -Pro a small leakage of the membrane interface was observed. Under high hydrostatic pressure conditions such a leakage would lead to a flooding of the entire sensor housing with ambient seawater and thus decrease the float's overall buoyancy tremendously. This would eventually cause the float to sink.

3.2.2 2G Float [Manuscript B]

This chapter is based on a manuscript that was published in the *Journal of Atmospheric and Ocean Technology*. Please refer to the manuscript list given at the outset of this thesis for more detail.

Citation: **Fiedler, B.**, P. Fietzek, N. Vieira, P. Silva, H. C. Bittig, and A. Körtzinger, 2013: In situ CO₂ and O₂ measurements on a profiling float, *J. Atmos. Oceanic Technol.*, **30**, 112-126.

In Situ CO₂ and O₂ Measurements on a Profiling Float

BJÖRN FIEDLER

GEOMAR Helmholtz Centre for Ocean Research Kiel, Kiel, Germany

PEER FIETZEK

GEOMAR Helmholtz Centre for Ocean Research Kiel, and CONTROS Systems & Solutions, Kiel, Germany

NUNO VIEIRA AND PÉRICLES SILVA

Instituto Nacional de Desenvolvimento das Pescas, Mindelo, Cape Verde

HENRY C. BITTIG AND ARNE KÖRTZINGER

GEOMAR Helmholtz Centre for Ocean Research Kiel, Kiel, Germany

(Manuscript received 23 February 2012, in final form 12 July 2012)

ABSTRACT

In recent years, profiling floats, which form the basis of the successful international Argo observatory, are also being considered as platforms for marine biogeochemical research. This study showcases the utility of floats as a novel tool for combined gas measurements of CO₂ partial pressure ($p\text{CO}_2$) and O₂. These float prototypes were equipped with a small-sized and submersible $p\text{CO}_2$ sensor and an optode O₂ sensor for high-resolution measurements in the surface ocean layer. Four consecutive deployments were carried out during November 2010 and June 2011 near the Cape Verde Ocean Observatory (CVOO) in the eastern tropical North Atlantic. The profiling float performed upcasts every 31 h while measuring $p\text{CO}_2$, O₂, salinity, temperature, and hydrostatic pressure in the upper 200 m of the water column. To maintain accuracy, regular $p\text{CO}_2$ sensor zeroings at depth and surface, as well as optode measurements in air, were performed for each profile. Through the application of data processing procedures (e.g., time-lag correction), accuracies of floatborne $p\text{CO}_2$ measurements were greatly improved (10–15 μatm for the water column and 5 μatm for surface measurements). O₂ measurements yielded an accuracy of 2 $\mu\text{mol kg}^{-1}$. First results of this pilot study show the possibility of using profiling floats as a platform for detailed and unattended observations of the marine carbon and oxygen cycle dynamics.

1. Introduction

Accurate knowledge of the interaction of atmosphere and ocean through air–sea gas exchange plays a key role in understanding the past and present states of the global carbon cycle and predicting its future (Takahashi et al. 2009). The ocean’s source–sink function for CO₂ can be investigated by measuring the differences of the CO₂ partial pressure ($\Delta p\text{CO}_2$) between surface ocean and atmosphere, which is the thermodynamic driving force of the net air–sea exchange (Boutin and Merlivat 2009;

Dore et al. 2003; Körtzinger et al. 2008). For many years now, modern observational networks, such as time series and voluntary observing ships (VOSs), have contributed high-quality data to the global assessment of $\Delta p\text{CO}_2$ (e.g., Takahashi et al. 2009; Watson et al. 2009). The most comprehensive dataset has recently been published in the Surface Ocean CO₂ Atlas (SOCAT), which contains nearly 7 million shipborne underway measurements of CO₂ in the surface ocean (Pfeil et al. 2012). Despite the growing database, the present global uptake rate of the World Ocean for anthropogenic CO₂ still has an uncertainty of 50% ($+2.0 \pm 1.0 \text{ Pg C yr}^{-1}$; Takahashi et al. 2009), which to a major extent is due to limited temporal and spatial coverage of large parts of the oceans, for example, the Southern Ocean.

Corresponding author address: Björn Fiedler, GEOMAR Helmholtz Centre for Ocean Research Kiel, Düsternbrooker Weg 20, 24105 Kiel, Germany.
E-mail: bfiedler@geomar.de

Dissolved CO_2 in the ocean is not only influenced by physical processes (e.g., warming/cooling, mixing) but also by biological processes (e.g., photosynthesis, bacterial oxidation of organic matter) and thus strongly linked to dissolved O_2 . The exchange of both gases at the ocean–atmosphere interface is rather decoupled from each other due to complex processes in the ocean, such as the chemistry of the carbonate system (Keeling et al. 2010) and their markedly different equilibration time scales. Knowledge of combined air–sea fluxes of O_2 and CO_2 can help to better understand and constrain atmospheric and oceanic tracers such as atmospheric potential oxygen (Stephens et al. 1998) and ocean potential oxygen (OPO) or C^* (Keeling et al. 2010; Gruber et al. 1996). Besides the above-named gas exchange processes at the air–sea interface, dynamics at the boundary of the mixed layer and the subsurface layer (e.g., entrainment of respiratory signals from subsurface waters into the mixed layer) play an important role in the understanding of carbon cycling (Gruber et al. 2010b). To investigate these processes, combined measurements of CO_2 and O_2 throughout the entire upper-water column (including the thermocline) are needed. Existing autonomous methods focus either on the ocean surface layer (VOS, buoys) or are performed at fixed locations and water column depths (moorings) and therefore are not capable of operating at high vertical resolution and in remote areas. While mixed layer and subsurface dynamics cannot be observed by these approaches at the desired resolution in space and time, profiling floats and gliders as new observation platforms have started to fill this gap.

The most sophisticated and ambitious project of the international research community to enhance spatio-temporal resolution of observations is the Argo network, consisting of >3000 autonomous profiling floats distributed over the oceans (Roemmich et al. 2009). Nowadays, this physical oceanographic observatory is used more and more by biogeochemists since novel sensors for the measurement of biological and chemical parameters have started to meet the requirements of deployment on profiling floats (e.g., low power consumption, small size, high accuracy, and long-term stability). Early pilot studies for O_2 measurements from this platform (Körtzinger et al. 2004; Riser and Johnson 2008) have demonstrated the utility of floats for biogeochemical studies and thus pushed forward the effort to augment the Argo float observatory with oxygen measurements (Gruber et al. 2010a). Other pilot studies have further demonstrated a broad range of measurements on floats, such as gas tension, turbidity, fluorescence, and nitrate (Johnson et al. 2010; Boss et al. 2008; D'Asaro and McNeil 2007; Bishop et al. 2004).

In contrast to these developments, accurate and precise measurements of $p\text{CO}_2$ have for a long time been restricted to relatively large experimental setups (Körtzinger et al. 1996; Pierrot et al. 2009). The first operational sensor for autonomous in situ $p\text{CO}_2$ measurements (DeGrandpre et al. 1995; Moore et al. 2011) has been used primarily in long-term observations on buoys and moorings at various fixed depths. Because of its semicontinuous measurement principle and rather long equilibration time scale, however, this instrument is not suitable for profiling applications on conductivity–temperature–depth (CTD) rosette water samplers, floats, and on other profiling platforms.

The demand for a new generation of $p\text{CO}_2$ sensors that can extend the present high-quality observations in time and space has fostered many recent developments within the scientific community (Byrne et al. 2010). One of the first small-sized in situ sensors is the HydroC sensor (CONTROS GmbH, Kiel, Germany), which can be deployed at pressures up to 6000 dbar. Power consumption and response time of the instrument as well as size and design of its housing enable this sensor to be deployed on autonomous platforms with limited space and energy availability, such as moorings, floating buoys, or profiling floats (Fietzek et al. 2011).

Here, we present results from an extensive field evaluation of a newly developed profiling float that for the first time was equipped with both an O_2 and $p\text{CO}_2$ sensor. First, we introduce instrumentation design, operational modes, and data processing. Then, we present sensor performance and assess the consistency and reliability of the obtained $p\text{CO}_2$ data. Finally, we examine the possibility of drift control and in situ calibration of the optode data by atmospheric measurements.

2. Methods

a. Float platform

A Navigating European Marine Observer profiling float (NEMO; Optimare GmbH, Bremerhaven, Germany) was used as a sensor carrier for this investigation (Fig. 1). This float's main design is based on the Sounding Oceanographic Lagrangian Observer float (SOLO; Davis et al. 2001). As typical for the Argo network, the NEMO float is equipped with a CTD unit (SBE 41, Sea-Bird Electronics Inc., Bellevue, Washington), Argos telemetry, and an oil and air bladder for buoyancy control. The latter is inflated when the float approaches the surface, thereby further significantly increasing the float's buoyancy and pushing the top cap, including sensors and telemetry, above the water level.

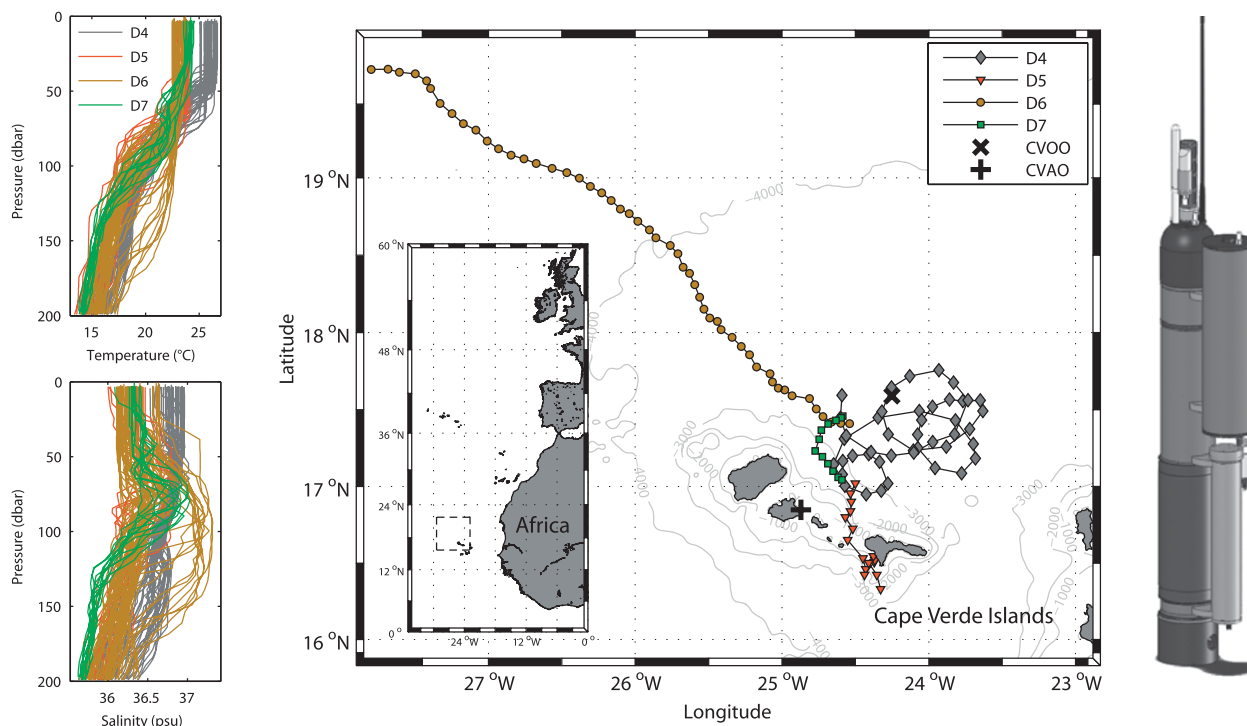


FIG. 1. (left) Depth profiles recorded by the profiling float for (top) temperature and (bottom) salinity during all four deployments. Water masses in the study area were affected by submerged waters originating in the North Atlantic subtropical gyre, as indicated by pronounced subsurface maxima of salinity (Stramma and Schott 1999). (middle) Map shows float trajectories for deployments D4–D7 carried out between November 2010 and June 2011 near the Cape Verde Islands off the coast of Mauritania. Black symbols indicate the location of the CVOO (×) as well as the CVAO (+). Gray contour lines show the ocean bathymetry obtained from the General Bathymetric Chart of the Oceans (GEBCO) dataset. The inset shows the location of the islands with regard to the African mainland. (right) Drawing shows Argo-type profiling float (Optimare GmbH) equipped with a HydroC $p\text{CO}_2$ sensor (including SBE 5M pump), an extra battery container above, an optode sensor, and Iridium and Argos telemetry.

The float underwent several modifications for enabling it to carry further sensor payload and functionality. Argos and Iridium (including GPS) telemetry for bi-directional communication between operator and instrument as well as underway software adaptations ensured full remote control during operations in the field. An O_2 sensor (model 4330 optode, Aanderaa Data Instruments AS, Bergen, Norway) was mounted next to the CTD. The optode sensor was chosen because of its small dimension, low energy consumption, and long-term stability. It has been used successfully in former studies on autonomous platforms (Körtzinger et al. 2005; Tengberg et al. 2006; Johnson et al. 2010).

Additionally, a HydroC $p\text{CO}_2$ sensor (CONTROS) fitted with a pump (SBE 5M, Sea-Bird Electronics) and a depth rating of 2000 dbar was attached to the side of the float with a vertical distance of 1 m to the sensor package described above. This sensor features a planar membrane interface fitted with a flow-through head that is continuously flushed with ambient seawater during measurement. CO_2 along with other dissolved gases as well as water vapor permeates the membrane and

equilibrates with the inner pumped gas circuit, where it is quantified by a temperature-stabilized, single-beam, dual-wavelength nondispersive infrared (NDIR) detector. For zeroing [zero-point measurement (ZP)] of the NDIR detector, a CO_2 -free gas stream can be produced by passing the air through an internal soda lime cartridge that scrubs the CO_2 . The ZPs represent a measure of the actual sensor's performance and are used to account for a zero drift, which is a common and the dominant cause for response change in NDIR instruments (Eckles et al. 1993; McDermitt et al. 1993; P. Fietzek et al. 2013, unpublished manuscript). All ZPs obtained over the course of deployments are considered during post-processing, and the sensor's ZP at any point in time is derived through linear interpolation of the initial ZPs. Furthermore, the signal recovery to ambient $p\text{CO}_2$ levels after a ZP interval is used to derive the actual response time of the sensor, as discussed later in more detail.

To provide energy to the HydroC and the water pump as well as to maintain sufficient buoyancy for the whole float, a battery container was mounted on the side of the float above the HydroC (see Fig. 1). A total of 16

primary lithium battery cells with an overall nominal capacity of 749 Wh were placed in the container, yielding sufficient energy for 39–44 $p\text{CO}_2$ profiles, depending on environmental conditions and configuration. Design and payload of this container result in positive buoyancy and thereby stabilize the vertical orientation of the float. Battery capacity for the remaining components (telemetry, buoyancy control, CTD, and optode) was designed for 150 profiles (1152 Wh in total) and placed in the main pressure housing of the float according to a configuration used for standard Argo floats.

b. CO_2 and O_2 sensor calibration

Prior to the first deployment, the HydroC and optode sensors were thoroughly calibrated in the laboratory. For this purpose, the HydroC sensor was submerged into a thermally insulated and closed water bath, wherein ambient $p\text{CO}_2$ values were varied at different temperatures between 200 and 800 μatm by changing the carbonate system in the bath (P. Fietzek et al. 2012, unpublished manuscript). A high-precision, classical, equilibrator-based $p\text{CO}_2$ system (Körtzinger et al. 1996), equipped with a CO_2 sensor (model 6262, LI-COR Inc., Lincoln, Nebraska) calibrated regularly against National Oceanic and Atmospheric Administration (NOAA)-certified standard gases, served as a reference system for the tank's $p\text{CO}_2$, thus providing an accuracy of 2–3 μatm , which is typical for these instrumental setups (Pierrot et al. 2009).

The optode sensor was calibrated with a recently developed high-accuracy electrochemical calibration setup for O_2 sensors (Bittig et al. 2012). Calibrations were done at stable and well-defined electrochemically generated dissolved O_2 concentrations in a flow system where the sensor was submerged into a thermally insulated water bath and the sensor head was attached to a miniaturized flow-through cell. Calibration was performed covering a temperature range from 8° to 25°C. Overall, seven calibration points between 129 and 317 $\mu\text{mol kg}^{-1} \text{O}_2$ were recorded and triplicate Winkler samples used as reference. Additionally, three zero oxygen measurements using sodium sulfite were performed within the calibration's temperature range. The optode's batch foil coefficients were refitted after Uchida et al. (2008), and all 10 laboratory calibration points were used for the raw phase calibration. Instead of the standard linear correction [Eq. (1)], Eq. (2) was used, resulting in an overall sensor accuracy of 1.2 $\mu\text{mol kg}^{-1}$ (rmse) from the laboratory calibration, defined as

$$\text{CalPhase} = A + B \times \text{TCPhase}, \quad (1)$$

$$\text{CalPhase} = A + B \times \text{TCPhase} + C \times T_{\text{opt}}, \quad (2)$$

where A , B , and C are fitting parameters, TCPhase is the raw sensor signal, T_{opt} is the sensor's temperature probe, and CalPhase is the laboratory-calibrated sensor signal.

c. Float operations

Unlike the common method of using an Argo float as a disposable device, we pursued an approach that included instrument recovery at the end of each mission. For the purpose of this study, we thereby achieved the following advantages: (i) the regular exchange of batteries enables the float to carry a sensor payload with enhanced power consumption and record data at a higher sampling rate; (ii) internally stored high-resolution data can be downloaded after each mission and are valuable for accurate postprocessing (e.g., profile hysteresis correction); (iii) identified suboptimal performance and (peripheral) malfunctions occurring during one deployment can potentially be fixed immediately, either via remote control access or rapid recovery; (iv) the instrument can be kept in the area of prime interest by timely recovery and subsequent redeployment; and (v) most importantly, sensor drift, and thus accuracy, can be monitored and corrected for properly with pre- and postdeployment calibrations.

The float with the sensor package described above was deployed 4 times between November 2010 and June 2011. During all of these deployments, this setup performed successfully and allowed for a detailed analysis of both the platform's and the sensor's performance (Table 1). All deployments were conducted in the vicinity of the Cape Verde Ocean Observatory (CVOO; 17.589°N, 24.252°W; <http://cvo0.geomar.de>) in the eastern tropical North Atlantic (ETNA) in close proximity to the Cape Verde Atmospheric Observatory (CVAO; 16.864°N, 24.867°W), which is located downwind of the study area (Fig. 1). Vertical profiles of salinity, temperature, hydrostatic pressure, $p\text{CO}_2$, and O_2 for the upper 200 m of the water column were measured every 31 h during upcasts with a mean ascent speed of 0.06 m s^{-1} and a vertical resolution of 5 dbar [low-resolution (LR) data]. Further, $p\text{CO}_2$ data were recorded in 5-s intervals during upcasts that correspond to a vertical resolution of ~ 0.3 dbar [high-resolution (HR) data]. At the parking depth of ~ 250 dbar and immediately before each profile, the float initializes a warm-up phase for the HydroC followed by a ZP. Directly after profiling to the surface, a second ZP is carried out. During the time of the second ZP, O_2 measurements are conducted, first in water and then in air. Measurements in air for in situ postcorrection of O_2 data (section 3c) were done after the float had inflated an air bladder and thus pushed the optode sensor, CTD, and telemetry–GPS antenna above water level. Once measurements were finished, LR data

TABLE 1. Field campaigns conducted and data obtained during 2010 and 2011 that form the basis of this study. Former deployments (D1–D3) were disregarded, since these were performed with a different float setup, that is, a different $p\text{CO}_2$ sensor that showed comparatively poor performance and did not allow for the measurement of continuous $p\text{CO}_2$ profiles. Duration of and gaps between consecutive deployments varied because of limited ship resources on site. The asterisk (*) indicates that the instrument got lost during deployment for unknown reason and thus no HR data are available for D7.

ID	Deployment time	No. of profiles	Duration (days)	No. of individual measurements		
				T, S, P	O_2	$p\text{CO}_2$
D4	Nov 2010–Jan 2011	44	56	2200	2200	31 223
D5	Jan–Feb 2011	16	21	800	800	17 489
D6	Mar–May 2011	51	65	2550	2550	42 253
D7	May–Jun 2011	12	14	600	600	600*
Total		123	156	6150	6150	91 565

and GPS location were telemetered to shore via the Iridium network. The dwell time at the surface was less than 1.5 h. Float missions are typically designed for durations of 2 months, but they can be extended depending on sampling frequency and sensor–battery payload.

d. Data processing

Calibrations described in section 2b were applied on recorded raw $p\text{CO}_2$ and O_2 sensor data. Sensor drift was taken into account for each profile by using the information from pre- and postprofile ZPs for the HydroC and atmospheric O_2 measurements for the optode, respectively. Oxygen concentration was derived from raw phase measurement (TCPhase), CTD temperature (T_{CTD}), and atmospheric pressure (recorded at nearby CVAO) using the laboratory calibration. For computation of O_2 measurements in air, values of the optode's temperature probe (T_{opt}) were used since these showed a lower noise level in air than T_{CTD} . In absence of steep temperature gradients, both temperature probes, T_{opt} and T_{CTD} , have shown no detectable deviation of each other ($<0.01^\circ\text{C}$). Subsequently, all LR data were merged in the time domain onto the HydroC HR grid by linearly interpolating O_2 , salinity (S), T_{CTD} , and pressure (P).

The response time of membrane-based sensors is a major constraint for profiling platforms (Edwards et al. 2010; Miloshevich et al. 2004). Although the float platform of this study is a rather slow profiling device, the HydroC response time is causing an appreciable hysteresis in obtained vertical $p\text{CO}_2$ profiles. Laboratory- and field-based experiments with the HydroC sensor have shown pronounced changes in sensor response time that linearly depends on water temperature (P. Fietzek et al. 2013, unpublished manuscript). Pressure vessel tests under different isothermal conditions have shown no significant effects of hydrostatic pressure up to 2000 dbar on sensor response time (data not shown here). Sensor response time in pumped mode further depends on the water flow rate provided here by an

SBE 5M pump. The actual in situ response time of the HydroC was determined by making use of the signal recovery after a ZP directly before (at depth) and after (at surface) each profile. Since the major volume of the inner gas stream is flushed with zero gas during ZP, the sensor needs a distinct time to fully reequilibrate to ambient $p\text{CO}_2$ afterward. Following the initial change after a ZP, which is mostly due to the mixing of the internal gas volumes (zero gas and equilibrated gas behind the membrane), the $p\text{CO}_2$ increase within the inner volume is determined only by the permeation of CO_2 from the water through the membrane layer. The time required for the mixing process is much shorter than the time constant of the permeation process that essentially follows first-order kinetics. Therefore, sensor response time can be assessed by applying an exponential fit to the signal increase following the short mixing interval after a ZP using Eq. (3), given as

$$\text{signal}(t) = (a - b)e^{-\Delta t/\tau} + b, \quad (3)$$

where a is the sensor signal for the well-mixed internal gas volume during ZP, b is the sensor signal after the measurement has reequilibrated with ambient $p\text{CO}_2$ levels, τ is the reciprocal e -folding response time, and Δt is the relative time domain between a and b . Next, a , b , and τ are derived as fitting parameters by an exponential fit (nonlinear least squares). This approach provides a sensor response time for every single measurement during an upcast, based on the two in situ determinations of the response time in combination with its determined linear dependence on water temperature. Further, this approach also accounts for other effects on sensor response time, such as potential biofouling, changes in water flow to the membrane, or other physical effects (e.g., pressure conditioning) on the membrane's structure that may develop during the course of a deployment.

A time-lag correction algorithm (Miloshevich et al. 2004) has been applied on carefully smoothed vertical

HR profiles of $p\text{CO}_2$ that takes varying response times of the HydroC with ambient conditions into account. By knowing sensor behavior and the exact time stamp for each measurement, one can apply the following model sequentially to time-lagged data:

$$U_C(t_1) = \frac{U_M(t_1) - [U_M(t_0)e^{-\Delta t/\tau}]}{1 - e^{-\Delta t/\tau}}, \quad (4)$$

where $U_M(t_0)$ is the measured value at the first time stamp; $U_M(t_1)$ is the measured value at the following time stamp; Δt is the time between t_0 and t_1 ; and $U_C(t_1)$ is the time-lag-corrected (TLC) measurement at t_1 , referred to as TLC data. To meet the requirements for the application of such a correction algorithm, one has to provide a sufficiently small sampling rate Δt relative to the response time and expected gradients (Miloshevich et al. 2004). HR data for $p\text{CO}_2$ fulfill these conditions and thus allow a careful application of this algorithm in order to examine the performance of $p\text{CO}_2$ measurements properly.

Response time of the optode sensor is about an order of magnitude faster than the HydroC as deployed here and laboratory experiments also show a distinct dependence of the response time on water temperature in a stationary setup (H. C. Bittig et al. 2013, unpublished manuscript). However, since an in situ determination of optode response times was not feasible and the originally recorded optode data (LR data) provide only an insufficiently short sampling interval, no TLC data could be derived from these measurements (refer to section 3c for further details).

e. Reference data

For validation of sensor accuracy and data processing described in section 2d, independent observations such as shipborne field tests in case of the HydroC sensor, hydrocast data in close proximity to float operations, and a global climatology have been used.

First, a similar HydroC sensor setup was tested during a hydrographic survey in the equatorial Atlantic in order to validate the applied correction algorithm on sensor output. The device was mounted on a CTD rosette equipped with an O_2 sensor (SBE43, Sea-Bird Electronics Inc.) and multiple upcasts and downcasts were performed. During the final upcast, discrete water samples for dissolved inorganic carbon (DIC) and total alkalinity (TA) were collected. Analysis of these samples was carried out immediately after sampling by using automated high-precision analyzing systems [single-operator multimetabolic analyzer (SOMMA) for DIC, Johnson et al. (1987); versatile instrument for the determination of titration alkalinity (VINDTA) for TA, Mintrop et al. (2000)]. Accuracy and precision of these

discrete measurements were assured by regular analysis of certified reference material (CRM; A. Dickson, Scripps Institution of Oceanography, La Jolla, California; Dickson 2010) and duplicate samples, respectively. DIC ($\pm 0.9 \mu\text{mol kg}^{-1}$) and TA ($\pm 1.9 \mu\text{mol kg}^{-1}$) measurements were converted into $p\text{CO}_2$ for comparison purposes, using the carbonic acid dissociation constants of Mehrbach et al. (1973) refit by Dickson and Millero (1987). Because of uncertainties in the used set of constants and in the DIC and TA measurements, the uncertainty of derived $p\text{CO}_2$ reference values is estimated to be $\pm 10 \mu\text{atm}$ (Millero 2007). Additionally, a fully automated $p\text{CO}_2$ measurement system [General Oceanics (GO), Miami, Florida] based on a spray head equilibrator and a CO_2 analyzer (model 6262, LI-COR Inc.) was operated in parallel during CTD tests. Data reduction procedures were applied after Pierrot et al. (2009).

Second, for comparison purposes, DIC, TA, and O_2 (Winkler method) data from ship expeditions in the vicinity of the study area were used. Furthermore, reference samples were taken immediately prior to the fourth and seventh deployment of the float (D4 and D7, respectively) in a distance of less than 100 m to the point of deployment. DIC and TA samples (500 mL) were preserved by poisoning with 100 μL of saturated mercury chloride solution, and onshore analysis was conducted following the procedures described above.

Third, float $p\text{CO}_2$ data obtained at the surface were compared with a global climatology (Takahashi et al. 2009) for a qualitative assessment of data reliability for the respective region and time of year. Climatology data were extrapolated to the time of float operations while taking into account an annual mean $p\text{CO}_2$ increase of $1.8 \mu\text{atm}$ in the mixed layer in this particular region.

3. Results and discussion

a. CO_2 sensor performance

The HydroC CO_2 sensor is a newly developed device that has recently become available for diverse marine research applications (Fietzek et al. 2011). Hence, this work provides some of the first field data acquired with this sensor, being deployed on a demanding platform. Other field surveys with this sensor (e.g., shipborne underway measurements) demonstrate an overall accuracy of about $5 \mu\text{atm}$ (P. Fietzek et al. 2013, unpublished manuscript). In case of measurements at nonequilibrium conditions caused by, for example, fast and large changes in water temperature or dissolved gas composition, as commonly present during profiling applications, accuracy might differ and has to be specified for each platform explicitly.

The use of a membrane-based NDIR sensor on autonomous profiling devices is a rather challenging task in terms of measurement stability and reliability under the tight constraints of limited energy resources and steep temperature gradients that are encountered during vertical profiling. Zero values show only a small and comprehensible drift over the course of each deployment, with a maximum drift rate of $0.15 \mu\text{atm day}^{-1}$, indicating that the sensor behaves in a stable and rather predictable way (Fig. 2). Even between consecutive deployments (including several weeks of storage without operation), no major change in the drift behavior was found. Also, for individual upcasts, the NDIR sensor signal was not subject to any significant drift. The latter finding is quite remarkable since during upcasts, the sensor experiences major changes in temperature and pressure over a very short time interval (~ 1.5 h), including a cold start and warm-up phase prior to each profile. This consistency of ZPs at surface and depth illustrates a high degree of sensor robustness and reliability under the encountered conditions. Temporal stability of the sensor response slope (span drift) could not be quantified in this study because of the lack of a postdeployment calibration. However, a comparison with reference samples shows no indication for a pronounced drift in the sensor response slope (section 3b).

The float enters the euphotic zone several times during a deployment. However, it spends about 80% of its full cycle time beneath it until the next profile starts. Although such an observational approach is not prone to major biofouling, adverse effects of this cannot be fully ruled out. For instance, a growing film of organic matter on the membrane interface would first and foremost decrease the membrane's permeability and thus slow down the sensor's response time. In addition, $p\text{CO}_2$ data could be biased because of biological production/respiration processes in this film. To account for the former process, in situ sensor response time was derived after every ZP. Figure 2 presents the observed in situ response times after each profile at the surface (black symbols, k_s) and prior to each upcast at depth (gray symbols, k_d). At the beginning of D4, this CO_2 sensor was deployed in the field the first time and thus experienced its first cycles of rapid temperature and hydrostatic pressure changes. The observed decreasing trends during D4 in both k_d and k_s seem to be indicative of a membrane conditioning phase, which has been observed for membrane-based instrumentation during former studies (Marin et al. 1992; Baudot et al. 1999; McNeil et al. 2006). The elevated scattering of k_d (rmse: 21.7 s) compared to k_s (rmse: 2.6 s) during D4 is due to a variable float depth during ZPs. These biased values have been flagged, and interpolated data points were

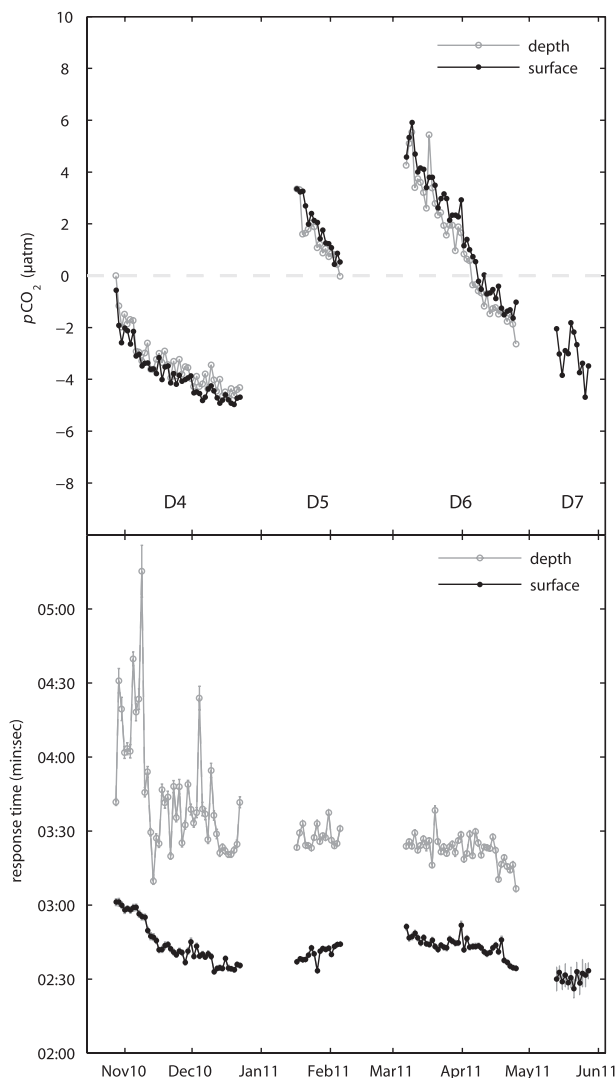


FIG. 2. (top) CO_2 sensor performance in terms of signal stability derived from regular ZPs referred to the first ZP signal (being set to $0 \mu\text{atm}$). The ZPs were carried out for a postcompensation of sensor drift that had occurred during the course of deployments. (bottom) In situ response times determined from ZPs. Note: Operation of the CO_2 sensor at the beginning of every profile was slightly changed after D4; therefore, systematic differences between surface and depth ZPs have slightly changed between D4 and the remaining deployments. Further, data at depth for D7 are missing because of the loss of the float.

used instead for later data processing. At the end of D4, values of k_d and k_s approach 230 and 161 s, respectively, which is the same for the following deployments until the end of D7.

In contrast to the obvious trends of k_d and k_s during the conditioning period, less pronounced trends are found afterward. Since no overall trend of k_d and k_s is observed, the development of a significant organic film impeding CO_2 permeation can be ruled out. The general

difference between k_d and k_s also must be explained in order to understand CO_2 sensor behavior under different environmental conditions. Since the kinetic response time depends first and foremost on the membrane's permeability, a distinct temperature dependence as found for membrane inlets in other studies (McNeil et al. 2006; Prabhakar et al. 2005) was expected. Indeed, values for k_d and k_s from D5 to D7 show a temperature dependence with ambient water temperature that indicates a linear dependence (Fig. 3). This finding is being corroborated by laboratory tests performed at various water temperatures (data not shown here). Data obtained during the D4 conditioning phase initially fall off this dependency but converge toward and eventually coincide with it too.

b. CO_2 data consistency

Determined in situ response times described in section 3a are of a magnitude that causes a pronounced hysteresis in the recorded raw sensor data. Using its observed temperature dependence, the sensor's response time can be explicitly calculated for each particular measurement, such that the time-lag correction algorithm described in section 2d can be applied (Fig. 4, right panel). Raw data are carefully smoothed in the time domain according to Miloshevich et al. (2004) without sacrificing much vertical structure (black solid line). TLC data (red solid line) represent the ambient $p\text{CO}_2$ profile.

For the purpose of this study, shipborne field tests were conducted to demonstrate the feasibility of using this sensor in a profiling approach in general and to validate the applicability of the TLC algorithm used. Figure 4 (left and middle panels) shows the results of a HydroC sensor, identical to the unit deployed on the float, being mounted on a CTD rosette sampler while profiling through the upper 500 m of the water column with ascent and descent rates of 0.5 and 0.3 m s^{-1} , respectively. In contrast to the float's measurement routine (right panel, mean ascent rate of 0.06 m s^{-1}) where only upcast data are available, hydrocast data provide both upcasts and downcasts and therefore allow more detailed analysis of the sensor's hysteresis. Recorded raw data ($\Delta t = 2\text{s}$) have been treated similarly to data obtained by the float, and TLC data were compared for internal consistency between upcasts and downcasts as well as with a set of reference samples collected during the upcasts. Remaining differences between time-lag-corrected upcasts and downcasts are being amplified in case of high ascent and descent rates (up to 60 μatm , left panel) and mainly result from (i) an inadequate modeling of the apparent sensor response time (only very few determinations of k_s and k_d are available) and (ii)

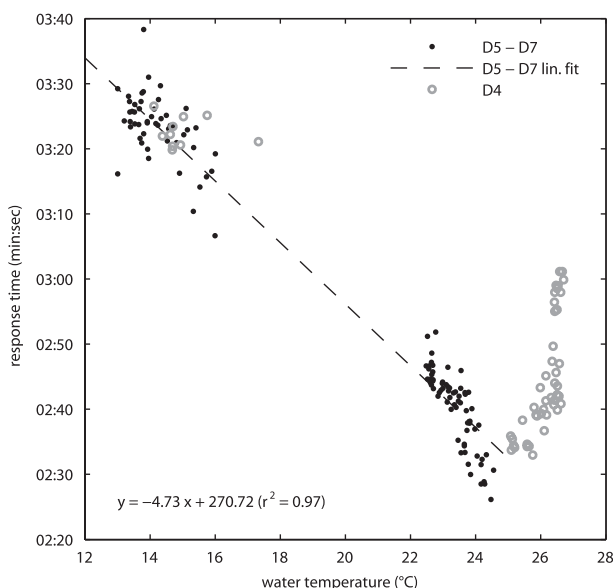


FIG. 3. Observed temperature dependence of sensor response time (k_s and k_d) during all deployments. Gray open circles highlight D4 values, since these deviate significantly from the overall dependence observed during remaining deployments. Inadequate values for k_d (D4) due to variable float depth during ZP were neglected. The equation for the straight line and the correlation coefficient are given in the lower left.

a relative decrease of the measurement interval Δt (section 2d) at higher profiling rates. However, slowing down these rates to 0.3 m s^{-1} (middle panel) already produces corrected data that have no systematic offset between upcast and downcast, although deviations still remain significant (particularly in areas of steep gradients). Averaged offsets ($\pm\text{rmse}$) of TLC data between upcasts and downcasts for both CTD tests were found to be $10 \pm 12.4 \mu\text{atm}$ (0.5 m s^{-1}) and $7.9 \pm 12 \mu\text{atm}$ (0.3 m s^{-1}), respectively, which provides a significant improvement compared to non-TLC data (69.8 ± 75.7 and $78.3 \pm 82.9 \mu\text{atm}$, respectively). The observed overall consistency for upcasts and downcasts after TLC therefore provides a measure of the quality of data processing procedures and further indicates an increasing precision with slowing ascent and descent rates. In case of floatborne $p\text{CO}_2$ profiles with very slow and varying ascent rates and a well-modeled sensor response time, the above observed deviations are assumed to become almost negligible relative to the measurement accuracy.

The assessment of overall $p\text{CO}_2$ data accuracy turned out to be a rather complicated issue. In contrast to underway measurements at the surface, and therefore the given opportunity to apply established high accuracy methods as a reference (e.g., Körtzinger et al. 1996; Pierrot et al. 2009), no direct and in situ reference

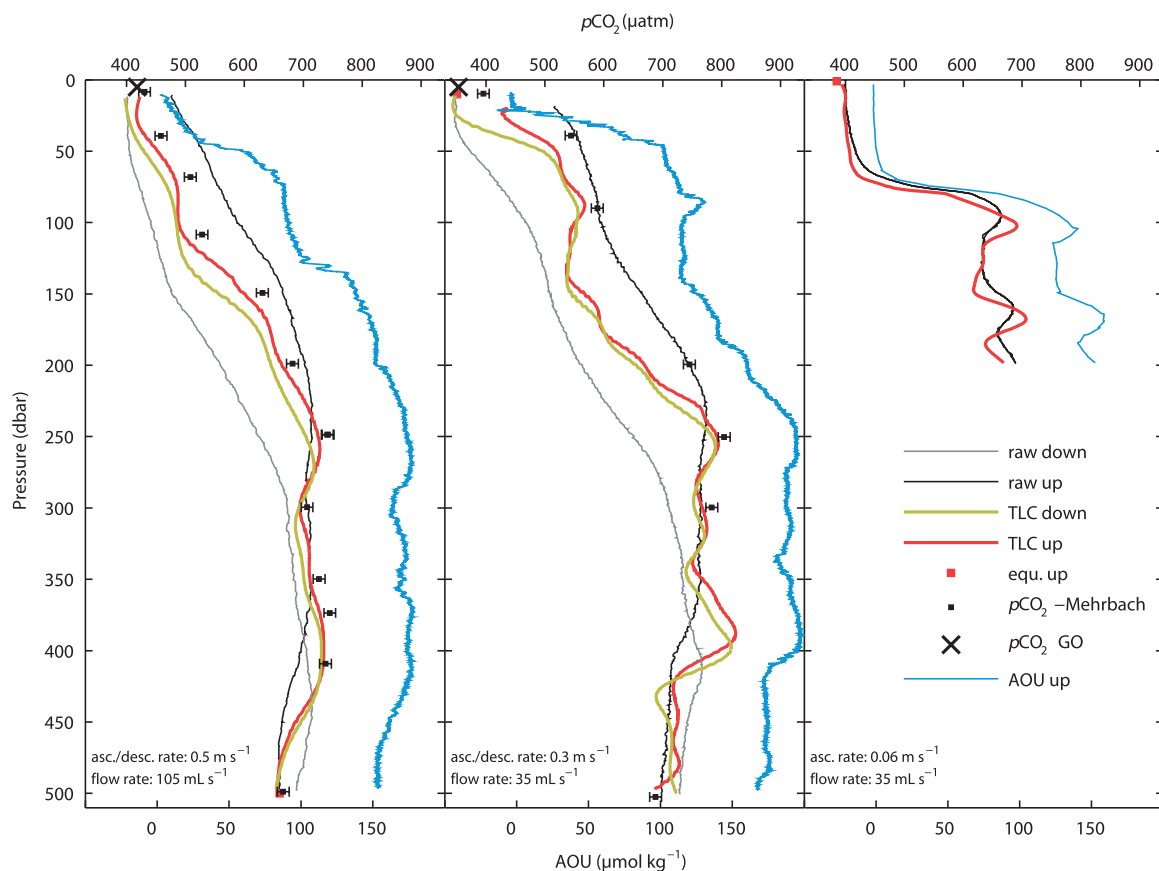


FIG. 4. TLC and original vertical $p\text{CO}_2$ profiles recorded during the hydrographic survey of research vessel (R/V) *Maria S. Merian* (MSM-18/3) with descent rates of (left) 0.5 and (middle) 0.3 m s^{-1} . HydroC was mounted on a CTD rosette sampler, reference samples for $p\text{CO}_2$ (DIC and TA) were taken during the upcast, and surface $p\text{CO}_2$ measurements were performed with a GO underway system ($p\text{CO}_2$, black crosses). Sensor configuration and ascent and descent rates were changed between the casts (see panels). (right) Float upcast recorded during D6 with raw and TLC data. AOU data (blue lines, all panels) represent a qualitative consistency check for the TLC HydroC data. Fully equilibrated (stationary) HydroC sensor signals (red squares, all panels) were achieved after ZPs.

measurements with the required accuracy are available for in situ measurements in the water column. Even $p\text{CO}_2$ values derived from discrete (ex situ) DIC and TA measurements during CTD tests (upcast) still carry an estimated uncertainty of $10 \mu\text{atm}$. Further, deviations between these measurements at the surface and an operated underway system (GO) during CTD tests are even above this threshold (Fig. 4, middle panel), pointing at the inadequate matching of these measurements (in space and/or time) and thus indicating an insufficient reliability for this in situ assessment. Despite these constraints, a good overall agreement of TLC data (upcast) with reference samples was found for both hydrocasts in areas of flat gradients ($-12.1 \pm 5.7 \mu\text{atm}$, $n = 10$). Additionally, fully equilibrated $p\text{CO}_2$ sensor data at the surface directly after an upcast (Fig. 4, middle panel) are in good agreement with the underway system (within $3 \mu\text{atm}$). Because of the above-described limitations, oxygen measurements [converted to apparent oxygen

utilization (AOU)] conducted during CTD tests and float profiles were used to serve as an independent and qualitative proxy of obtained $p\text{CO}_2$ data reliability. In all three cases (Fig. 4), a strong anticorrelation between both gases beneath the mixed layer was found even in the fine vertical structure. These results point at the validity of the applied algorithm as a robust tool for postprocessing of obtained float data.

Postprocessing of time-lagged sensor data removed most of the hysteresis effects; however, other effects on a different time scale still remain in recorded profiles. In particular, TLC data within the mixed layer after an upcast still deviate from final equilibrated values at the end of each upcast (Fig. 4, middle and right panels). This effect could not be fully compensated for by time-lag corrections for $p\text{CO}_2$, and thus it must be caused by other effects on a different time scale. Such effects on measurements could be due to remaining physicochemical influences, such as changes in internal headspace gas

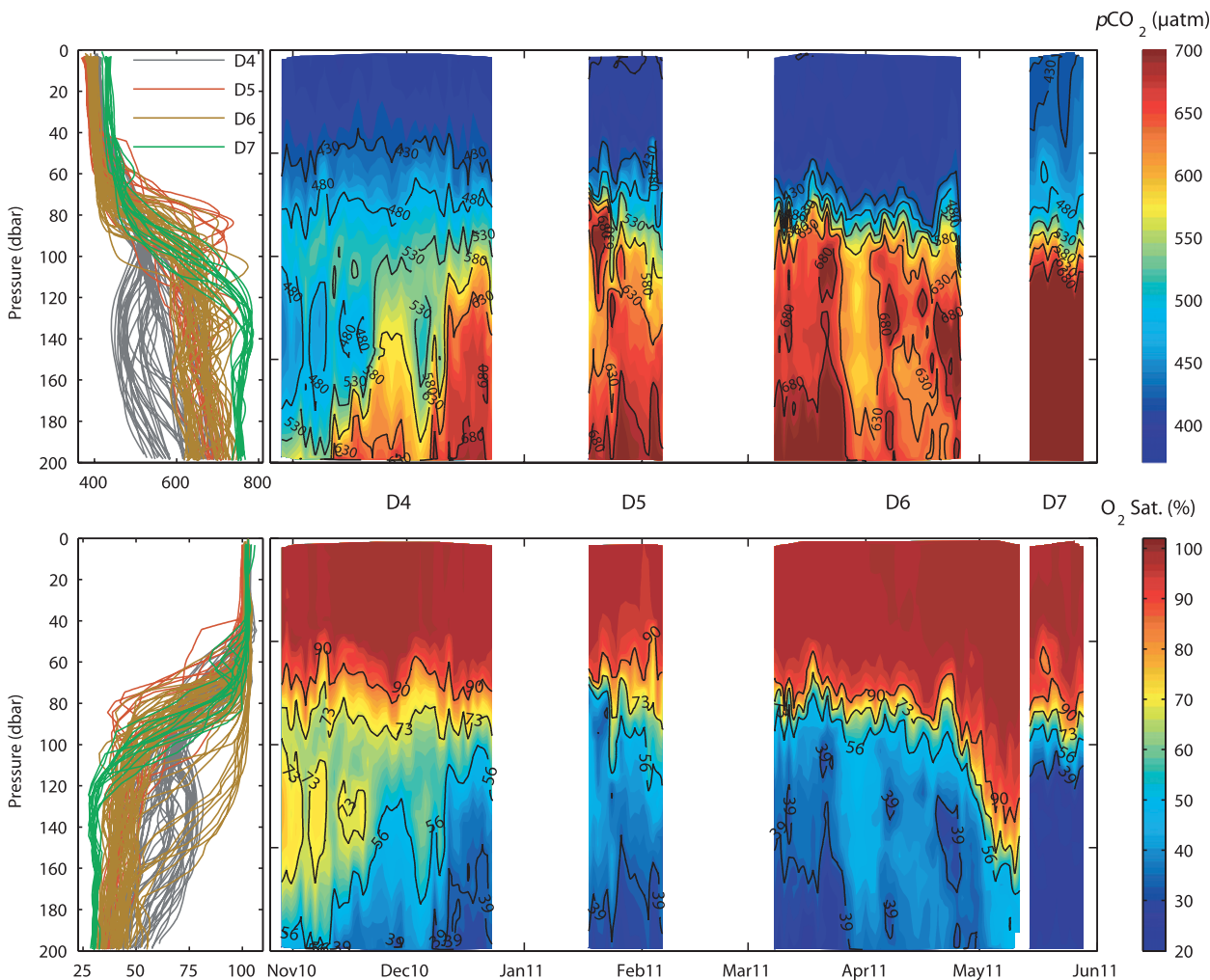


FIG. 5. Final (top) $p\text{CO}_2$ and (bottom) O_2 data collected in the vicinity of CVOO. Time series for both parameters are strongly complementary to each other. Blank areas indicate times when the instrument was refurbished on land-ship for the next deployment. Note: Rapid change in water column properties between D6 and D7 results from the large distance (~ 280 nm) between recovery and redeployment (see Fig. 1).

temperature and pressure during an upcast or a varying gas matrix composition. The latter might be triggered by steep O_2 gradients in the water column that the sensor experiences during the ascent. Oxygen shows a fivefold reduced permeability for polydimethylsiloxane (PDMS)-type membranes compared to CO_2 (Merkel et al. 2000), and this difference in permeabilities between both gases may result in transient pressure disequilibria that also affect the CO_2 mole fraction during the matrix re-equilibration phase. While equilibration of CO_2 occurs faster than the remaining part of the gas matrix, the measured CO_2 mole fraction $x\text{CO}_2$ might be affected by the slow response of O_2 equilibration. This effect could potentially explain observed deviations in the mixed layer (after the float has passed the oxycline) toward an increased $x\text{CO}_2$ in the sample gas. These dynamic processes

at the membrane interface are not fully understood yet, and further experiments in the laboratory and the field are needed to fully understand these transient processes.

All recorded $p\text{CO}_2$ data during D4 and D7 were postprocessed following the validated procedures described in section 2d. Final data (Fig. 5) were found to be tightly anticorrelated for the subsurface and most parts of the surface layers. Some features toward the end of D7, however, show some decoupling in the surface layer. High frequency profiling of the float (every 31 h) allowed to resolve dynamic features in the water column, such as the ventilation of the subsurface layer with low $p\text{CO}_2$ and enhanced O_2 concentrations during D4 or enhanced supersaturation for O_2 and $p\text{CO}_2$ at the end of D7.

To validate TLC $p\text{CO}_2$ data at deployments, $p\text{CO}_2$ reference data (see section 2e) collected either next to

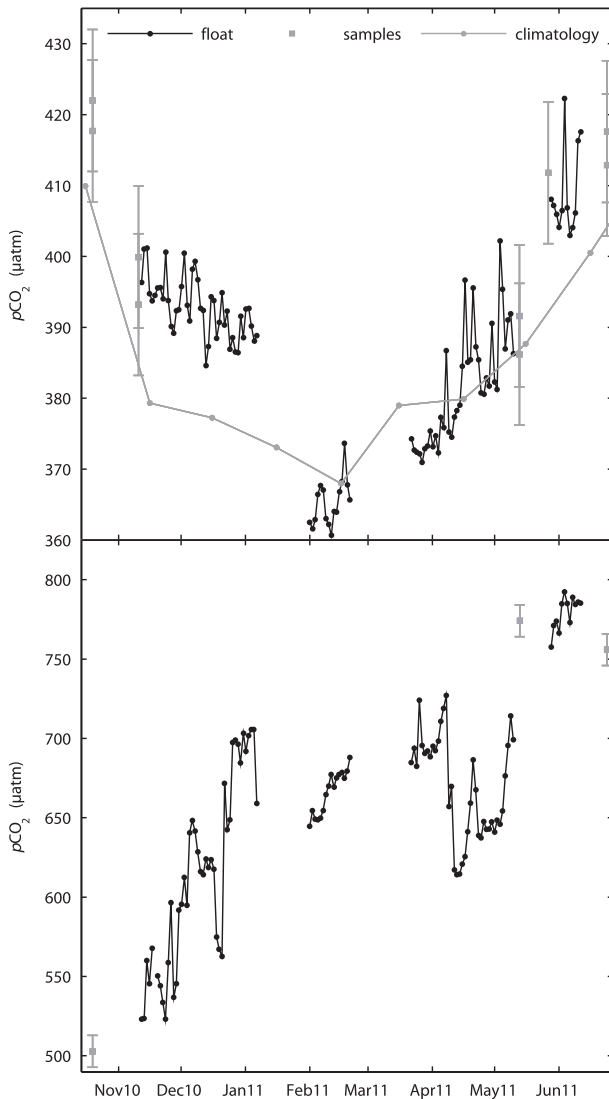


FIG. 6. Floatborne $p\text{CO}_2$ observations at CVOO for the (top) surface ocean (~ 1 dbar, black solid line) and (bottom) 26.55 sigma-theta isopycnal. Discrete reference samples for $p\text{CO}_2$ were derived from DIC and TA measurements taken in the vicinity of the study area. Climatological $p\text{CO}_2$ values were derived from Takahashi et al. (2009).

the float deployment sites or in the vicinity of CVOO have been used for comparison purposes. Figure 6 shows $p\text{CO}_2$ data from all four deployments for the surface layer (~ 1 dbar, top panel) and for a density layer (26.55 isopycnal, bottom panel) along the float trajectories. Because of limited sampling capabilities during consecutive deployments and recoveries, no highly resolved vertical profiles for reference samples could be conducted next to float positions. Therefore, only a small number of surface samples and an even smaller set of samples from depth are available for comparison.

However, despite lateral displacement all reference samples, both at the surface and at depth, show a good agreement with floatborne observations to within the uncertainty of the calculated $p\text{CO}_2$ ($\pm 10 \mu\text{atm}$). Furthermore, climatology data for this particular region and time of year fit well with the seasonal cycle observed by the float. Minor differences could be due to both extrapolation errors of climatology data (from the reference year 2000 to the present) and nonclimatological situations in the field data. Further evidence for robust measurements over the course of all four deployments is given by ZPs illustrated in Fig. 2 (top panel) that followed a very consistent drift pattern. Even though no postdeployment calibration could be realized, the overall agreement with the above named reference points at a consistent signal drift even for the response slope. Therefore, ZPs provide an appropriate basis for post-correction of the signal drift encountered during this study.

In summary, all available reference sources provide the evidence for reliable $p\text{CO}_2$ measurements conducted by a profiling float for the first time. The estimated accuracy ranged from 10 to 15 μatm for the water column and 5 μatm for surface measurements.

c. O_2 data consistency

Laboratory-calibrated optode data were treated according to the methods described in section 2d but could not be considered for TLC processing because of inadequately coarse (given the sensor's rather short response time) temporal resolution of measurements. However, the response times of the used optode sensor (18–23 s) observed during laboratory experiments are an order of magnitude faster than the HydroC ones. Thus, an applied time-lag correction would have only an impact of $< 2 \mu\text{mol kg}^{-1}$ on oxygen float data in areas of steep O_2 gradients, as being encountered during D4–D7. In absence of such dynamic processes, calibrated optode measurements at the surface did show, however, a discrepancy in reference samples (see below). Therefore, the results of the newly developed approach for an in situ offset correction of biased optode data are being discussed in the following.

The demonstrated long-term stability of optode-based O_2 measurements on unattended platforms is a major advantage of this method, although on most autonomous applications, such as Argo floats, the long-term stability of a given sensor cannot be proven easily. As proposed by Körtzinger et al. (2005), the possibility to measure atmospheric O_2 with the optode sensor can be used as a means of drift control. In this study, five O_2 measurements (quintuplicates) were performed at 90-s intervals in the surface ocean and the overlying air

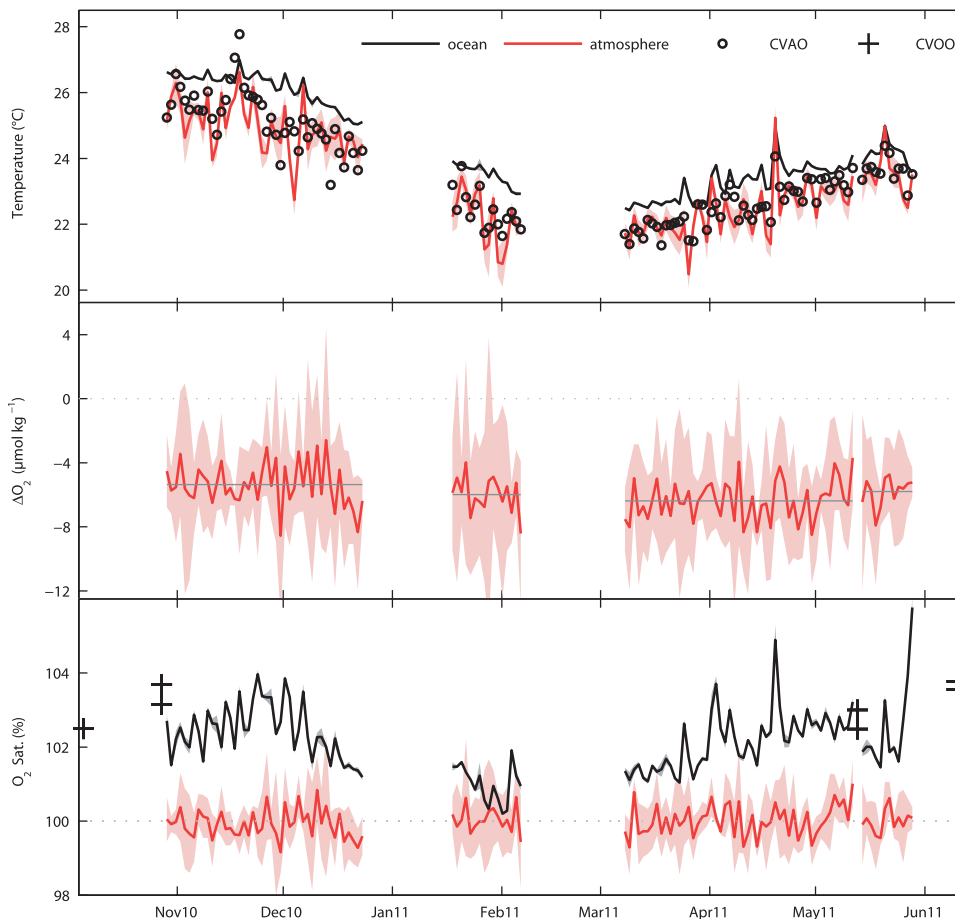


FIG. 7. Temperature and O_2 measurements at the ocean–atmosphere boundary from all four deployments. Shaded areas in all panels give the standard error of the respective property. (top) Temperature readings of the optode sensor in seawater and air as well as air temperature measurements conducted at CVAO. (middle) Differences between measured $O_{2,air}$ and computed $O_{2,air-calc}$ (see text). Gray lines indicate mean offset for each deployment. (bottom) Calibrated and drift-corrected O_2 saturation levels in the atmosphere (red lines) and in the surface ocean (black lines) with the changing degree of supersaturation. Reference Winkler data (+) were in agreement with corrected optode measurements.

(typically 30 cm above and below the air–sea interface). The resulting precision (rmse for quintuplicates) was found to be $3.2 \mu\text{mol kg}^{-1}$ for $O_{2,air}$ and $0.3 \mu\text{mol kg}^{-1}$ for corresponding oxygen measurements in the water ($O_{2,water}$). Weighted means of these measurements are shown in Fig. 7. The elevated noise level of atmospheric O_2 is probably due to rough sea conditions and therefore occasional submersion of the sensor by waves and/or due to a drying sensor foil while measuring in air. However, neither a systematic warming of the sensor in air (due to sunlight) nor a significant cooling (due to evaporation) has been observed (Fig. 7, top panel). The detected mean temperature difference for the optode temperature probe between the surface ocean and atmosphere ($1.02 \pm 0.62^\circ\text{C}$) is therefore assumed to be real, which is corroborated by land-based measurements at CVAO.

Calibration-based O_2 measurements in air ($O_{2,air}$) underestimate calculated O_2 levels in air at the sea surface ($O_{2,air-calc}$ after García and Gordon 1992), using an O_2 mixing ratio of 0.20946, and atmospheric pressure and relative humidity, both measured at CVAO. In case no atmospheric in situ data from nearby monitoring sites are available, one could also make use of National Centers for Environmental Prediction (NCEP) reanalysis data (Kanamitsu et al. 2002). However, reported uncertainties in NCEP data (Padin et al. 2007) could negatively affect the accuracy of computed $O_{2,air-calc}$ and thereby limit this approach. The offset (ΔO_2) between $O_{2,air}$ and $O_{2,air-calc}$ over time was then used to postcorrect $O_{2,water}$, thereby removing an offset of -5.4 to $-6.4 \mu\text{mol kg}^{-1}$ (rmse: $1.2 \mu\text{mol kg}^{-1}$) that slightly varied between consecutive deployments (Fig. 7, middle panel). The change in this offset is very small and not significant. However,

a similar magnitude, sign, and variability of such an offset between deployment and (re) calibration has been observed already during other investigations (Bittig et al. 2012). Taking into account uncertainties of measurements, derived $O_{2,\text{air-calc}}$, and observed stepwise sensor offset, we estimate an overall accuracy of $2 \mu\text{mol kg}^{-1}$ for floatborne O_2 concentrations in absence of dynamical effects (e.g., time lag). Derived O_2 saturation levels for the topmost part of the mixed layer match well with independent O_2 reference samples (see Fig. 7, bottom panel). Thus, atmospheric measurements during the entire float lifetime appear to provide a valuable tool for in situ drift correction.

Observed O_2 disequilibrium at the ocean–atmosphere interface throughout the deployments (Fig. 7, bottom panel) points at a variability of O_2 that follows a seasonal pattern and a pronounced variability on shorter time scales (e.g., days). Slightly supersaturated waters around CVOO are quite common for this region and even enhanced supersaturation (at the end of D7) can be caused by more productive filaments that are being transported offshore from the Mauritanian upwelling (Fischer et al. 2009).

4. Conclusions

With a new generation of $p\text{CO}_2$ sensors that feature small dimensions and power requirements as well as sufficient precision and accuracy, autonomous $p\text{CO}_2$ measurements become feasible for autonomous profiling applications. In this study we demonstrated the capability of such a sensor being mounted on an Argo-type profiling float for reliable $p\text{CO}_2$ measurements in midterm deployments. First results point at good stability of measurements, absence of biofouling issues and reasonably good agreement with reference data (estimated accuracy: $5 \mu\text{atm}$ for surface measurements and $10\text{--}15 \mu\text{atm}$ in profiling mode). Because of the slow sensor response time, a postprocessing of profiling $p\text{CO}_2$ data is crucial for obtaining unbiased profiles. Such a correction algorithm was validated by extended field tests of the HydroC sensor on a water sampling rosette and applied successfully to reconstruct ambient $p\text{CO}_2$ profiles from time-lagged sensor data. Optode-based O_2 measurements made directly at the ocean–atmosphere boundary provide valuable results for an accurate drift correction of optode data (within $2 \mu\text{mol kg}^{-1}$ in absence of dynamic effects) and therefore enable precise air–sea gas exchange studies.

Future improvements of the $p\text{CO}_2$ sensor, as well as increasing the pumped water flow on the float platform by a stronger pump (SBE 5P pump, $\sim 5.4 \text{ W}$ instead of SBE 5M, $\sim 1.8 \text{ W}$), clearly have the potential to further reduce the sensor's response time and hence minimize

the magnitude of time-lag correction. Thus, accuracy and precision of measurements from profiling or moving platforms can likely be further improved.

Adaption of the presented measurement approach toward an Argo-like mission without redeployments could be made possible in the future. The conducted midterm deployments have demonstrated reliable $p\text{CO}_2$ measurements with a comprehensible drift pattern that could be monitored and accounted for. In addition, promising ongoing developments of the HydroC toward reduced sensor size and energy consumption could significantly extend possible deployment times. Further improvements of the NEMO platform, such as higher battery or sensor payload capacity, also help increase deployment duration and thereby enable long-term deployments for this sensor suite. A fair balance between deployment duration, sampling interval, energy consumption, and accuracy demands has to be assessed for future deployment needs.

The feasibility of combined $p\text{CO}_2$ and O_2 measurements on an autonomous profiling platform has successfully been shown within this work, even though new methodological questions for future investigations have to be addressed (e.g., potential gas matrix effects on $p\text{CO}_2$ data). However, these results demonstrate the potential for this type of measurement for future detailed autonomous investigations of O_2 and carbon dynamics in both the ocean's interior and the ocean–atmosphere boundary layer.

Acknowledgments. The authors thank Ivanice Monteiro and Carlos Santos from the Instituto Nacional de Desenvolvimento das Pescas (INDP) in Mindelo, Cape Verde, as well as the entire crew of R/V *Islândia* for their tremendous support of the field work conducted at CVOO. We further thank the team of Optimare GmbH (Timo Witte, Michael Busack, Günter Buss, Oliver Zenk, Harald Rohr, and Barbara Cembella) for their passionate and professional work on the construction of the prototype float(s). Thanks are also due to CONTROS personnel who have supported the endeavor of measuring $p\text{CO}_2$ profiles on a profiling float and to Sebastian Fessler and Tobias Steinhoff for the analysis of reference samples. Acknowledgement is made to the Facility for Ground-Based Atmospheric Measurement (FGAM) and the National Centre for Atmospheric Science (NCAS) for the use of the Cape Verde Atmospheric Observatory meteorological data. We also like to thank Larry Miloshevich for his helpful comments on the time-lag corrections. This work was funded by the German Federal Ministry of Education and Research under the SOPRAN project (Grants 03F0462A and 03F0611A).

REFERENCES

- Baudot, A., I. Souchon, and M. Marin, 1999: Total permeate pressure influence on the selectivity of the pervaporation of aroma compounds. *J. Membr. Sci.*, **158**, 167–185.
- Bishop, J. K. B., T. J. Wood, R. E. Davis, and J. T. Sherman, 2004: Robotic observations of enhanced carbon biomass and export at 55°S during SOFeX. *Science*, **304**, 417–420.
- Bittig, H. C., B. Fiedler, T. Steinhoff, and A. Körtzinger, 2012: A novel electrochemical calibration setup for oxygen sensors and its use for the stability assessment of Aanderaa optodes. *Limnol. Oceanogr. Methods*, **10**, 921–933.
- Boss, E., D. Swift, L. Taylor, P. Brickley, R. Zaneveld, S. Riser, M. J. Perry, and P. G. Strutton, 2008: Observations of pigment and particle distributions in the western North Atlantic from an autonomous float and ocean color satellite. *Limnol. Oceanogr.*, **53**, 2112–2122.
- Boutin, J., and L. Merlivat, 2009: New in situ estimates of carbon biological production rates in the Southern Ocean from CARIOCA drifter measurements. *Geophys. Res. Lett.*, **36**, L13608, doi:10.1029/2009GL038307.
- Byrne, R. H., and Coauthors, 2010: Sensors and systems for in situ observations of marine carbon dioxide system variables. *Proceedings of OceanObs'09: Sustained Ocean Observations and Information for Society*, J. Hall, D. E. Harrison, and D. Stammer, Eds., Vol. 2, ESA Publ. WPP-306, doi:10.5270/OceanObs09.cwp.13.
- D'Asaro, E., and C. McNeil, 2007: Air–sea gas exchange at extreme wind speeds measured by autonomous oceanographic floats. *J. Mar. Syst.*, **66**, 92–109, doi:10.1016/j.jmarsys.2006.06.007.
- Davis, R. E., J. T. Sherman, and J. Dufour, 2001: Profiling ALACEs and other advances in autonomous subsurface floats. *J. Atmos. Oceanic Technol.*, **18**, 982–993.
- DeGrandpre, M. D., T. R. Hammar, S. P. Smith, and F. L. Sayles, 1995: In-situ measurements of seawater $p\text{CO}_2$. *Limnol. Oceanogr.*, **40**, 969–975.
- Dickson, A. G., 2010: Standards for ocean measurements. *Oceanography*, **23**, 34–47.
- , and F. J. Millero, 1987: A comparison of the equilibrium constants for the dissociation of carbonic acid in seawater media. *Deep-Sea Res. I*, **34**, 1733–1743, doi:10.1016/0198-0149(87)90021-5.
- Dore, J. E., R. Lukas, D. W. Sadler, and D. M. Karl, 2003: Climate-driven changes to the atmospheric CO_2 sink in the subtropical North Pacific Ocean. *Nature*, **424**, 754–757.
- Eckles, R. D., J. M. Welles, and K. Peterson, 1993: CO_2 and $\text{CO}_2/\text{H}_2\text{O}$ infrared gas analyzers. *Meas. Control*, **161**, 83–89.
- Edwards, B., D. Murphy, C. Janzen, and N. Larson, 2010: Calibration, response, and hysteresis in deep-sea dissolved oxygen measurements. *J. Atmos. Oceanic Technol.*, **27**, 920–931.
- Fietzek, P., S. Kramer, and D. Esser, 2011: Deployment of the HydroC (CO_2/CH_4) on stationary and mobile platforms – Merging the trends in the field of platform and sensor development. *Proc. Oceans '11 MTS/IEEE Kona*, Waikoloa, Hawaii, MTS and IEEE/EOS, 9 pp.
- Fischer, G., C. Reuter, G. Karakas, N. Nowald, and G. Wefer, 2009: Offshore advection of particles within the Cape Blanc filament, Mauritania: Results from observational and modelling studies. *Prog. Oceanogr.*, **83**, 322–330, doi:10.1016/j.pocean.2009.07.023.
- García, H. E., and L. I. Gordon, 1992: Oxygen solubility in seawater: Better fitting equations. *Limnol. Oceanogr.*, **37**, 1307–1312.
- Gruber, N., J. L. Sarmiento, and T. F. Stocker, 1996: An improved method for detecting anthropogenic CO_2 in the oceans. *Global Biogeochem. Cycles*, **10**, 809–837.
- , and Coauthors, 2010a: Adding oxygen to Argo: Developing a global in-situ observatory for ocean deoxygenation and biogeochemistry. *Proceedings of OceanObs'09: Sustained Ocean Observations and Information for Society*, J. Hall, D. E. Harrison, and D. Stammer, Eds., ESA Publ. WPP-306, doi:10.5270/OceanObs09.cwp.39.
- , and Coauthors, 2010b: Toward an integrated observing system for ocean carbon and biogeochemistry at a time of change. *Proceedings of OceanObs'09: Sustained Ocean Observations and Information for Society*, J. Hall, D. E. Harrison, and D. Stammer, Eds., ESA Publ. WPP-306, doi:10.5270/OceanObs09.pp.18.
- Johnson, K. M., J. M. Sieburth, P. J. L. Williams, and L. Brändström, 1987: Coulometric total carbon dioxide analysis for marine studies: Automation and calibration. *Mar. Chem.*, **21**, 117–133.
- Johnson, K. S., S. C. Riser, and D. M. Karl, 2010: Nitrate supply from deep to near-surface waters of the North Pacific subtropical gyre. *Nature*, **465**, 1062–1065, doi:10.1038/nature09170.
- Kanamitsu, M., W. Ebisuzaki, J. Woollen, S.-K. Yang, J. J. Hnilo, M. Fiorino, and G. L. Potter, 2002: NCEP–DOE AMIP-II Reanalysis (R-2). *Bull. Amer. Meteor. Soc.*, **83**, 1631–1643.
- Keeling, R. F., A. Körtzinger, and N. Gruber, 2010: Ocean deoxygenation in a warming world. *Annu. Rev. Mar. Sci.*, **2**, 199–229, doi:10.1146/annurev.marine.010908.163855.
- Körtzinger, A., H. Thomas, B. Schneider, N. Gronau, L. Mintrop, and J. C. Duinker, 1996: At-sea intercomparison of two newly designed underway $p\text{CO}_2$ systems – Encouraging results. *Mar. Chem.*, **52**, 133–145.
- , J. Schimanski, U. Send, and D. Wallace, 2004: The ocean takes a deep breath. *Science*, **306**, 1337, doi:10.1126/science.1102557.
- , —, and —, 2005: High quality oxygen measurements from profiling floats: A promising new technique. *J. Atmos. Oceanic Technol.*, **22**, 302–308.
- , and Coauthors, 2008: The seasonal $p\text{CO}_2$ cycle at 49°N/16.5°W in the northeastern Atlantic Ocean and what it tells us about biological productivity. *J. Geophys. Res.*, **113**, C04020, doi:10.1029/2007JC004347.
- Marin, M., K. Kalantzi, and H. Gibert, 1992: Pervaporation process: Membrane conditioning and experimental mass transfer analysis. *J. Membr. Sci.*, **74**, 105–114.
- McDermitt, D. K., R. D. Eckles, G. L. Biggs, and J. M. Welles, 1993: Effects on temperature and pressure on CO_2 infrared absorption with special emphasis on problems resulting from operation at high flow rates. LI-COR Inc. Application Note 117, 12 pp.
- McNeil, C., E. D'Asaro, B. Johnson, and M. Horn, 2006: A gas tension device with response times of minutes. *J. Atmos. Oceanic Technol.*, **23**, 1539–1558.
- Mehrbach, C., C. H. Culberso, J. E. Hawley, and R. M. Pytkowic, 1973: Measurement of apparent dissociation constants of carbonic acid in seawater at atmospheric pressure. *Limnol. Oceanogr.*, **18**, 897–907.
- Merkel, T. C., V. I. Bondar, K. Nagai, B. D. Freeman, and I. Pinnau, 2000: Gas sorption, diffusion, and permeation in poly(dimethylsiloxane). *J. Polym. Sci.*, **38B**, 415–434.
- Millero, F. J., 2007: The marine inorganic carbon cycle. *Chem. Rev.*, **107**, 308–341, doi:10.1021/cr0503557.
- Miloshevich, L. M., A. Paukkunen, H. Vömel, and S. J. Oltmans, 2004: Development and validation of a time-lag correction for

- Vaisala radiosonde humidity measurements. *J. Atmos. Oceanic Technol.*, **21**, 1305–1327.
- Mintrop, L., F. F. Perez, M. Gonzalez-Davila, M. J. Santana-Casiano, and A. Körtzinger, 2000: Alkalinity determination by potentiometry: Intercalibration using three different methods. *Cienc. Mar.*, **26**, 23–37.
- Moore, T. S., M. D. DeGrandpre, C. L. Sabine, R. C. Hamme, C. J. Zappa, W. R. McGillis, R. A. Feely, and W. M. Drennan, 2011: Sea surface $p\text{CO}_2$ and O_2 in the Southern Ocean during the austral fall, 2008. *J. Geophys. Res.*, **116**, C00F11, doi:10.1029/2010JC006560.
- Padin, X. A., M. Vázquez-Rodríguez, A. F. Rios, and F. F. Pérez, 2007: Atmospheric CO_2 measurements and error analysis on seasonal air–sea CO_2 fluxes in the Bay of Biscay. *J. Mar. Syst.*, **66**, 285–296, doi:10.1016/j.jmarsys.2006.05.010.
- Pfeil, B., and Coauthors, 2012: A uniform, quality controlled Surface Ocean CO_2 Atlas (SOCAT). *Earth Syst. Sci. Data Discuss.*, **5**, 735–780, doi:10.5194/essdd-5-735-2012.
- Pierrot, D., and Coauthors, 2009: Recommendations for autonomous underway $p\text{CO}_2$ measuring systems and data-reduction routines. *Deep-Sea Res. II*, **56**, 512–522, doi:10.1016/j.dsr2.2008.12.005.
- Prabhakar, R. S., R. Raharjo, L. G. Toy, H. Lin, and B. D. Freeman, 2005: Self-consistent model of concentration and temperature dependence of permeability in rubbery polymers. *Ind. Eng. Chem. Res.*, **44**, 1547–1556, doi:10.1021/ie0492909.
- Riser, S. C., and K. S. Johnson, 2008: Net production of oxygen in the subtropical ocean. *Nature*, **451**, 323–325, doi:10.1038/nature06441.
- Roemmich, D., G. Johnson, S. Riser, R. Davis, and J. Gilson, 2009: The Argo program: Observing the global ocean with profiling floats. *Oceanography*, **22**, 34–43.
- Stephens, B. B., R. F. Keeling, M. Heimann, K. D. Six, R. Murnane, and K. Caldeira, 1998: Testing global ocean carbon cycle models using measurements of atmospheric O_2 and CO_2 concentration. *Global Biogeochem. Cycles*, **12**, 213–230, doi:10.1029/97GB03500.
- Stramma, L., and F. Schott, 1999: The mean flow field of the tropical Atlantic Ocean. *Deep-Sea Res. II*, **46**, 279–303.
- Takahashi, T., and Coauthors, 2009: Climatological mean and decadal change in surface ocean $p\text{CO}_2$, and net sea–air CO_2 flux over the global oceans. *Deep-Sea Res. II*, **56**, 554–577, doi:10.1016/j.dsr2.2008.12.009.
- Tengberg, A., and Coauthors, 2006: Evaluation of a lifetime-based optode to measure oxygen in aquatic systems. *Limnol. Oceanogr. Methods*, **4**, 7–17.
- Uchida, H., T. Kawano, I. Kaneko, and M. Fukasawa, 2008: In situ calibration of optode-based oxygen sensors. *J. Atmos. Oceanic Technol.*, **25**, 2271–2281.
- Watson, A. J., and Coauthors, 2009: Tracking the variable North Atlantic sink for atmospheric CO_2 . *Science*, **326**, 1391–1393, doi:10.1126/science.1177394.

3.3 Discussion

Evaluated sensors in section 3.1 represent a new generation of $p\text{CO}_2$ sensors which has become available for both conventional (e.g., underway) and sophisticated (e.g., profiling) applications. Both have been tested successfully in underway applications. Here, sensors encountered a broad range of environmental conditions during these cruises which caused significant differences in performance between the sensors.

The PSI CO₂-Pro showed a pronounced drift in NDIR cell temperature that clearly followed the SST pattern along the cruise track and was correlated with observed $p\text{CO}_2$ offsets from the reference. Thus, a potential bias on the factory calibration cannot be ruled out, as observed during the evaluation cruise ANT-XXVI/4. The HydroC, encountering the same ranges for SST, did not show such effects. This finding is very important if one considers these sensors for profiling applications, where rapid changes in environmental conditions occur.

Established and high accuracy methods were conducted during the above mentioned cruises successfully, enabling a careful assessment of sensor measurement accuracy. Again, major differences between both sensors were found. The PSI CO₂-Pro showed a clear and pronounced offset varying between 1 – 15 μatm when compared to reference underway measurements. A mean offset of $-11.8 \pm 3.4 \mu\text{atm}$ (RMSE: 12.3 μatm) was found. The sensor's real-time correction (ZP) of NDIR signal drift could not compensate this offset. Hence, this artifact might be due to insufficient temperature control of the NDIR detector which affects the factory calibration significantly.

In contrast, measurements of the HydroC during sensor evaluation cruises demonstrated reliable measurements that were not affected by environmental conditions. By means of pre- and post-calibrations of the HydroC the offset pattern (when compared to reference measurements) resulted in a mean $p\text{CO}_2$ offset of $-0.7 \pm 3.0 \mu\text{atm}$ (RMSE: 3.7 μatm). Signal drift of the HydroC was comprehensible and could be compensated for by the above mentioned calibrations in combination with thoroughly post-processing of sensor data. Therefore, measurements of the HydroC sensor appear to be more suitable for profiling applications than the PSI CO₂-Pro.

However, findings of this evaluation cannot be transferred easily to other, different observation platforms. Therefore, an intensive field evaluation of the newly developed float platform was crucial. Results of these field missions were illustrated in section 3.2. When comparing these two evaluations with each other, one has to consider the major difference in the profiling approaches (as shown in section 2.3.1). Figure 3.16 shows this difference on the basis of two example profiles for each float.

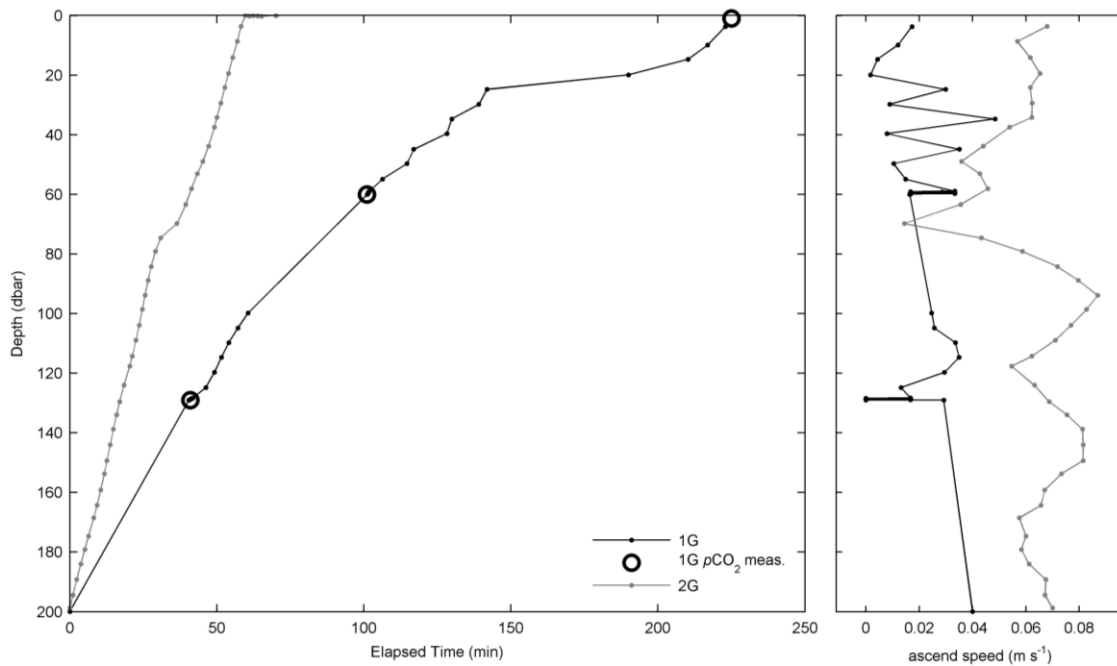


Figure 3.16 Comparison of profiling approaches for float 1G and 2G. Left: Timelines for both prototype floats. Each data point (dots) represents a measurement of CTD and O₂ sensors. Discontinuous measurements for pCO₂ are marked as black circles for the 1G float, whereas pCO₂ measurements on the 2G float were performed continuously along with each CTD measurement. Right: Derived profiling velocity for both floats. Straight lines in both panels indicate areas of the upcast where no measurements are available (see text for further detail).

The STS approach used for the 1G float turned out to be a rather insufficient and time-consuming method. While ascending, the float was unable to approach the designated depth levels (200, 100 and 1 dbar) precisely in most cases. This was due to the float's own impulse and conservatively set algorithms for buoyancy control (in order to keep power consumption low), even when nominal ascent rates were kept as low as possible. When the float approached a predefined depth level, start-up procedures for the PSI CO₂-Pro were started (including warm-up and ZP) and no other data could be recorded in the meantime (data gaps in Figure 3.16). The following pCO₂ measurements on these nominal depths were biased due to a still ascending float and thereby a changing ambient pCO₂ during the sensor's signal recovery time. The change of this ambient pCO₂ during the sensor equilibration phase complicated the extrapolation procedure (section 3.2.1) that had to be applied to estimate the final equilibrium pCO₂. Some of rather large noise level of these pCO₂ data is due to this variable change in ambient pCO₂. In general, the STS approach applied during D1 – D3 turned out to be not an appropriate method for pCO₂ measurements on a profiling float platform.

To overcome these constraints one has to use instrumentation that features sufficiently small values for k_{63} , thereby enabling continuous measurements during the ascent. Figure 3.17 illustrates the observed difference for in situ derived k_{63} values between the 1G and 2G float. Major differences in the magnitude of k_{63} were observed, particularly at greater depth. Obtained data suggest the

influence of environmental variables such as temperature or hydrostatic pressure as the main reason for these differences. This was previously found also for other membrane interfaces (McNeil et al. 2006; Prabhakar et al. 2005). In test series with the HydroC conducted in a pressure chamber (max. pressure applied: 2000 dbar) under isothermal conditions no significant dependence of k_{63} to hydrostatic pressure was detected. However, a clear linear dependence to water temperature was found in lab test series and during underway applications. The PSI CO₂-Pro sensor also showed a linear temperature dependence during field tests (under isobaric conditions). However, this does not fully explain the observed pattern during float deployments. Hence, there appears to be at least a co-dependence with hydrostatic pressure as well.

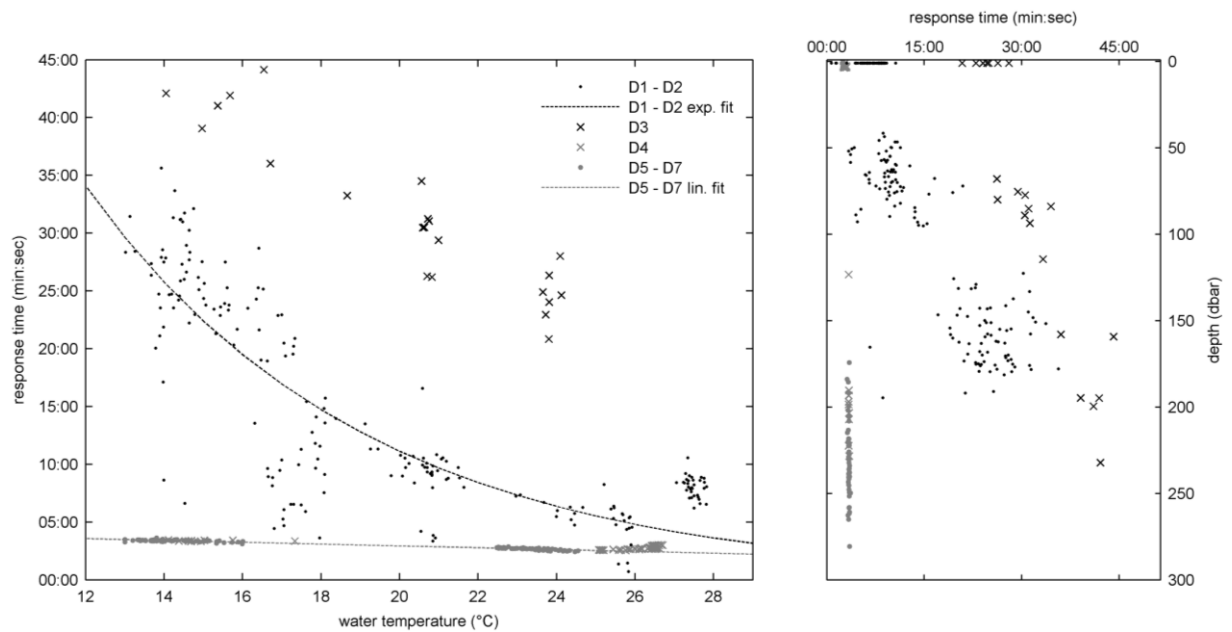


Figure 3.17 Observed in situ k_{63} for the PSI CO₂-Pro (black dots) and HydroC (grey dots) both being deployed on prototype floats. Crosses indicate deployments during which k_{63} was affected by a membrane conditioning (D4) or by unknown reason (D3). The left panel highlights the temperature dependence of k_{63} whereas the right panel shows the k_{63} distribution against depths. Presented data underlines the much better performance of the HydroC in terms of k_{63} .

The constraint discussed above points out the difficulties with performing membrane-based $p\text{CO}_2$ measurements on a profiling device in the water column. Even the pursued STS approach didn't allow the sensor signal to fully recover from the ZP towards ambient $p\text{CO}_2$ for the majority of determinations due to its high k_{63} values, particularly at depth (Figure 3.18, left panel). When comparing these with signal recovery times obtained by the 2G float a greatly improved performance is obvious. But even k_{63} values of the HydroC were still large enough to cause a significant time-lag effect in continuously measured profile data. However, thorough back-folding correction of 2G float data removed most of the sensor time-lag (Figure 3.18, right panel) leading to an overall accuracy of 10 – 15 μatm (as validated in section 3.2.2).

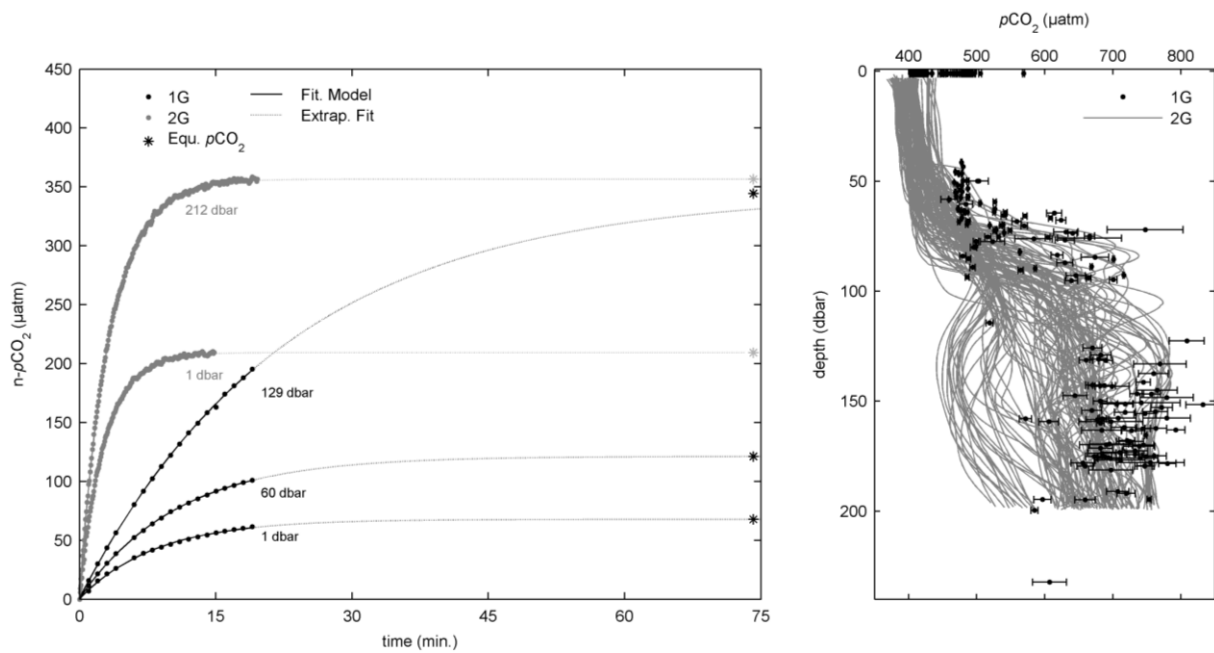


Figure 3.18 Comparison of 1G and 2G float data. The left panel illustrates the method for deriving $p\text{CO}_2$ values with the STS approach (black lines and symbols, 1G, prof. no. 71). Signal recoveries after the ZP on 3 different depths are presented, each characterized with a different k_{63} . By fitting eqn. 3 (section 3.2.2) to the recorded data (black dots) the sensor signal is being extrapolated in time and the actual (fully equilibrated) ambient $p\text{CO}_2$ (black stars) can be derived. Common signal recovery times for the 2G float (prof. no 92) are presented as well (grey lines and symbols). The right panel compares finally derived $p\text{CO}_2$ values for the 1G and 2G floats. A significant improvement of spatial resolution and measurement quality for the 2G float is obvious.

Comparison of final $p\text{CO}_2$ data of 1G and 2G floats in terms of accuracy and data resolution (Figure 3.18, right panel) emphasizes the major improvement for float-borne $p\text{CO}_2$ measurements that has been achieved from 1G to 2G floats. The high resolution $p\text{CO}_2$ dataset of the 2G float could be used for the extension of the CVOO carbon time-series data. Additionally, the 2G float data could highly resolve seasonal variability of the carbon cycle at CVOO, as illustrated and further described in the following chapter.

4 Scientific Results

This chapter presents first scientific results from CVOO. The observatory is comparatively young and still in the process of being established. Nevertheless, observations have started in 2006 and new or extended methods have been developed and established within the framework of this thesis in order to facilitate an adequate characterization of biogeochemical dynamics in the ETNA region. Thus, a composite data set was created that contains a broad range of different observational approaches (e.g., ship based sampling, long-term mooring, mobile autonomous platforms, etc.). Details about data set contents can be found in appendix I.b.

The following sections provide a comprehensive phenomenological characterization of carbon and oxygen dynamics at CVOO. In order to present results in a comprehensible manner this chapter is divided into processes either occurring at the surface (section 4.1) or within the upper water column (>200 m, section 4.2). Using classical (e.g., ship-based sampling) as well as advanced methods (e.g., autonomous instruments) biogeochemical dynamics on different timescales could be resolved, ranging from annual (4.1.1) to seasonal (4.1.2) and even diurnal (4.1.3) scales. Subsequently, carbonate system parameters in the upper water column derived from float-borne (2G float) observations are portrayed (4.2.1). Finally, as a combined result of different observational approaches used at CVOO, evidence for the occurrence of anoxic and severe hypoxic water masses in the open ocean ETNA region is being presented (4.2.2).

4.1 Surface Processes

4.1.1 Long-term Temporal Variability

So far, CVOO still holds only comparatively short data records and thus doesn't allow for a robust analysis of inter-annual variability or temporal trends. However, there are already some existing data that cover a range between 2006 and 2012 which will be used to describe the typical biogeochemical situation at Cape Verde in the following.

Sea Surface Temperature

Temperature measurements obtained from mooring deployments at CVOO illustrate seasonal and inter-annual changes in SST as well as temperature-derived MLD (Figure 4.1). These changes affect biogeochemical cycles as will be discussed in the following section (4.1.2). Despite these seasonal variations inter-annual changes of SST clearly point out an anomalous period during the surface cooling phase in the first half of 2010. Wintertime cooling stopped at SST levels of ~24°C which is significantly higher than during previous years.

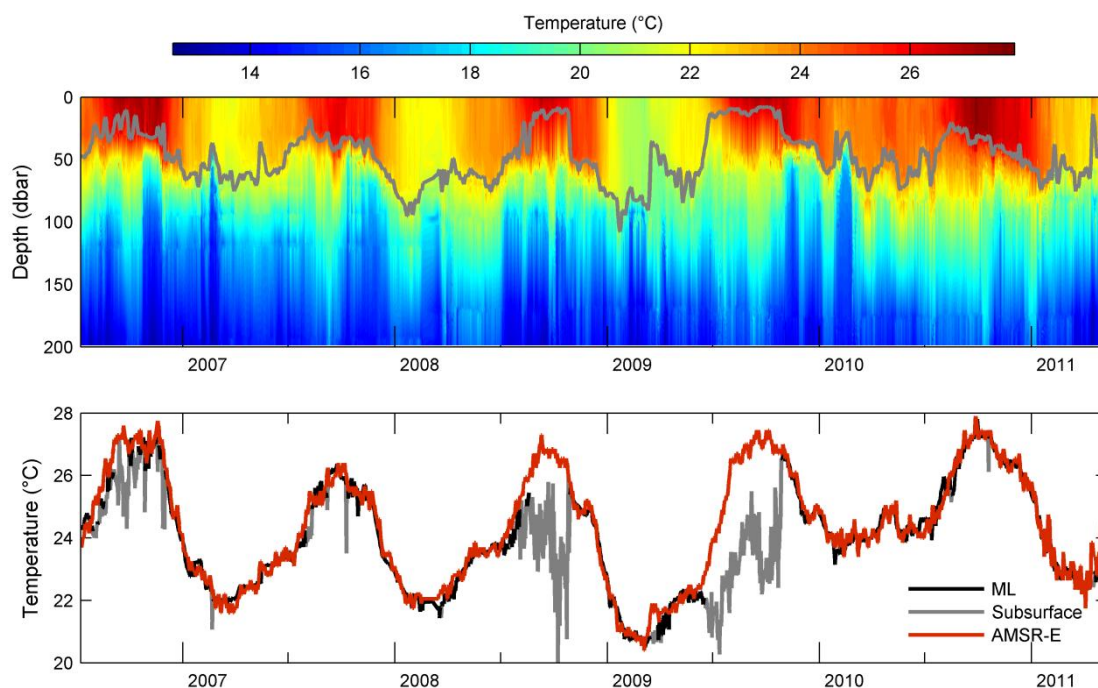


Figure 4.1 Vertical temperature distribution for the upper 200 m of the water column at CVOO as observed during 3 consecutive mooring deployments (upper panel). Temperature data at the surface (SST) were taken from satellite measurements (AMSR-E, www.discover-earth.org). The gray line in the upper panel denotes the temperature derived ($\Delta T = 0.8^\circ\text{C}$) MLD. Mooring SST and satellite SST are in good agreement with each other, except during periods of shallow MLD when the moored temperature sensor recorded subsurface temperature (lower panel).

These measurements were confirmed by satellite SST observations (Figure 4.1, lower panel). A possible explanation for this SST anomaly was found in the record of the North Atlantic Oscillation Index (NAO, Hurrell 1995) which is a measure for natural mode variations of atmospheric pressure over the North Atlantic. It has been shown that phase shifts in this index impact upper ocean properties such as SST and MLD and thereby also affect biogeochemical cycling (Cayan 1992; Gruber et al. 2002).

Exceptionally low NAO values were detected for winter months in 2010 (Figure 4.2) that appear to be related to this distinct SST anomaly. Unfortunately, consequences for O_2 or CO_2 cycles at CVOO cannot be revealed for this period due to a lack of sample data at this time. However, future data records at CVOO will allow a more robust investigation of the impact of long-term NAO variability on gas dynamics in the ETNA region.

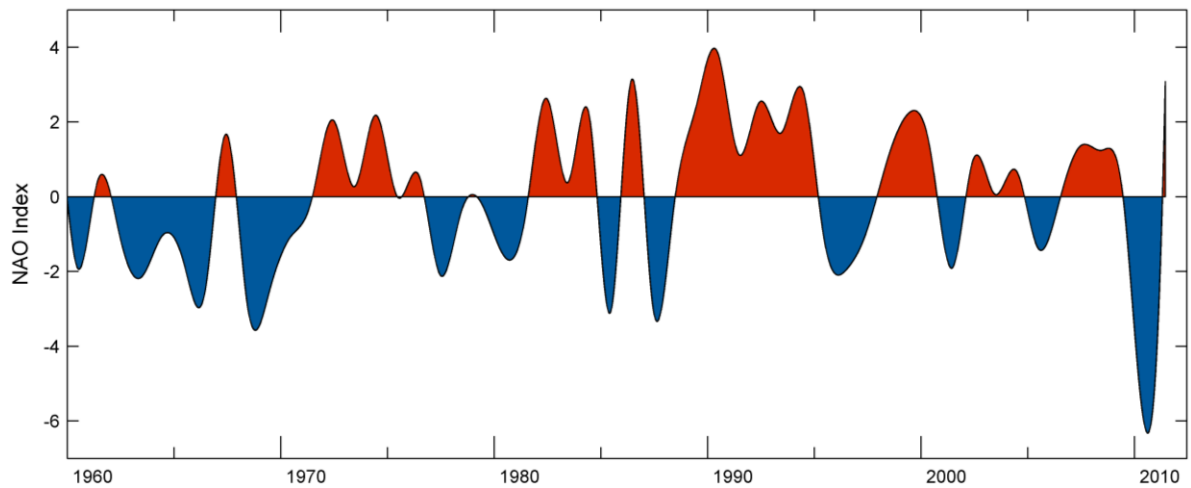


Figure 4.2 NAO index record for the past 52 years. Data provided by the Climate Analysis Section, Boulder, USA, Hurrell (1995), updated regularly.

Chlorophyll a

Measurements of Chlorophyll a (chl a) are included into the regular monthly sampling scheme at CVOO. Due to sparse coverage of these samplings satellite derived values for chl a were used for a better description of the inter-annual distribution over the last 7 years (Figure 4.3). This data, illustrated as the temporal evolution of a meridional section at CVOO, show low chl a concentrations which are typical for oligotrophic ocean basins (Morel et al. 2010). The major part of each year is dominated by very low chl a concentrations ($<0.2 \mu\text{g L}^{-1}$) whereas periodic events of slightly elevated levels are found (up to $\sim 0.7 \mu\text{g L}^{-1}$). These events mainly occur during winter months (see next section) and might be related to horizontal advection of water masses originating in the Mauritanian upwelling (Figure 1.6; Gabric et al. 1993; Kostianoy and Zatsepin 1996).

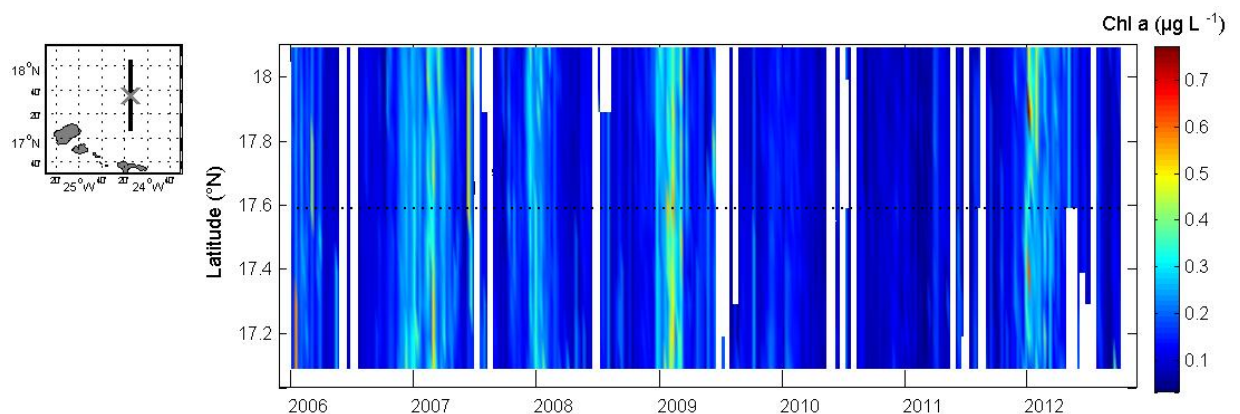


Figure 4.3 chl a distribution along a meridional section at CVOO. Satellite derived chl a data (MODIS-terra) are shown for the last 7 years as a Hovmöller plot.

CO₂ and O₂ records at CVOO and CVAO

The generated composite data set for oceanic CO₂ and O₂ parameters contains earliest data from a cruise in 2006 and number of continued samplings has subsequently increased over the past years. With augmentation by float data collected in close proximity to CVOO this data set enables a first analysis of seasonal variability (refer to next section). The full record is shown in Figure 4.4 (upper panel).

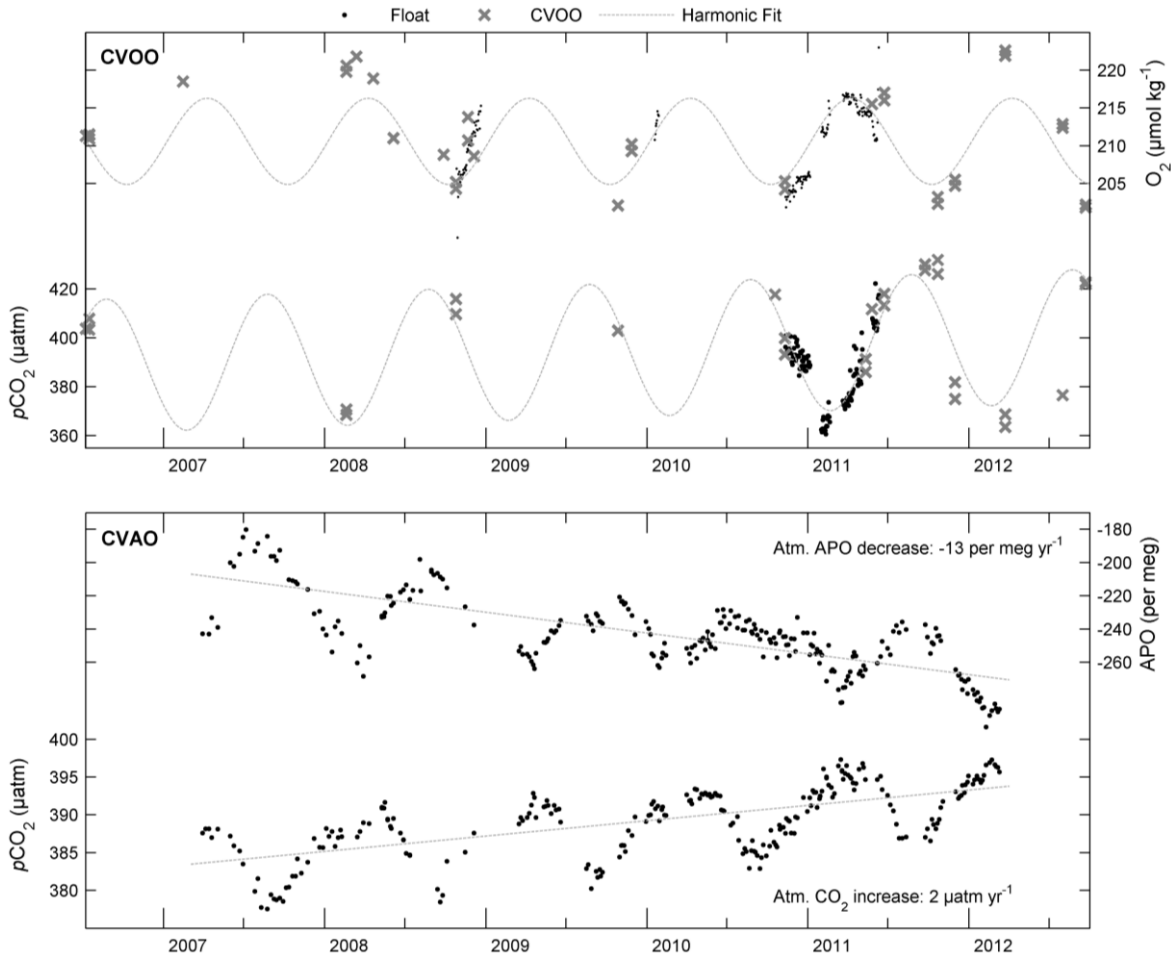


Figure 4.4 Time series measurements for $p\text{CO}_2$ and O_2 in the ocean (CVOO, upper panel) and for $p\text{CO}_2$ and APO in the atmosphere (CVAO, lower panel). An estimated annual increase rate of $2.0 \mu\text{atm}$ for oceanic $p\text{CO}_2$ data was added to the harmonic fit (gray dashed line for $p\text{CO}_2$ data, upper panel). Dashed lines in the lower panel (lin. regression) describe mean annual increase/decrease in atmospheric $p\text{CO}_2$ and APO, respectively. CVAO data were provided by MPI Jena (Heimann/Kozlova).

At CVOO, both O_2 and $p\text{CO}_2$ data (partly derived from DIC/TA) show clear seasonal variability which will be discussed further in section 4.1.2. Data coverage in early years is rather poor due to very limited ship resources. However, when assuming a harmonic annual variability for both parameters (eqn. 4.1), even periods with fewer samples fit well into this pattern.

$$F(t) = a + b \cdot \cos\left(t \cdot 2 \cdot \frac{\pi}{365}\right) + c \cdot \sin\left(t \cdot 2 \cdot \frac{\pi}{365}\right), \quad 4.1$$

where a , b , c are fitting parameters, t is time and $F(t)$ is the final harmonic function describing the annual cycle.

$p\text{CO}_2$ and O_2 show an inverse relationship to each other, mainly driven by thermodynamics and biological processes. The annual net increase of $2.0 \mu\text{atm yr}^{-1}$ in oceanic $p\text{CO}_2$ was taken into account for the harmonic analysis since this trend cannot be derived from the sparse data set yet. However, this increase rate was found for the region already during a previous assessment (Takahashi et al. 2009) and similar values were also found either on a global scale (Lenton et al. 2012) or at similar time series sites (Bates 2001; Dore et al. 2009).

The assumption made above for the annual $p\text{CO}_2$ increase rate in the ocean is in good agreement with observed atmospheric $p\text{CO}_2$ levels at CVAO (Figure 4.4, lower panel). Collection of discrete air samples has started in 2007 and a good coverage for the past years was achieved. Data clearly reveal annual cycles for $p\text{CO}_2$ as expected for the northern hemisphere. Continuing the present annual $p\text{CO}_2$ increase rate the $400 \mu\text{atm}$ threshold will likely be reached in spring 2013 at CVAO.

In addition to $p\text{CO}_2$ also O_2 measurements were performed at CVAO which allow computation of the tracer APO described in section 1.1. Being essentially a tracer for oceanic sea-to-air O_2 fluxes, the record (Figure 4.4) reflects the atmospheric O_2 exchange with the ocean along air mass trajectories approaching CVAO. Due to steady NE trade winds (Figure 4.5) APO records can potentially contain valuable information about ASE of CO_2 and O_2 at CVOO, which is directly located upwind of CVAO.

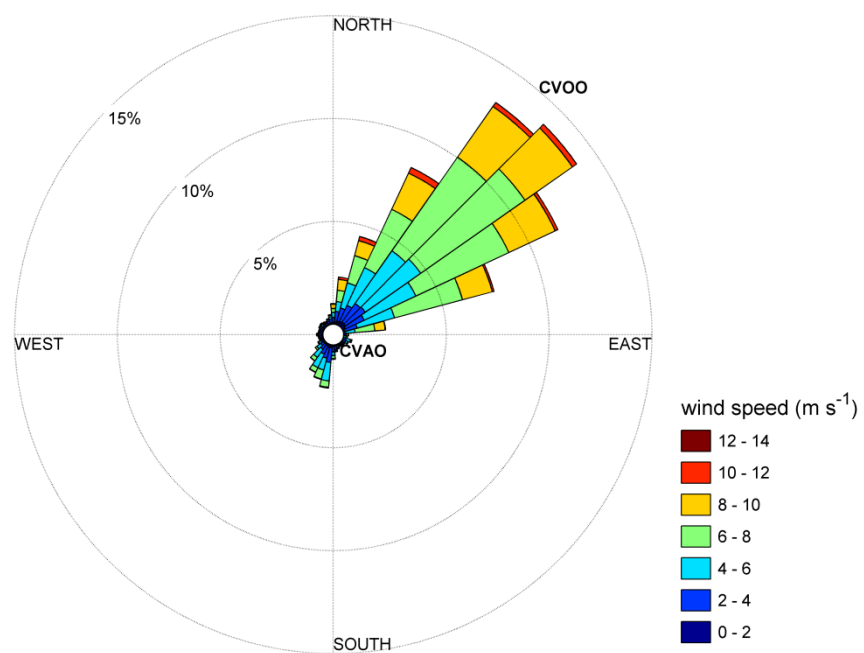


Figure 4.5 Distribution of wind fields at Cape Verde observed during the past 6 years at CVAO. CVOO is located directly upwind of CVAO, denoted by the names of both observatories in the figure (heading: 38°).

However, signatures are small and thus highly resolved APO measurement are needed in order to link atmospheric signals to oceanic processes, as has been shown elsewhere (Lueker 2003). Such a continuous measurement technique has recently been established at CVAO and will allow a more detailed analysis in future.

However, concurrent atmospheric and oceanic measurements of CO₂ and O₂, the close proximity of both observatories as well as a steady NE trade wind regime (Figure 4.5) facilitate a precise determination of ASE for CO₂ and O₂ (see next section).

4.1.2 Seasonal Variability

CVAO and Satellite Data

Data obtained between 2006 and present were used to investigate the seasonal variability of environmental conditions at CVOO. Therefore, the full record spanning 6 years for various parameters was projected on a seasonal scale, assuming inter-annual trends and variability to be negligible for this period.

Since CVOO is located in the tropics seasonal variability is assumed to be rather homogenous with lower amplitudes compared to extratropical regions. Figure 4.6 illustrates data for wind speed and dust deposition, both measured at CVAO, as well as chl a and SST derived from satellite data for CVOO. A low seasonal amplitude was found for wind speed with slightly enhanced values during winter/spring and lowered values during summer/fall. Therefore, wind speed apparently does only have a moderate impact on the overall seasonal distribution of ASE fluxes at CVOO (fluxes will be presented later on), as wind speed is one of the driving forces for the gas exchange coefficient (section 1.1).

SST data derived from satellite observations show a pronounced seasonal variation, which is in agreement with mooring based in situ temperature measurements (Figure 4.1) and ship-borne data (Figure 4.6). Satellite-derived chl a data suggest elevated concentration during winter months and a minimum during summer. Compared to chl a measured in situ in the ML at CVOO this pattern cannot yet be confirmed due to insufficient seasonal coverage of the in situ data. Since remotely sensed chl a concentrations can be biased by environmental conditions, such as bubble entrainment (Stramski and Tegowski 2001) and atmospheric dust (Schollaert et al. 2003), rates for dust deposition at CVAO can be seen as a proxy for potentially biased chl a data.

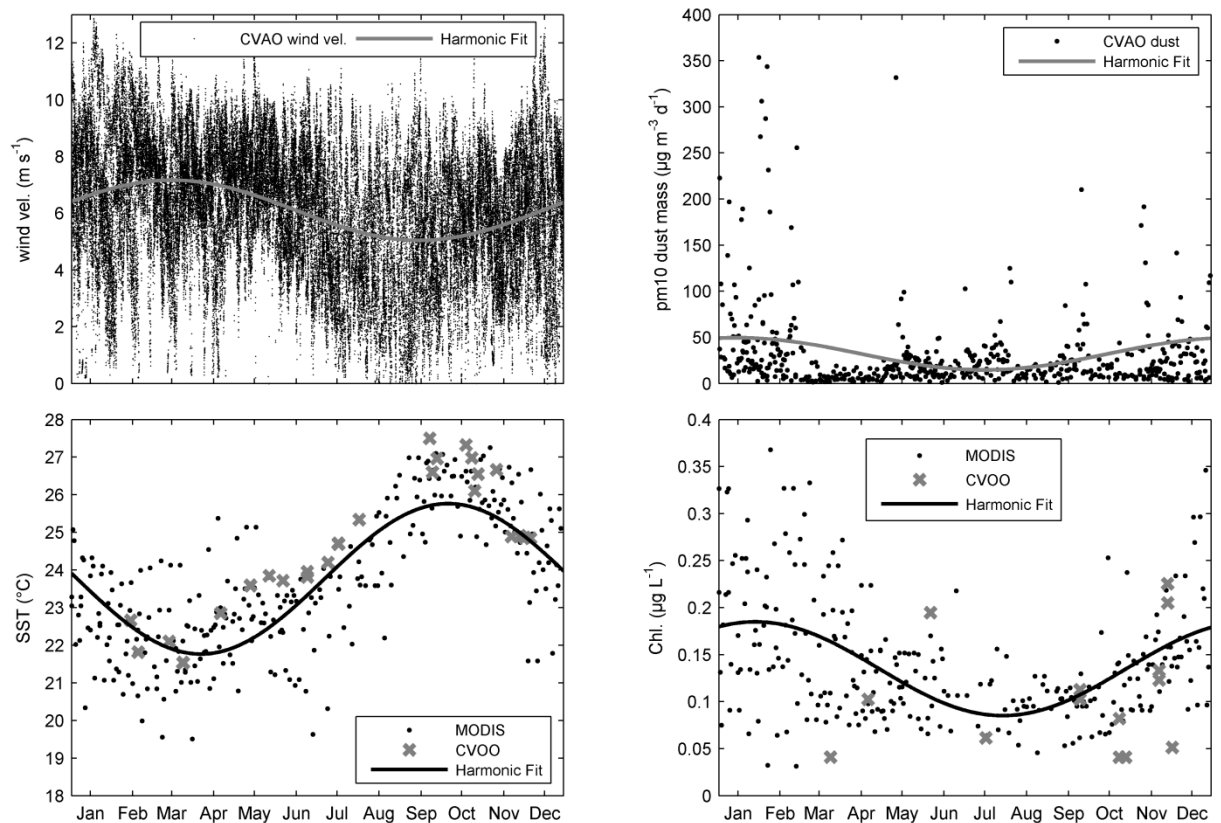


Figure 4.6 Seasonal variations for wind speed (upper left), dust deposition rates (upper right), SST (lower left) and chl a (lower right) for the past 6 years. All records are shown on annual scales and harmonic analysis was performed following eqn. 4.1 (solid lines). Satellite data were obtained from MODIS-aqua (<http://ocean-color.gsfc.nasa.gov/>).

Indeed, deposition rates are slightly enhanced during winter months which might be a potential bias for the observed high chl a values during these months. However, one could also argue that enhanced dust deposition is a source of nutrients (e.g., N, P, etc.) as well as trace elements (e.g., iron, aluminum etc.) and thereby facilitating primary production in the ocean upper layer. Either way, more in situ measurements will be available in nearby future and thus allow a better assessment of seasonal biomass distribution at CVOO.

Air-Sea Gas Exchange of CO₂ and O₂

Time series stations are a valuable tool for determining and understanding seasonal variability of oceanic carbon pools and related fluxes (Bates et al. 1996; Dore et al. 2003; González-Dávila 2003). So far, the only seasonal assessment for CO₂ ASE in the ETNA region has been published by Takahashi et al. (2009) as part of a global climatology for oceanic pCO₂. Measurements conducted at CVOO are thus helpful to check the climatology data and even to better assess the magnitude of ASE.

The following data between 2006 and 2012 were used to determine the seasonal variation in CO_2 ASE:

- Discrete samples for DIC, TA (converted to $p\text{CO}_2$) and O_2 taken during various ship campaigns performed at CVOO,
- Underway measurements for $p\text{CO}_2$ during ship surveys,
- Float-borne $p\text{CO}_2$ and O_2 measurements in the vicinity of CVOO.

Figure 4.7 shows the seasonal distribution for CO_2 and O_2 in the ocean ML in relation to atmospheric levels for each gas (measured at CVAO). This approach allows to exclude the net annual increase of CO_2 in both the atmosphere and the ocean since increase rates for both spheres are similar ($\sim 2.0 \mu\text{atm yr}^{-1}$, Figure 4.4 and Takahashi et al. 2009). $\Delta p\text{CO}_2$ data show a pronounced seasonal cycle with a peak-to-peak amplitude of $\sim 75 \mu\text{atm}$, mainly driven by the seasonal SST cycle (Figure 4.6). During winter months a pronounced undersaturation of $p\text{CO}_2$ in the ocean occurs, followed by a steep increase in $p\text{CO}_2$ levels towards summer months. Peak values for $\Delta p\text{CO}_2$ were detected in September. However, due to a lack of observations during summer months $p\text{CO}_2$ levels might even exceed peak values of $\sim 40 \mu\text{atm}$ as indicated by the $p\text{CO}_2$ climatology of Takahashi et al. (2009). Oceanic $p\text{CO}_2$ levels then begin to decrease rapidly towards equilibrium with the atmosphere in November and December.

Overall, measurements are roughly in agreement with climatological data. Discrepancies between CVOO and climatological data were found during winter months, where CVOO data suggest a more intensified $p\text{CO}_2$ minimum than climatological data.

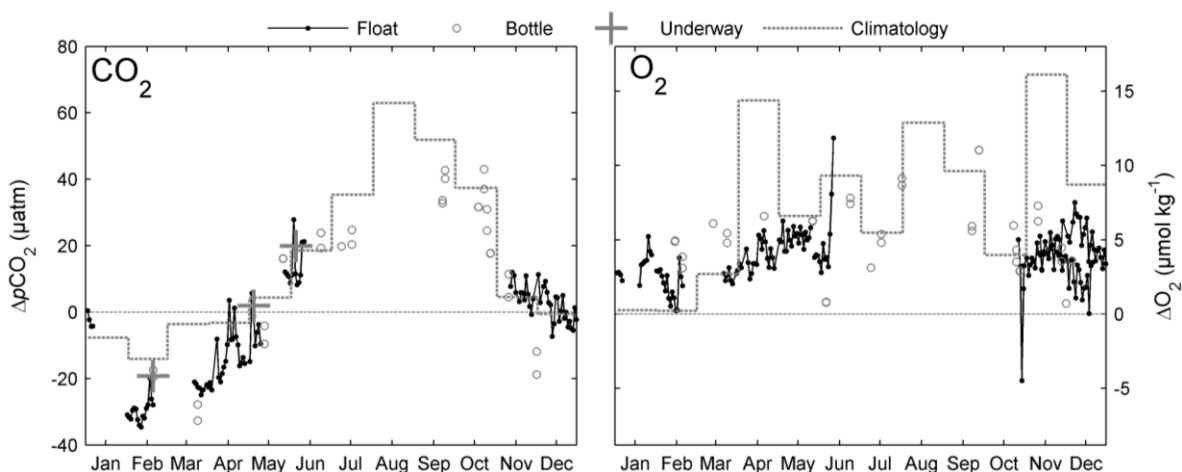


Figure 4.7 Differences between atmospheric and oceanic levels for $p\text{CO}_2$ (as $\Delta p\text{CO}_2$, left) and O_2 (as ΔO_2 , right) on the basis of observations occurred during the past 6 years at CVOO and CVAO. Positive values in both panels describe oversaturation of water masses, negative values an undersaturation and dashed thin lines the equilibrium threshold. Bold dashed lines denote climatology data.

The seasonal pattern of oceanic O_2 levels (Figure 4.7 right; expressed as ΔO_2 , eqn. 1.11) shows a permanent oversaturation over the entire year. No clear seasonal cycle could be detected with the current data set. O_2 levels were largely in agreement with levels taken from the World Ocean Atlas 2009 (WOA09, Garcia et al. 2010) for the location of CVOO. Climatology as well as CVOO data suggest only a weak annual cycle of ΔO_2 . However, some gaps in the recent data set still remain and therefore limit the characterization of seasonal ΔO_2 variations.

The close proximity of both observatories to each other, as well as steady NE trade winds at Cape Verde (Figure 4.5), allow an accurate assessment of ASE fluxes for both gases. In order to cover the entire season all data were binned into monthly averages. ASE flux densities for CVOO data were derived following procedures described in section 1.1. Figure 4.8 illustrates monthly averages of obtained ASE fluxes for CO_2 as a mean seasonal cycle at CVOO.

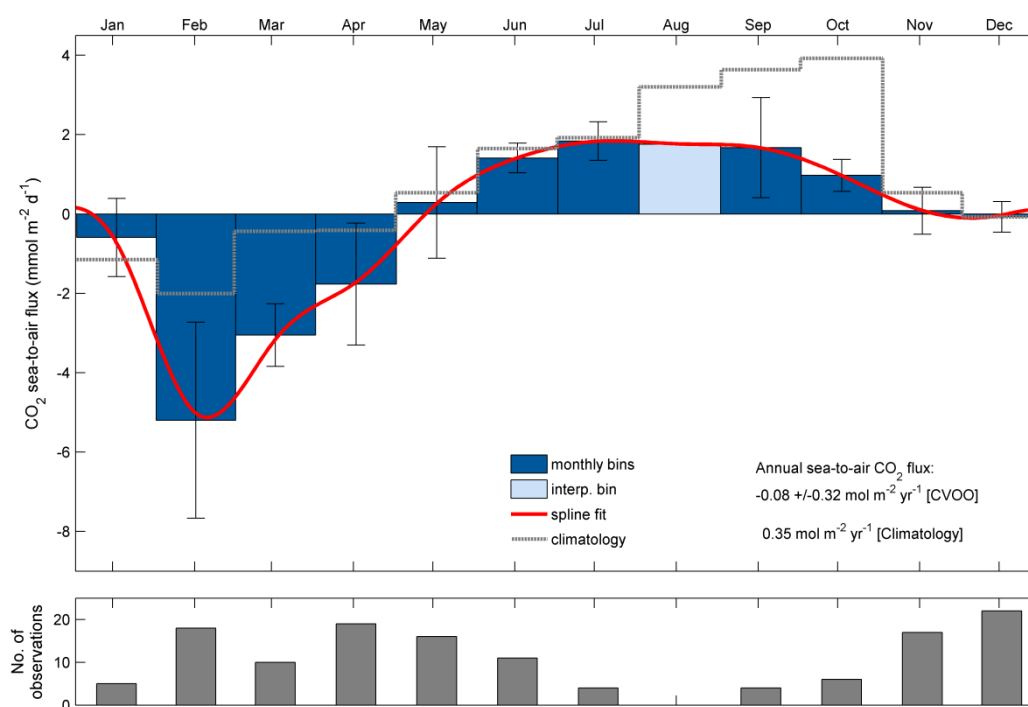


Figure 4.8 Computed monthly averaged ASE fluxes for CO_2 at CVOO (upper panel). Since no data are yet available for August this data point was linearly interpolated between neighboring months (light blue bar). Climatology data (dashed gray line) was taken from Takahashi et al. (2009). Error bars denote the RMSE for observations contained in each bin (lower panel).

Negative values denote a net flux from air to sea and positive values vice versa. Seasonal distribution of ASE fluxes mainly reflects ΔpCO_2 variability at CVOO since the seasonal wind speed distribution shows only a small variation (Figure 4.6). Net CO_2 uptake by the ocean is strongest from February through April whereas CO_2 outgassing is occurring from June through October. When compared to climatological fluxes the net CO_2 sink during winter/spring is significantly stronger by a factor of 3 – 4 and summertime outgassing is less intense (factor ~ 2) than stated by

Takahashi et al. (2009). This leads to a total annual net CO₂ flux of $-0.08 \pm 0.32 \text{ mol m}^{-2} \text{ yr}^{-1}$ (net uptake) derived from CVOO observations, which is less compared to climatological data ($0.35 \text{ mol m}^{-2} \text{ yr}^{-1}$, net outgassing).

ASE fluxes for O₂ were derived as described in section 1.1 and seasonal distribution of these is presented in Figure 4.9. The apparent oversaturation of water masses at CVOO clearly results in continuous outgassing over the entire year. A weak seasonal signal in O₂ ASE fluxes with highest values in May could be observed. Annual net sea to air fluxes determined at CVOO are $5.0 \pm 2.5 \text{ mol m}^{-2} \text{ yr}^{-1}$, whereas climatology data suggest somewhat higher fluxes of $9.0 \text{ mol m}^{-2} \text{ yr}^{-1}$ (Garcia et al. 2010). However, the patchy distribution of climatology data does not allow an accurate comparison.

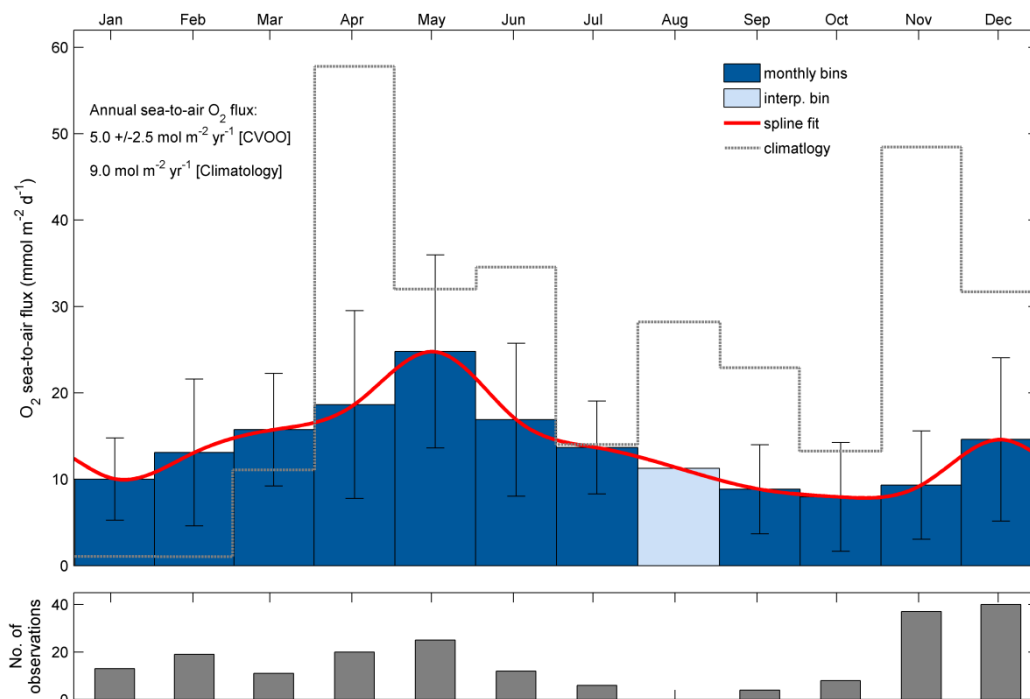


Figure 4.9 Computed monthly binned ASE fluxes for O₂ at CVOO (upper panel). Since no data is yet available for August this data point was linearly interpolated (light blue bar). Climatology data (dashed gray line) was taken from the World Ocean Atlas 2009 (Garcia et al. 2010). Error bars denote the RMSE for observations contained in each bin (lower panel).

Atmospheric Potential Oxygen

Concurrent measurements of CO₂ and O₂ in the atmosphere allow to separate terrestrial and marine processes that alter the abundance of these gases. The tracer APO (Stephens et al. 1998) can be computed by employing eqn. 1.13. Results for APO observed at CVAO were presented in Figure 4.4 and show clear seasonal variations, indicating a similar seasonal variation in ASE O₂ fluxes upwind of the station.

Since concurrent measurements were also performed at CVOO, which is located upwind of CVAO (Figure 4.5), ASE fluxes of APO can be explicitly calculated and compared to observations at CVAO. For instance, Lueker (2003) has linked atmospheric APO measurements to a nearby costal upwelling system and thereby detected upwelling of O_2 undersaturated water masses in the atmospheric APO signals. Körtzinger et al. (2008b) showed that seasonal variations in ASE for O_2 , CO_2 and thus APO in the Labrador Sea are in accordance with atmospheric APO observations for that region.

Observed ASE flux densities for CO_2 and O_2 at CVOO (Figure 4.10, upper panel) were used to calculate APO fluxes following eqn. 1.13 (middle panel). Note that positive APO fluxes indicate a net uptake of APO for the atmosphere.

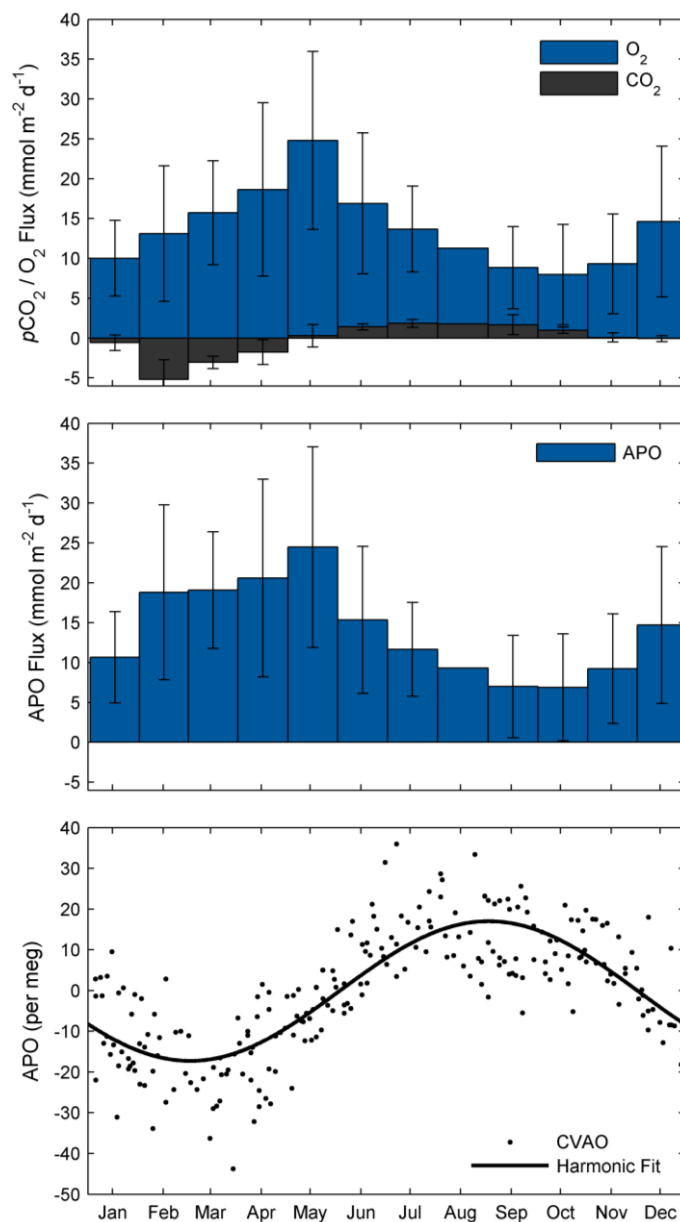


Figure 4.10 Concurrent determinations of ASE fluxes for CO_2 and O_2 (upper panel) were used to derive the seasonal distribution of related ASE fluxes for APO (middle panel). Measurements of APO performed at CVAO (lower panel) show a different seasonal pattern.

Distribution of APO clearly follows the seasonal distribution of O₂ ASE fluxes as expected. Data suggest a seasonal maximum in APO during spring followed by a decrease during summer towards a minimum in fall. When compared to APO measurements performed at CVAO a clear discrepancy between both records is obvious. Atmospheric APO measurement have a distinct maximum during fall and a minimum during spring, respectively. This apparent discrepancy might be due to the fact, that in general seasonal amplitudes of dissolved gases in the tropics are very small when compared to extratropical regions (Garcia and Keeling 2001; Takahashi et al. 2009). Such a seasonal variation in oceanic O₂ data might be difficult to detect, particularly when underlying data are sparse and don't cover the full seasonal cycle adequately. Furthermore, such low seasonal signals at CVOO might be suppressed by more pronounced signals originated somewhere along the footprint of the particular air mass (e.g., the Mauritanian upwelling with its undersaturated water masses for O₂ during winter months). Indeed, these air masses can be traced back to the west African coast and even to extratropical regions in the North Atlantic with more pronounced seasonal signals of O₂ ASE fluxes that might dominate APO measurements at CVAO.

However, the comparison of APO fluxes above shows that the present CVOO data set needs to be extended by more frequent observations with enhanced resolution in order to better assess APO at Cape Verde.

Net Community Production Estimates

The carbon data set presented above was also used to investigate processes other than ASE that also might affect the seasonal carbon cycle at CVOO. In order to determine such processes, *p*CO₂ data from float observations were converted into DIC concentrations as follows: TA values, derived from a well-defined salinity-temperature-alkalinity relationship for CVOO (section 4.2.1), were assigned to each float-borne *p*CO₂ measurement. Subsequently, employing equilibrium constants for the seawater carbonate system, as introduced in section 1.1, yielded high resolution data for DIC which are very well in accordance with discrete DIC samples (Figure 4.11).

Furthermore, in order to minimize variations in DIC due to water mass changes or precipitation/evaporation processes, DIC values were normalized (nDIC) to a constant mean ML salinity at CVOO of $S_M = 36.5$ psu as follows:

$$\text{nDIC} = S_M \cdot \frac{\text{DIC}}{S} \quad 4.2$$

Resulting normalized values for DIC show a distinct annual cycle which is presented in Figure 4.11. The nDIC variation over the year shows a mean peak-to-peak amplitude of $\sim 35 \mu\text{mol kg}^{-1}$ with its peak during spring months and a clear minimum during winter months. Comparable amplitudes of 25

and $45 \mu\text{mol kg}^{-1}$ were observed at ESTOC and BATS, respectively (Bates 2001; González-Dávila 2003). During summertime, when MLD shoals (Figure 4.11, lower panel), the DIC pool is characterized by a steady decrease which is also observed at other time series sites in the Atlantic and Pacific (Michaels et al. 1994; Bates et al. 1996; Dore et al. 2003).

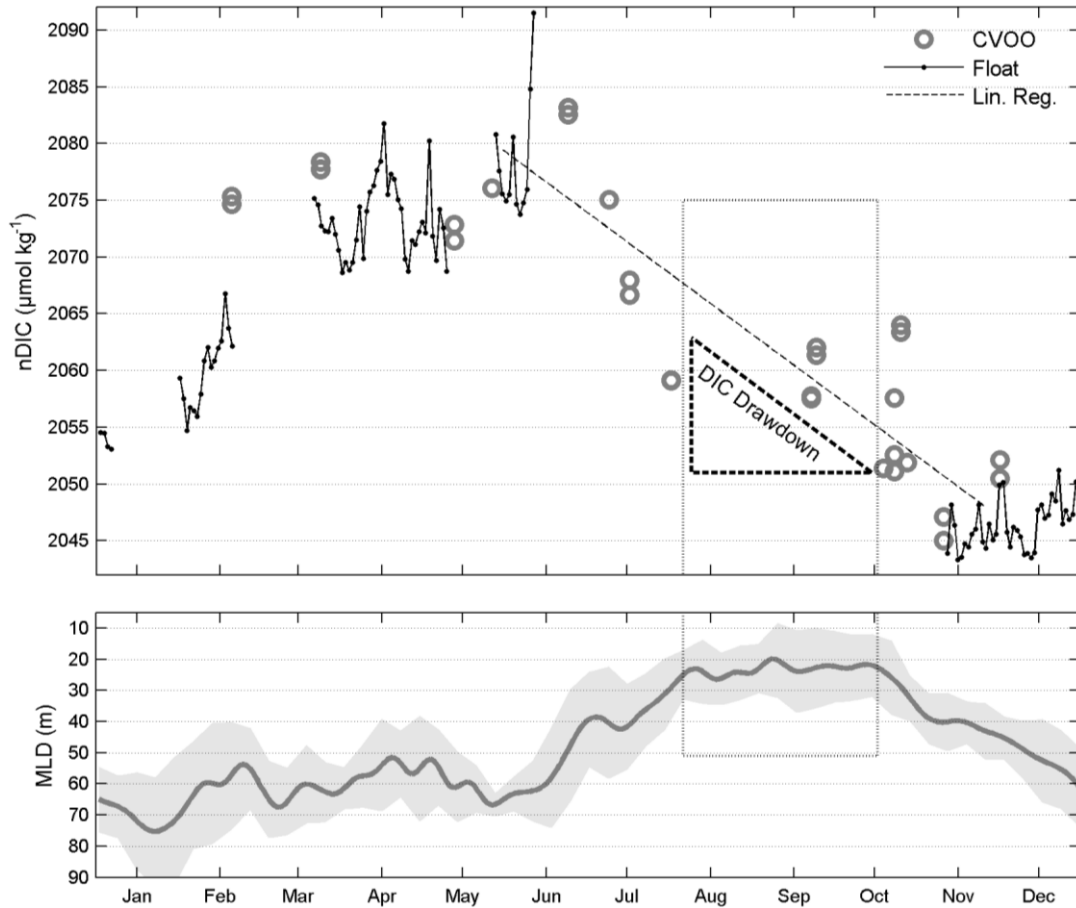


Figure 4.11 Seasonal distribution of salinity normalized DIC (nDIC) based on discrete samples as well as float-borne observations (upper panel). A linear regression (dashed line) was applied in order to estimate the mean summer drawdown in nDIC. Mean MLD (lower panel) was derived from 3 consecutive mooring deployments. The gray shaded area denotes inter-annual variations in MLD (RMSE) and the dotted box in both panels indicate the chosen period for further calculations (see text).

The observed seasonal changes in ML DIC can be described as a sum of the following processes:

$$\frac{\Delta n\text{DIC}}{\Delta t} = F_{\text{BIO}} + F_{\text{ASE}} + F_{\text{MIX}}, \quad 4.3$$

where F_{BIO} is the carbon flux driven by biological processes such as photosynthesis and respiration, F_{ASE} is the loss or gain of carbon via air-sea exchange, F_{MIX} is de- or entrainment of carbon by vertical or horizontal mixing and $\Delta n\text{DIC}/\Delta t$ is the change in nDIC over time.

In order to determine the magnitude of biological net community production (NCP) at CVOO, one needs to deconvolute observed changes in nDIC. A 1D box model approach was chosen in order to obtain NCP by separating F_{BIO} from other processes described by eqn. 4.3. The rectangle in Figure

4.11 denotes the season which has been considered for mass budget calculations. At this time of the year the water column is highly stratified and MLD is rather shallow and stable over this period (72 days). Thus, F_{MIX} is assumed to be a less significant driver for temporal changes in nDIC due to the absence of de- or entrainment fluxes between subsurface waters and the ML. However, two processes within F_{MIX} still remain: Diapycnal fluxes (F_{DIAP}) and horizontal advection (F_{HADV}). The latter one cannot be fully ruled out when using an Eulerian approach such as a (fixed point) time series station. However, strong horizontal gradients in DIC in the vicinity of CVOO during this season could not be observed on several cruises in that region, except for mesoscale features (section 4.2.2). Further, changes in salinity due to different water masses are accounted for by using nDIC instead of DIC. Thus, F_{HADV} is assumed to be negligible for this approach.

Since subsurface DIC concentration increases with depth the vertical carbon flux into the ML (as F_{DIAP}) can be calculated as follows:

$$F_{\text{DIAP}} = K_{\rho} \cdot \frac{\Delta \text{DIC}}{\Delta z}, \quad 4.4$$

where K_{ρ} is the mean diapycnal diffusivity for the open ocean in the ETNA region ($1 \cdot 10^{-5} \text{ m}^2 \text{ s}^{-1}$, Fischer et al. 2012) and $\Delta \text{DIC}/\Delta z$ a typical vertical DIC gradient at CVOO ($0.8 \mu\text{mol L}^{-1} \text{ m}^{-1}$). Positive fluxes describe a net flux into the ML, thereby increasing nDIC levels.

The seasonal variation of F_{ASE} for carbon was already described above and constitutes a net sink for the ML budget of DIC for that time of the year.

In order to close the mass budget for the chosen box the total drawdown of ML-integrated nDIC (mean MLD: 23 m) of -3.70 g C m^{-2} has to be corrected for F_{ASE} and F_{DIAP} (Figure 4.12). F_{ASE} compensated inventory loss yields a residual ML inventory drawdown of -2.33 g C m^{-2} . Further, a diapycnal flux (F_{DIAP}) of $+0.60 \text{ g C m}^{-2}$ from subsurface waters was calculated. Hence, nDIC drawdown due to F_{BIO} was found to be -2.93 g C m^{-2} for the 72 days lasting period. This yields an estimated NCP of $0.041 \text{ g C m}^{-2} \text{ d}^{-1}$ or $3.4 \text{ mmol C m}^{-2} \text{ d}^{-1}$, respectively.

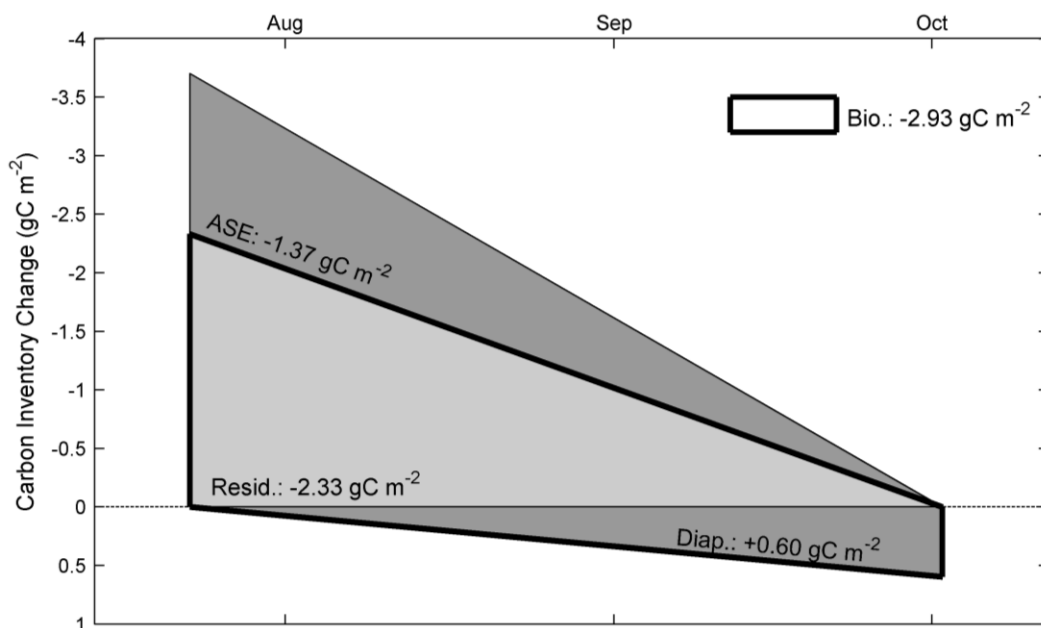


Figure 4.12 Schematic drawing of the 1D box model calculations. The observed total carbon inventory decrease over the 72 day lasting period was 3.70 g C m^{-2} . Over the same period a simultaneous increase of 0.60 g C m^{-2} due to diapycnal mixing was estimated to partially compensate the observed inventory change. Thus, after accounting for carbon loss due to ASE an overall biologically driven drawdown of 2.93 g C m^{-2} was found (see text).

A comparison with other oligotrophic time series stations in the Atlantic and Pacific shows a good agreement of NCP determined within the framework of this thesis (Table 4.1). However, one has to consider that water column properties at the sites are quite different (e.g. MLD) and thus depth integrated NCP values might vary. For instance, MLDs at CVOO were found to be rather shallow when compared to MLDs observed at ESTOC and thereby overall NCP at CVOO is lower than NCP values found at ESTOC. Nevertheless, the estimated mean daily rate for DIC drawdown at CVOO is $0.15 \mu\text{mol L}^{-1} \text{ d}^{-1}$ and very similar to rates observed at ESTOC ($0.12 \mu\text{mol L}^{-1} \text{ d}^{-1}$, González-Dávila et al. 2003).

Time Series Station	NCP ($\text{mmol m}^{-2} \text{ d}^{-1}$)	Method	Reference
Cape Verde Ocean Observatory (CVOO)	3.4	DIC drawdown	this study
Bermuda Time Series Station (BATS)	3.8 – 5.9	O ₂ /Ar	Luz and Barkan (2009)
Hawaii Ocean Time Series (HOT)	4.3 – 9.3	O ₂ /N ₂	Emerson et al. (2008)
European Time Series Station (ESTOC)	5.5 – 13.7	DIC drawdown	Neuer et al. (2007)

Table 4.1 Comparison of NCP rates for different oceanographic time series sites.

Due to a lack of data the recent NCP estimate provides only a snapshot of the seasonal cycling at CVOO. More data will be available in nearby future and thus allow a more accurate determination of processes affecting the carbon cycle at CVOO.

4.1.3 Diel Variability

High-frequency observations of O_2 concentration by means of autonomous instruments allow resolving variability patterns on short timescales. The newly developed in situ offset correction approach for O_2 measurements (section 2.3.2 and 3.2.2) features very precise ($\pm 0.3 \mu\text{mol kg}^{-1}$) O_2 measurements both in water (~ 30 cm beneath) and in air (~ 30 cm above sea level). Due to a float cycle time of 31 h, in-water measurements at the air-sea interface can be used to resolve diel concentration changes of O_2 over the course of D4 – D7. For this purpose, superimposed seasonal changes in O_2 were removed (detrending) and remaining O_2 concentrations were converted to $\Delta O_{2, \text{Detr}}$ in order to discard solubility driven variations in O_2 (eqn. 1.11). Resulting values for $\Delta O_{2, \text{Detr}}$ and temperature are shown in Figure 4.13 (left panels).

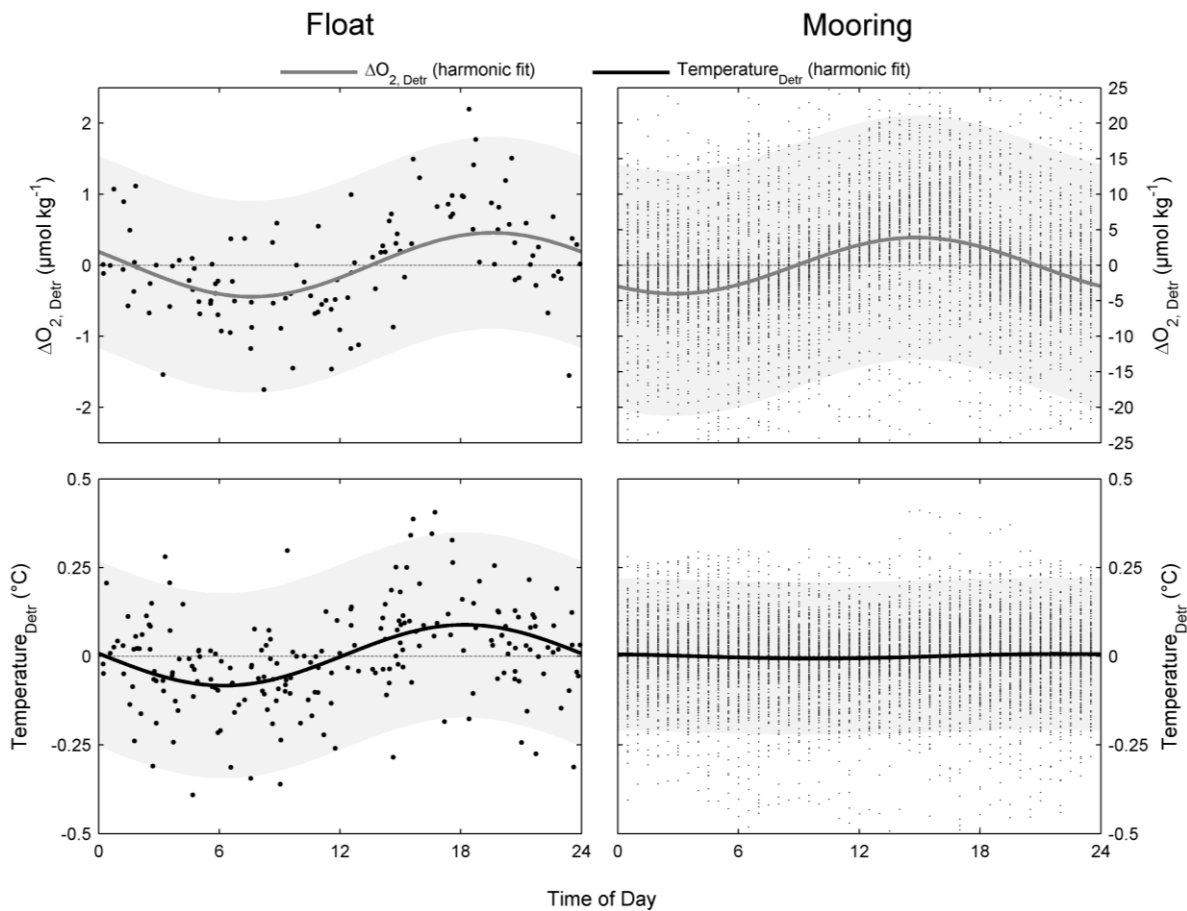


Figure 4.13 Diel Cycles for $\Delta O_{2, \text{Detr}}$ and ML temperature observed during float (left panels) and mooring (right panels) deployments. Solid lines denote the harmonic analyses of diel cycles and gray shaded area indicates the resulting 95% prediction intervals.

Obtained data were then fitted with the following harmonic function (Fourier-type) in order to derive a mean diel peak-to-peak amplitude for $\Delta O_{2, \text{Detr}}$:

$$\Delta O_{2,\text{Detr}}(t) = a + b \cdot \cos(t \cdot 2 \cdot \pi) + c \cdot \sin(t \cdot 2 \cdot \pi), \quad 4.5$$

where a , b , c are fitting parameters, t is time of day and $\Delta O_{2,\text{Detr}}$ is the final harmonic function describing the diel cycle.

Fitted data show a clear diel cycle for $\Delta O_{2,\text{Detr}}$ with a minimum in the morning due to net respiration and a maximum in the evening due to net production of organic matter. A peak-to-peak amplitude of $0.9 \mu\text{mol kg}^{-1}$ was found. For instance, diel cycles for O_2 in eutrophic upwelling regions (equatorial/coastal) were found to vary between ~ 4 to $\sim 40 \mu\text{mol kg}^{-1}$ (Steinhoff et al., unpublished data). Hence, observed diel $\Delta O_{2,\text{Detr}}$ changes at CVOO are at the low end of this range and close to the detection limit, as found for oligotrophic open ocean water masses (Lefèvre and Merlivat 2012). Changes in $\Delta O_{2,\text{Detr}}$ coincide with the diel cycle in temperature that occurs at least at the topmost part of the ML (Figure 4.13, left lower panel).

Furthermore, $\Delta O_{2,\text{Detr}}$ based on long-term mooring observations was taken for a comparison between the Lagrangian (float) and the Eulerian (mooring) approach. For this purpose O_2 measurements from an optode sensor deployed at a nominal depth of 54 m between Oct. 2009 and May 2011 were used. In order to discard O_2 data measured below the ML (MLD < 54 m) only those were taken that are in agreement with satellite SST measurements within $0.3 \text{ }^\circ\text{C}$ (AMSR-E). Following processing procedures as described above, the data show a distinct scattering compared to float-borne observations. A mean peak-to-peak amplitude of $7.9 \mu\text{mol kg}^{-1}$ for $\Delta O_{2,\text{Detr}}$ was found which is almost one order of magnitude higher than float-borne observations. The discrepancy between both observations remains unclear: High scattering of data due to potential mixing processes either occurring at the base of the ML or through horizontal advection of different water masses (Emerson and Stump 2010) might bias the harmonic analysis of small diel gradients. On the other hand, magnitude of biological production might be not homogeneously distributed through the ML. $\Delta O_{2,\text{Detr}}$ mooring observations are performed close to the base of the ML and thus close to the chl a maximum. In addition, measurements at this depth might be less affected by ASE. These circumstances could potentially lead to a stronger diel signal in O_2 than observed by the float at the upper end of the ML. However, this hypothesis can only be proven for robustness when time series records extend in future.

4.2 Subsurface Processes

4.2.1 Carbon and Oxygen Distributions

Measurements for DIC/TA, O_2 , temperature (T) and salinity (S) from various cruises were used to characterize water column structure that is characteristic of CVOO. Figure 4.14 illustrates the vertical distribution of these parameters, from surface to bottom.

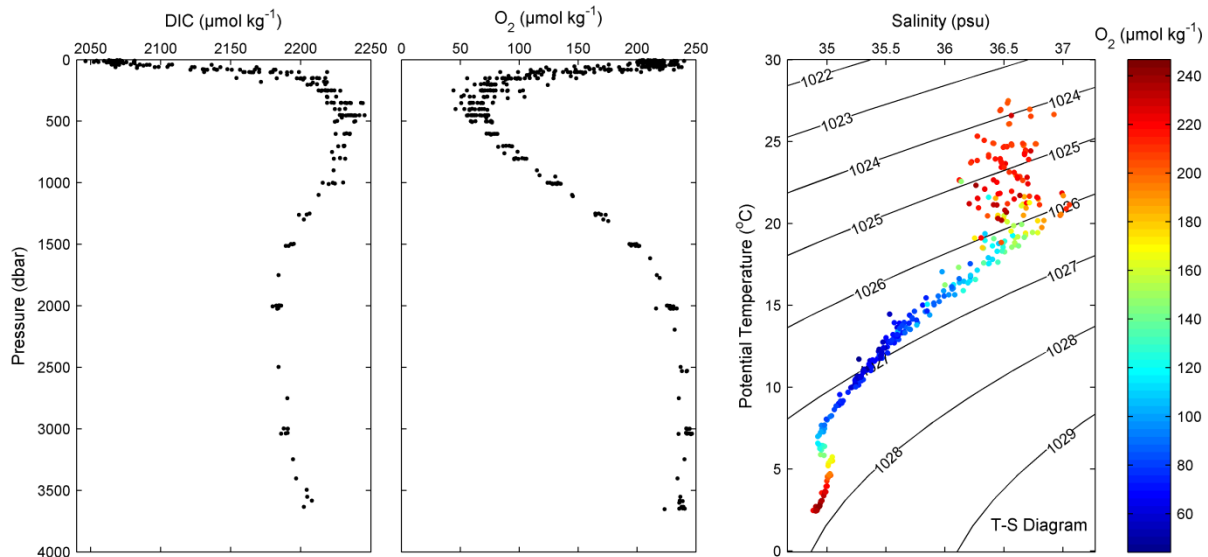


Figure 4.14 Cumulative vertical profiles for DIC and O_2 at CVOO between July 2006 and September 2012 (left and middle panel). Water mass properties observed at CVOO are illustrated as a T - S diagram with color-coded O_2 levels (right panel).

Strong vertical gradients are present in the upper ~ 250 m pointing to a distinct maximum in DIC and a minimum in O_2 , respectively, at 400 – 500 dbar. These pronounced peaks result from microbial respiration of organic matter produced above in combination with a comparatively poorly ventilated ocean basin (Stramma et al. 2005; Brandt et al. 2010). Minimum O_2 concentrations usually don't fall below a threshold of $\sim 40 \mu\text{mol kg}^{-1}$ in the ETNA region (Karstensen et al. 2008; Stramma et al. 2008). Far below the thermocline southbound NACW carries water masses with higher O_2 and lower DIC concentrations, respectively.

Measurements conducted by the 2G float (section 3.2.2) were used to highly resolve biogeochemical distributions in the upper 200 m of the water column. In order to obtain insights into the carbonate system based on float-borne $p\text{CO}_2$ measurements TA as a second carbonate system parameter was used for calculation of the remaining parameters. Therefore, a parameterization approach for TA was applied which describes TA as a function of T and S after Lee et al. (2006). Figure 4.15 shows TA, T and S data for the upper 500 m taken from the CVOO data set.

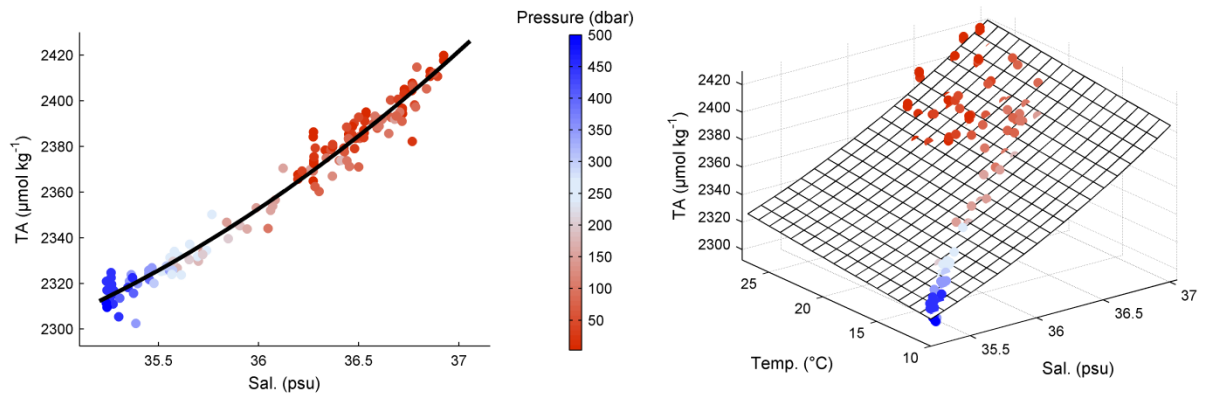


Figure 4.15 Illustration of the TA parameterization by means of T , S and TA measurements conducted at CVOO. A clear correlation was found (eqn. 4.6) within the upper 500 m of the water column.

A clear relationship between these variables was found that enables a robust calculation of TA for each float-borne $p\text{CO}_2$ measurement:

$$\begin{aligned} \text{TA} = & 2361 + 53.1 \cdot (S - 36) + 9.8 \cdot (S - 36)^2 \\ & + 0.9 \cdot (T - 18) + 4.0 \cdot 10^{-3} \cdot (T - 18)^2 \end{aligned} \quad 4.6$$

$$\begin{aligned} \text{RMS} &= 5.2 \mu\text{mol kg}^{-1} \\ n &= 141 \end{aligned}$$

Predicted TA concentrations for D4 – D7 are illustrated in Figure 4.16 (panel a) and show a highly dynamic distribution over the course of all deployments. Water masses high in TA denote high salinity waters originating from the North Atlantic subtropical gyre across the CVFZ.

Determinations of high resolution DIC and Ω_{Ar} distribution at CVOO were done using the parameterization introduced above, float-borne $p\text{CO}_2$ measurements and by employing equilibration constants for the carbonate system in seawater (section 1.1). Furthermore, the respiration index (RI) after Brewer and Peltzer (2009), being a proxy for physiological limits to marine life, was derived from float-borne $p\text{CO}_2$ and $p\text{O}_2$ measurements as follows:

$$\text{RI} = \log_{10} \frac{p\text{O}_2}{p\text{CO}_2}, \quad 4.7$$

Results for DIC, Ω_{Ar} , and RI are illustrated in Figure 4.16 (panel b – d). Vertical DIC patterns show a strong gradient between ML and subsurface waters with highest gradients up to $174 \mu\text{mol kg}^{-1}$ in the upper 200 m in Feb. 2011.

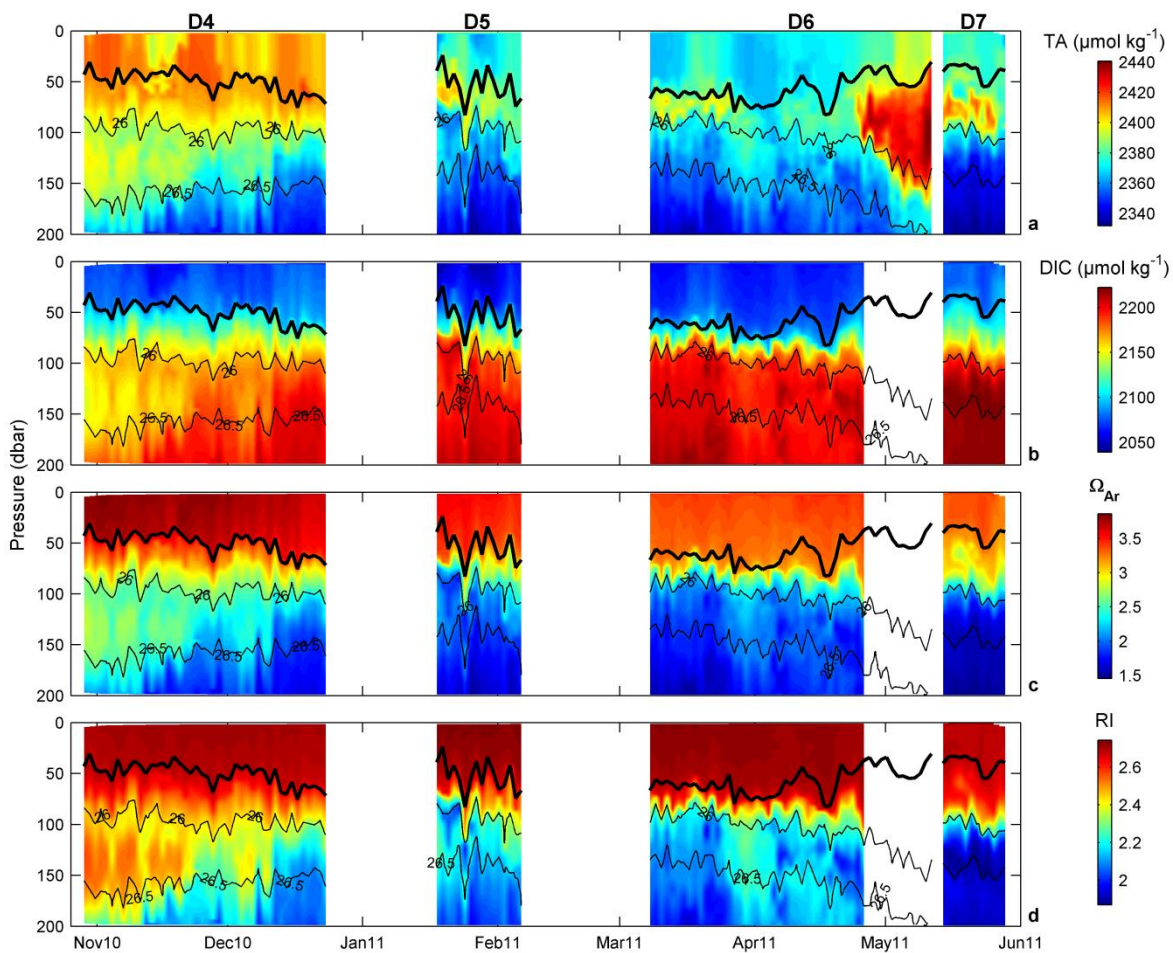


Figure 4.16 Computed components of the carbonate system (panel a – c) derived from the TA parameterization (Figure 4.15) and float-borne $p\text{CO}_2$ measurements in the vicinity of CVOO. The respiration index (RI) after Brewer and Peltzer (2009) was computed by means of $p\text{CO}_2$ and O_2 measurements (eqn. 4.7, panel d). Bold solid lines indicate MLD and thin solid lines isopycnals 26.0 and 26.5 (all panels).

Despite these gradients, subsurface waters show variability on both short-term and long-term scales. Fluctuation on timescales of days seems to be an artifact of ocean tides and internal waves, thereby lifting isopycnals up and down. At the beginning of D4 the water column was ventilated rather well when compared to remaining deployments. DIC concentrations, as well as $p\text{CO}_2$ and O_2 values (section 3.2.2, Fig. 5), below 90 m were closer to ML values as usual while MLD remained almost unchanged. These comparatively well ventilated water masses can also be found in Ω_{Ar} and RI. The latter clearly shows the absence of a distinct respiration signature. This feature originates from the North Atlantic subtropical gyre system across the CVFZ, as TA distribution (Figure 4.16, panel a) or T - S relationships (Figure 4.17) confirm. High salinity (and TA) waters with enhanced levels in O_2 are an indicator for this assumption (subducted Subtropical Underwater; Stramma et al. 2005). Similar observations were made, when the float crossed the CVFZ and entered the subtropical gyre at the end of D6 (refer to 3.2.2 for O_2 measurements). In general, the water mass distribution during D4 – D7 (Figure 4.17) essentially indicates a balanced presence of both NACW and SACW for subsurface layers.

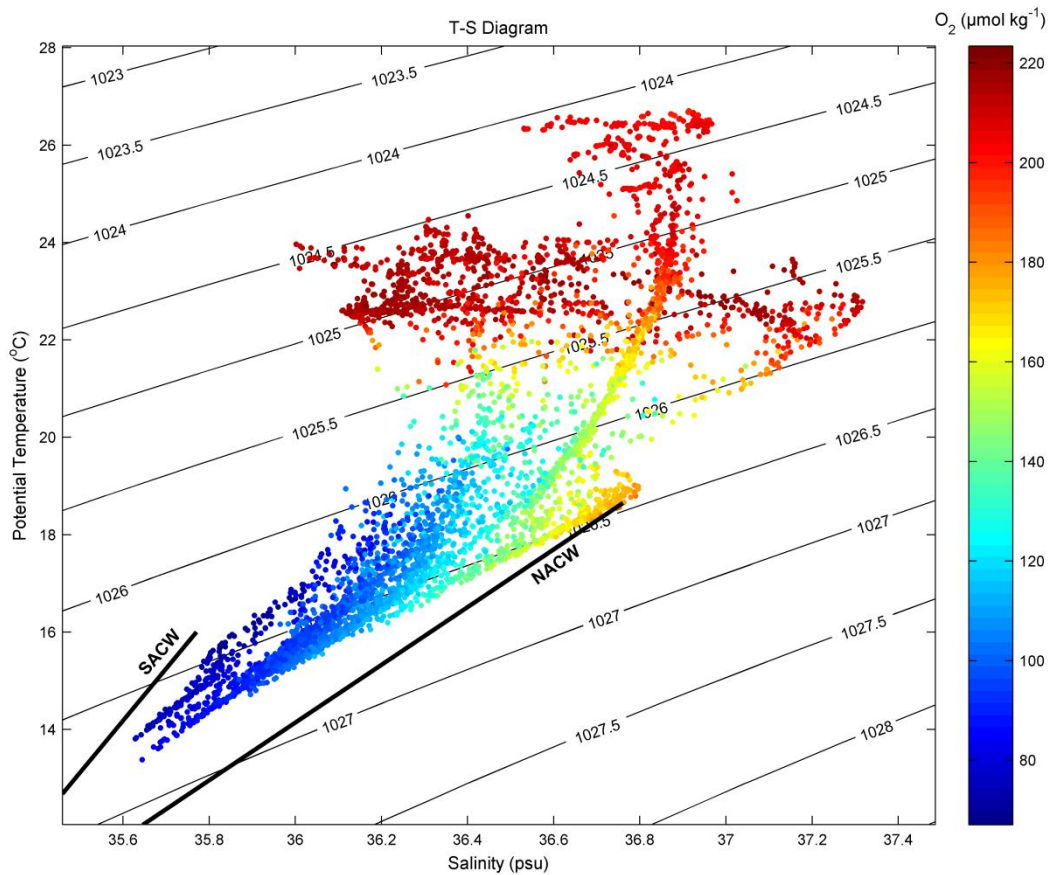


Figure 4.17 Water mass properties encountered during consecutive float deployments (T-S diagram). Straight black lines define typical water masses for that region after Tomczak (1981). Data are color-coded with O_2 concentrations. A general description of the oceanographic setting at CVOO is given in section 1.2.

However, intrusion of a well ventilated NACW water mass which must have crossed the CVFZ was found to affect carbon and oxygen water column (<200 m) inventories at CVOO (inventory data not shown here).

Overall, the combination of a robust TA parameterization with high resolution float-borne pCO_2 measurement enables comprehensive insights into the carbon cycle dynamics at CVOO.

4.2.2 Episodic Anoxic and Hypoxic Events [Manuscript C]

This chapter is based on a manuscript that has been submitted to *Nature*. Please refer to the manuscript list given at the outset of this thesis for more detail.

Citation: Karstensen, J., **B. Fiedler**, P. Brandt, R. Zantopp, J. Hahn, A. Körtzinger, M. Visbeck, G. Fischer, O. Melicio, and D.R. Wallace, 2012: Dead-Zone Eddies in the Tropical Eastern North Atlantic Ocean, *Nature*, under review.

Abstract

The amount of dissolved oxygen in seawater is of critical importance to nearly all marine life and biogeochemical cycling. As the supply of available oxygen drops below severely hypoxic levels ($<20 \mu\text{mol kg}^{-1}$), profound changes occur within the ecosystem, including alterations to microbial processes (Wright et al. 2012; Vaquer-Sunyer and Duarte 2008), the release of nitrogen (a greenhouse gas, Zehr 2009), and the establishment of inhabitable environments (Vaquer-Sunyer and Duarte 2008; Stramma et al. 2012). Therefore the detection of low oxygen environments and the full comprehension of their generation processes, from the large scale oxygen minimum zones (OMZ) to anoxic microenvironments in marine snow (Alldredge and Cohen 1987), is of major interest. Here we report on the first-ever detection of unexpected low oxygen levels in the open waters of the eastern tropical North Atlantic Ocean. These very low oxygen concentrations represent dead-zone environments (Diaz and Rosenberg 2008) embedded in dynamically isolated open-ocean eddies. Respiration and carbon export rates in the eddies are elevated and comparable to those found in highly productive eastern boundary upwelling regions. The evidence shows that mobile macroorganisms actively avoided entering the hostile environment. These dead-zone eddies are a mesoscale representation of the major OMZs and must be fully considered when interpreting and modelling the functionality of biogeochemical cycling and marine ecosystems of the tropical eastern North Atlantic.

C.1 Dead-Zone Eddies in the Tropical Eastern North Atlantic Ocean

For the open eastern tropical North Atlantic (ETA) OMZ region, minimal oxygen concentrations of only little below $40 \mu\text{mol kg}^{-1}$ have been reported in the past (Stramma et al. 2009; Karstensen et al. 2008). Based on these observations, the region is considered 'hypoxic', indicating a limitation on biodiversity primarily driven by avoidance or increased mortality (Wright et al. 2012; Vaquer-Sunyer and Duarte 2008). As such, the low oxygen tipping points which are reached in the major OMZs of the eastern Pacific Ocean, northern Indian Ocean, and eastern South Atlantic Ocean (Lam et al. 2009; Kuypers et al. 2005) did not apply to the present ETA OMZ. These tipping-points include: oxygen concentrations below $20 \mu\text{mol kg}^{-1}$ ('severe hypoxia'), where mass mortality of fish has been reported (Diaz and Rosenberg 2008) and where microbes begin to utilize nitrate for respiration via the anammox process (Wright et al. 2012; Kalvelage et al. 2011); oxygen concentrations below $5 \mu\text{mol kg}^{-1}$, where microbes undergo a second nitrate utilization process, known as denitrification (Wright et al. 2012; Kalvelage et al. 2011), which is of fundamental importance for the release of the nitrogen gas; and oxygen concentrations below $1 \mu\text{mol kg}^{-1}$ which characterize 'anoxia' and where only specifically adapted microbes can exist (Wright et al. 2012).

In shallow (less than a few 100 meters), semi-enclosed coastal areas, severe hypoxia and anoxia have been reported in the context of dead-zones, also for the ETA (Diaz and Rosenberg 2008). Dead-zones are created by intense phytoplankton blooms stimulated by intermittent nutrient input. After the bloom, the algae die and sink as particulate material to the sea-floor where oxygen is respired through enhanced microbial activity. So far the open ocean has been excluded from possible dead-zone formation mainly because (i) ocean transport processes supply sufficient oxygen to balance the water-column oxygen utilization by respiration, and (ii) the sea-floor, as a boundary where particulate material accumulates and respiration increases, is far away from the euphotic zone.

Dynamically created boundaries exist in the open ocean along frontal zones and within mesoscale (~ 10 to 150 km diameter) ocean eddies. Eddies are of particular interest because they not only create a boundary but, given a sufficiently strong rotational speed, isolate their water mass within from the surrounding waters (Chelton et al. 2011b; Early et al. 2011). This isolation preserves and generates anomalies (Chelton et al. 2011b; Lukas and Santiago-Mandujano 2001; Menkes et al. 2002; McGillicuddy et al. 2007) which may also have an integrated impact on the large-scale ocean (Falkowski et al. 1991; Oschlies and Garcon 1998; Chelton et al. 2011a).

An unexpected low oxygen event was detected in an oxygen time series (Figure 4.18a) record from a deep-sea mooring, located about 100 km north-east of the Cape Verde Islands. For most of the deployment period the oxygen concentrations at nominal 45 m depth were within 10% of air

saturation values, indicating that the sensor was placed within the well-mixed upper layer (ML). In February 2010, a dramatic drop in oxygen concentrations occurred, lasting for about 1 month, and reaching anoxic levels ($<1 \mu\text{mol kg}^{-1}$). Additional sensors report colder and less saline (Figure 4.18b) waters during the event, accompanied by strong and reversing meridional flow over the top 350–400 m (Figure 4.18c).

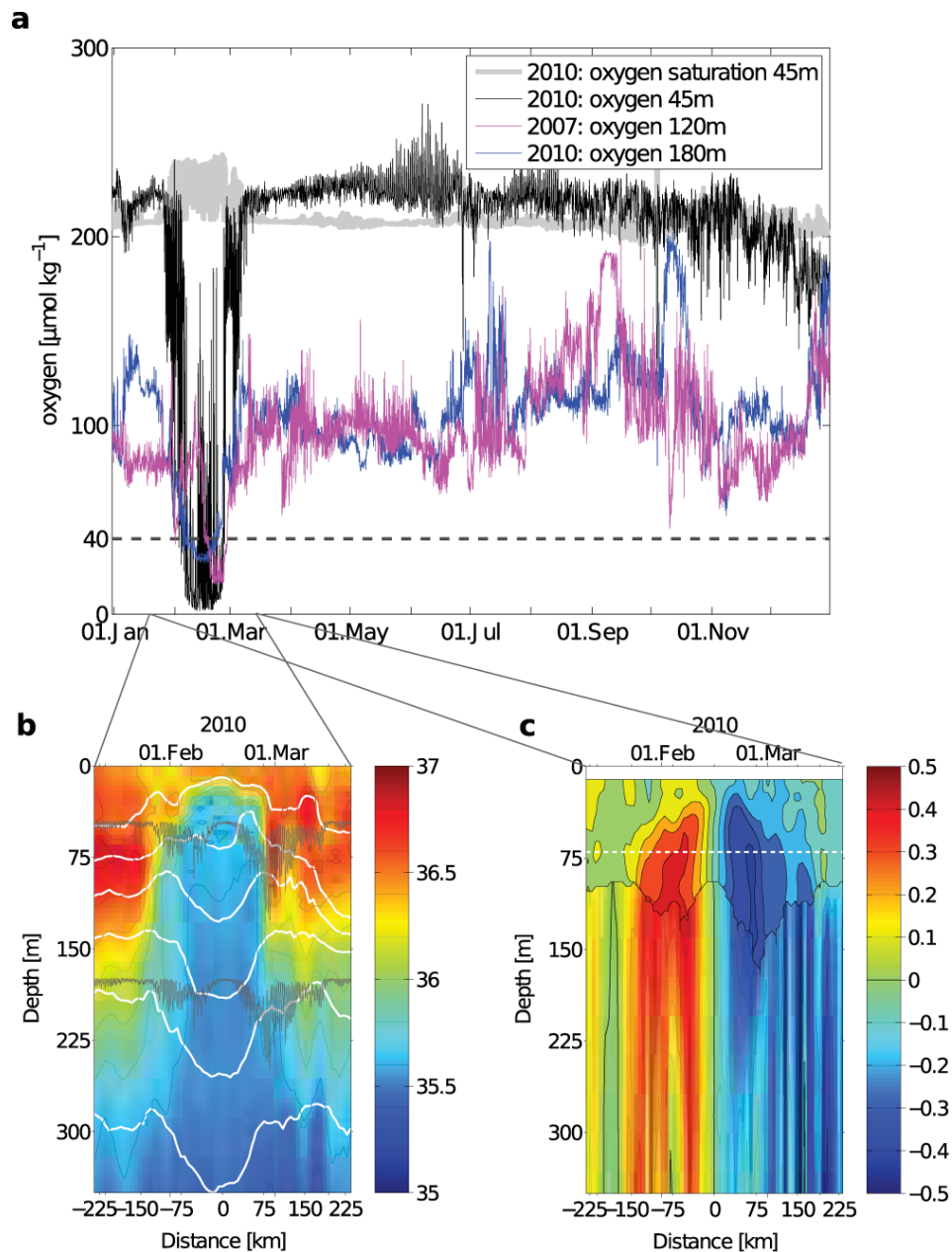


Figure 4.18 (a) Annual time series of observed oxygen concentration (black, blue, magenta lines) and calculated oxygen saturation (gray line) at the Cape Verde Ocean Observatory mooring site. The broken horizontal line indicates the so far lowest reported oxygen concentration (Stramma et al. 2009). (b) Vertical salinity structure shortly before, during and shortly after the passage of the ACME (grey lines indicate varying depth of 2010 oxygen sensors shown in (a)) (in PSS-78). Selected potential density anomaly surfaces are shown as white contours. (c) Meridional velocity during the time period shown in (b) (in m s^{-1}). The upper part (approx. 100 m) are direct observations obtained from a current profiler, the part underneath is the geostrophic velocity derived from the density field and referenced to the observed currents at 75m depth.

The flow direction and the orientation of the density surfaces revealed the passage of a mode-water type anticyclonic eddy (ACME). A second oxygen sensor at about 180 m depth recorded oxygen concentrations of less than $30 \mu\text{mol kg}^{-1}$, still significantly lower than historical records (Stramma et al. 2009). Almost exactly 3 years before, in February 2007, a single oxygen sensor installed at the same location but at about 120 m depths, recorded concentrations down to about $15 \mu\text{mol kg}^{-1}$, indicating severe hypoxia. This event was initially interpreted as a calibration problem of the oxygen sensor, however, in combination with the subsequent 2010 event, and considering that hydrography and meridional flow also indicate the passage of an ACME, we now consider the signal to be real.

The pathways of the two ACMEs were reconstructed using satellite altimeter sea level anomaly (SLA) data. A first clear signatures of both eddies were detected in the boundary current region, off Mauritania, at approximately 18°N , 16°W in boreal summer 2006 and 2009, respectively. The zonal propagation was surprisingly constant at about 5 to 6 cm s^{-1} suggesting the 'beta effect' (Van-Leeuwen 2007) to be the primary driver. The average SLA signature was about $+5 \text{ cm}$ and the eddy radius was about 70 km which implies a geostrophic flow of about 0.20 m s^{-1} , in agreement with the observed currents.

Another case of very low oxygen concentrations ($<20 \mu\text{mol kg}^{-1}$) was observed in a cyclonic eddy (CE) by an Argo float. The float measured temperature, salinity, oxygen (Figure 4.19a) and particle concentration.

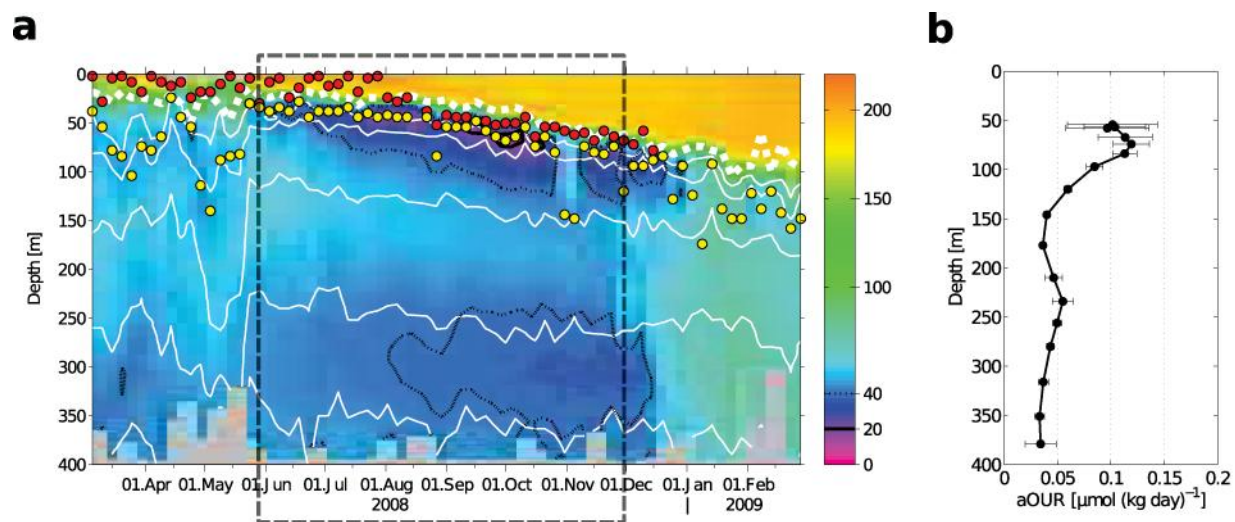


Figure 4.19 (a) Oxygen concentrations sections constructed from 5-day profiling float data (in $\mu\text{mol kg}^{-1}$). The black box indicates the period when the float was trapped in the CE. Red dots indicate depth of maximum particle concentration, yellow dots the depth of minimum oxygen. The thick white dashed line indicates the depth of the MUL. Potential density anomaly between 26.1 and 27.1 kg m^{-3} in 0.2 kg m^{-3} increments are shown as white contours. (b) Average profile of the apparent oxygen utilization rate for the period when the float was trapped in the CE. To take into account the deepening of the isopycnals along the float path, calculations were done in density classes and subsequently converted back to depth using the mean density profile recorded in the CE.

After deployment in the Mauritanian upwelling region in February 2 2008, the float started to move north-westward, into the open ETA OMZ region in May 2008. The SLA along the float trajectory revealed that the float was caught in a CE. The average SLA signature was similar to the ACMEs reported above but of opposite sign. During the following 6 months, the float surveyed the eddy by profiling every 5 days. Lowest oxygen concentrations in the eddy were found about 20 to 30 m below the base of the ML, underneath the depth of maximum particle concentration. A rather steady deepening of the ML occurred from about 30 m in May 2008 to 80 m in December. As the vertical integral of density in the upper 100 m did not show an increase concurrent with the deepening of the ML, surface buoyancy forcing cannot be the primary driver for the deepening. The oxygen minimum deepened along with the ML deepening.

The float-based oxygen profile time series was used to derive oxygen utilization rates (OUR) by calculating the oxygen decrease between successive dives (Figure 4.19b). High OUR, up to $0.15 \mu\text{mol kg}^{-1} \text{day}^{-1}$, were found just below the ML where the particle concentration maximum was also observed. Even at deeper levels, the OUR was about three times higher than typical rates for the thermocline (Jenkins 1982; Karstensen et al. 2008). Via a Redfield-type stoichiometric ratio (Körtzinger et al. 2001), the OUR was converted to carbon remineralization rates (CRR) and a carbon export flux of $0.24 \pm 0.07 \text{ g C m}^{-2} \text{day}^{-1}$ out of the euphotic zone ($\sim 100 \text{ m}$ in depth) was estimated (Jenkins 1982; Martin et al. 1987). The flux is comparable to what is reported for eastern boundary upwelling regions (Messié et al. 2009). Anomalous high sediment trap catches at the mooring were also found during the ACME passage in 2010. Assuming export flux to balance net community production (NCP) in the euphotic zone, the NCP is comparable to what has been reported for the Mauritanian upwelling region (Martin et al. 1987; Messié et al. 2009; Steinhoff et al. 2012). Again using a Redfield-type stoichiometric ratio (Körtzinger et al. 2001) a total draw-down of nitrate concentrations by about $12 \mu\text{mol kg}^{-1}$ over the 6 months was calculated, comparable to surface nitrate concentrations in the Mauritanian upwelling region (Minas et al. 1982; Loucaides et al. 2012). This indicates that solely the upper layer nutrient content in the eddy source region (Mauritanian upwelling) is sufficient to support the observed productivity.

The sluggish background flow in the eastern boundary region of the ETA (Lumpkin and Garzoli 2005) supports the existence of isolated eddies (Chelton et al. 2011a,b; Early et al. 2011), even if the eddies we observed have rather low rotational speeds ($\sim 0.2 \text{ m s}^{-1}$) when compared to global statistics (Risien and Chelton 2008; Chelton et al. 2011b). Isolated eddies allow only minimal lateral exchange to occur and thus make respiration more efficient in lowering their oxygen concentrations. It is for this reason that we term this isolated eddies 'dead-zone eddies' because they depict a semi-enclosed

environment as for coastal ocean dead-zones (Diaz and Rosenberg 2008; Vaquer-Sunyer and Duarte 2008).

The eddy rotation has also an impact on the efficiency of the momentum flux acting at the eddy surface (McGillicuddy et al. 2007). Based on typical wind speeds (7 m s^{-1} ; Risien and Chelton 2008) and SLA-derived surface velocities ($\sim 0.2 \text{ m s}^{-1}$), an upwelling (downwelling) of 70 m y^{-1} is expected for the ACME (CE). This wind-induced up/downwelling can explain the difference in the efficiency of oxygen removal in ACMEs compared to CEs: The upwelling within an ACME will maintain a ML base at constant and shallow depth throughout the eddy lifetime. Consequently the zone with highest respiration remains at a constant depth (just below the ML base) and oxygen removal is particular efficient here, creating an anoxic zone. The situation in a CE differs since the eddy/wind-driven downwelling weakens the initial, rotation-induced upwelling. In response, the ML base is slowly lowered to deeper levels and, with this relocation of the ML, the layer of maximum particle concentration moves to deeper depths. Light availability at the ML base will decrease and as such productivity, particle concentration and in turn respiration. Moreover, the deepening of the ML will successively entrain water from the oxygen minimum into the ML and convert the layer underneath into the new oxygen minimum. This mechanism prevents the development of anoxia in CE.

The population of dead-zone eddies in the ETA OMZ region is difficult to assess and as such their integral effect. Inspection of SLA variability along 18°N , where the ACMEs and the CE reported here originated, suggests that perhaps two to three dead-zone eddies are generated every year at this latitude. They carry an extreme signature into the open ETA OMZ region and as such provide a threat to an ecosystem that, in contrast to the intense OMZ of the Pacific and Indian Ocean, is not adapted to such low oxygen concentrations. Acoustic backscatter data from the mooring shows a striking absence of scatterers within the ACME and right below the ML (Figure 4.20), suggesting that all zooplankter abruptly stopped their natural diurnal migration to avoid entering the eddy interior.

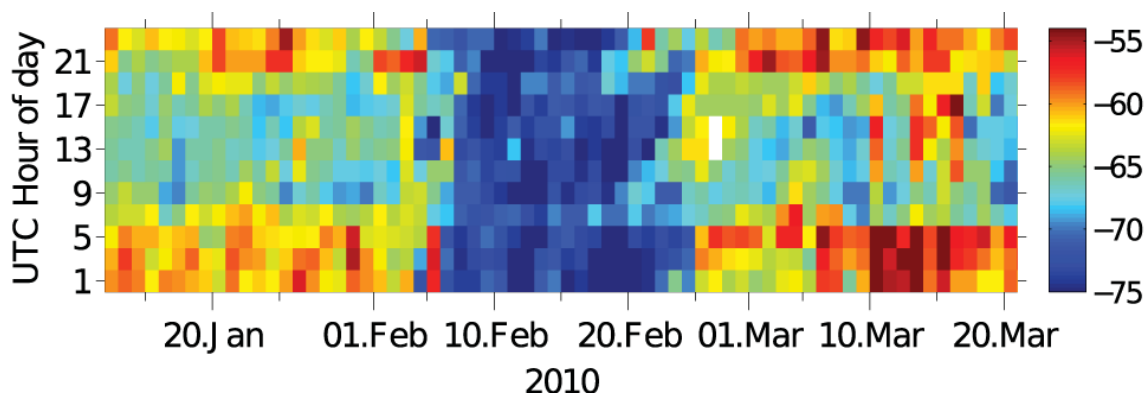


Figure 4.20 Time series of target strength at 65 m depth calculated from the acoustic current profiler data at the Cape Verde Ocean Observatory mooring site and plotted against hours of the day (in dB). Minimal target strength during all hours between 8th and 25th February 2010 coincide with the passage of the anoxic ACME.

It is not unrealistic that a dead-zone eddy could 'strand' on islands, such as the Cape Verdes. Here, and in many other coastal regions, there have been numerous reports of sudden and unexplained fish death. The fatal features carried by eddies, such as those reported here, may provide an answer to these baffling questions.

In general our findings underline the importance of differentiating the three types of eddies (CE, ACME, and classical anticyclones) when discussing the effect of eddies on the oceanic ecosystem. Such classification must be considered in eddy parametrization algorithms that are widely used in numerical ocean models with non-eddy-resolving grid spacing. It also suggests that the use of a bulk eddy-kinetic energy may not be sufficient to study the effect of eddies on productivity, e.g. in eastern boundary upwelling areas. Clearly an open question is the eddy generation process in the ETA OMZ region. Our study shows that both, CE and ACME, have similar regions of origin. For the tropical eastern Pacific, so-called eddy generation 'hot spots' have been identified and related to topographic features along the coast in combination with wind patterns and topographic waves (Willett et al. 2006). In this context it is also important to understand the processes that control the generation process of either an ACME or a classical anticyclone.

Acknowledgements:

We thank A. Oschlies for comments on the manuscript. Financial support is acknowledged from: the European Commission for FP7 GROOM (284321), FP7 EuroSITES (202955), and FP7-CARBOOCEAN (264879); the DFG for Collaborative Research Centre 'SFB 754'; the BMBF for SOPRAN (03F0462A). CVOO is part of the OceanSITES network. SLA data was produced by Ssalto/Duacs and distributed by Aviso (www.aviso.oceanobs.com/duacs/). MyOcean products have been used. Argo float data is available from Coriolis data centre (www.coriolis.eu.org).

Author Contributions:

J.K. manuscript writing, J.K., P.B., A.K., G.F., O.M., D.R.W., and M.V. design observations, B.F., J.K., R.Z, J.H. data processing. All authors discussed the results and commented on the manuscript.

Methods Summary:

Oxygen measurements at the CVOO mooring were done with AADI Aanderaa oxygen optodes (type 3830). A calibration was done against CTD/oxygen sensor (Sea-Bird Electronics 43 Clark electrode) data for the deployment period from 2009 to 2011 before and after the deployment phase. For each optode, 17 independent calibration points were obtained, choosing locations with weak vertical

oxygen gradient. A lab calibration at zero oxygen concentration was also performed by submerging the optodes into a sodium sulfite solution. All calibration points were used to derive a final calibration equation, while the chemically forced (and thus more precise) zero oxygen calibration was weighted three times higher than the CTD/oxygen cast references. The difference between calibration point observations and calibrated optode suggests an overall rms error of $3 \mu\text{mol kg}^{-1}$. Comparison of the chemically forced zero oxygen phase data and the phase readings during the anoxic event suggests a higher accuracy of about $1 \mu\text{mol kg}^{-1}$. Pressure and salinity variability was corrected according to the Aanderaa manual.

The PROVOR Profiling Argo Float (WMO 6900632) was equipped with a CTD (Sea-Bird Electronics 41CP), an oxygen optode (similar to CVOO mooring), and a transmissometer (WETLabs CRV5). The float acquired vertical profiles at 5dbar resolution between 400 db and the surface every 5 days. The oxygen concentrations were corrected for salinity and pressure effects. DO data were compared to a CTD/oxygen cast taken next to the deployment location and suggested an accuracy of $5 \mu\text{mol kg}^{-1}$. The transmissometer data was corrected for biofouling by subtracting the minimum beam attenuation value of each profile.

Eddy tracking was based on 7-day merged sea level anomalies data provided by Aviso, using subjective visual tracking only, without any automatized tracking algorithms. The ACMEs at CVOO were tracked starting at the mooring position at the time the ACMEs appeared. The CE was tracked until the moment the float reported warmer and less salty water.

5 Conclusions & Outlook

The major goal of this thesis was to better observe, describe and understand the exchange of CO₂ and O₂ between the atmosphere and the ocean in the ETNA. This was addressed on the one hand by pursuing new methodological pathways (e.g., autonomous platforms for biogeochemical observations) and on the other hand by establishing laborious time series measurements at Cape Verde (e.g., monthly samplings for biogeochemical parameters). Hence, a short summary of major achievements made over the course of this thesis is listed below, first highlighting technical and then scientific results. Finally, a proposed perspective for future work is given at the end of this chapter.

- Evaluations of novel submersible CO₂ sensors (PSI CO₂-Pro and CONTROS HydroC) have been successfully performed in underway operation during ANT-XXVI/4 and MSM-18/3 cruises. Comparisons with established methods (GO *p*CO₂ system, discrete DIC/TA samples) have revealed major differences between both sensors in terms of measurement accuracy and robustness.
- The PSI CO₂-Pro sensor showed an inconsistent accuracy pattern of 1–15 µatm (RMSE: 12.3 µatm) over the entire cruise which was driven by SST. Temperature stabilization of the NDIR detector was insufficient and deviated up to 1.5°C from the preconfigured temperature (55°C). Thus, the sensor accuracy turned out to be highly sensitive to ambient temperature gradients which alter the overall sensor accuracy significantly.
- In contrast, measurements of the HydroC during sensor evaluation cruises demonstrated very reliable measurements (RMSE: 3.7 µatm) that were not affected by environmental conditions. Signal drift of the HydroC was comprehensible and could be compensated for by pre- and post-calibrations in combination with thoroughly post-processing of sensor data.
- Over the course of this thesis prototype profiling floats for each type of the evaluated *p*CO₂ sensors were developed in collaboration with a German manufacturer. Both floats were successfully field tested at CVOO prior to regular deployments.
- The 1G Float (PSI CO₂-Pro) was operating in three consecutive deployments yielding 92 profiles in total. Measurements of *p*CO₂ were conducted discontinuously on three certain depths during ascent, as sensor response time turned out to be too slow for continuous profiling. A strong response time dependence on hydrostatic pressure further hampered a continuous profiling approach for the 1G float.
- The 2G float was equipped with a HydroC sensor and was operated during 4 consecutive deployments at CVOO. A total of 123 vertical profiles were obtained covering a semi-annual biogeochemical cycle at CVOO. First-ever continuous *p*CO₂ profiles on an autonomous profiling platform were achieved. Comparison of float data with available reference data at

CVOO as well as profiling tests of the HydroC during MSM-18/3 provided evidence for an overall accuracy of float-borne $p\text{CO}_2$ data within 10 – 15 μatm for subsurface and 5 μatm for surface measurements, respectively.

- Oxygen measurements on the profiling float were performed for the first time with a new model of the Aanderaa optode sensor (Model 4330) which was thoroughly calibrated in the laboratory prior to deployment. In order to ensure high accuracy for measurements of small O_2 gradients between the surface ocean and the atmosphere an elaborate in situ offset correction was developed and applied. Oxygen measurements were performed in the surface ocean and the overlying air (typically 30 cm above and below the air-sea interface). The resulting precision was found to be 3.2 $\mu\text{mol kg}^{-1}$ for in-air and 0.3 $\mu\text{mol kg}^{-1}$ for corresponding in-water oxygen measurements. An overall accuracy of 2 $\mu\text{mol kg}^{-1}$ was achieved. Sensor data are well in agreement with reference (Winkler) data.
- Beside float-based observations, time series measurements of biogeochemical parameters (e.g., DIC, TA, O_2 , etc.) at CVOO were established successfully. A composite data set was obtained which consists of data from site occupations by regular monthly cruises (R/V Islândia) and numerous international research expeditions (SOPRAN, SFB754, OCEANET) as well as float operations in the vicinity of CVOO. Data cover, albeit with significant data gaps, a time range from 2006 until 2012 and allowed first detailed insights into seasonal variability of O_2 and CO_2 . Both O_2 and $p\text{CO}_2$ data from float observations match remarkably well with the remaining data set.
- By combination of atmospheric (CVAO) and oceanic (CVOO) observations, first assessments of seasonal cycles for O_2 and CO_2 ASE fluxes for this region were done. Continuous O_2 supersaturation of the surface layer drives a permanent outgassing over the year ($5.0 \pm 2.5 \text{ mol m}^{-2} \text{ yr}^{-1}$) with slightly elevated fluxes during May and lowest values during October. In contrast, CO_2 fluxes show a pronounced uptake of atmospheric CO_2 during winter/spring which turns into a moderate outgassing during early summer/spring. On an annual scale in- and outgassing was found to be nearly balanced with a net CO_2 flux of $-0.08 \pm 0.32 \text{ mol m}^{-2} \text{ yr}^{-1}$. Seasonal distribution of CO_2 fluxes are in overall accordance with climatology data. However, CVOO data revealed a rather slight net sink for atmospheric CO_2 whereas climatology data suggests a weak source.
- Fluxes for APO were derived from corresponding O_2 and CO_2 fluxes and compared to those measured at CVAO. APO fluxes derived from CVOO data showed a distinct maximum during spring and a minimum during fall whereas data from CVAO shows a reverse seasonal cycle. Thus, atmospheric APO signatures at Cape Verde were found to be rather affected by other oceanic regions along the air mass trajectory (e.g., the Mauritanian upwelling).

- DIC data calculated from float-borne $p\text{CO}_2$ measurements were further used to close the seasonal DIC cycle at CVOO. Highest concentrations of DIC are regularly observed during winter/spring months after entrainment of subsurface waters during winter mixing. A steady decrease of DIC during summer months is followed by a pronounced minimum during fall/winter. The summer decrease in DIC of $\sim 35 \mu\text{mol kg}^{-1}$ mainly coincides with shallow MLD. Mass budget calculation revealed this decrease to be driven mainly by NCP ($\sim 79\%$) and to a lesser extent by ASE ($\sim 21\%$). Overall, NCP derived from mass budget calculations was found to be $3.4 \text{ mmol C m}^{-2} \text{ d}^{-1}$ which is in accordance with NCP estimates at other oligotrophic open ocean time series sites.
- High frequency variations in O_2 in the ML were observed by two independent measurement approaches at CVOO. The novel in situ offset correction performed on the 2G float enabled highly precise measurement of O_2 in the upper 30 cm of the water column. A profiling interval of 31 h allowed resolving mean diel cycles over the course of all deployments. A diel peak-to-peak amplitude of $\sim 0.9 \mu\text{mol kg}^{-1}$ was observed. In contrast, O_2 measurement at the base of the ML ($\sim 45 \text{ m}$) performed on the long-term mooring at CVOO revealed a more pronounced diel cycle of $\sim 7.9 \mu\text{mol kg}^{-1}$.
- Independent autonomous O_2 measurements in the ETNA have revealed the existence of hypoxic ($\sim 20 \mu\text{mol kg}^{-1}$) and even anoxic ($< 1 \mu\text{mol kg}^{-1}$) water masses just below the ML in the open North Atlantic Ocean. In general, the OMZ of the ETNA is known to be rather well ventilated with O_2 levels usually not much less than $40 \mu\text{mol kg}^{-1}$. The oxygen depleted water masses were found to be isolated and transported by mesoscale eddies which originated in the coastal Mauritanian upwelling and propagated westwards. Obtained data suggest that the eddies' subsurface layers were subject to intensified respiration (up to $0.15 \mu\text{mol O}_2 \text{ kg}^{-1} \text{ d}^{-1}$) due to high payloads of organic matter resulting in strong hypoxic and anoxic conditions. A carbon export flux of $0.24 \pm 0.07 \text{ g C m}^{-2} \text{ day}^{-1}$ out of the euphotic zone was determined for the hypoxic cyclone.

The present thesis provides a comprehensive description of ASE fluxes for CO_2 and O_2 in the ETNA on different timescales and how progress was made towards this assessment. In chapter 3.1 novel instrumentation for in situ $p\text{CO}_2$ measurements was evaluated. Underway measurements during two expeditions turned out to be a suitable platform for precise field evaluation of new sensor technique. Application of these sensors as part of the development of profiling float prototypes was shown in chapter 3.2. Here, the successive development of the float platform led to major improvements of the prototypes resulting in the first-ever high resolution $p\text{CO}_2$ profiles performed on a profiling float.

Results of the in-air O₂ measurements on the prototype float have shown that highly accurate O₂ measurements at the air-sea boundary were possible, facilitating an accurate determination of O₂ ASE fluxes on unattended platforms.

Chapter 4.1 presented a broad overview of achieved results gained from different observational perspectives. First results of the established time series observations were combined with high resolution observations of the developed float platform. It was clearly shown that both ship-based time series and float measurements could be combined with each other in a highly consistent manner which helped to better resolve and understand seasonal variations in the carbon cycle at CVOO.

The need for highly resolved in situ observations of biogeochemical parameters in space and time was emphasized by findings presented in chapter 4.2.2. Detecting, and more importantly, understanding the presented anoxic and hypoxic water masses in the ETNA was only made possible by means of novel autonomous O₂ measurements on both a mooring and a float platform. Evidence was provided for episodic existence of anoxic and hypoxic mesoscale features in the vicinity of CVOO which must be fully considered when interpreting and modeling the functionality of biogeochemical cycling in the ETNA region.

The scope of this thesis covered both classical as well as novel methods for investigating biogeochemical processes in the ocean. Novel autonomous platforms and sensor technology will become more important in future chemical oceanography in order to fully understand biogeochemical processes that occur on various spatial and temporal scales. Findings presented in chapter 3.2.2 were only made possible by first the availability of reliable sensor technology for O₂ measurements and second by enhancing spatial and temporal resolutions of these measurements. Thus, further development of sensor technology and its implementation into novel platforms such as profiling floats or gliders will provide valuable insights into highly dynamic biogeochemical processes. The prototype float developed over the course of this thesis showed promising results towards this direction. Used *p*CO₂ sensor technology for this prototype is still subject to further improvements and recent efforts are being underway to integrate these sensors into novel autonomous platforms such as a Wave Glider or a moored profiler. Both platforms would complement current time series observations at CVOO by significantly increasing resolution of high quality biogeochemical observations in space and time.

Beside this novel direction for biogeochemical observations first results from CVOO demonstrated the importance of dedicated time series observations for an assessment of seasonal ecosystem variability. However, establishment of accurate time series observations in a sustainable manner

turned out to be highly ambitious. Thus, more sustained effort has to be made in order to ensure high quality of data and to maintain continuous operations. The core sampling program has to be maintained properly and quality controlled data must be made available to the scientific community. As the time series grows the more detailed and valuable information can be extracted from it and thereby detect and quantify long-term trends and changes such as ocean acidification or the ETNA's function as a net source or sink for atmospheric CO₂.

Finally, both autonomous as well as classical time series observations have to be combined with each other in an elaborate manner. Such an approach will help to better address the question of which impact for instance observed episodic dust deposition events or anoxic mesoscale water masses have on biogeochemical processes in this region.

6 References

- Alkire, M. B. and Coauthors, 2012: Estimates of net community production and export using high-resolution, Lagrangian measurements of O₂, NO₃⁻, and POC through the evolution of a spring diatom bloom in the North Atlantic. *Deep-Sea Res., Part I*, **64**, 157–174.
- Allredge, A. L., and Y. Cohen, 1987: Can microscale chemical patches persist in the sea? Microelectrode study of marine snow, fecal pellets. *Science*, **235**, 689–691.
- Bates, N. R., 2001: Interannual variability of oceanic CO₂ and biogeochemical properties in the Western North Atlantic subtropical gyre. *Deep-Sea Res., Part II*, **48**, 1507–1528, doi:DOI: 10.1016/S0967-0645(00)00151-X.
- Bates, N. R., 2007: Interannual variability of the oceanic CO₂ sink in the subtropical gyre of the North Atlantic Ocean over the last 2 decades. *J. Geophys. Res.*, **112**, C09013, doi:10.1029/2006JC003759.
- Bates, N. R., A. F. Michaels, and A. H. Knap, 1996: Seasonal and interannual variability of oceanic carbon dioxide species at the U.S. JGOFS Bermuda Atlantic Time-series Study (BATS) site. *Deep-Sea Res., Part II*, **43**, 347–383, doi:DOI: 10.1016/0967-0645(95)00093-3.
- Bates, N. R., A. C. Pequignet, R. J. Johnson, and N. Gruber, 2002: A short-term sink for atmospheric CO₂ in subtropical mode water of the North Atlantic Ocean. *Nature*, **420**, 489–493, doi:10.1038/nature01253.
- Benson, B. B., and D. Krause, 1984: The concentration and isotopic fractionation of oxygen dissolved in freshwater and seawater in equilibrium with the atmosphere. *Limnol. Oceanogr.*, **29**, 620–632, doi:10.1016/0198-0254(84)93289-8.
- Bishop, J. K. B., T. J. Wood, R. E. Davis, and J. T. Sherman, 2004: Robotic Observations of Enhanced Carbon Biomass and Export at 55°S During SOFeX. *Science*, **304**, 417–420.
- Bittig, H. C., B. Fiedler, T. Steinhoff, and A. Körtzinger, 2012: A Novel Electrochemical Calibration Setup for Oxygen Sensors. *Limnol. Oceanogr.: Methods*, **10**, 921–933.
- Boden, T. A., G. Marland, and R. J. Andres, 2012: Global, Regional, and National Fossil-Fuel CO₂ Emissions. *Information Analysis Center, Oak Ridge National Laboratory, U.S. Department of Energy, Oak Ridge, Tenn., U.S.A.*, doi:10.3334/CDIAC/00001_V2012.
- Boss, E., D. Swift, L. Taylor, P. Brickley, R. Zaneveld, S. Riser, M. J. Perry, and P. G. Strutton, 2008: Observations of pigment and particle distributions in the western North Atlantic from an autonomous float and ocean color satellite. *Limnol. Oceanogr.*, **53**, 2112–2122.
- Brandt, P., V. Hormann, A. Körtzinger, M. Visbeck, G. Krahnemann, L. Stramma, R. Lumpkin, and C. Schmid, 2010: Changes in the Ventilation of the Oxygen Minimum Zone of the Tropical North Atlantic. *J. Phys. Oceanogr.*, **40**, 1784–1801, doi:10.1175/2010JPO4301.1.
- Brewer, P. G., and E. T. Peltzer, 2009: Limits to Marine Life. *Science*, **324**, 347–348.
- Byrne, R. H., and W. Yao, 2008: Procedures for measurement of carbonate ion concentrations in seawater by direct spectrophotometric observations of Pb(II) complexation. *Mar. Chem.*, **112**, 128–135, doi:10.1016/j.marchem.2008.07.009.
- Byrne, R. H., X. Liu, and E. A. Kaltenbacher, 2002: Spectrophotometric measurement of total inorganic carbon in aqueous solutions using a liquid core waveguide. *Anal. Chim. Acta*, **451**, 221–229, doi:10.1016/S0003-2670(01)01423-4.
- Byrne, R. H. and Coauthors, 2010: Sensors and Systems for in situ Observations of Marine Carbon Dioxide System Variables. *Proceedings of OceanObs'09: Sustained Ocean Observations and Information for Society*, J. Hall, D.E. Harrison, and D. Stammer, Eds., Venice, Italy, ESA Publication WPP-306.
- Carpenter, J. H., 1965: The accuracy of the Winkler method for dissolved oxygen analysis. *Limnol. Oceanogr.*, **10**, 135–140.
- Carpenter, L. and Coauthors, 2010: Seasonal characteristics of tropical marine boundary layer air measured at the Cape Verde Atmospheric Observatory. *J. Atmos. Chem.*, **67**, 87–140.

- Cayan, D. R., 1992: Latent and Sensible Heat Flux Anomalies over the Northern Oceans: Driving the Sea Surface Temperature. *J. Phys. Oceanogr.*, **22**, 859–881, doi:10.1175/1520-0485(1992)022<0859:LASHFA>2.0.CO;2.
- Chavez, F. P., and M. Messié, 2009: A comparison of Eastern Boundary Upwelling Ecosystems. *Prog. Oceanogr.*, **83**, 80–96.
- Chelton, D. B., P. Gaube, M. G. Schlax, J. J. Early, and R. M. Samelson, 2011a: The Influence of Nonlinear Mesoscale Eddies on Near-Surface Oceanic Chlorophyll. *Science*, **334**, 328–332.
- Chelton, D. B., M. G. Schlax, and R. M. Samelson, 2011b: Global observations of nonlinear mesoscale eddies. *Prog. Oceanogr.*, **91**, 167–216, doi:10.1016/j.pocean.2011.01.002.
- Clark Jr., L. C., 1959: Electrochemical device for chemical analysis. US Patent, 2,913,386.
- Davis, R. E., J. T. Sherman, and J. Dufour, 2001: Profiling ALACEs and Other Advances in Autonomous Subsurface Floats. *J. Atmos. Oceanic Technol.*, **18**, 982–993, doi:10.1175/1520-0426(2001)018<0982:PAAOAI>2.0.CO;2.
- DeGrandpre, M. D., T. R. Hammar, S. P. Smith, and F. L. Sayles, 1995: In-Situ Measurements of Seawater $p\text{CO}_2$. *Limnol. Oceanogr.*, **40**, 969–975.
- Diaz, R. J., and R. Rosenberg, 2008: Spreading Dead Zones and Consequences for Marine Ecosystems. *Science*, **321**, 926–929.
- Dickson, A., C. Sabine, and J. Christian (Eds.), 2007: Guide to best practices for ocean CO_2 measurements. *PICES Special Publication*, **3**, 191 pp.
- Dickson, A. G., 2010: Standards for Ocean Measurements. *Oceanography*, **23**, 34–47.
- Doney, S. C., V. J. Fabry, R. A. Feely, and J. A. Kleypas, 2009: Ocean Acidification: The Other CO_2 Problem. *Ann. Rev. Mar. Sci.*, **1**, 169–192, doi:10.1146/annurev.marine.010908.163834.
- Dore, J. E., R. Lukas, D. W. Sadler, and D. M. Karl, 2003: Climate-driven changes to the atmospheric CO_2 sink in the subtropical North Pacific Ocean. *Nature*, **424**, 754–757.
- Dore, J. E., R. Lukas, D. W. Sadler, M. J. Church, and D. M. Karl, 2009: Physical and biogeochemical modulation of ocean acidification in the central North Pacific. *Proc. Natl. Acad. Sci. USA.*, **106**, 12235–12240.
- Ducklow, H. W., S. C. Doney, and D. K. Steinberg, 2009: Contributions of Long-Term Research and Time-Series Observations to Marine Ecology and Biogeochemistry. *Ann. Rev. Mar. Sci.*, **1**, 279–302, doi:10.1146/annurev.marine.010908.163801.
- D’Asaro, E., and C. McNeil, 2007: Air–sea gas exchange at extreme wind speeds measured by autonomous oceanographic floats. *J. Marine Syst.*, **66**, 92–109, doi:10.1016/j.jmarsys.2006.06.007.
- Early, J. J., R. M. Samelson, and D. B. Chelton, 2011: The Evolution and Propagation of Quasigeostrophic Ocean Eddies. *J. Phys. Oceanogr.*, **41**, 1535–1555, doi:10.1175/2011JPO4601.1.
- Eckles, R. D., J. M. Welles, and K. Peterson, 1993: CO_2 and $\text{CO}_2/\text{H}_2\text{O}$ infrared gas analyzers. *Meas. Control-US*, **161**, 83–89.
- Edwards, B., D. Murphy, C. Janzen, and N. Larson, 2010: Calibration, Response, and Hysteresis in Deep-Sea Dissolved Oxygen Measurements. *J. Atmos. Oceanic Technol.*, **27**, 920–931, doi:10.1175/2009JTECHO693.1.
- Emerson, S., and C. Stump, 2010: Net biological oxygen production in the ocean—II: Remote in situ measurements of O_2 and N_2 in subarctic pacific surface waters. *Deep-Sea Res., Part I*, **57**, 1255–1265.
- Emerson, S., C. Stump, and D. Nicholson, 2008: Net biological oxygen production in the ocean: Remote in situ measurements of O_2 and N_2 in surface waters. *Global Biogeochem. Cycles*, **22**, 1–13, doi:10.1029/2007GB003095.
- Falkowski, P. and Coauthors, 2000: The Global Carbon Cycle: A Test of Our Knowledge of Earth as a System. *Science*, **290**, 291–296.
- Falkowski, P. G., D. Ziemann, Z. Kolber, and P. K. Bienfang, 1991: Role of eddy pumping in enhancing primary production in the ocean. *Nature*, **352**, 55–58.

- Fiedler, B., P. Fietzek, N. Vieira, P. Silva, H. C. Bittig, and A. Körtzinger, 2013: In situ CO₂ and O₂ measurements on a profiling float. *J. Atmos. Oceanic Technol.*, **30**, 112–126, doi:10.1175/JTECH-D-12-00043.1.
- Fietzek, P., S. Kramer, and D. Esser, 2011: Deployment of the HydroCTM (CO₂/CH₄) on stationary and mobile platforms - Merging the trends in the field of platform and sensor development. *Oceans 11 MTS/IEEE Conference*, Kona, Hawaii, USA.
- Fischer, T., D. Banyte, P. Brandt, M. Dengler, G. Krahnmann, T. Tanhua, and M. Visbeck, 2012: Diapycnal oxygen supply to the tropical North Atlantic oxygen minimum zone. *Biogeosciences Discussions*, **9**, 14291–14325, doi:10.5194/bgd-9-14291-2012.
- Friedrichs, G., J. Bock, F. Temps, P. Fietzek, A. Körtzinger, and D. W. R. Wallace, 2010: Toward continuous monitoring of seawater ¹³CO₂/¹²CO₂ isotope ratio and pCO₂: Performance of cavity ringdown spectroscopy and gas matrix effects. *Limnol. Oceanogr.: Methods*, **8**, 539–551, doi:10.4319/lom.2010.8.539.
- Gabric, A. J., L. Garcia, L. Van Camp, L. Nykjaer, W. Eifler, and W. Schrimpf, 1993: Offshore Export of Shelf Production in the Cape Blanc (Mauritania) Giant Filament as Derived From Coastal Zone Color Scanner Imagery. *J. Geophys. Res.*, **98**, 4697–4712, doi:10.1029/92JC01714.
- Garcia, H. E., and R. F. Keeling, 2001: On the global oxygen anomaly and air-sea flux. *J. Geophys. Res.*, **106**, 31155–31166, doi:10.1029/1999JC000200.
- Garcia, H. E., R. A. Locarnini, T. P. Boyer, J. I. Antonov, O. K. Baranova, M. W. Zweng, and D. R. Johnson, 2010: *World Ocean Atlas 2009, Volume 3 : Dissolved Oxygen, Apparent Oxygen Utilization, and Oxygen Saturation*. S. Levitus, Ed. NOAA Atlas NESDIS 70, U.S. Government Printing Office, Washington, D. C., 344 pp.
- García, H. E., and L. I. Gordon, 1992: Oxygen solubility in seawater: Better fitting equations. *Limnol. Oceanogr.*, **37**, 1307–1312, doi:10.4319/lo.1992.37.6.1307.
- González-Dávila, M., 2003: Seasonal and interannual variability of sea-surface carbon dioxide species at the European Station for Time Series in the Ocean at the Canary Islands (ESTOC) between 1996 and 2000. *Global Biogeochem. Cycles*, **17**, doi:10.1029/2002GB001993.
- Gruber, N., C. D. Keeling, and N. R. Bates, 2002: Interannual Variability in the North Atlantic Ocean Carbon Sink. *Science*, **298**, 2374–2378, doi:10.1126/science.1077077.
- Gruber, N. and Coauthors, 2010a: Toward an Integrated Observing System for Ocean Carbon and Biogeochemistry at a Time of Change. *Proceedings of OceanObs'09: Sustained Ocean Observations and Information for Society*, J. Hall, D.E. Harrison, and D. Stammer, Eds., Venice, Italy, ESA Publication WPP-306.
- Gruber, N. and Coauthors, 2010b: Adding oxygen to Argo: Developing a global in-situ observatory for ocean deoxygenation and biogeochemistry. *Proceedings of OceanObs'09: Sustained Ocean Observations and Information for Society*, J. Hall, D.E. Harrison, and D. Stammer, Eds., Venice, Italy, ESA Publication WPP-306.
- Gutiérrez, D., E. Enríquez, S. Purca, L. Quipúzcoa, R. Marquina, G. Flores, and M. Graco, 2008: Oxygenation episodes on the continental shelf of central Peru: Remote forcing and benthic ecosystem response. *Prog. Oceanogr.*, **79**, 177–189.
- Hagen, E., 2001: Northwest African upwelling scenario. *Oceanol. Acta*, **24**, 113–128.
- Hall, C. A. S., C. A. Ekdahl, and D. E. Wartenberg, 1975: A fifteen-year record of biotic metabolism in the Northern Hemisphere. *Nature*, **255**, 136–138.
- Hurrell, J. W., 1995: Decadal Trends in the North Atlantic Oscillation: Regional Temperatures and Precipitation. *Science*, **269**, 676–679.
- IPCC, 2005: IPCC special report on carbon dioxide capture and storage. Prepared by working group III of the Intergovernmental Panel on Climate Change. *IPCC Special Report on Carbon Dioxide Capture and Storage*, B. Metz, O. Davidson, H.. De Coninck, M. Loos, and L.A. Meyer, Eds., Vol. 2 of, Cambridge University Press, p. 442.

- Jenkins, W. J., 1982: Oxygen utilization rates in North Atlantic subtropical gyre and primary production in oligotrophic systems. *Nature*, **300**, 246–248.
- Jickells, T. D. and Coauthors, 2005: Global Iron Connections Between Desert Dust, Ocean Biogeochemistry, and Climate. *Science*, **308**, 67–71.
- Johnson, K. M., K. D. Wills, D. B. Butler, W. K. Johnson, and C. S. Wong, 1993: Coulometric total carbon dioxide analysis for marine studies: maximizing the performance of an automated gas extraction system and coulometric detector. *Mar. Chem.*, **44**, 167–187, doi:10.1016/0304-4203(93)90201-X.
- Johnson, K. S., J. a Needoba, S. C. Riser, and W. J. Showers, 2007: Chemical sensor networks for the aquatic environment. *Chem. Rev.*, **107**, 623–640, doi:10.1021/cr050354e.
- Johnson, K. S. and Coauthors, 2009: Observing biogeochemical cycles at global scales with profiling floats and gliders: prospects for a global array. *Oceanography*, **22**, 216–224.
- Johnson, K. S., S. C. Riser, and D. M. Karl, 2010: Nitrate supply from deep to near-surface waters of the North Pacific subtropical gyre. *Nature*, **465**, 1062–1065, doi:10.1038/nature09170.
- Kalvelage, T. and Coauthors, 2011: Oxygen Sensitivity of Anammox and Coupled N-Cycle Processes in Oxygen Minimum Zones. *PLoS ONE*, **6**, e29299, doi:10.1371/journal.pone.0029299.
- Kanwisher, J., 1959: Polarographic Oxygen Electrode. *Limnol. Oceanogr.*, **4**, 210–217.
- Karl, D. M., 2010: Oceanic Ecosystem Time-Series Programs: Ten Lessons Learned. *Oceanography*, **23**, 104–125.
- Karstensen, J., L. Stramma, and M. Visbeck, 2008: Oxygen minimum zones in the eastern tropical Atlantic and Pacific oceans. *Prog. Oceanogr.*, **77**, 331–350.
- Keeling, R., 1988: Measuring correlations between atmospheric oxygen and carbon dioxide mole fractions: A preliminary study in urban air. *J. Atmos. Chem.*, **7**, 153–176 LA – English, doi:10.1007/BF00048044.
- Keeling, R. F., A. Körtzinger, and N. Gruber, 2010: Ocean Deoxygenation in a Warming World. *Ann. Rev. Mar. Sci.*, **2**, 199–229, doi:10.1146/annurev.marine.010908.163855.
- Kostianoy, A. G., and A. G. Zatsepin, 1996: The West African coastal upwelling filaments and cross-frontal water exchange conditioned by them. *J. Marine Syst.*, **7**, 349–359, doi:10.1016/0924-7963(95)00029-1.
- Kuypers, M. M. M., G. Lavik, D. Woebken, M. Schmid, B. M. Fuchs, R. Amann, B. B. Jørgensen, and M. S. M. Jetten, 2005: Massive nitrogen loss from the Benguela upwelling system through anaerobic ammonium oxidation. *Proc. Natl. Acad. Sci. USA.*, **102**, 6478–6483.
- Körtzinger, A., 2010: Der globale Kohlenstoffkreislauf im Anthropozän. Betrachtung aus meereschemischer Perspektive. *Chem. unserer Zeit*, **44**, 118–129, doi:10.1002/ciuz.201000507.
- Körtzinger, A., H. Thomas, B. Schneider, N. Gronau, L. Mintrop, and J. C. Duinker, 1996: At-sea intercomparison of two newly designed underway $p\text{CO}_2$ systems - encouraging results. *Mar. Chem.*, **52**, 133–145.
- Körtzinger, A. and Coauthors, 2000: The international at-sea intercomparison of $f\text{CO}_2$ systems during the R/V Meteor Cruise 36/1 in the North Atlantic Ocean. *Mar. Chem.*, **72**, 171–192, doi:10.1016/S0304-4203(00)00080-3.
- Körtzinger, A., W. Koeve, P. Kähler, and L. Mintrop, 2001: C:N ratios in the mixed layer during the productive season in the northeast Atlantic Ocean. *Deep-Sea Res., Part I*, **48**, 661–688.
- Körtzinger, A., J. Schimanski, U. Send, and D. Wallace, 2004: The Ocean Takes a Deep Breath. *Science*, **306**, 1337.
- Körtzinger, A., J. Schimanski, and U. Send, 2005: High Quality Oxygen Measurements from Profiling Floats: A Promising New Technique. *J. Atmos. Oceanic Technol.*, **22**, 302, doi:10.1175/JTECH1701.1.
- Körtzinger, A., U. Send, D. W. R. Wallace, J. Karstensen, and M. DeGrandpre, 2008: Seasonal cycle of O_2 and $p\text{CO}_2$ in the central Labrador Sea: Atmospheric, biological, and physical implications. *Global Biogeochem. Cycles*, **22**, 1–16, doi:10.1029/2007GB003029.
- Lam, P. and Coauthors, 2009: Revising the nitrogen cycle in the Peruvian oxygen minimum zone. *Proc. Natl. Acad. Sci. USA.*, **106**, 4752–4757.

- Lee, K. and Coauthors, 2006: Global relationships of total alkalinity with salinity and temperature in surface waters of the world's oceans. *Geophys. Res. Lett.*, **33**, 1–5, doi:10.1029/2006GL027207.
- Lefèvre, N., and L. Merlivat, 2012: Carbon and oxygen net community production in the eastern tropical Atlantic estimated from a moored buoy. *Global Biogeochem. Cycles*, **26**, GB1009, doi:10.1029/2010GB004018.
- Lefèvre, N., J. P. Ciabrini, G. Michard, B. Briant, M. DuChaffaut, and L. Merlivat, 1993: A new optical sensor for $p\text{CO}_2$ measurements in seawater. *Mar. Chem.*, **42**, 189–198, doi:10.1016/0304-4203(93)90011-C.
- Lenton, A. and Coauthors, 2012: The observed evolution of oceanic $p\text{CO}_2$ and its drivers over the last two decades. *Global Biogeochem. Cycles*, **26**, GB2021, doi:10.1029/2011GB004095.
- Liss, P. S., and L. Merlivat, 1986: Air–sea gas exchange rates: introduction and synthesis. *The Role of Air–Sea Exchange in Geochemical Cycling*, P. Buat-Menard, Ed., D. Reidel Publishing Co., Dordrecht, Netherlands, 113–127.
- Loucaides, S. and Coauthors, 2012: Biological and physical forcing of carbonate chemistry in an upwelling filament off northwest Africa: Results from a Lagrangian study. *Global Biogeochem. Cycles*, **26**, GB3008, doi:10.1029/2011GB004216.
- Lueker, T. J., 2003: Coastal upwelling air-sea fluxes revealed in atmospheric observations of O_2/N_2 , CO_2 and N_2O . *Geophys. Res. Lett.*, **30**, 1–4, doi:10.1029/2002GL016615.
- Lukas, R., and F. Santiago-Mandujano, 2001: Extreme water mass anomaly observed in the Hawaii ocean time series. *Geophys. Res. Lett.*, **28**, 2931–2934, doi:10.1029/2001GL013099.
- Lumpkin, R., and S. L. Garzoli, 2005: Near-surface circulation in the Tropical Atlantic Ocean. *Deep-Sea Res., Part I*, **52**, 495–518, doi:10.1016/j.dsr.2004.09.001.
- Luz, B., and E. Barkan, 2009: Net and gross oxygen production from O_2/Ar , $^{17}\text{O}/^{16}\text{O}$ and $^{18}\text{O}/^{16}\text{O}$ ratios. *Aquat. Microb. Ecol.*, **56**, 133–145.
- Martin, J. H., G. A. Knauer, D. M. Karl, and W. W. Broenkow, 1987: VERTEX: carbon cycling in the northeast Pacific. *Deep-Sea Res., Part I*, **34**, 267–285, doi:10.1016/0198-0149(87)90086-0.
- Martz, T., K. Johnson, and S. Riser, 2008: Ocean metabolism observed with oxygen sensors on profiling floats in the South Pacific. *Limnol. Oceanogr.*, **53**, 2094–2111.
- Martz, T. R., J. G. Connery, and K. S. Johnson, 2010: Testing the Honeywell Durafet for seawater pH applications. *Limnol. Oceanogr.: Methods*, **8**, 172–184, doi:10.4319/lom.2010.8.172.
- McDermitt, D. K., R. D. Eckles, G. L. Biggs, and J. M. Welles, 1993: Effects on temperature and pressure on CO_2 infrared absorption with special emphasis on problems resulting from operation at high flow rates. *LI-COR Inc, Lincoln, USA*, **117**, 1–12.
- McGillicuddy, D. J. and Coauthors, 2007: Eddy/Wind Interactions Stimulate Extraordinary Mid-Ocean Plankton Blooms. *Science*, **316**, 1021–1026, doi:10.1126/science.1136256.
- McNeil, C., E. D'Asaro, B. Johnson, and M. Horn, 2006: A Gas Tension Device with Response Times of Minutes. *J. Atmos. Oceanic Technol.*, **23**, 1539, doi:10.1175/JTECH1974.1.
- Menkes, C. E. and Coauthors, 2002: A whirling ecosystem in the equatorial Atlantic. *Geophys. Res. Lett.*, **29**, 1553, doi:10.1029/2001GL014576.
- Merkel, T. C., V. I. Bondar, K. Nagai, B. D. Freeman, and I. Pinnau, 2000: Gas sorption, diffusion, and permeation in poly(dimethylsiloxane). *J. Polym. Sci., Part B: Polym. Phys.*, **38**, 415–434, doi:10.1002/(SICI)1099-0488(20000201)38:3<415::AID-POLB8>3.0.CO;2-Z.
- Messié, M., J. Ledesma, D. D. Kolber, R. P. Michisaki, D. G. Foley, and F. P. Chavez, 2009: Potential new production estimates in four eastern boundary upwelling ecosystems. *Prog. Oceanogr.*, **83**, 151–158, doi:10.1016/j.pocean.2009.07.018.
- Michaels, A. F., N. R. Bates, K. O. Buesseler, C. A. Carlson, and A. H. Knap, 1994: Carbon-cycle imbalances in the Sargasso Sea. *Nature*, **372**, 537–540.
- Millero, F. J., 2007: The marine inorganic carbon cycle. *Chem. Rev.*, **107**, 308–341, doi:10.1021/cr0503557.

- Minas, H. J., T. T. Packard, M. Minas, and B. Coste, 1982: An Analysis of the Production-Regeneration System in the Costal Upwelling Area off NW Africa based on Oxygen, Nitrate and Ammonium Distributions. *J. Mar. Res.*, **40**, 615–641.
- Mintrop, L., F. F. Perez, M. Gonzalez-Davila, M. J. Santana-Casiano, and A. Körtzinger, 2000: Alkalinity determination by potentiometry: Intercalibration using three different methods. *Cienc. Mar.*, **26**, 23–37.
- Mittelstaedt, E., 1991: The ocean boundary along the northwest African coast: Circulation and oceanographic properties at the sea surface. *Prog. Oceanogr.*, **26**, 307–355.
- Mojica Prieto, F. J., and F. J. Millero, 2002: The values of $pK_1 + pK_2$ for the dissociation of carbonic acid in seawater. *Geochim. Cosmochim. Acta*, **66**, 2529–2540.
- Moore, C. M. and Coauthors, 2009: Large-scale distribution of Atlantic nitrogen fixation controlled by iron availability. *Nat. Geosci.*, **2**, 867–871.
- Moore, T. S., M. D. DeGrandpre, C. L. Sabine, R. C. Hamme, C. J. Zappa, W. R. McGillis, R. A. Feely, and W. M. Drennan, 2011: Sea surface pCO_2 and O_2 in the Southern Ocean during the austral fall, 2008. *J. Geophys. Res.*, **116**, C00F11, doi:10.1029/2010JC006560.
- Morel, A., H. Claustre, and B. Gentili, 2010: The most oligotrophic subtropical zones of the global ocean: similarities and differences in terms of chlorophyll and yellow substance. *Biogeosciences*, **7**, 3139–3151, doi:10.5194/bg-7-3139-2010.
- Neuer, S., M. E. Torres-Padrón, M. D. Gelado-Caballero, M. J. Rueda, J. Hernández-Brito, R. Davenport, and G. Wefer, 2004: Dust deposition pulses to the eastern subtropical North Atlantic gyre: Does ocean's biogeochemistry respond? *Global Biogeochem. Cycles*, **18**, GB4020, doi:10.1029/2004GB002228.
- Neuer, S. and Coauthors, 2007: Biogeochemistry and hydrography in the eastern subtropical North Atlantic gyre. Results from the European time-series station ESTOC. *Prog. Oceanogr.*, **72**, 1–29.
- Nightingale, P. D., G. Malin, C. S. Law, A. J. Watson, P. S. Liss, M. I. Liddicoat, J. Boutin, and R. C. Upstill-Goddard, 2000: In situ evaluation of air-sea gas exchange parameterizations using novel conservative and volatile tracers. *Global Biogeochem. Cycles*, **14**, 373–387, doi:10.1029/1999GB900091.
- Orr, J. C. and Coauthors, 2005: Anthropogenic ocean acidification over the twenty-first century and its impact on calcifying organisms. *Nature*, **437**, 681–686.
- Oschlies, A., and V. Garçon, 1998: Eddy-induced enhancement of primary production in a model of the North Atlantic Ocean. *Nature*, **394**, 266–269.
- Parard, G., N. Lefèvre, and J. Boutin, 2010: Sea water fugacity of CO_2 at the PIRATA mooring at 6°S, 10°W. *Tellus B*, **62**, 636–648, doi:10.1111/j.1600-0889.2010.00503.x.
- Pastor, M., J. Pelegri, a Hernandezguerra, J. Font, J. Salat, and M. Emelianov, 2008: Water and nutrient fluxes off Northwest Africa. *Cont. Shelf Res.*, **28**, 915–936, doi:10.1016/j.csr.2008.01.011.
- Pennington, J. T., K. L. Mahoney, V. S. Kuwahara, D. D. Kolber, R. Calienes, and F. P. Chavez, 2006: Primary production in the eastern tropical Pacific: A review. *Prog. Oceanogr.*, **69**, 285–317.
- Pfeil, B., A. Olsen, and D. C. E. Bakker, 2011: A uniform, quality controlled, Surface Ocean CO_2 Atlas (SOCAT). *Earth Syst. Sci. Data*, in preparation.
- Pierrot, D. and Coauthors, 2009: Recommendations for autonomous underway pCO_2 measuring systems and data-reduction routines. *Deep-Sea Res., Part II*, **56**, 512–522, doi:DOI: 10.1016/j.dsr2.2008.12.005.
- Prabhakar, R. S., R. Raharjo, L. G. Toy, H. Lin, and B. D. Freeman, 2005: Self-Consistent Model of Concentration and Temperature Dependence of Permeability in Rubbery Polymers. *Ind. Eng. Chem. Res.*, **44**, 1547–1556, doi:10.1021/ie0492909.
- Riebesell, U., I. Zondervan, B. Rost, P. D. Tortell, R. E. Zeebe, and F. M. Morel, 2000: Reduced calcification of marine plankton in response to increased atmospheric CO_2 . *Nature*, **407**, 364–367.
- Riser, S. C., and K. S. Johnson, 2008: Net production of oxygen in the subtropical ocean. *Nature*, **451**, 323–325, doi:10.1038/nature06441.
- Risien, C. M., and D. B. Chelton, 2008: A Global Climatology of Surface Wind and Wind Stress Fields from Eight Years of QuikSCAT Scatterometer Data. *J. Phys. Oceanogr.*, **38**, 2379–2413, doi:10.1175/2008JPO3881.1.

- Robb, W. L., 1968: Thin silicone membranes - Their permeation properties and some applications. *Ann. NY. Acad. Sci.*, 119–137.
- Roemmich, D., S. Riser, R. Davis, and Y. Desaubies, 2004: Autonomous profiling floats: Workhorse for broadscale ocean observations. *Mar. Technol. Soc. J.*, **38**, 31–39, doi:10.4031/002533204787522802.
- Roemmich, D., G. Johnson, S. Riser, R. Davis, and J. Gilson, 2009: The Argo Program: observing the global ocean with profiling floats. *Oceanography*, **22**, 34–43.
- Rogner, H. H., D. Zhou, R. Bradley, P. Crabbé, O. Edenhofer, B. Hare (Australia), L. Kuijpers, and M. Yamaguchi, 2007: Introduction. In *Climate Change 2007: Mitigation. Contribution of Working Group III to the Fourth Assessment Report of the Intergovernmental Panel on Climate Change*. B. Metz, O.R. Davidson, P.R. Bosch, R. Dave, and L.A. Meyer, Eds., Cambridge University Press.
- Sabine, C. L., and T. Tanhua, 2010: Estimation of Anthropogenic CO₂ Inventories in the Ocean. *Ann. Rev. Mar. Sci.*, **2**, 269–292, doi:10.1146/annurev-marine-120308-080947.
- Sabine, C. L. and Coauthors, 2004: The Oceanic Sink for Anthropogenic CO₂. *Science*, **305**, 367–371.
- Sarmiento, J. L., and N. Gruber, 2006: *Ocean Biogeochemical Dynamics*. Princeton University Press, Princeton, New Jersey, USA.
- Sarthou, G. and Coauthors, 2003: Atmospheric iron deposition and sea-surface dissolved iron concentrations in the eastern Atlantic Ocean. *Deep-Sea Res., Part I*, **50**, 1339–1352.
- Sarthou, G. and Coauthors, 2007: Influence of atmospheric inputs on the iron distribution in the subtropical North-East Atlantic Ocean. *Mar. Chem.*, **104**, 186–202.
- Schepanski, K., I. Tegen, and A. Macke, 2009: Saharan dust transport and deposition towards the tropical northern Atlantic. *Atmos. Chem. Phys.*, **9**, 1173–1189, doi:10.5194/acp-9-1173-2009.
- Schollaert, S. E., J. A. Yoder, J. E. O'Reilly, and D. L. Westphal, 2003: Influence of dust and sulfate aerosols on ocean color spectra and chlorophyll a concentrations derived from SeaWiFS off the U.S. east coast. *J. Geophys. Res.*, **108**, 3191, doi:10.1029/2000JC000555.
- Seidel, M. P., M. D. DeGrandpre, and A. G. Dickson, 2008: A sensor for in situ indicator-based measurements of seawater pH. *Mar. Chem.*, **109**, 18–28, doi:10.1016/j.marchem.2007.11.013.
- Severinghaus, J. W., and A. F. Bradley, 1958: Electrodes for Blood pO₂ and pCO₂ Determination. *J. Appl. Physiol.*, **13**, 515–520.
- Solomon, S., D. Qin, M. Manning, Z. Chen, M. Marquis, K. B. Averyt, M. Tignor, and H. L. Miller, 2007: *IPCC, 2007: Climate Change 2007: The Physical Science Basis. Contribution of Working Group I to the Fourth Assessment Report of the Intergovernmental Panel on Climate Change*. S. Solomon, D. Qin, M. Manning, Z. Chen, M. Marquis, K.B. Averyt, M. Tignor, and H.L. Miller, Eds. Cambridge University Press.
- Steinberg, D. K., C. A. Carlson, N. R. Bates, R. J. Johnson, A. F. Michaels, and A. H. Knap, 2001: Overview of the US JGOFS Bermuda Atlantic Time-series Study (BATS): a decade-scale look at ocean biology and biogeochemistry. *Deep-Sea Res., Part II*, **48**, 1405–1447, doi:DOI: 10.1016/S0967-0645(00)00148-X.
- Steinhoff, T., H. W. Bange, A. Kock, D. W. R. Wallace, and A. Körtzinger, 2012: Biological productivity in the Mauritanian upwelling estimated with a triple gas approach. *Biogeosciences Discussions*, **9**, 4853–4875, doi:10.5194/bgd-9-4853-2012.
- Stephens, B. B., R. F. Keeling, M. Heimann, K. D. Six, R. Murnane, and K. Caldeira, 1998: Testing global ocean carbon cycle models using measurements of atmospheric O₂ and CO₂ concentration. *Global Biogeochem. Cycles*, **12**, 213–230, doi:10.1029/97GB03500.
- Stow, R. W., R. F. Baer, and B. F. Randall, 1957: Rapid measurement of the tension of carbon dioxide in blood. *Arch. Phys. Med. Rehab.*, **38**, 646–650.
- Stramma, L., and G. Siedler, 1988: Seasonal Changes in the North Atlantic Subtropical Gyre. *J. Geophys. Res.*, **93**, 8111–8118, doi:10.1029/JC093iC07p08111.
- Stramma, L., S. Hüttl, and J. Schafstall, 2005: Water masses and currents in the upper tropical northeast Atlantic off northwest Africa. *J. Geophys. Res.*, **110**, C12006, doi:10.1029/2005JC002939.

- Stramma, L., G. C. Johnson, J. Sprintall, and V. Mohrholz, 2008: Expanding Oxygen-Minimum Zones in the Tropical Oceans. *Science*, **320**, 655–658.
- Stramma, L., M. Visbeck, P. Brandt, T. Tanhua, and D. Wallace, 2009: Deoxygenation in the oxygen minimum zone of the eastern tropical North Atlantic. *Geophys. Res. Lett.*, **36**, L20607, doi:10.1029/2009GL039593.
- Stramma, L. and Coauthors, 2012: Expansion of oxygen minimum zones may reduce available habitat for tropical pelagic fishes. *Nature Clim. Change*, **2**, 33–37.
- Stramski, D., and J. Tegowski, 2001: Effects of intermittent entrainment of air bubbles by breaking wind waves on ocean reflectance and underwater light field. *J. Geophys. Res.*, **106**, 31345–31360, doi:10.1029/2000JC000461.
- Sweeney, C., E. Gloor, A. R. Jacobson, R. M. Key, G. McKinley, J. L. Sarmiento, and R. Wanninkhof, 2007: Constraining global air-sea gas exchange for CO₂ with recent bomb ¹⁴C measurements. *Global Biogeochem. Cycles*, **21**, GB2015, doi:10.1029/2006GB002784.
- Takahashi, T., 1961: Carbon dioxide in the atmosphere and in Atlantic Ocean water. *J. Geophys. Res.*, **66**, 477–494.
- Takahashi, T., J. Olafsson, J. G. Goddard, D. W. Chipman, and S. C. Sutherland, 1993: Seasonal variation of CO₂ and nutrients in the high-latitude surface oceans: A comparative study. *Global Biogeochem. Cycles*, **7**, 843–878.
- Takahashi, T. and Coauthors, 2009: Climatological mean and decadal change in surface ocean pCO₂, and net sea–air CO₂ flux over the global oceans. *Deep-Sea Res., Part II*, **56**, 554–577, doi:10.1016/j.dsr2.2008.12.009.
- Tamburri, M. N. and Coauthors, 2011: Alliance for Coastal Technologies: Advancing Moored pCO₂ Instruments in Coastal Waters. *Mar. Technol. Soc. J.*, **45**, 43–51, doi:10.4031/MTSJ.45.1.4.
- Tengberg, A. and Coauthors, 2006: Evaluation of a lifetime-based optode to measure oxygen in aquatic systems. *Limnol. Oceanogr.: Methods*, **4**, 7–17.
- Tomczak, M., 1981: An analysis of mixing in the frontal zone of South and North Atlantic Central Water off North-West Africa. *Prog. Oceanogr.*, **10**, 173–192, doi:10.1016/0079-6611(81)90011-2.
- Uchida, H., T. Kawano, I. Kaneko, and M. Fukasawa, 2008: In Situ Calibration of Optode-Based Oxygen Sensors. *J. Atmos. Oceanic Technol.*, **25**, 2271, doi:10.1175/2008JTECHO549.1.
- Van-Der-Laan-Luijckx, I. T., U. Karstens, J. Steinbach, C. Gerbig, C. Sirignano, R. E. M. Neubert, S. van der Laan, and H. A. J. Meijer, 2010: CO₂, Delta-O₂/N₂ and APO: observations from the Lutjewad, Mace Head and F3 platform flask sampling network. *Atmos. Chem. Phys.*, **10**, 10691–10704, doi:10.5194/acp-10-10691-2010.
- Van-Leeuwen, P. J., 2007: The Propagation Mechanism of a Vortex on the β Plane. *J. Phys. Oceanogr.*, **37**, 2316–2330, doi:10.1175/JPO3107.1.
- Vaquer-Sunyer, R., and C. M. Duarte, 2008: Thresholds of hypoxia for marine biodiversity. *Proc. Natl. Acad. Sci. USA.*, **105**, 15452–15457.
- Wang, Z. A., X. Liu, R. H. Byrne, R. Wanninkhof, R. E. Bernstein, E. A. Kaltenbacher, and J. Patten, 2007: Simultaneous spectrophotometric flow-through measurements of pH, carbon dioxide fugacity, and total inorganic carbon in seawater. *Anal. Chim. Acta*, **596**, 23–36.
- Wanninkhof, R., 1992: Relationship Between Wind Speed and Gas Exchange Over the Ocean. *J. Geophys. Res.*, **97**, 7373–7382, doi:10.1029/92JC00188.
- Watson, A. J. and Coauthors, 2009: Tracking the variable North Atlantic sink for atmospheric CO₂. *Science*, **326**, 1391–1393, doi:10.1126/science.1177394.
- Weiss, R., 1980: Nitrous oxide solubility in water and seawater. *Mar. Chem.*, **8**, 347–359, doi:10.1016/0304-4203(80)90024-9.
- Weiss, R. F., 1974: Carbon dioxide in water and seawater: the solubility of a non-ideal gas. *Mar. Chem.*, **2**, 203–215.

- Willett, C. S., R. R. Leben, and M. F. Lavín, 2006: Eddies and Tropical Instability Waves in the eastern tropical Pacific: A review. *Prog. Oceanogr.*, **69**, 218–238, doi:10.1016/j.pocean.2006.03.010.
- Winkler, L. W., 1888: The determination of dissolved oxygen. *Ber. Dtsch. Chem. Ges.*, **21**, 2843–2846.
- Wolf-Gladrow, D. A., R. E. Zeebe, C. Klaas, A. Körtzinger, and A. G. Dickson, 2007: Total alkalinity: The explicit conservative expression and its application to biogeochemical processes. *Mar. Chem.*, **106**, 287–300.
- Wright, J. J., K. M. Konwar, and S. J. Hallam, 2012: Microbial ecology of expanding oxygen minimum zones. *Nat. Rev. Microbiol.*, **10**, 381–394.
- Zehr, J. P., 2009: New twist on nitrogen cycling in oceanic oxygen minimum zones. *Proc. Natl. Acad. Sci. USA.*, **106**, 4575–4576.

7 Acknowledgements

First of all, I would like to thank my doctoral adviser Prof. Dr. Arne Körtzinger who gave me the opportunity to work on this exciting project. Arne is always ready to help and advise me whenever support is needed; his open mind for new ideas and approaches has greatly fostered the outcome of this thesis work.

Furthermore, I would very much like to thank my friends and CVOO colleagues from Cape Verde – Ivanice, Nuno, Péricles and Carlos. Without their motivation and tremendous effort for this ambitious bilateral project we would not have achieved any success. *...Muit'obrigad pa besot apoie e grande morabeza na kab verd!*

I also would like to acknowledge my colleagues from the CVOO team at GEOMAR: Cordula, Martina and Sebastian for their highly motivated way of pushing things forward. Acknowledgement is also made to Hermann Bange and Douglas Wallace for their commitment for the BMBF project SOPRAN and the EU project “TENATSO”, which facilitated the outcome of this thesis and provided funding.

Thanks are also due to the (C)O₂ working group and all my colleagues from the chemical oceanography department at GEOMAR. I found the “working environment” always very stimulating, productive, and more importantly, very pleasant in terms of personal cooperation. Many special thanks to my office fellows who endured all the hours I spent on the phone... and special thanks to Peer, who usually spent the same amount of time at the other end of the line.

For receiving exciting data from CVAO I would like to make acknowledgements to Elena Kozlova, Martina Heimann, Konrad Müller and Katie Read. I also greatly appreciated last-minute proofreading by Chrissi and Franzì.

I'm very grateful for all the encouragement I received from my parents, my brother and my grandmother during my studies in Kiel.

Finally, I particularly would like to thank two persons whose extensive support helped me throughout this PhD thesis:

Tobi was always present as a friend and a colleague. He was the first person to approach when things became complicated and he always found a solution to the problem. Additionally, during the final stage of my PhD he helped considerably by covering for me.

However, the fundament to withstand the PhD was clearly Tinaa. This project gave me the occasion to meet her for the first time... which has changed my life. Finally, Tina definitely has given me the strength to finish this thesis.

I. Appendix

I.a Abbreviations

1D	1-dimensional
1G	1 st generation
2G	2 nd generation
ACME	Mode-water type anticyclonic eddy
AMSR-E	Advanced Microwave Scanning Radiometer - Earth Observing System; satellite data
APEX	Autonomous Profiling Explorer; profiling float
APO	Atmospheric Potential Oxygen
Argo	International research collaboration (profiling float network)
ARGOS	satellite array for real-time tracking of mobile transmitters
ASE	Air-sea gas exchange
AUV	Autonomous underwater vehicle
BATS	Bermuda Atlantic Time Series
CE	Cyclonic Eddy
Chl a	Chlorophyll a
CRM	Certified reference material
CRR	Carbon remineralization rate
CTD	Conductivity-temperature-depth
CVAO	Cape Verde Atmospheric Observatory
CVFZ	Cape Verde frontal zone
CVOO	Cape Verde Ocean Observatory
DIC	Dissolved inorganic carbon
EBUS	Eastern boundary upwelling system
Eqn.	Equation
ESTOC	European Station for Time Series in the Ocean
ETA / ETNA	Eastern tropical North Atlantic
GO	General Oceanics
GPS	Global Positioning System
(H)GTD	(Hurricane) gas tension device; measure of total gas pressure
HOT	Hawaii Ocean Time Series
IR	Infrared
ITCZ	Intertropical Convergence Zone
ML(D)	Mixed layer (depth)
MODIS	Moderate Resolution Imaging Spectroradiometer
NACW	North Atlantic central water
NAO	North Atlantic Oscillation
NCEP	National Centers for Environmental Prediction; providing reanalysis data
NCP	Net community production
NDB	Niskin database
nDIC	Normalized dissolved inorganic carbon
NDIR	Non-dispersive infrared
NE	Northeast
NEMO	Navigating European Marine Observer; profiling float
NOAA	National Oceanic and Atmospheric Administration
n-pCO ₂	Normalized CO ₂ partial pressure
OMZ	Oxygen minimum zone
OPO	Oceanic Potential Oxygen
OUR	Oxygen utilization rate
PAR	Photosynthetically active radiation
pCO ₂	CO ₂ partial pressure
PDMS	Polydimethylsiloxane
PFA	Perfluoroalkoxy

pH	Decimal logarithm of the reciprocal of the H ⁺ activity in seawater
pO ₂	Oxygen partial pressure
POC	Particulate organic carbon
PON	Particulate organic nitrogen
ppmv	Parts per million by volume
PROVOR	Trademark name for a certain profiling float (MARTEC Inc.)
PSI	Pro-Oceanus Systems Incorporated
RI	Respiration Index
RMSE	Root mean square error
ROV	Remotely operated vehicle
SACW	South Atlantic central water
SAMI	Submersible Autonomous Moored Instrument; CO ₂ sensor
SFB	Sonderforschungsbereich (Collaborative Research Centre)
SLA	Sea level anomaly
SOLO	Sounding Oceanographic Lagrangian Observer
SOMMA	Single-Operator Multi-Metabolic Analyzer; DIC analyzing instrument
SOPRAN	Surface Ocean Processes in the Anthropocene; Research project
SST	Sea surface temperature
STS	Stop-then-sample
SUW	Subtropical underwater
TA	Total Alkalinity
TLC	Time-lag correction
TOC	Total organic carbon
TON	Total organic nitrogen
VINDTA	Versatile Instrument for the Determination of Titration Alkalinity
VOS	Volunteering observing ship
WOA09	World Ocean Atlas 2009
ZP	Zero point

1.b Cruises, Deployments and Data

Metadata presented in the following can be accessed via the CVOO data portal at GEOMAR:

<https://portal.geomar.de/group/cvoo/>

Field data of respective cruises and mooring deployments is currently being prepared for database publication pursuing a two-stage approach. First, quality controlled CVOO cruise data will be made available to project members and collaborators via a “Niskin Database” (NDB). Few data sets are already available via the CVOO data portal (see weblink above). Second, data sets are supposed to be published at Pangaea (<http://www.pangaea.de/>) within one year after publication in the NDB.

Data obtained from the profiling float prototypes can be accessed via the CVOO data portal and will be published at Pangaea in 2013.

Cruises occupied CVOO:

R/V	Cruise ID	From	To	Date	Parameter
Meteor	M-68/2	Recife (BR)	Mindelo (CV)	07/08/2006	O ₂ , DIC/TA
Meteor	M-68/3	Mindelo (CV)	Las Palmas (ES)	07/16/2006	O ₂ , DIC/TA
Poseidon	POS-348	Las Palmas (ES)	Las Palmas (ES)	02/13/2007	O ₂
Pelagia	64PE280	Fortaleza (BR)	Las Palmas (ES)	01/12/2008	DIC
L'Atalante	ATA-3	Dakar (SN)	Mindelo (CV)	02/19/2008	O ₂ , DIC/TA
L'Atalante	ATA-4	Mindelo (CV)	Mindelo (CV)	03/13/2008	O ₂
Maria S. Merian	MSM-08/1	Mindelo (CV)	Mindelo (CV)	04/20/2008	O ₂
Maria S. Merian	MSM-08/2	Mindelo (CV)	Emden (DE)	06/05/2008	O ₂
Islândia	ISL0008	Mindelo (CV)	Mindelo (CV)	09/26/2008	O ₂
Islândia	ISL0108	Mindelo (CV)	Mindelo (CV)	10/24/2008	O ₂ , DIC/TA
Islândia	ISL0208	Mindelo (CV)	Mindelo (CV)	11/20/2008	O ₂
Maria S. Merian	MSM-10/1	Ponta Delgada (PT)	Mindelo (CV)	12/04/2008	O ₂
Islândia	ISL0109	Mindelo (CV)	Mindelo (CV)	03/11/2009	O ₂ , DIC/TA
Islândia	ISL0209	Mindelo (CV)	Mindelo (CV)	04/16/2009	O ₂
Islândia	ISL0309	Mindelo (CV)	Mindelo (CV)	05/30/2009	O ₂ , DIC/TA
Meteor	M-80/1	Mindelo (CV)	Mindelo (CV)	10/26/2009	O ₂ , DIC/TA
Meteor	M-80/2	Mindelo (CV)	Dakar (SN)	11/26/2009	O ₂
Polarstern	ANT-XXVI/4	Punta Arenas (CL)	Bremerhaven (DE)	05/04/2010	DIC/TA
Poseidon	POS-399/2	Las Palmas (ES)	Las Palmas (ES)	06/04/2010	O ₂ , DIC/TA
Meteor	M-83/1	Las Palmas (ES)	Mindelo (CV)	10/18/2010	DIC/TA
Bebiche	Beb_D4	Mindelo (CV)	Mindelo (CV)	11/09/2010	O ₂ , DIC/TA
Maria S. Merian	MSM-18/2	Mindelo (CV)	Mindelo (CV)	05/12/2011	O ₂ , DIC/TA
Islândia	ISL_00111	Mindelo (CV)	Mindelo (CV)	05/25/2011	O ₂ , DIC/TA
Maria S. Merian	MSM-18/3	Mindelo (CV)	Libreville (GA)	06/23/2011	O ₂ , DIC/TA
Islândia	ISL_00311	Mindelo (CV)	Mindelo (CV)	09/23/2011	O ₂ , DIC/TA
Islândia	ISL_00611	Mindelo (CV)	Mindelo (CV)	11/30/2011	O ₂ , DIC/TA
Islândia	ISL_00112	Mindelo (CV)	Mindelo (CV)	03/23/2012	-
Islândia	ISL_00312	Mindelo (CV)	Mindelo (CV)	07/31/2012	O ₂
Islândia	ISL_00612	Mindelo (CV)	Mindelo (CV)	09/21/2012	O ₂ , DIC/TA

Mooring deployments at CVOO:

Deployment ID	Deployment Date	Deployment Cruise ID	Recovery Date	Recovery Cruise ID	Biogeochemical Parameters
CV01 (V440-01)	07/08/2006	M-68/2	02/19/2008	ATA-3	O ₂ (127 m), chl a (40 m)
CV02 (V440-02)	03/13/2008	ATA-4	10/26/2009	M-80/1	O ₂ (401, 127, 79 m)
CV03 (V440-03)	10/27/2009	M-80/1	05/11/2011	MSM-18/2	O ₂ (182, 54 m), CO ₂ /SAMI (181 m)
CV04 (V440-04)	06/18/2011	MSM-18/2	10/24/2012	MSM-22	O ₂ (181, 53 m), CO ₂ /SAMI (181, 87 m)
CV05 (V440-05)	10/25/2012	MSM-22	tbd	tbd	O ₂ (120, 45 m) , CO ₂ /SAMI-2 (121 m)

Float deployments at CVOO:

For detailed information please refer to section 3.2 (Table 3.3) and 3.2.2 (Table 1).

I.c Curriculum Vitae**Björn Fiedler**

Herderstr. 7
24116 Kiel
Germany
bfiedler@geomar.de

Date of birth: 04.12.1981

Place of birth: Emden, Germany

EDUCATION

- Since 07/2007 PhD student of Prof. Dr. Arne Körtzinger at the GEOMAR Helmholtz Centre for Ocean Research Kiel, Kiel, Germany. Thesis title: "CO₂ and O₂ Dynamics and Ocean-Atmosphere Fluxes in the Eastern Tropical North Atlantic".
- 04/2007 Diploma degree in Chemistry, Christian-Albrechts University of Kiel, Germany.
- 08/2006 – 04/2007 Preparation of diploma thesis at the Leibniz Institute for Marine Sciences (IFM-GEOMAR), Kiel, Germany. Thesis title: "Improvement of Processing Algorithms and Field Evaluation of an UV-Based Nitrate Sensor".
- 10/2001 – 04/2007 Studies of Chemistry, Christian-Albrechts University of Kiel, Germany.

PUBLICATIONS

- Zielinski, O., D. Voß, B. Saworski, **B. Fiedler**, and A. Körtzinger, 2011: Computation of nitrate concentrations in turbid coastal waters using an in situ ultraviolet spectrophotometer. *J. Sea Res.*, **65**(4), 456-460.
- Becker, M., N. Andersen, **B. Fiedler**, P. Fietzek, A. Körtzinger, T. Steinhoff, and G. Friedrichs, 2011: Using Cavity Ringdown Spectroscopy for Continuous Monitoring of $\delta^{13}\text{C}(\text{CO}_2)$ and $f\text{CO}_2$ in the Surface Ocean, *Limnol. Oceanogr.: Methods*, **10**, 752-766.
- Fiedler, B.**, P. Fietzek, N. Vieira, P. Silva, H. C. Bittig, and A. Körtzinger, 2013: In situ CO₂ and O₂ measurements on a profiling float, *J. Atmos. Oceanic Technol.*, **30**, 112-126.
- Bittig, H.C., **B. Fiedler**, T. Steinhoff, and A. Körtzinger, 2012: A novel electrochemical calibration setup for oxygen sensors and its use for the stability assessment of Aanderaa optodes, *Limnol. Oceanogr.: Methods*, **10**, 921-933.
- Karstensen, J., **B. Fiedler**, P. Brandt, R. Zantopp, J. Hahn, A. Körtzinger, M. Visbeck, G. Fischer, O. Melicio, and D.R. Wallace, 2012: Dead-Zone Eddies in the tropical Eastern North Atlantic Ocean, *Nature*, under review.

PRESENTATIONS

Talks:

Fiedler, B. und Körtzinger, A. (2009), High resolution $p\text{CO}_2$ measurements from profiling floats - a promising approach for in situ determination of air-sea fluxes of CO_2 and O_2 in the tropical eastern North Atlantic. In: *8th International Carbon Dioxide Conference*, 13th – 19th Sept. 2009, Jena, Germany.

Fiedler, B., Stiebens, V., Kanzow, T. und Eizaguirre, C. (2011), Animal-Borne Oxygen Measurements on Loggerhead Turtles - An Interdisciplinary Research Project at Cape Verde. In: *MASTS Workshop on Fluorometry, Chlorophyll and Oxygen measurements from Animal-borne platforms*, 3rd – 4th Oct. 2011, St. Andrews, Scotland.

Fiedler, B. (2012), From Teething Problems to Science Cases – First Scientific Highlights from the Cape Verde Ocean Observatory (CVOO). In: *Oceanography Seminar Series, University of Hawaii*, 4th Oct. 2012, Honolulu, Hawaii, USA.

Fiedler, B. (2012), When Chemical Oceanographers go Robotic - Resolving CO_2 and O_2 Dynamics in the Eastern Tropical North Atlantic. In: *XXIII. Dissertations in Chemical Oceanography Symposium (DISCO)*, 8th Oct. 2012, Lihue, Hawaii, USA.

Poster:

Fiedler, B., Kihm, C. und Körtzinger, A. (2008), A novel experimental approach for determining CO_2 and O_2 fluxes in the Tropical Eastern North Atlantic - Experimental setup and first tests. In: *International Symposium on Eastern Boundary Upwelling Ecosystems*, 2nd – 6th June 2008, Las Palmas, Gran Canaria, Spain.

Fiedler, B., T. Steinhoff, and A. Körtzinger (2012), Observing diel cycles of biogeochemical parameters with an autonomous lagrangian surface drifter. In: *SOLAS Open Science Conference*, 7th - 10th May 2012, Cle Elum, WA, USA.

Fiedler, B., P. Fietzek, N. Vieira, P. Silva, H. C. Bittig, and A. Körtzinger (2012), Going Beyond Argo- O_2 : In Situ CO_2 and O_2 Measurements on Argo Floats. In: *4th Argo Science Workshop*, 27th-29th Oct. 2012, Venice, Italy.

Fiedler, B., P. Silva, I. Monteiro, N. Vieira, M. Lohmann, J. Karstensen, T. Steinhoff, C. Zenk, C. Santos, A. Körtzinger (2012), The Cape Verde Ocean Observatory | CVOO. In: *Global Inter-comparability in a Changing Ocean – An International Time-Series Methods Workshop*, 28th - 30th Nov. 2012, BIOS, Bermuda.

OCEANOGRAPHIC CRUISES

Vessel	Cruise ID	Year	From – To	Duration (weeks)	Conducted work
R/V Polarstern	ANT 22/1	2004	Bremerhaven(DE) – Cape Town(SA)	4	underway sampling DIC/TA
M/V Falstaff	FALCO_03	2006	Bremerhaven(DE) – Charleston(US)	2	VOS line, underway $p\text{CO}_2/\text{O}_2$ measurements, O_2 titration
R/V Poseidon	P347	2007	Las Palmas(ES) – Las Palmas(ES)	3	Sensor validation (UV Nitrate), nutrient measurements
R/V Poseidon	P350	2007	Funchal(Portugal) – Lisbon(Portugal)	2	CTD/XBT measurements, data processing
R/V L'Atalante	ATA3	2008	Dakar(SN) – Mindelo(CV)	2.5	DIC/TA, $p\text{CO}_2$ measurements, Float deployments, 24h Drift stations
M/V Atlantic Companion	n/a	2008	Hamburg(DE) – Gothenburg(SE)	2/7	Maintenance of VOS line underway equipment
R/V Islândia	ISL_00808	2008	Mindelo(CV) – Mindelo(CV)	1/7	First monthly site occupation of CVOO, sampling of various parameters, Prototype Float deployment
R/V Islândia	ISL_01208	2008	Mindelo(CV) – Mindelo(CV)	3/7	Prototype Float recovery
R/V Polarstern	ANT 25/5	2009	Punta Arenas(CL) – Bremerhaven(DE)	6	Underway $p\text{CO}_2/\text{O}_2$ measurements, $p\text{CO}_2$ sensor evaluation
R/V Polarstern	ANT 26/4	2010	Punta Arenas(CL) – Bremerhaven	5.5	Underway $p\text{CO}_2/\text{O}_2$ measurements, $p\text{CO}_2$ and CRDS sensor evaluation
R/V Islândia	ISL_00111	2011	Mindelo(CV) – Mindelo(CV)	3/7	Prototype Float recovery and redeployment, collecting reference samples
R/V Maria S. Merian	MSM 18/3	2011	Mindelo(CV) – Libreville(GA)	4	DIC/TA, $p\text{CO}_2$ measurements, Float deployments, 24h Drift stations (Lagrangian Prototype Drifter)

Eidesstattliche Versicherung

Hiermit erkläre ich, dass ich die vorliegende Doktorarbeit - abgesehen von der Beratung durch meine Betreuer - selbstständig und ohne Zuhilfenahme unerlaubter Hilfsmittel erstellt habe. Alle benutzten Quellen habe ich vollständig angegeben. Die Zusammenarbeit mit Dritten habe ich detailliert und vollständig beschrieben. Weder diese noch eine ähnliche Arbeit wurden an einer anderen Abteilung oder Hochschule im Rahmen eines Prüfungsverfahrens vorgelegt, veröffentlicht oder zur Veröffentlichung vorgelegt. Ferner versichere ich, dass die Arbeit unter Einhaltung der Regeln guter wissenschaftlicher Praxis der Deutschen Forschungsgemeinschaft entstanden ist.

Kiel, den _____

Björn Fiedler